Solution Processable Nanostructures for Molecular Electronics

Jingyuan Zhu

A dissertation

Submitted to the School of Biological and Chemical Sciences

in partial fulfilment of the requirements of the Degree of

Doctor of Philosophy

Under the supervision of

Dr Matteo Palma

and

Professor William Gillin

Queen Mary, University of London

September 2017

Statement of Originality

I, Jingyuan Zhu, confirm that the research included within this thesis is my own work or that where it has been carried out in collaboration with, or supported by others, that this is duly acknowledged below and my contribution indicated. Previously published material is also acknowledged below.

I attest that I have exercised reasonable care to ensure that the work is original, and does not to the best of my knowledge break any UK law, infringe any third party's copyright or other Intellectual Property Right, or contain any confidential material.

I accept that the College has the right to use plagiarism detection software to check the electronic version of the thesis.

I confirm that this thesis has not been previously submitted for the award of a degree by this or any other university.

Signature: Jingyuan Zhu

Date: 13/09/2017

Details of collaboration and publications:

1. Jingyuan Zhu, Joseph Mcmorrow, Rachel Crespo-Otero, Geyou Ao, Ming Zheng, William P. W. P. William P. Gillin, et al. Solution-Processable Carbon Nanoelectrodes for Single-Molecule Investigations. Journal of the American Chemical Society. 2016;138(9):2905-8.

2. Jian Wang, Inmaculada Campos, Fan Wu, Jingyuan Zhu, Gleb B Sukhorukov, Matteo Palma, et al. The effect of gold nanoparticles on the impedance of microcapsules visualized by scanning photo-induced impedance microscopy. Electrochimica Acta. 2016;208:39-46.

3. Jian Wang, Fan Wu, Michael Watkinson, Jingyuan Zhu, Steffi Krause. “Click” patterning of self-assembled monolayers on hydrogen-terminated silicon surfaces and their characterisation using light-addressable potentiometric sensors. Langmuir. 2015;31(35):9646-54.

4. Catalina Vallejo-Giraldo, Ivo Calaresu, Jingyuan Zhu, Beom Soo Koo, Marc Fernandez, Dilip Thomas, Matteo Palma, Nathalia Peixoto, Nazar Farid, Gerard O'connor, Eilís Dowd, Laura Ballerini, Abhay Pandit, and Manus Jonathan Paul Biggs. The Neural Response to PEDOT:PTS Neuroelectrodes Topographically Functionalised via Microimprint Lithography. 2017. (submitted)

Abstract

In molecular electronics, the building material (traditionally elemental semiconductor) is replaced by single molecules or a nanoscale collection of molecules. Key to molecular electronics is the ability to precisely embed molecules into a nano device/structure and to manipulate large numbers of functional devices so they can be built in parallel, with each nano-device precisely located on the electrodes.

In this work, the assembly of organic and inorganic nanostructures dispersed in aqueous solutions has been controlled via chemical functionalisation. By combining this bottom-up assembly strategy with traditional top-down lithographic apporaches, the properties of these nanostructures have been investigated via a range of different techniques. The high degree of control on the molecular design through chemical synthesis and the scalability by self-assembly make this approach of interest in the field of molecular electronics.

In this regard, this dissertation presents a solution-based assembly method for producing molecular transport junctions employing metallic single-walled carbon nanotubes as nanoelectrodes. On solid substrates, electrical and electronic properties have been investigated by Conducting Atomic Force Microscopy (C-AFM). Furthermore, different strategies for asymmetric junction formation have been explored towards the development of a potential nanoscale Schottky diode.

Moreover, various patterning techniques based on shadow evaporation and AFM probe scratching have been investigated for the assembly of 1-D nanostructures. Nanostructures dispersed in solution were organised onto surfaces by means of

dielectrophoretic assembly, and their electronic properties was then measured by the means of a probing station.

In addition to the aforementioned organic nanostructures, we also report on the dispersion of boron nitride nanotubes (BNNT) by DNA wrapping, followed by the formation of nano-hybrids of boron nitride nanotubes and carbon nanotubes. Previously, researchers have adopted BNNT as a 2D dielectric layer. The work inspires me to adopt boron nitride nanotubes as 1D dielectric materials.

The techniques developed in this thesis are of interest for fundamental studies of electron transport in molecules and nanostructures. Addtionally, the approaches developed in this work may facilitate the advancement of new technologies for electronics, including, but not limited to, future circuits based on single-wall carbon/boron nitride nanotubes with specific functionality.

Table of Contents

List of figures

List of Acronyms

AFM	Atomic Force Microscopy
BCN	Bicyclo[6.1.0]nonyne
BNNT	Boron Nitride Nanotube
C-AFM	Conductive Atomic Force Microscopy
CNT	Carbon Nanotube
COSMO	Conductor-like Screening Model
DDS	Direct Digital Synthesizer
DEP	Dielectrophoresis
DFT	Density Functional Theory
DNA	Deoxyribonucleic acid
DPBS	Dulbecco's phosphate-buffered saline
EDC	1-ethyl-3-(3-dimethylaminopropyl)carbodiimide hydrochloride
FTIR	Fourier-transform infrared spectroscopy
HMD	Hexamethylenediamine
I-V	Current-Voltage
MES	2-(N-morpholino)ethanesulfonic acid
MTJ	Molecular Transport Junction
NHS	N-hydroxysuccinimide
NMP	N-Methyl-2-pyrrolidone
PEG	Polyethylene glycol
PF-TUNA	PeakForce-Tunneling
PMMA	Poly(methyl methacrylate)
PPD	P-Phenylenediamine
SEM	Scanning Electron Microscopy
SPAAC	Strain-Promoted Azide-Alkyne Cycloaddition
sulfo-NHS	N-hydroxysulfosuccinimide
SWCNT	Single Walled Carbon Nanotube
UV-vis	Ultraviolet–visible spectroscopy

Acknowledgements

Now that I am coming to the end of the preparation of the thesis and my PhD life, I would like to take this opportunity to offer my special thanks to those without who I would never make thus far. Like most other doctorate students, the past four years for me have been an up and down. The time spent on the compilation and completion of the thesis has been a unique and novel adventure in my life to the Nano World during which I have learned, lived and enjoyed every moment. There is no way for me to acknowledge all the great help, advice and impact as they deserve.

First of all, I would like to express my very great appreciation to my supervisor Dr Matteo Palma. He is the first person to spark my interest in nanoelectronics and accept me as the PhD student, fulfilling my dream of Science. As a PhD student, I have been provided with the opportunity to take part in several international research projects and collaborations at his discernment. As a mentor, he provided the advice from research questions to life experience while keeping encouraging me through the years. He is one of the hardest working people I know and pushed me to strive hard myself. Meanwhile, he is supportive even for the minor details of lab work. Together we built a successful and competitive lab from almost scratch which is a priceless experience. He will always be my mentor and a precious friend.

Secondly, I am particularly grateful for the help provided by my second supervisor Professor William Gillin. Nanoelectronics is a novel research area where multi-subject

knowledge is required for chemical synthesis to device fabrication. His erudite knowledge in physics and semiconductors have been helpful and vital for my work. He spent countless hours sharing his wisdom with me.

I would also like to thank all of my colleagues and friends in Palma's research group for making my PhD life enjoyable. Dr Pierrick Clement has kindly shared his experience in nanofabrication and chemistry of carbon nanotubes with me. He was a great partner for games as well. I wish him success in his research and life in the future. Dr Marina Bantzi has been an amazing lab-mate, and I truly appreciate her for all her advice towards my experiments. Joesph McMorrow has taught me everything about organic chemistry. He has been very much missed after he went to Unilever to start his career as a chemist. Da Huang has always shared his knowledge in biotechnology and never showed impatience to my stupid questions. Being an expert in design and image processing, he has helped so much in terms of mask designing and data analysis. Mark Freeley has been the lab Wikipedia and always ready to drop everything and help me. I would also like to thank the junior member in the lab. It was a great pleasure and happy experience to work with them: the hyper energetic Antonio Attanzio has been an awesome lab-mate, kind and professional, and always fun to work with; Sandra Perez, being such a warm-hearted and always willing to listen to my complaints to my experiments, she have shared her passion and happiness with me. I do wish her great success in her career. I would also like to thank Xinzhao Xu, Qinyu Ye and Giuseppe Amoroso for patiently listening to my long and detailed explanations.

I receive a lot of help from people in School of Astronomy and Physics. I am grateful to Geoff Gannaway, Dr Ken Scott, and George Nevill for their help in nanofabrication.

I have received a lot of help out of Queen Mary during the thesis. Thirdly, I would like to show my gratitude to Dr Ming Zheng and Dr Ao Geyou from the National Institute

of Standards and Technology for their supply of metallic DNA wrapped Carbon nanotubes: their help and continues support was of paramount importance for my project.

I would also like to express my thanks to Dr Khaled Kaja from Bruker for teaching conductive AFM to me. Moreover, I would like to thank Dr Vina Farmanzi for sharing her knowledge and ideas on the fabrication of nanotrenches.

Finally, I would like to thank my parents for always supporting me and giving me the freedom when choosing the path of my life. Although they are far from me, I know you love me all the time. And last I would like to thank Fan for spending the past years with me sharing the happiness and bitterness. She is the best friend who gives advice and lover who gives all.

To my parents, Xingfa Zhu and Shuzhen Fang, because without their support I would have never made it here; and to Fan, the best companion in this adventure.

Chapter 1 Introduction

Ever since their invention in 1958, integrated circuit technologies have been developing exponentially in power and size according to the well-known Moore's Law. Traditional electronics are mainly made from bulk materials;[1] the gate length in the transistor was approximately 10 μm forty years ago, and 10 nm (commercially available) today[2]. However, the bulk approach has inherent limitations in addition to becoming increasingly demanding and expensive when the gate length comes down to below 10 nm.[3] Additionally, electron transfer mechanisms in nanostructures, and in particular at the single-molecule level, are still not fully understood.

Thus, the idea was born that the components could instead be built up atom by atom in a chemistry lab (bottom up) as opposed to carving them out of a bulk material (top down).[4] A molecular approach will enable the construction of much smaller circuits than is currently possible using the more conventional semiconductors such as silicon. In single molecule electronics, the bulk material (traditionally metal-semiconductor) is replaced by single molecules or a nanoscale collection of molecules. The motion of the electrons in such devices is inherently governed by quantum mechanics, while the chemically identical molecules utilised have properties that resemble traditional electronic components such as wires, transistors, switches or rectifiers. The appealing features of organic molecular devices are the high degree of control on molecular design possible through chemical synthesis and scalability by self-assembly. Thus far, many

molecules with desired properties, such as electromechanical, optical, thermoelectric, magnetic, and molecular recognition behaviour have been designed.[5-13]

Single-molecule electronics is a field with great potential, and entire electronic circuits consisting exclusively of molecular sized compounds are still far from being realised. However, the continuous demand for more computing power together with the inherent limitations of the present day lithographic methods make the transition seem in demand. The most basic and simple unit in molecular electronics would be one molecule between two leads (electrodes). The electric behaviour would not only depend on the intrinsic properties of the molecule but also on the external electrodes.[14]

Currently, the focus is on discovering molecules with interesting properties and on finding ways to obtain reliable and reproducible contacts between the molecular components and the electrodes. Despite the potential difficulties, continuous progress has been made in recent years on both theoretical aspects and experimental methods. A variety of important mechanistic insights have been obtained, and molecular conductance values have been measured.[15-22] However, the field of molecular electronics is still in its infancy considering the many possible molecular structures to be employed as active components in a single-molecule device.

In this thesis, we will present strategies to assemble in solution different nanostructures of interest in nanoscale electronics and to fabricate from solution to surface all-carbon based molecular transport junctions. Chapter 1 will describe the mechanism for electron transport in single molecules and will address some existing approaches for fabricating molecular junctions, including the use of carbon nanostructures as electrodes in single-molecule devices. Chapter 2 presents the experimental techniques applied in this thesis. The results presented in this thesis are essentially articulated in three sections. In the

first section (chapter 3 and 4), we will present a solution-based assembly method for producing molecular transport junctions employing metallic single-walled carbon nanotubes as nanoelectrodes. On solid substrates, electrical properties have been investigated by Conducting Atomic Force Microscopy (C-AFM). The molecular junction conductance of a series of oligophenyls was successfully measured, highlighting the potential of an all-carbon based approach for the fabrication of solution-processable single-molecule junction for molecular electronics. Additionally, different strategies for asymmetric junction formation have been explored towards the development of a nano size Schottky diode (chapter 4).

In the second section (chapter 5), we will discuss the assembly of nanostructures on predefined metal electrodes to form a Field-Effect Transistor. In detail, a process has been developed using standard optical lithography to make gap devices consisting of two planar electrodes separated by a "nanotrench" of 20 to 100 nm wide. Avoiding the use of more sophisticated lithography techniques makes our fabrication strategy more relevant for industrial scaling up, and it is very practical for speeding the necessary electrodes fabrication. Nanostructures dispersed in solution are organised onto surfaces by means of dielectrophoretic assembly. I-V response for molecular junctions was then measured by a probing station.

In the third section of this thesis (chapter 6), we explore the dispersion of boron nitride nanotubes (BNNTs) by DNA wrapping followed by the formation of nano-hybrids of boron nitride nanotubes and carbon nanotubes. Previously, researchers have adopted BNNT as a 2D dielectric layer; the work inspired us to adopt BNNTs as 1D dielectric materials. Finally, the Conclusions chapter 7 will discuss the main findings of this thesis and future challenges in the development of solution processable nanostructures for molecular electronics.

1.1 Transport properties of a single molecule

1.1.1 Conductivity

It is widely known that macroscopic conductors have a conductance obeying Ohm's law as G = I/V (where G is conductance, I is the current passing through the conductor and V is the potential difference between terminals) or R = V/I (where R is resistance). Even this is a successful statement about conductance that covers nearly all the materials when it was discovered by Ohm in 1827; the formula only applies to certain materials which have constant current to voltage ratios like metals or ionic solution. However, more and more non-ohmic materials are popularly used now like semiconductors, p-n junction, and transistors. The various electrical characterisations offer the possibility of modern integrated circuits which form the current information age.

The different characteristics are based on the principle of electron transport within materials. A microscopic view of conductors suggests that resistance comes from the fact that an applied voltage will impose a drift velocity of the free electrons in the conductor. The current density J (electrical current per unit are, J=I/A) is determined as below.

$$J = n * e * v_d \tag{1-1}$$

Where n is the free electron density, e is the charge of carrier, v_d is the drift velocity. For conductors like metals, the number of free electron per volume is dependent on the atom as.

$$n = \frac{N_A * \rho}{M} * n_e \tag{1-2}$$

Where N_A is Avogadro's number, ρ is the density of metal, M is the molar mass, and n_e is the number of free electrons per atom.

Furthermore, the drift velocity can be expressed in terms of accelerating electric field E, the electron mass and average time between collisions.

$$v_d = \frac{e * E}{m} * \tau = \frac{e * E}{m} * \frac{d}{v_f} \tag{1-3}$$

Where m is the electron mass, d is the mean free path and v_f is the Fermi speed (moving velocity corresponding to a kinetic energy equal to the Fermi energy). In this way, the conductivity of metal could be expressed as below.

$$\mathrm{J} = \sigma * \mathrm{E} = \frac{n * e^2 * d}{m * v_f} * \mathrm{E} \tag{1-4}$$

The σ is the electric conductivity.

1.1.2 Semiconductor conductivity

It has been shown that the conductivity of metal depends on the concentration of free electrons, mean free path and Fermi velocity of the metal itself. Good conductors consist of a large number of free electrons while insulators consist very few free electrons. For semiconductors, they have a concentration of free electrons between conductors and insulators so that they behave as semiconducting. Typically, the valence electrons in the semiconductor are not free as in metals while trapped by bonds between atoms. In this way, there should be no free electrons at absolute zero temperature and semiconductors will behave as insulators. However, at a higher temperature (e.g. room temperature), the available energy will break the covalent bond in the crystal and provides free electrons out of the bond, leaving a vacant place behind. These two will form the carriers in the semiconductor, electrons and holes (vacancies). Since they have

opposite charges, these carriers will move in different directions. The holes will move towards the applied electric field (positive charge), and the current density of drifting holes will be [23]:

$$J_h = \mathrm{h} * \mathrm{e} * v_h \tag{1-5}$$

Where h is the concentration of holes, e is the electron charge, v_h is the drift velocity of holes in crystal.

The current density due to the electron drift will be:

$$J_e = \mathrm{n} * \mathrm{e} * v_e \tag{1-6}$$

Where n is the concentration of free electrons, v_e is the drift velocity of electrons in crystal.

Even the two carriers are moving in opposite, the summary current is the mathematic sum of two current due to the different charges. Hence, the current density in the semiconductor would be as followed:

$$\mathrm{J} = J_h + J_e = h * e * v_h + n * e * v_e \tag{1-7}$$

1.1.3 Band theory

Atomic orbitals are adopted in quantum mechanics to describe the wave-like behaviour of electrons in one atom. The orbital is actually a mathematic wave function which can represent the probability of finding electrons at a certain position (energy level). Each orbital is formed at a discrete energy level (as illustrated in **Figure 1-1**).

If a large number (N) of atoms come together and form a solid (crystal), their atomic orbital will overlap. According to the Pauli Exclusion Principle, no two electrons in the same crystal will occupy the same quantum states. Each atomic orbital from all atoms will split into N discrete molecular orbitals. Since the number of atoms in a macroscopic

crystal is large (~10^{23}), the split orbitals are so closely spaced in energy that they can be treated as a continuum and form energy bands.[24] While the bands have a limited width, the range of energy which is not covered by any bands is called band gap.

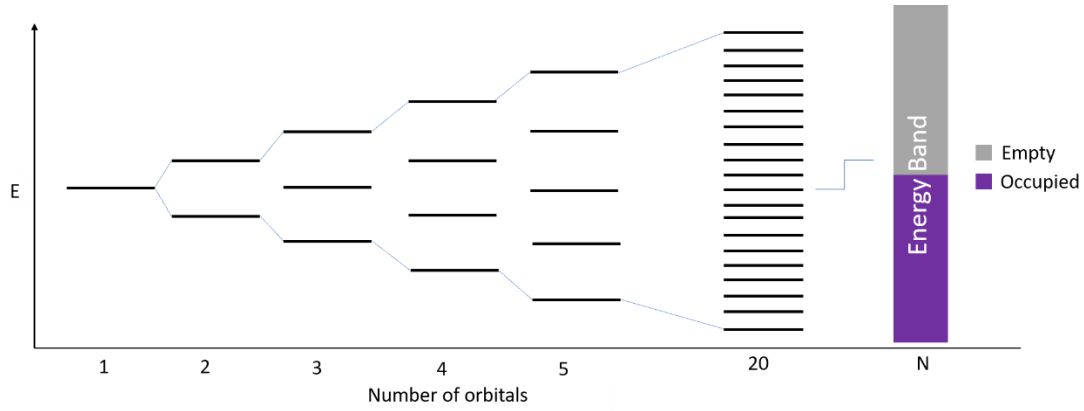

Figure 1-1 The molecular orbital energy-level diagram for a linear arrangement of n Atoms, each of which contains a singly occupied orbital

Usually, the highest band occupied by electrons at zero temperature is called valence band, and the lowest range of energies which are vacant are the conduction band. Electrons cannot have any energies outside these orbitals and can only be promoted between bands when given a sufficient energy compared to the band gap. To further simplify the analysis, we assume that only the valence electrons (the electrons in the outer shell) are of interest. The core electrons are tightly bound to the atom and are not allowed to freely move in the material. Four different possible scenarios are shown in **Figure *1-2***. A half-filled band is shown in **Figure *1-2*** a. This situation occurs in materials consisting of atoms, which contain only one valence electron per atom. Most highly conducting metals including copper, gold and silver satisfy this condition. Materials consisting of atoms that contain two valence electrons can still be highly conducting if the resulting filled band overlaps with an empty band. The crystal will be an insulator when the band gap (**Figure *1-2*** b) is large and a semiconductor when the gap is relatively small (typically < 3 eV) (**Figure *1-2*** c). In the semiconductor, the band

gap is so small that thermal or other excitations (photon) can bridge the gap. In this way, the conductivity of semiconductors will increase with temperature as the charge carrier density in the conduction band increases. For extrinsic semiconductors, the dopant material (intentional introduction of impurities) will increase the carrier concentration by either providing electrons in the conduction band or vacancies in the valence band. Hence, highly doped semiconductors behave metallically.

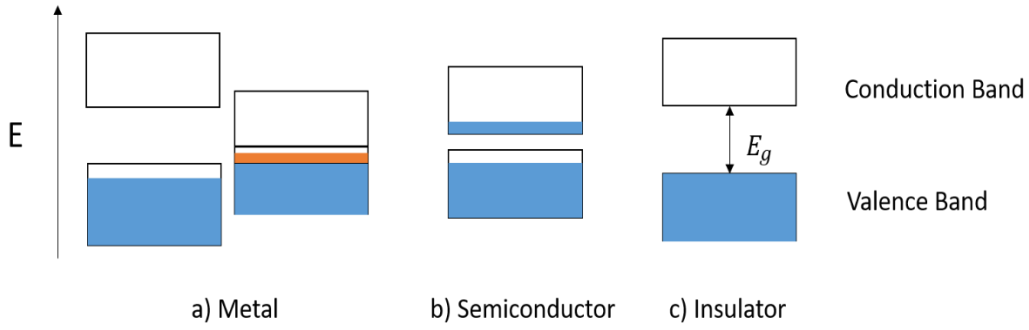

Figure 1-2 a) is the possible band diagram for metal where the valence band is half-filled or conduction and valence band overlap; b) shows semiconductor where a small band gap is between bands; c) is the insulator where a large bandgap is separating a full band and an empty band.

1.1.4 Single-molecule conductivity

Similar to band theory, when several atoms join together to form a molecule, new molecular orbitals are formed. In theory, a molecular orbital is a linear combination of the component atomic orbitals. The wave function is shown as:

$$\psi_j = \sum_{i=1}^{n} c_{i,j} * \chi_j \tag{1-8}$$

Where χ_j is the atomic orbital, $c_{i,j}$ is the numerical coefficients.

As electrons occupy the atomic orbital in each atom, the electrons in the molecule will only occupy the molecular orbital. Considering the different overlapping conditions of atoms, there are three types of MO, bonding, antibonding and nonbonding.[25]

Bonding orbitals are formed when atomic orbitals wave functions were added in phase. The in-phase overlap concentrates the electron density between the atoms so that they can be attracted and tighten the binding. Conversely, when the out-phase add up happens, the electrons in the antibonding MO will weaken the bonds and increase the energy of the molecule compared to the separated atoms. For the non-binding orbitals, the occupant electrons don't contribute to the bond order in the molecules. **Figure 1-3** displays the molecular orbital diagram for the O_2 molecule where electrons have occupied the energy levels from low to high. The key orbitals in the MO theory are the frontier orbitals, in particular, the Highest Occupied Molecular Orbital (HOMO) and the Lowest Unoccupied Molecular Orbital (LUMO). The difference between the HOMO and LUMO is termed as an HOMO-LUMO gap. When a molecule absorbs energy, it is typical for a HOMO electron to transit from the HOMO band to the LUMO excited-state orbital. Similar to the band gap in solids, it can predict the conductivity of the molecule.

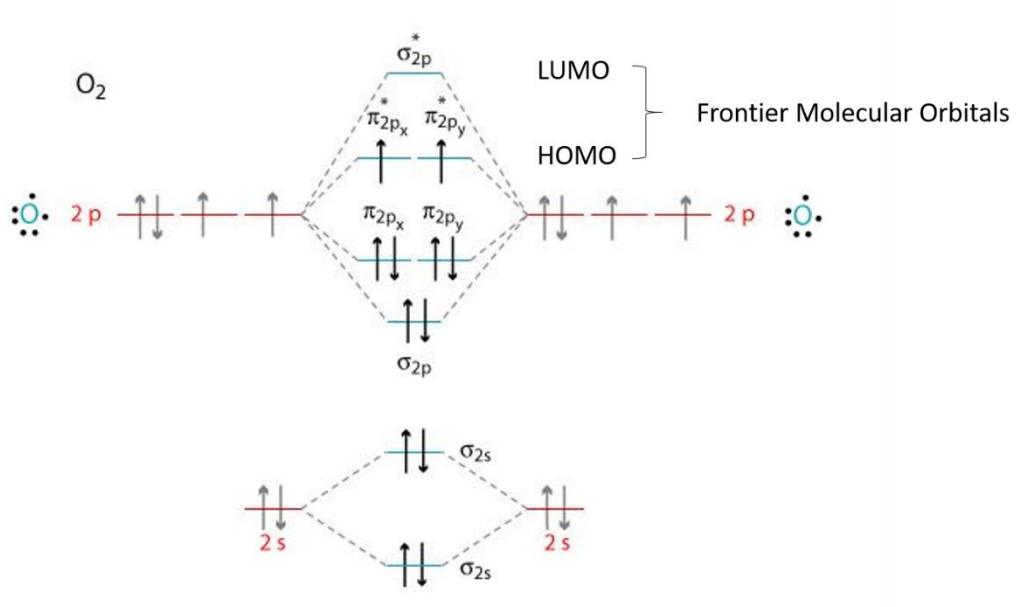

Figure 1-3 Molecular orbital energy diagram for oxygen molecule; π^*_{2px} and π^*_{2py} are the HOMO and σ^*_{2p} is the LUMO.

To measure the conductivity of single molecules, actual contacts of the molecule to two electrodes (molecular junction) has been pursued. Usually, the electrodes are microscopically large but macroscopic contacts are needed so that they can be connected to battery and measuring units. Accordingly, most of the theoretical and experimental studies about molecular conductivity have been focused on electron transport through molecular junctions as shown in Figure 1-4.

As it is illustrated in **Figure 1-4** a, structures in the left and right are metallic electrodes while the line segments in the centre represent the molecules. The stripped arrows indicate the coupling between molecular orbitals and electrodes. Moreover, interactions between MOs are shown in black arrows. Once the bridge is formed and bias is applied, the charge will flow, and the equilibrium is achieved as indicated in **Figure 1-4** b. In practical, electron transport in junctions is always accompanied by nuclear motions in the environment. The coupling between electronic and vibrational degrees of freedom would underlie the interactions between coherent electron tunnelling through the junction and inelastic thermally assisted hopping transport. Additionally, electron-phonon interplay may result in polaronic conduction, and resulting in junction heating.

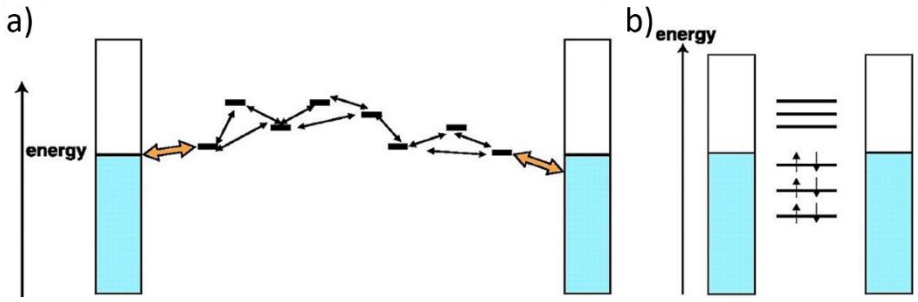

Figure 1-4 a) Electron transport path through the molecular linker; b) schematic of modified electron energy levels from reference[20]

To simplify the calculation, we assume that incoming electrons through the junction will scatter both at the electrode-molecule interface and along the molecule itself. The conductance is then given as in equation (1-9):

$$\mathrm{G} = \frac{2 * e^2}{h} * \sum_{i,j} T_{i,j}(E,V) = G_0 * \sum_{i,j} T_{i,j}(E,V) \quad (1\text{-}9)$$

Where h is Planck constant, $T_{i,j}$ is the probability that electron can be transported from the left electrode in transverse mode *i* to the right electrode in transverse mode *j*.

By substituting the constants, quantum conductance denoted as G_0 equals $(25.8k\Omega)^{-1}$ or $7.7480917310 * 10^{-5}S$. This indicates the maximum conductance of a quantum transport channel and the minimum resistance will be $25.8k\Omega$. Obviously, the current through the junction depends on the quality of contacts between electrodes and the molecule ends.

Experiments have found that conductance (G) of wire molecules decreased exponentially with molecular length (L) as equation (1-10).

$$\mathrm{G} = \mathrm{A} * \exp(-\beta * \mathrm{L}) \quad (1\text{-}10)$$

Where A is a constant and β is a decay constant. The exponential decay together with temperature independence suggests electron tunnelling as the main mechanism for electron transport of these molecules.

1.2 Molecular electronics: existing fabrication approaches

Dating back to 1974, Arieh Aviram and Mark Ratner [26] envisioned the use of individual molecules as electronic components. In 1971, Hans Kuhn and Dietmar Möbius [27] experimented with single layers of molecules. The gate length in the circuits was up to 10 μm.[27] In the past 40 years, various methods of fabrication of molecular electronics have been designed and tested despite the difficulties. The research on reaction chemistry has successfully built covalent connections between molecules and metallic electrodes. Most common approaches are based on the connection of molecules with a pair of gold (or metal) electrodes.(**Figure 1-5**)[28]

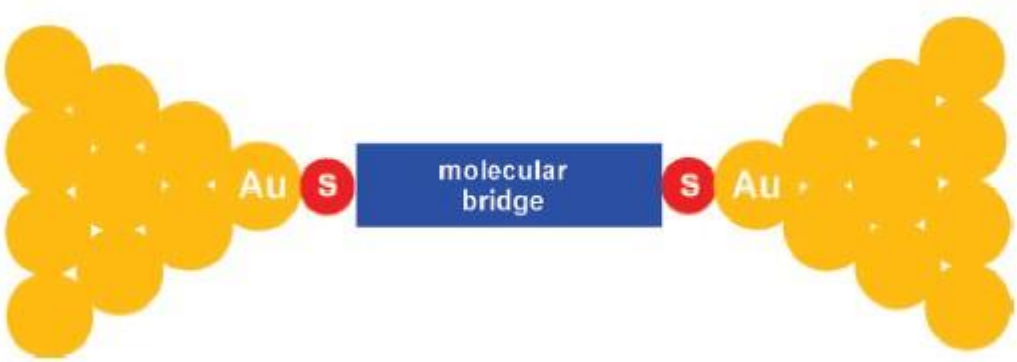

Figure 1-5 Schematic of a molecular between two gold electrodes

Traditionally, molecular optoelectronic devices are achieved by insertion of α, ω-dithiols between gold electrodes. Although this method has many advantages, it suffers from some limitations: thiols are susceptible to air oxidation; precise control over contact geometry is challenging due to the high mobility of gold atoms; it is difficult to control the exact number of molecular bridges.

As discussed by Dong Xiang and Xuefeng Guo [29, 30] among the systems that have been developed in the past decade, two have gained very successful results employing different electrodes. One is based on the use of metallic electrodes (gold, titanium etc.), and the other is based on the use of carbon nanostructures, such as single-walled carbon nanotubes or graphene as contact electrodes. These metal electrode apporach is at the basis of different strategies in molecular electronics, namely: 1) break junctions,[31] scanning probes [15, 32], sandwich large-area molecular junctions,[33] liquid metal contacts,[34] self-aligned lithography,[35] and on-wire lithography,[36, 37] 2) Differently, e-beam lithographic and electroburning methods have been developed to cut 1– 10 nm gaps in single-walled carbon nanotubes (SWCNTs) and graphene to be used as nanoelectrodes. [38-43]

1.2.1 Molecular electronics based on metal electrodes

1.2.1.1 Break Junctions

In general, the strategy to form break junctions in metal nanowires is based on mechanically bending or electro migration methods. The approach was first put forward by Reed et al. in 1997.[31] Two years later, Hongkun Park [44] reported the initial example of electro migration by using electron-beam lithography and shadow evaporation. Despite the breakthrough of the approach in controlling the size of gaps, the break junction methods failed to precisely achieve exact geometry of the molecules, electrodes and the number of molecules in the gap. The schematic of break junctions method and the molecules bridging electrodes is shown in **Figure 1-6**.

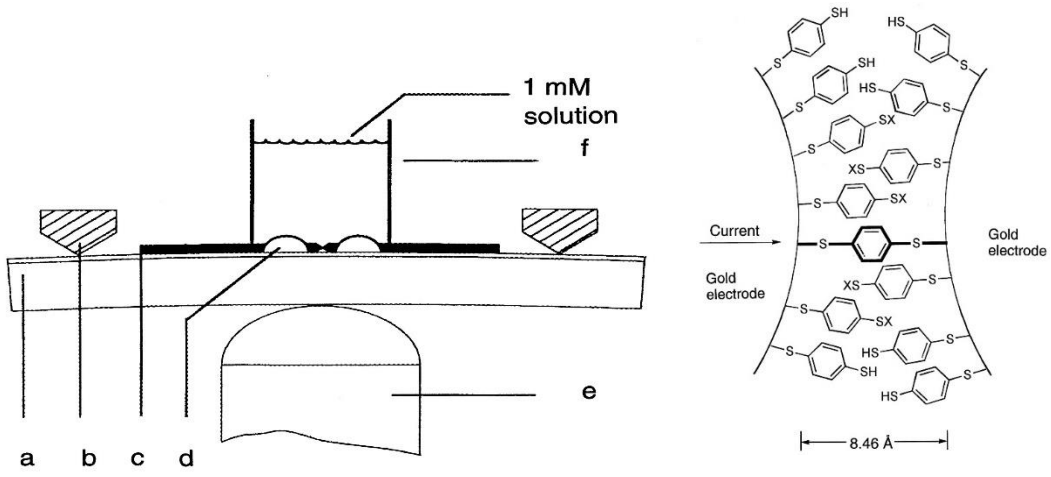

Figure 1-6 Left: A schematic of the MCB junction with (a) the bending beam, (b) the counter supports, (c) the notched gold wire, (d) the glue contacts, (e) the piezo element, and (f) the glass tube containing the solution. Right: A schematic of a benzene-1,4-dithiolate SAM between proximal gold electrodes formed in an MCB. [45]

1.2.1.2 Sandwich large-area molecular junctions

Self-assembled monolayers (SAMs) are organic assemblies that tend to organise spontaneously into crystalline (or semi crystalline) structures on the surface of solids or in regular arrays on the surface of liquids.[46, 47] The method has drawn great attention because it provides a convenient and flexible method to coat surfaces and hence tailors the properties of the surfaces. However, defects due to the thermodynamics of electrode evaporation process are intrinsic. An improvement based on SAMs has been reported by de Boer.[48] By processing the molecular junctions in the holes of a nanopatterned photoresist, a layer of conducting polymer is implanted between the SAM and the electrode. Under the protection of polymer layer, good SAM with fewer defects is achieved. The schematic of SAMs is shown as below in **Figure 1-7**.[48]

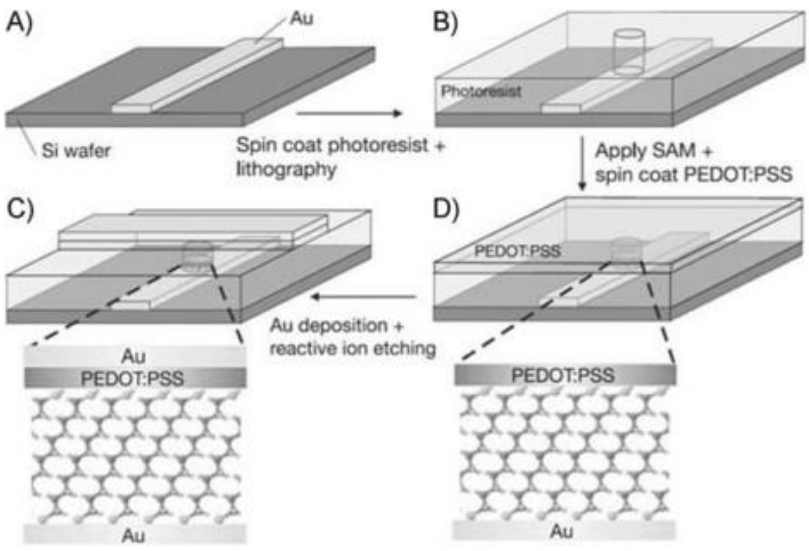

Figure 1-7 Schematic of Sandwich Large-Area Molecular Junctions[48]

1.2.1.3 Scanning probe Microscopy break junction

The invention of Scanning Tunnelling Microscopy (STM)[49] and conductive atomic force microscopy (C-AFM)[50] offers the possibility to form a molecular junction at the nanoscale, employing the tip of the scanning probe microscope as one electrode and a surface metallic contact as the counter electrode, with the molecule embedded between the two.

Wold et al. and his collaborators reported the characterisation of metal-molecule-metal junctions by contacting self-assembled monolayers (SAMs) alkanethiols on a gold substrate with conductive AFM tip.[21] With independent feedback signals, AFM can control the tip height so that good contact between tips and SAMs without damage can be achieved. Using the C-AFM method, they measured the conductance of alkane chains as a function of the number of carbons or the loaded forces applied to the tip-SAMs contact. Schematic of the tip-SAM contact is shown in **Figure 1-8**.

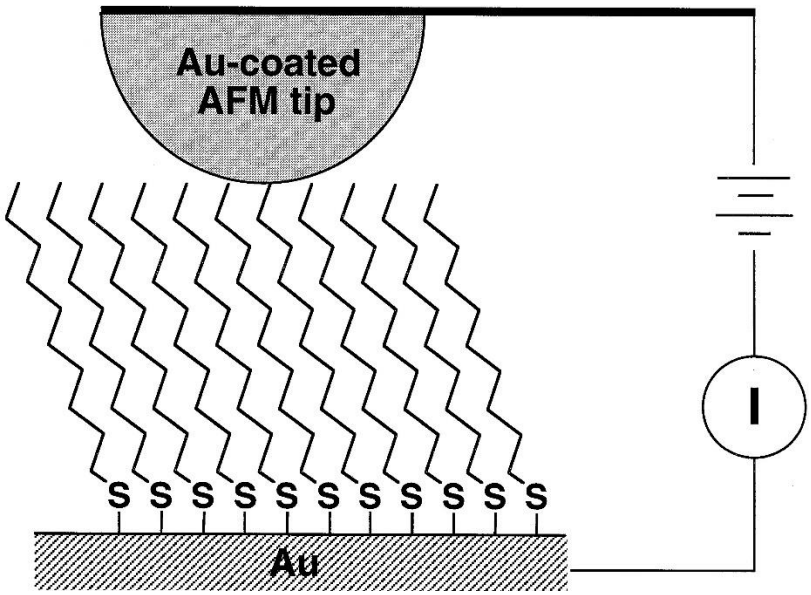

Figure 1-8 Formation of a Metal-Molecule-Metal Junction by Contacting an Alkanethiol Self-Assembled Monolayer with an Au-Coated AFM Tip.[21]

Measurements of electrical conductance of conjugated molecular SAMs have been reported by Ishida et al. following similar methods.[51]

Xu et al. reported the formation of individual molecular junctions based on Scanning Tunnelling Microscopy in 2003.[52] In this work, thousands of molecular junctions are created by repeatedly moving a gold STM tip in and out of contact with the substrate electrode adsorbed with the sample molecules. The tip movement can be precisely controlled by a piezoelectric transducer. Typically, the molecules in the study have two end groups that bind to the tip and the substrate electrodes. The molecules have an opportunity to bridge both the tip and the substrate electrode when the tip is brought close enough to the substrate, as indicated in **Figure 1-9**. During pulling the tip out of contact with the gold substrate, gold-gold contact is firstly broken followed by the break of molecular binding. The corresponding conductance histogram illustrates well-defined peaks near 1 G_0, 2 G_0, and 3 G_0 due to the conductance quantisation. After the gold–gold contact is completely broken, a new series of conductance steps appear due to the formation of the molecular junctions. A conductance histogram shows peaks near 0.01 G_0, 0.02 G_0, and 0.03 G_0, which can be ascribed to one, two, and three molecules, respectively.

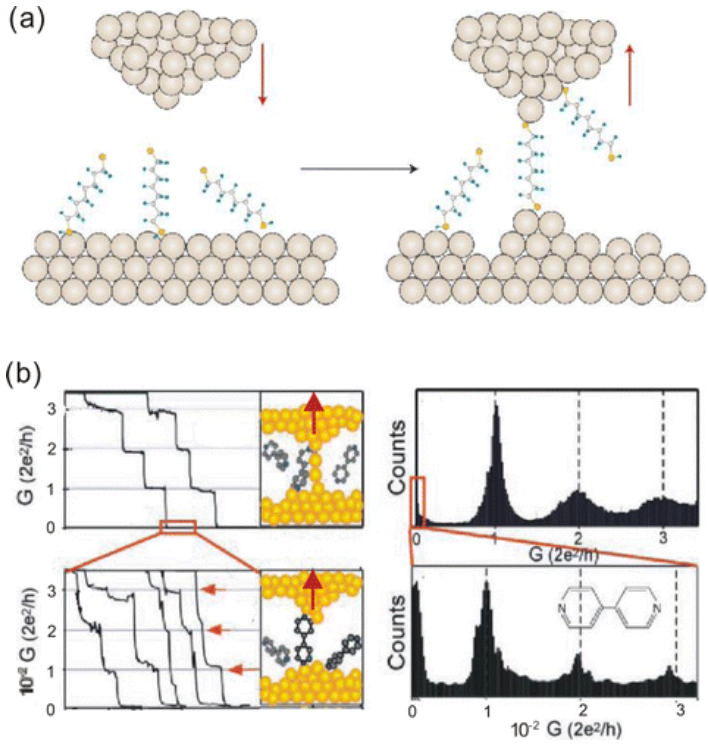

Figure 1-9 (a) STM-based technique used to form single Au–molecule–Au junctions. When the Au tip moves near the Au substrates, which are covered with target molecules, Au–molecule–Au junctions are formed. When the Au tip is pulled away, the molecular bridges then lose contact with either the tip or the Au substrate. (b) Single-molecule conductance measurement. [52]

1.2.1.4 Liquid metal contacts

The other solution to the fabrication of molecular junctions based on the use of SAMs comes out by utilising mercury as the second electrode. The liquid state of mercury offers a clean, defect-less, good-contact material as the electrode. The first example of the liquid metal molecular junction is made of two parts. One is the silver (Ag) based SAM, and the other is a SAM with the mercury as the substrate.[53] To be mentioned, the silver side can have two forms: as-deposited silver film and template-stripping one.[54] This kind of electrode group offers the opportunities to test the conduction across the electrodes to see how the structural and electrical of SAMs will be affected by forms.[55]

1.2.1.5 Self-aligned lithography

Self-aligned lithography is based on the idea of forming the molecular bridge between two electrodes separated by a nanogap. First, a nanoscale electrode ranging from 3 to 10nm [56, 57] is fabricated by self-aligned lithography. Utilizing the aluminium oxide layer above the Pt layer offers a tiny shadow mask adjacent to the pattern. In this way, the second electrode is deposited on the substrate compromising the nanoscale gap. Bridging gaps is achieved by first forming a thiol-terminated monolayer and then reacting with a diamine. The schematic image is shown in Figure 1-10.[56]

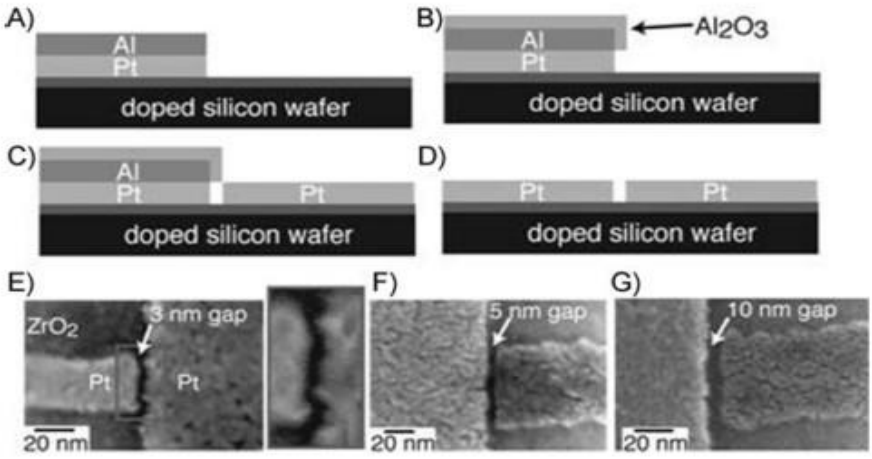

Figure 1-10 Schematic image of Self-aligned lithography[56]

1.2.1.6 On-wire lithography

Another interesting approach to fabricate nanowires with nanogaps has been put forward by the Mirkin Group.[36, 37] Usually Au-Ag or Au-Ni is used as the nanowire material. The idea is based on the fact that part of the nanowire is removable via a wet etching process while the other is stable. Firstly, the nanowire is fabricated in aqueous solution by electrodeposition on the templates (Aluminium). The length is controlled

by the charge passed in the electrodeposition circuits. Then the nanowires are dispersed in the solution after removing the templates. The aqueous solution is then cast and spin coated on the substrate followed by deposition of gold-titanium bilayer. Nanowires are finally released by sonication in the ethanol solvent. The key step to fabricate nanogaps is to do the selective etching to remove part of the nanowire. **Figure 1-11** shows the schematic of the on-wire Lithography. In a further report, they reported a method for the insertion of molecules by using the alkyne–azide 'click reaction'. [58]

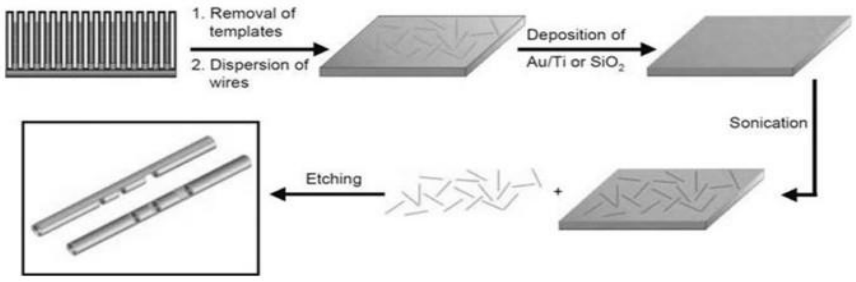

Figure 1-11 Schematic of On-wire Lithographic method[37]

1.2.2 Molecular electronics based on carbon nano-electrodes

1.2.2.1 E-beam lithographic method on Single Wall Carbon Nanotubes

One of the latest improvement for fabrication of molecular junctions was reported by the Nuckolls group. This method is based on the use of Single Wall Carbon Nanotubes (SWCNTs) as nanoscale electrodes. [28, 59, 60] Amide chemistry is employed to connect the electrodes to molecules as bridges. SWCNTs have an average diameter of 1.2nm[61] while the scale of an individual molecule is nanometre from 0.74 A to 100 nm. [62] This makes the components naturally match each other and binding possible.

SWCNTs are first grown by chemical vapour deposition (CVD). Subsequently, a layer of polymethylmethacrylate (PMMA) resist is spun on the surface. E-beam lithography is then used to open a nanoscale window in the PMMA mask above the nanotube. Finally, oxygen plasma is employed which can cut the SWCNTs and so create a nano gap in an individual CNT, down to 10nm. **Figure 1-12** displays the process.

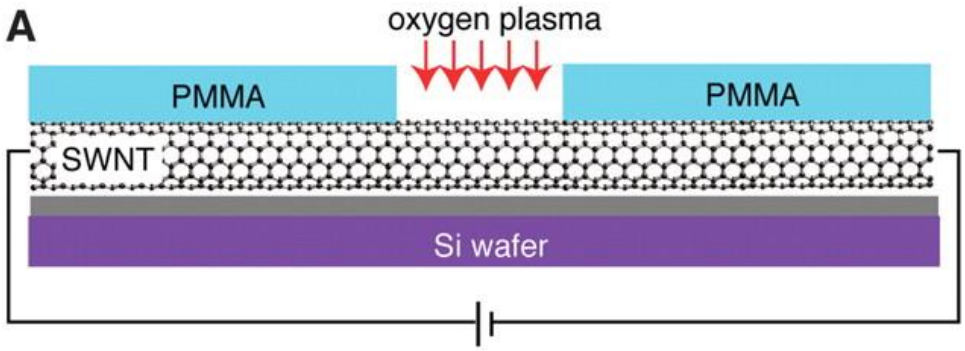

Figure 1-12 Schematic of SWCNTs cutting [63]

The strong oxidation process creates carboxylic acids the end of the carbon nanotube's segments of the gap (shown in **Figure 1-13**). The gap distance can be controlled by changing the oxygen plasma intensity and time.

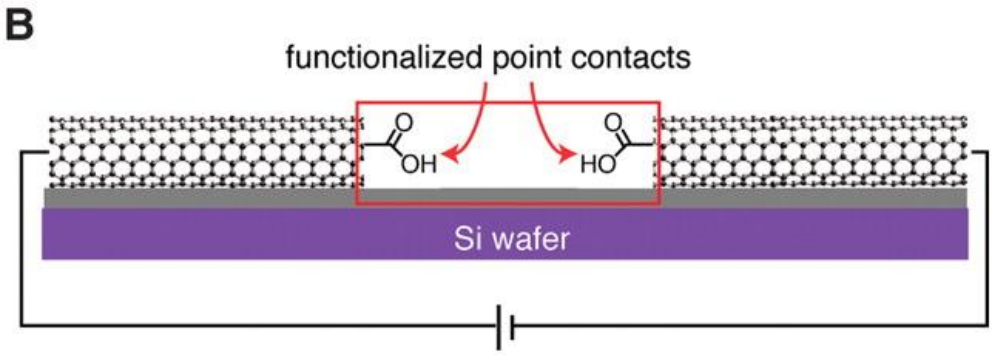

Figure 1-13 Schematic of carboxylic acids on end of SWCNTs [63]

Taking advantage of the carboxylic acid function on the nanotubes, molecules with amine functional groups can be connected to the electrodes by a covalent bond (an amidation). The detailed approach is to use a pyridine solution containing the

carbodiimide dehydrating agent EDCI. The connection by amine chemistry is so robust and reproducible that different functionalities can be installed on the molecular bridge. This offers the possibility to make PH-, redox-, photo-gated switches. [59, 64-66] Moreover, the same approach has now been employed on graphene layers, showing an improvement of the yield of junction formation (up to 20%)[67]

1.2.2.2 Feedback-controlled electroburning of Single Layer Graphene

Prins et al. presented one method of using graphene as electrodes in molecular electronics.[68]In this study, they used feedback-controlled electroburning to cut a few-layer graphene sheet. The gaps have separations of approximately 1−2 nm, as estimated from a Simmons model for tunnelling.[69] The devices then were created by assembling molecules of interest inside the graphene nanogaps using π−π stacking. However, it is difficult to control the electrode geometry and the resulting gap size due to the use of the electroburning process and the few-layer graphene sheets.

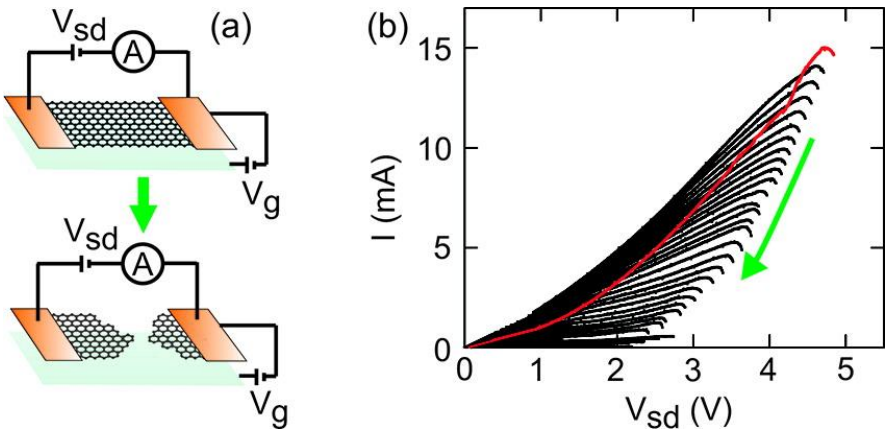

Figure 1-14 . (a) Schematic of the feedback-controlled electroburning process, before (top) and after (bottom), the formation of nanometer sized gaps in few-layer graphite flakes. (b) Current-voltage (I-V) traces of the evolution (green arrow) of the feedback-controlled electroburning. The first I-V trace is displayed in red.[68]

Later, Lau et al. reported the fabrication of single layer graphene nano-gaps via applying the method of electroburning to notched ribbon devices, which are plasma etched from CVD grown graphene that is wet-transferred onto pre-patterned metal electrodes.[70] The nanogap fabrication strategy comprises a lithography process where the minimum feature size is 200 nm followed by a feedback-controlled electroburning process which results in 0.5–2.5 nm sized gaps.

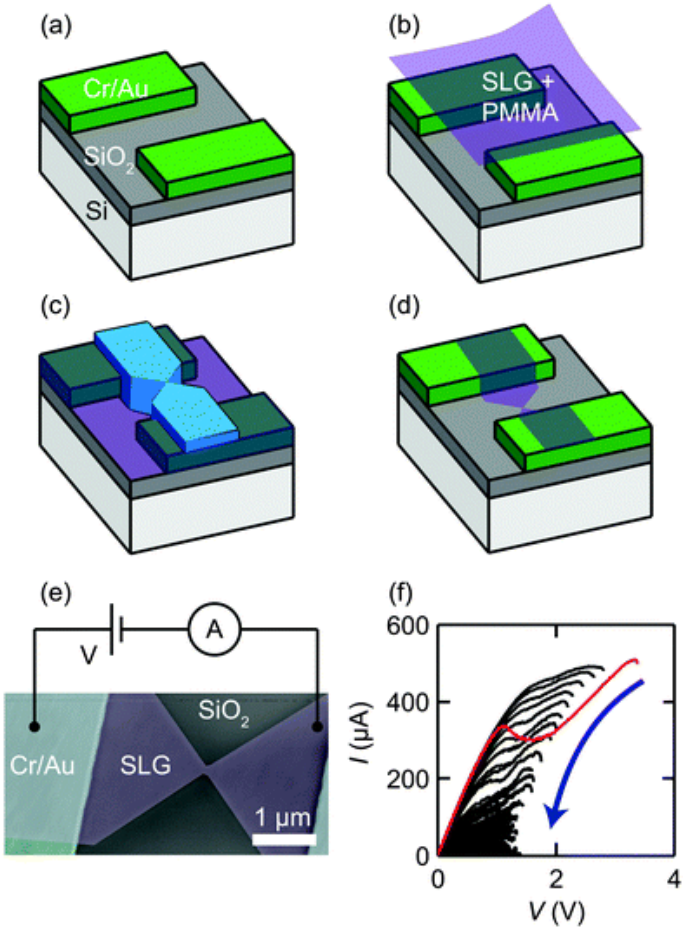

Figure 1-15 (a–d) Schematics for the process flow of our device fabrication. (e) Scanning electron micrograph of a single layer graphene (SLG) notched ribbon between two Cr/Au contacts. (f) Current–voltage (I–V) traces recorded during the feedback-controlled electroburning.[70]

Based on the nanogap mentioned above, Gehring et al. have shown single-electron tunnelling through a molecule that has been anchored to two graphene electrodes.[71] Schematic of the junction is shown in **Figure 1-16**. In the work, a nanogap is formed

on the graphene mat followed by the deposition of the investigated molecules in chloroform solution. The molecule is anchored on the graphene by the π-π interaction between the bulky side pyrene groups and the aromatic ring on the graphene. The graphene electrodes coupled electrostatically to a global back gate which results in the fluctuations of the density of states. The fluctuations could potentially obscure the intrinsic conductance of the molecule under investigation. Using ensemble averaged magneto-conductance measurements, lead and molecule states are then disentangled, enabling spectroscopic investigation of the single molecule.

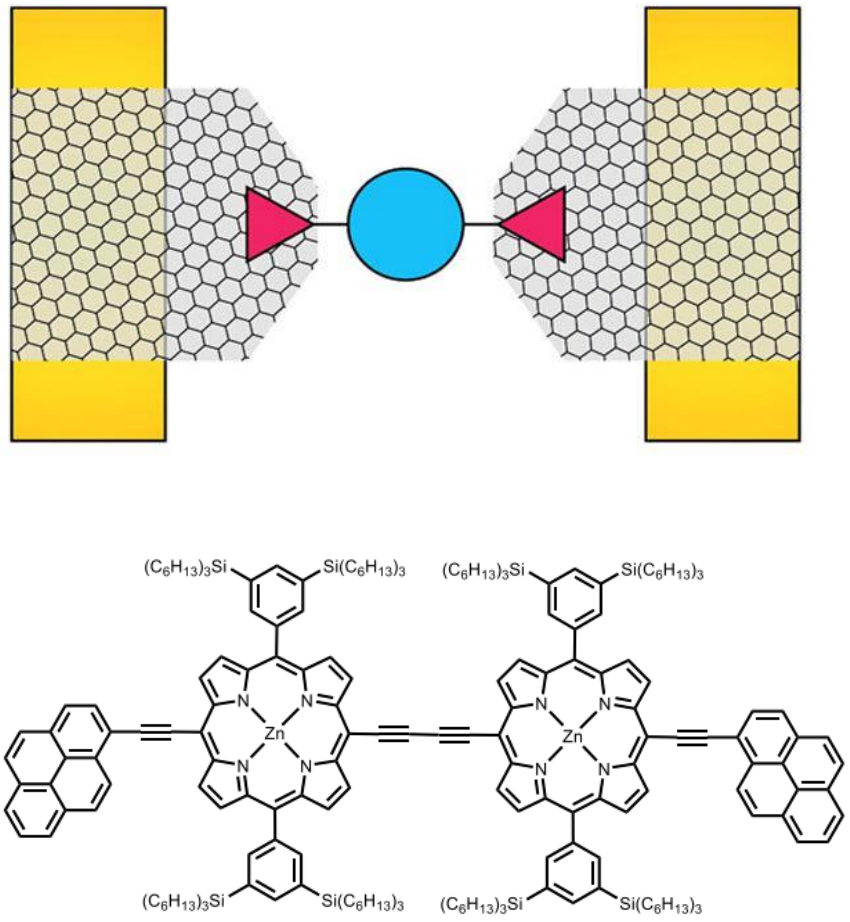

Figure 1-16 Schematic depiction of the device. Upper: Graphene lead electrodes are connected to gold reservoirs left and right; a single molecule bridges the gap between the graphene electrodes. Bottom: Chemical structure of the molecular wire which consists of two zinc-porphyrin units, pyrene anchor groups and bulky side groups.[71]

1.2.2.3 Scanning probe method on Graphene

Recently, Rudnev explored the anchoring group chemistry effects on the conductance properties of graphite-molecule contacts by probing them with gold STM tips.[72] Instead of a metal electrode (Au/Pd) as mentioned in 1.2.1.3, robust graphite/graphene substrates are used. Common metal electrodes pose fabrication and operational problems due to the high mobility of the surface atoms. In this work, interested molecules are bonded to graphene by electrochemically grafting of the diazonium salt. By adopting covalent bond, molecular junctions show a single well-defined conductance.[72]

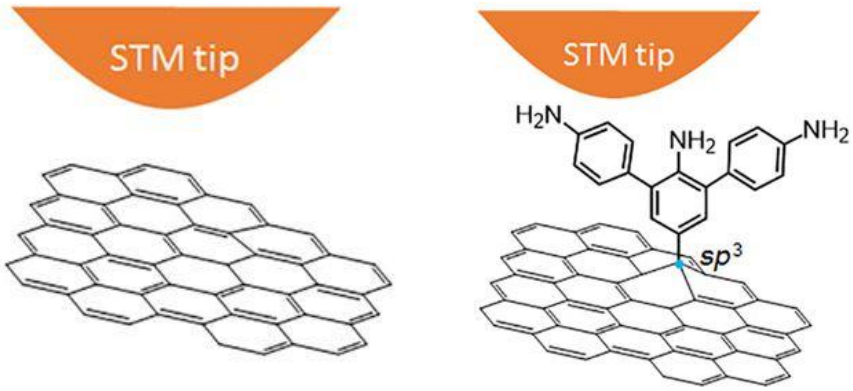

Figure 1-17 The schematics of Au/HOPG junctions in (Left) blank experiment without adding molecules and (Right) molecular junction with a probable dendrimeric structure, which can be obtained upon grafting.[72]

By forming a direct C-C binding, the covalent attachment of molecules to the highly ordered graphite surface results in well-defined narrow conductance values and stability at room temperature.

1.3 Carbon Nanotubes

1.3.1 Structure of carbon nanotubes

Carbon nanotubes are one of the allotropes of carbon, together with diamond, graphite, and fullerenes. The name comes from the cylindrical nanostructure of a nanotube which can have an extraordinary high length-to-diameter ratio of 132,000,000:1.[73] In 1960, straight hollow tubes of carbon had been observed in the catalysis-enhanced chemical vapour deposition process of producing fullerenes. However, it was not until 1991 that the tubular shape in the form of coaxial tubes of graphitic sheets, ranging from 2 to 50 shells, were observed by Iijima [74] and named multi-walled carbon nanotubes(MWCNT) later. Two years later, single walled carbon nanotube(SWCNT) which has only one layer of graphene was found by Bethune [75] and Iijima & Ichiashi.[76]

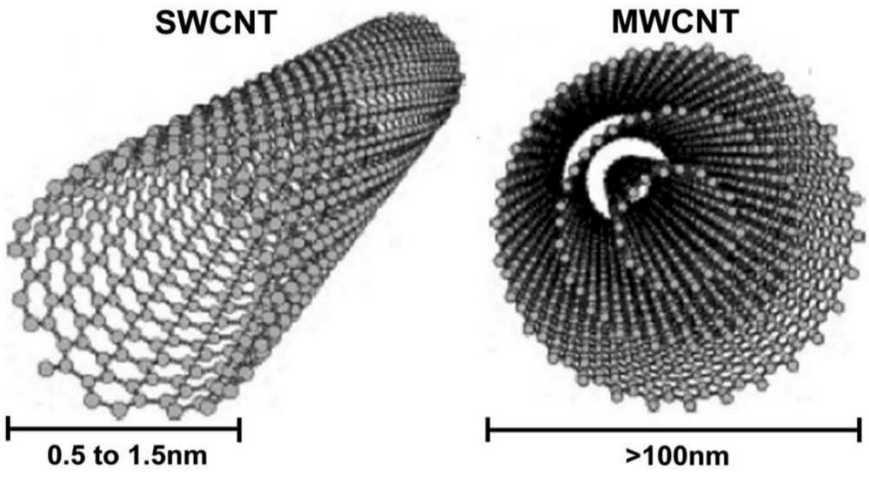

Figure 1-18 Schematic of Single Wall Carbon Nanotube and Multi-Wall Carbon nanotube

For SWCNT, the structure can be conceptualised by wrapping a single atom layer of graphene. In this way, MWCNT could be treated as several SWCNT in concentric cylinders as shown in **Figure 1-18**. Due to the honeycomb lattice of graphite, the

various ways to roll graphene into tubes are therefore mathematically defined by the vector of helicity **Ch**, as follows.

$$\mathrm{OA} = \boldsymbol{C_h} = n * \boldsymbol{a_1} + m * \boldsymbol{a_2}$$

Where n and m are the integers of the vector OA considering the unit vectors a_1 and a_2. (shown in **Figure 1-19** a) The diameter of the tube D and angle of helicity **θ** will be given by

$$\mathrm{D} = \frac{|\boldsymbol{C_h}|}{\pi} = \frac{a*\sqrt{m^2+n^2+mn}}{\pi} \text{ and } \cos\theta = \frac{2*n+m}{2*\sqrt{m^2+n^2+nm}}$$

where a is the length of the carbon-carbon bond.

Since **Ch**, and D are all expressed as a function of the integers n and m, they are sufficient to define any particular SWNT by denoting them (n, m). **Figure 1-19** b gives an example of different types of SWCNT, zig-zag SWCNT (with an angle of helicity = 0, n=0), armchair SWCNT (with an angle of helicity =30, m=n) and a chiral SWCNT (the rest helicity).

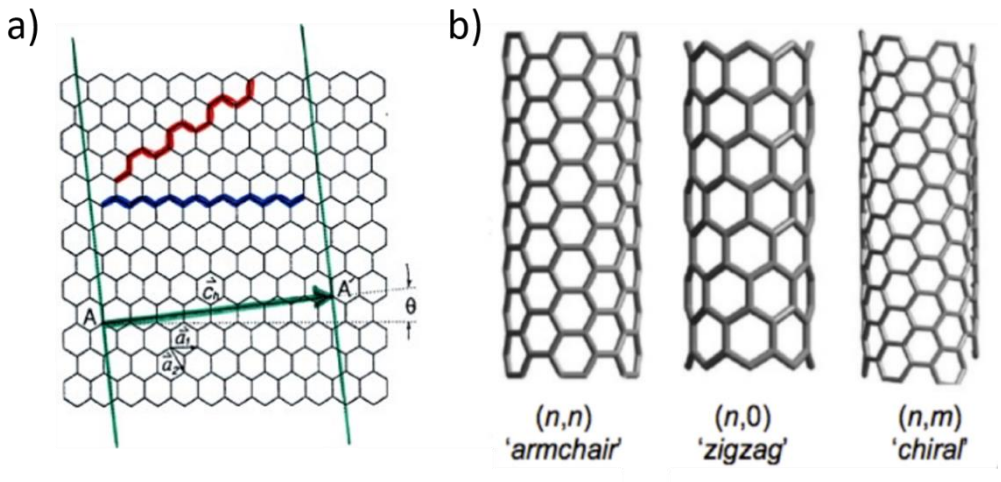

Figure 1-19 a): Graphene honeycomb network with lattice vectors a_1 and a_2. b): Schematic of zigzag, armchair and chiral carbon nanotubes. From reference [77]

The covalent sp^2 bond between Carbon atoms provides the NT with great mechanical, thermal and electrical properties. However, challenges in applying SWCNT remain including defects, dispersion and purification. Among all the synthesis methods for SWCNT, high pressure or high temperature would introduce defects in the tube like atomic vacancies, bond rotations, and non-hexagonal rings. The number of defects would damage the nanostructure and therefore affect the physical properties. For example, the tensile strength of the tube is dependent on its weakest segment in a similar manner to a chain, where the strength of the weakest link becomes the maximum strength of the chain. Furthermore, individual nanotubes tend to align together naturally by pi-stacking effects which make them difficult to be separated. Because of their hydrophobic nature, carbon nanotubes tend to agglomerate even in the organic solvents hindering further chemical reaction. Beyond that, many SWCNT fabrication processes cause metallic catalyst residual which is a detriment to performance. In this way, methods to purify and separate the tubes would be a key issue for further research and applications.

1.3.2 Carbon nanotube electrical properties

Carbon nanotubes are expected to be the future materials for CMOS technology to replace silicon while Moore's Law approaching the physics limit. The electronic structure and electrical properties have been well theoretically studied and has also been tested experimentally. As is mentioned in chapter 1.3.1, their properties change significantly with the (n, m) values. New periodic boundary conditions are imposed on the electronic wave functions when assuming the graphite is wrapped, which give rise to one-dimensional subbands:

$$Ch*K = 2\pi*j$$

Where j is an integer and Ch is the roll-up vector for the tubes which indicate their helicity.

In general, for n=m, tubes behave as metals with zero bandgaps; for n-m=3i (i is a non-zero integer), tubes are semiconductors with small band gap; for the rest, tubes are semiconductors with large band gap.

Figure 1-20 shows the band structure of graphene near the Fermi level. In the hexagonal first Brillouin zone (the primitive unit cell in wave vector space), the Fermi level lies at the crossing point between the cone-like dispersions (**Figure 1-20** (a) and (b)). [78]

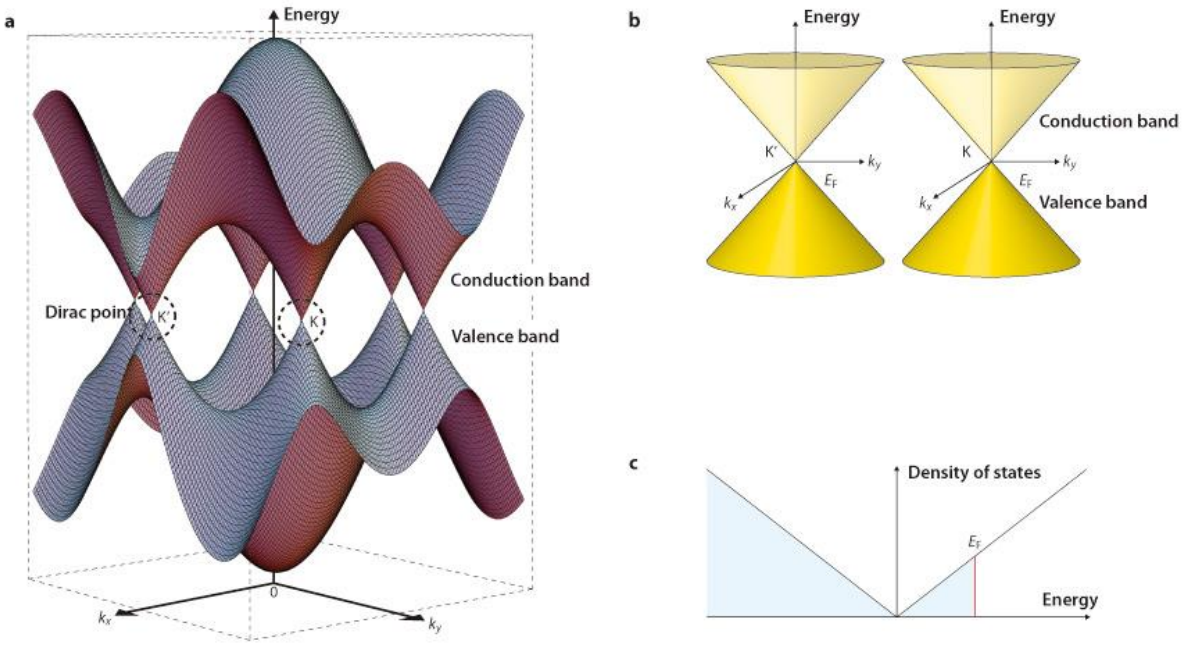

Figure 1-20 (a) Energy bands near the Fermi level in graphene. The conduction and valence bands cross at points K and K'. (b) Conic energy bands in the vicinity of the K and K' points. (c) Density of states near the Fermi level with Fermi energy EF. From reference [78]

One interesting aspect of transport in nano structure systems is that the characteristic length scales span the transition from classical to quantum transport. Depending on certain critical length scales, transport may be semi-classical or purely quantum, or even

more difficult, a mixture of the two in which the effects of decoherence and dissipation play important roles, while at the same time, quantum effects still dominant. In this way, electron transport in a CNT depends on the tube length L, and width W. Depending on how the coherence length L_φ (without electron-photon scattering) compare to L (the length of the nanotube), different conduction modes are observed:

Ballistic if $L < L_\varphi$. And Quasi-ballistic if $L > L_\varphi$.

For ballistic conduction (short tubes with a small number of defects), the predicted electronic conductance is independent of the tube length. The transport would be elastic scattering in the tube and the Landauer model can be written as

$$G = G_0 * \sum T_i \tag{1-11}$$

The theoretical conductance value of tube is then twice the fundamental conductance unit G_0= 4e/h or a resistance of 6.5 kΩ due to the existence of two propagating modes.

Due to the reduced electron scattering observed for metallic CNTs and their stability at high temperatures, CNTs can support high current densities (4A/cm2).[79] However, structural defects can lead to quantum interference of the electronic wave function, which localises the charge carriers in one-dimensional systems and increases resistivity dramatically. [80]

Besides, the influence of the electrodes where Schottky barriers are formed should be taken into account. [81, 82] Palladium electrodes have been shown to form excellent junctions with nanotubes. In particular, their band gap can vary from zero to about 2 eV, and their electrical conductivity can show metallic or semiconducting behaviour. Single-walled nanotubes are likely candidates for miniaturising electronics especially as the most basic component in circuits—molecule wire.

1.3.3 DNA wrapped single wall carbon nanotubes

To overcome the remaining limitations, including but not limited to, lack of stable dispersion in solvents, various methods have been studied to increase the solubility of CNTs without altering their properties.[83, 84] One of the first and commonly used approaches was the use of strong acids.[85] Even if this method has increased the solubility by introducing carboxylic acid groups on the tubes, it produces defects along the tubes compromising their electronic properties. Therefore, chemical functionalisation strategies have been adopted to improve the nanotubes' solubility by either covalent or non-covalent binding. Compared to a covalent functionalisation, the noncovalent one will preserve the desired properties of CNTs. By far, different molecules like polymer, biomolecules, surfactants and polyaromatic compounds have been employed as surfactants. Meanwhile, the formation of a complex between CNTs and DNA has drawn great attention since these hybrids will then take advantages of both the outstanding properties of CNTs and the selective recombination ability of DNA strands. In 2003, Zheng [86, 87] had successfully bound the single-strand DNA (ssDNA) to nanotubes through π-πstacking, in the form of helical wrapping on the surface(shown in **Figure 1-21**). The strong noncovalent interaction between CNTs and DNA makes SWCNTs soluble and effectively dispersed in aqueous solutions. Moreover, compared to other polymer wrapping methods, the DNA coupling offers a high CNT concentration as much as 4 mg/ml. Additionally, the phosphate groups on the DNA in the hybrids provide a negative charge density which depends on the DNA sequence and the CNT electrical property (chirality).

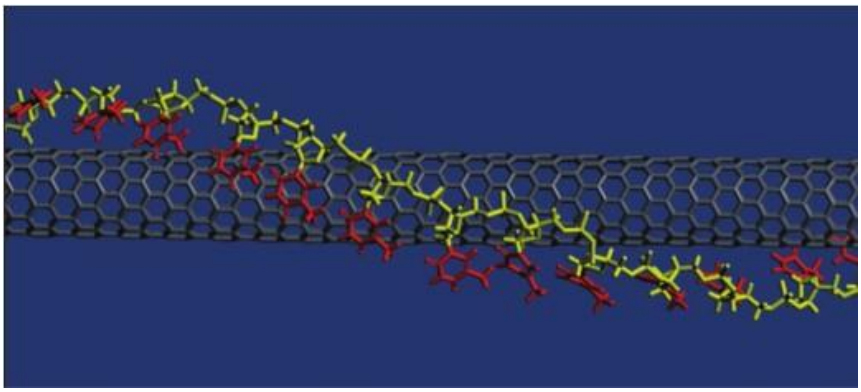

Figure 1-21 Carbon Nanotube wrapped by ssDNA[88]

Further work has been done by Zheng and his collaborators in the separation of carbon nanotubes based on their electronic characteristics. This has been achieved by ion-exchanging chromatography.[89, 90] Recently, Zheng et al. report a systematic study of the spontaneous partition of DNA-wrapped SWCNTs in several polymer aqueous two-phase systems.[91] In this research, 15 single-chirality nanotube species have been purified from a synthetic mixture by a combination of DNA sequence, polymer two-phase system and partition modulators. Moreover, size exclusion chromatography has been adopted to purify CNTs and sort them into fractions of uniform length.[92] Since the report of the synthesis of DNA-wrapped CNTs, many applications of these hybrids have been explored including chemical biosensors,[93-99] DNA hybridization biosensors,[100] and bioelectrodes for fuel cells.[101]

Recently, Penzo et al. reported the fabrication of a single wall carbon nanotube transistor by a directed assembly method.[102] In their work, they have passivated the oxidised silicon substrate with predefined electrodes via PEG Silanization and an e-beam lithography was then introduced to pattern the surface while exposing the area to oxygen plasma. Magnesium ions in the SWCNT solution bridged the negative charges on the post-O2 plasma SiO2 surface and the ones on the DNA sugar − phosphate

backbone, allowing for the selective deposition of the DNA-wrapped SWCNTs on the patterned area.

The existing applications of DNA-wrapped CNTs prove that the hybrids can be utilised in electronics applications. The solubility of carbon nanotubes in aqueous solution provides the possibility of scalability and low cost by self-assembly strategies. On the other hand, the functional terminal ends of DNA-CNTs makes them potential good candidates as nanoelectrodes for molecular junctions: the work of the thesis presented here demonstrates precisely this.

References

1. Gray, P.R., et al., *Analysis and design of analog integrated circuits*. 2001: Wiley.
2. *Internationaly Technology Roadmap for semiconductor 2.0*. 2015, ESIA, JEITA, KSIA, TSIA, SIA.
3. Silvia, K., *Control of molecule-based transport for future molecular devices.* Journal of Physics: Condensed Matter, 2011. **23**(1): p. 013001.
4. Lu, W. and C.M. Lieber, *Nanoelectronics from the bottom up.* Nat Mater, 2007. **6**(11): p. 841-850.
5. Xu, B.Q., et al., *Electromechanical and Conductance Switching Properties of Single Oligothiophene Molecules.* Nano Letters, 2005. **5**(7): p. 1491-1495.
6. Ward, D.R., et al., *Electronic and optical properties of electromigrated molecular junctions.* Journal of Physics: Condensed Matter, 2008. **20**(37): p. 374118.
7. Reddy, P., et al., *Thermoelectricity in Molecular Junctions.* Science, 2007. **315**(5818): p. 1568.
8. Bogani, L. and W. Wernsdorfer, *Molecular spintronics using single-molecule magnets.* Nat Mater, 2008. **7**(3): p. 179-186.
9. Metzger, R.M., *Electrical rectification by a molecule: The advent of unimolecular electronic devices.* Accounts of Chemical Research, 1999. **32**(11): p. 950-957.
10. Heath, J.R. and M.A. Ratner, *Molecular Electronics.* Physics Today, 2003. **56**(5): p. 43-49.
11. Joachim, C. and M.A. Ratner, *Molecular electronics: some views on transport junctions and beyond.* Proc Natl Acad Sci U S A, 2005. **102**(25): p. 8801-8.
12. Cuniberti, G., G. Fagas, and K. Richter, *Introducing molecular electronics: A brief overview*. 2005: Springer.
13. Selzer, Y. and D.L. Allara, *Single-molecule electrical junctions.* Annu. Rev. Phys. Chem., 2006. **57**: p. 593-623.
14. Jia, C. and X. Guo, *Molecule-electrode interfaces in molecular electronic devices.* Chemical Society reviews, 2013. **42**(13): p. 5642-60.
15. Venkataraman, L., et al., *Dependence of single-molecule junction conductance on molecular conformation.* Nature, 2006. **442**(7105): p. 904-7.
16. Venkataraman, L., et al., *Single-Molecule Circuits with Well-Defined Molecular Conductance.* Nano Letters, 2006. **6**(3): p. 458-462.
17. Hong, W., et al., *Single molecular conductance of tolanes: experimental and theoretical study on the junction evolution dependent on the anchoring group.* Journal of the American Chemical Society, 2012. **134**(4): p. 2292-2304.
18. Mujica, V., et al., *Electron transfer in molecules and molecular wires: Geometry dependence, coherent transfer, and control.* Electron Transfer-from Isolated Molecules to Biomolecules, Pt 2, 1999. **107**: p. 403-429.
19. Nitzan, A., *Electron transmission through molecules and molecular interfaces.* Annual Review of Physical Chemistry, 2001. **52**: p. 681-750.
20. Nitzan, A. and M.A. Ratner, *Electron Transport in Molecular Wire Junctions.* Science, 2003. **300**(5624): p. 1384-1389.
21. Wold, D.J., et al., *Distance dependence of electron tunneling through self-assembled monolayers measured by conducting probe atomic force microscopy: Unsaturated versus saturated molecular junctions.* Journal of Physical Chemistry B, 2002. **106**(11): p. 2813-2816.
22. Ratner, M.A., et al., *Molecular Wires: Charge Transport, Mechanisms, and Control.* Annals of the New York Academy of Sciences, 1998. **852**(1): p. 22-37.
23. Principles, B., *Semiconductor physics and devices*. Vol. 9. 2006. 57-57.
24. Calloway, J. and G.G. Johnson, *Energy band theory.* Physics Today, 1964. **17**: p. 61.

25. Cotton, F.A. and G. Wilkinson, *Advanced inorganic chemistry*. Vol. 594. 1988: Wiley New York.
26. Aviram, A. and M.A. Ratner, *MOLECULAR RECTIFIERS.* Chemical Physics Letters, 1974. **29**(2): p. 277-283.
27. Kuhn, H. and D. Möbius, *Systeme aus monomolekularen Schichten – Zusammenbau und physikalisch-chemisches Verhalten.* Angewandte Chemie, 1971. **83**(17-18): p. 672-690.
28. Feldman, A.K., et al., *Molecular electronic devices based on single-walled carbon nanotube electrodes.* Accounts of chemical research, 2008. **41**(12): p. 1731-41.
29. Shen, Q., et al., *Integrating reaction chemistry into molecular electronic devices.* Chemistry, an Asian journal, 2010. **5**(5): p. 1040-57.
30. Xiang, D., et al., *Molecular-Scale Electronics: From Concept to Function.* Chem Rev, 2016. **116**(7): p. 4318-440.
31. Reed, M.a., *Conductance of a Molecular Junction.* Science, 1997. **278**(5336): p. 252-254.
32. Collier, C.P., *Electronically configurable molecular-based logic gates.* Science, 1999. **285**: p. 391-394.
33. Reed, M.A., et al., *Molecular random access memory cell.* Appl. Phys. Lett., 2001. **78**: p. 3735-3737.
34. Metzger, R.M. and M.P. Cava, *Molecular Electronics: Science and Technology*. 1998.
35. Chen, J., et al., *Large on-off ratios and negative differential resistance in a molecular electronic device.* Science, 1999. **286**: p. 1550-1552.
36. Mbindyo, J.K.N., et al., *Template synthesis of metal nanowires containing monolayer molecular junctions.* Journal of the American Chemical Society, 2002. **124**(15): p. 4020-6.
37. Qin, L., et al., *On-Wire Lithography.* Science, 2005. **309**(5731): p. 113-115.
38. Ziegler, K.J., et al., *Controlled oxidative cutting of single-walled carbon nanotubes.* Journal of the American Chemical Society, 2005. **127**(5): p. 1541-1547.
39. Pei, T., et al., *Electronic transport in single-walled carbon nanotube/graphene junction Enhancement of interfacial thermal transport by carbon nanotube-graphene junction.* Citation: Appl. Phys. Lett. Phys. Lett. Appl. Phys. Lett. Appl. Phys. Lett, 2011. **991**(10).
40. Cao, Y., et al., *Building High-Throughput Molecular Junctions Using Indented Graphene Point Contacts.* Angewandte Chemie-International Edition, 2012. **51**(49): p. 12228-12232.
41. Sadeghi, H., S. Sangtarash, and C. Lambert, *Robust Molecular Anchoring to Graphene Electrodes.* Nano Letters, 2017. **17**(8): p. 4611-4618.
42. Xu, Q., et al., *Single Electron Transistor with Single Aromatic Ring Molecule Covalently Connected to Graphene Nanogaps.* Nano Lett, 2017.
43. Mol, J.A., et al., *Graphene-porphyrin single-molecule transistors.* Nanoscale, 2015. **7**(31): p. 13181-13185.
44. Park, J., *Coulomb blockade and the Kondo effect in single-atom transistors.* Nature, 2002. **417**: p. 722-725.
45. Reed, M.a., et al., *Conductance of a Molecular Junction.* Science, 1997. **278**(5336): p. 252-254.
46. Love, J.C. and E. Al, *Self-Assembled Monolayers of Thiolates on Methals as a Form of Nanotechnology*. Vol. 4. 2005.
47. Newton, L., et al., *Self assembled monolayers (SAMs) on metallic surfaces (gold and graphene) for electronic applications.* Journal of Materials Chemistry C, 2013. **1**(3): p. 376-393.
48. Akkerman, H.B., et al., *Towards molecular electronics with large-area molecular junctions.* Nature, 2006. **441**(7089): p. 69-72.
49. Binnig, G. and H. Rohrer, *Scanning tunneling microscopy.* Surface science, 1983. **126**(1-3): p. 236-244.

50. Murrell, M.P., et al., *Spatially resolved electrical measurements of SiO2 gate oxides using atomic force microscopy.* Applied Physics Letters, 1993. **62**(7): p. 786-788.
51. Ishida, T., et al., *Electrical conduction of conjugated molecular SAMs studied by conductive atomic force microscopy.* Journal of Physical Chemistry B, 2002. **106**(23): p. 5886-5892.
52. Xu, B.Q. and N.J.J. Tao, *Measurement of single-molecule resistance by repeated formation of molecular junctions.* Science, 2003. **301**(5637): p. 1221-1223.
53. Holmlin, R.E., et al., *Electron Transport through Thin Organic Films in Metal−Insulator−Metal Junctions Based on Self-Assembled Monolayers.* Journal of the American Chemical Society, 2001. **123**(21): p. 5075-5085.
54. Sek, S., R. Bilewicz, and K. Slowinski, *Electrochemical wiring of alpha, omega-alkanedithiol molecules into an electrical circuit.* Chem Commun (Camb), 2004(4): p. 404-5.
55. Weiss, E.A., et al., *Influence of Defects on the Electrical Characteristics of Mercury-Drop Junctions: Self-Assembled Monolayers of n-Alkanethiolates on Rough and Smooth Silver.* Journal of the American Chemical Society, 2007. **129**(14): p. 4336-4349.
56. Tang, J., et al., *Encoding Molecular-Wire Formation within Nanoscale Sockets.* Angewandte Chemie, 2007. **119**(21): p. 3966-3969.
57. Tang, J., et al., *Single-molecule transistor fabrication by self-aligned lithography and in situ molecular assembly.* Microelectronic Engineering, 2006. **83**(4–9): p. 1706-1709.
58. Chen, X., et al., *Spectroscopic Tracking of Molecular Transport Junctions Generated by Using Click Chemistry.* Angewandte Chemie, 2009. **121**(28): p. 5280-5283.
59. Guo, X. and C. Nuckolls, *Functional single-molecule devices based on SWNTs as point contacts.* Journal of Materials Chemistry, 2009. **19**(31): p. 5470-5473.
60. Cao, Y., et al., *Current Trends in Shrinking the Channel Length of Organic Transistors Down to the Nanoscale.* Advanced Materials, 2010. **22**(1): p. 20-32.
61. Odom, T.W., et al., *Atomic structure and electronic properties of single-walled carbon nanotubes.* Nature, 1998. **391**(6662): p. 62-64.
62. Mann, B.F., et al., *Sub 2-µm Macroporous Silica Particles Derivatized for Enhanced Lectin Affinity Enrichment of Glycoproteins.* Analytical Chemistry, 2013. **85**(3): p. 1905-1912.
63. Guo, X., et al., *Covalently Bridging Gaps in Single-Walled Carbon Nanotubes with Conducting Molecules.* Science, 2006. **311**(5759).
64. Guo, X., et al., *Chemoresponsive monolayer transistors.* Proceedings of the National Academy of Sciences, 2006. **103**(31): p. 11452-11456.
65. Guo, X., et al., *Single-Molecule Devices as Scaffolding for Multicomponent Nanostructure Assembly.* Nano Letters, 2007. **7**(5): p. 1119-1122.
66. Whalley, A.C., et al., *Reversible switching in molecular electronic devices.* Journal of the American Chemical Society, 2007. **129**(42): p. 12590-12591.
67. Chuancheng Jia, A.M.N.X.S.H.J.W.Q.Y.S.W.H.C.D.W.B.F.Z.L.G.Z.D.-H.Q.H.T.M.A., et al., *Covalently bonded single-molecule junctions with stable and reversible photoswitched conductivity.* Science (New York, N.Y.), 2016. **352**(6292): p. 1443-5.
68. Prins, F., et al., *Room-Temperature Gating of Molecular Junctions Using Few-Layer Graphene Nanogap Electrodes.* Nano Letters, 2011. **11**(11): p. 4607-4611.
69. Simmons, J.G., *Generalized Formula for the Electric Tunnel Effect between Similar Electrodes Separated by a Thin Insulating Film.* Journal of Applied Physics, 1963. **34**(6): p. 1793-1803.
70. Lau, C.S., et al., *Nanoscale control of graphene electrodes.* Physical Chemistry Chemical Physics, 2014. **16**(38): p. 20398-20401.
71. Gehring, P., et al., *Distinguishing Lead and Molecule States in Graphene-Based Single-Electron Transistors.* ACS Nano, 2017. **11**(6): p. 5325-5331.

72. Rudnev, A.V., et al., *Stable anchoring chemistry for room temperature charge transport through graphite-molecule contacts.* Science Advances, 2017. **3**(6).
73. Wang, X., et al., *Fabrication of Ultralong and Electrically Uniform Single-Walled Carbon Nanotubes on Clean Substrates.* Nano Letters, 2009. **9**(9): p. 3137-3141.
74. Iijima, S., *Helical microtubules of graphitic carbon.* Nature, 1991. **354**(6348): p. 56-58.
75. Bethune, D.S., et al., *Cobalt-catalysed growth of carbon nanotubes with single-atomic-layer walls.* Nature, 1993. **363**(6430): p. 605-607.
76. Iijima, S. and T. Ichihashi, *Single-shell carbon nanotubes of 1-nm diameter.* Nature, 1993. **363**(6430): p. 603-605.
77. Scarselli, M., P. Castrucci, and M.D. Crescenzi, *Electronic and optoelectronic nano-devices based on carbon nanotubes.* Journal of Physics: Condensed Matter, 2012. **24**(31): p. 313202.
78. Ando, T., *The electronic properties of graphene and carbon nanotubes.* October, 2009. **1**(October 2005): p. 17-21.
79. Zhu, W., et al., *Large current density from carbon nanotube field emitters.* Applied Physics Letters, 1999. **75**(6): p. 873-875.
80. Collins, P.G., *Defects and disorder in carbon nanotubes.* Oxford Handbook of Nanoscience and Technology: Volume 2: Materials: Structures, Properties and Characterization Techniques, 2010. **2**: p. 31.
81. Zhu, W., *Carbon Nanotube-Metal Contact*, in *Encyclopedia of Nanotechnology*, B. Bhushan, Editor. 2012, Springer Netherlands: Dordrecht. p. 388-391.
82. Cao, Q., et al., *End-bonded contacts for carbon nanotube transistors with low, size-independent resistance.* Science, 2015. **350**(6256): p. 68.
83. Baughman, R.H., A.A. Zakhidov, and W.A. de Heer, *Carbon nanotubes--the route toward applications.* science, 2002. **297**(5582): p. 787-792.
84. Sun, Y.-P., et al., *Functionalized Carbon Nanotubes: Properties and Applications.* Accounts of Chemical Research, 2002. **35**(12): p. 1096-1104.
85. Saito, T., K. Matsushige, and K. Tanaka, *Chemical treatment and modification of multi-walled carbon nanotubes.* Physica B: Condensed Matter, 2002. **323**(1): p. 280-283.
86. Zheng, M., et al., *Structure-based carbon nanotube sorting by sequence-dependent DNA assembly.* Science (New York, N.Y.), 2003. **302**(5650): p. 1545-8.
87. Zheng, M., et al., *DNA-assisted dispersion and separation of carbon nanotubes.* Nature materials, 2003. **2**(5): p. 338-42.
88. Smit, R.H.M., et al., *Measurement of the conductance of a hydrogen molecule.* Nature, 2002. **419**(6910): p. 906-909.
89. Tu, X. and M. Zheng, *A DNA-based approach to the carbon nanotube sorting problem.* Nano Research, 2008. **1**(3): p. 185-194.
90. Tu, X.M., et al., *DNA sequence motifs for structure-specific recognition and separation of carbon nanotubes.* Nature, 2009. **460**(7252): p. 250-253.
91. Ao, G., C.Y. Khripin, and M. Zheng, *DNA-Controlled Partition of Carbon Nanotubes in Polymer Aqueous Two-Phase Systems.* Journal of the American Chemical Society, 2014. **136**(29): p. 10383-10392.
92. Huang, X., R.S. McLean, and M. Zheng, *High-resolution length sorting and purification of DNA-wrapped carbon nanotubes by size-exclusion chromatography.* Anal Chem, 2005. **77**(19): p. 6225-8.
93. Karachevtsev, V., et al., *Glucose sensing based on NIR fluorescence of DNA-wrapped single-walled carbon nanotubes.* Chemical physics letters, 2007. **435**(1): p. 104-108.
94. Xu, Y., et al., *Double-stranded DNA single-walled carbon nanotube hybrids for optical hydrogen peroxide and glucose sensing.* The Journal of Physical Chemistry C, 2007. **111**(24): p. 8638-8643.

95. Liang, Z., et al., *Solubilization of single-walled carbon nanotubes with single-stranded DNA generated from asymmetric PCR.* International Journal of Molecular Sciences, 2007. **8**(7): p. 705-713.
96. Ma, Y., et al., *Enhanced sensitivity for biosensors: multiple functions of DNA-wrapped single-walled carbon nanotubes in self-doped polyaniline nanocomposites.* The Journal of Physical Chemistry B, 2006. **110**(33): p. 16359-16365.
97. Hu, C., et al., *DNA functionalized single-walled carbon nanotubes for electrochemical detection.* The Journal of Physical Chemistry B, 2005. **109**(43): p. 20072-20076.
98. Viswanathan, S., H. Radecka, and J. Radecki, *Electrochemical biosensor for pesticides based on acetylcholinesterase immobilized on polyaniline deposited on vertically assembled carbon nanotubes wrapped with ssDNA.* Biosensors and Bioelectronics, 2009. **24**(9): p. 2772-2777.
99. Staii, C., et al., *DNA-Decorated Carbon Nanotubes for Chemical Sensing.* Nano Letters, 2005. **5**(9): p. 1774-1778.
100. Chen, R.J. and Y. Zhang, *Controlled precipitation of solubilized carbon nanotubes by delamination of DNA.* The Journal of Physical Chemistry B, 2006. **110**(1): p. 54-57.
101. Lee, J.Y., et al., *Use of bioelectrode containing DNA-wrapped single-walled carbon nanotubes for enzyme-based biofuel cell.* Journal of Power Sources, 2010. **195**(3): p. 750-755.
102. Penzo, E., et al., *Directed Assembly of Single Wall Carbon Nanotube Field Effect Transistors.* ACS Nano, 2016. **10**(2): p. 2975-2981.

Chapter 2 Atomic Force Microscopy Techniques

2.1 The techniques

What is AFM?

Atomic force microscopy (AFM), also called scanning force microscopy (SFM) is a type of scanning probe microscopy (SPM). AFM allows the mapping of the topography/morphology of surfaces and interfaces with a vertical resolution on the order of fractions of a nanometre and lateral resolution of a few nm.[1] Binning invented and made the first experimental implementation of AFM in 1986. [2]

How does AFM work?

AFM probes the surface by using a sharp tip with a radius usually smaller than 12 nm.[3] By measuring forces (typically of the Van der Waals type,) between the tip and surface at very short distances (0.2-10 nm probe-sample), AFM provides a 3D profile of the surface at the nanoscale. Unlike scanning tunnelling microscopy[4], the AFM tip is supported by a flexible cantilever with a sensitive spring constant. In detail, by approaching the tip to the surface, the force between them leads to a deflection of the cantilever according to Hooke's law. Meanwhile, the laser beam which reflects from the back side of the cantilever is detected by the photodetector. The position of the beam

in the sensor measures the deflection of the cantilever and in turn the force. A feedback loop is introduced to maintain the tip in a constant length above the surface (depending on the working mode).

Figure 2-1 shows the typical AFM configuration. The small spring-like cantilever (4) is carried by the support (3) where a piezoelectric element (3) oscillates the cantilever (4). The sharp tip (5) is fixed to the free-end of the cantilever (4). The detector (2) records the deflection and motion of the cantilever (4) through reflected laser beam from a laser source (1). The sample (6) is mounted on the sample stage (7). Numbers in parentheses correspond to numbered featured in **Figure 2-1**.

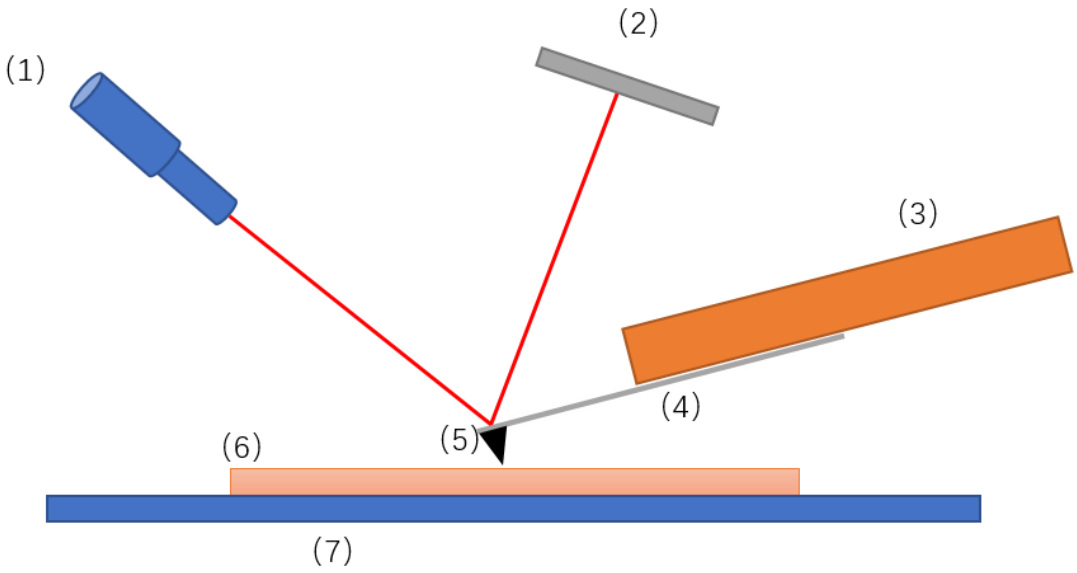

Figure 2-1 (1): Laser beam, (2): Detector of deflection and motion of the cantilever, (3): Piezoelectric element (to oscillate cantilever at its eigen frequency.), (4): Cantilever, (5): Tip (Fixed to open end of a cantilever, acts as the probe), (6): Sample to be measured by AFM, (7): stage.

According to the configuration described above, the interaction between tip and sample, which can be an atomic scale phenomenon, is transduced into changes of the motion of

cantilever which, is a macro scale phenomenon. Most commonly, the value of deflection is used to quantify the interaction between the tip and sample.

Usually, the Lennard-Jones potential $U_{L\text{-}J}$.[5] describes mutual tip-surface interaction as

$$U_{L-J}(r) = U_0\left\{-2\left(\frac{r_0}{r}\right)^6 + \left(\frac{r_0}{r}\right)^{12}\right\} \quad (2\text{-}1)$$

where**:**

r is the tip-surface distance, r_0 – the tip-surface distance at which the potential reaches its minimum, whereas U_0 is the minimal value of the potential. By taking the derivative of the potential over distance, the force between tip and surface can be obtained from the above equation. **Figure 2-2** graphically displays the relationship between tip-surface force and distance. In general, there are two regimes where different forces will dominate. At a very small distance (a few angstrom), a very strong repulsive force appears between the tip and the sample atoms (that scales as r^{-12} in equation (1)). The force originates from the exchange interactions due to the overlap of the electronic orbitals at atomic distances.

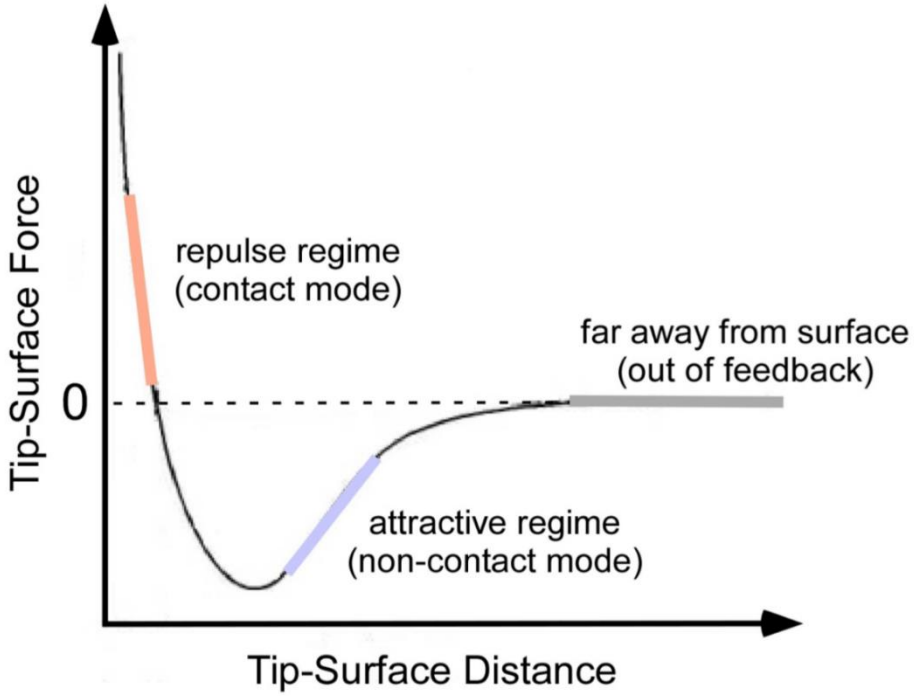

Figure 2-2 Tip-surface Force VS Distance

When the repulsive force is dominant, the tip is in said to be "contact" with the sample. As the tip moves away from the surface, a polarisation interaction between atoms results in attraction between (Van der Waals).

Therefore, there are three main working modes for AFM: contact mode(distance<0.5nm), non-contact mode (0.5-2nm) and tapping mode (1-10nm).

In contact mode, the tip is kept constant on the surface in the repulsive zone. Contours are measured using the feedback loop signal which is tuned to keep the cantilever at a constant position/force. For non-contact mode, the tip oscillates at the resonant frequency of the cantilever (about 100-400 kHz) and the oscillation amplitude (<10nm) is kept constant. As the tip approaches the surface, the Van dee Walls force acts to decrease resonant frequency which is then measured by the system. The frequency deviation is then used to make an image of the sample. Non-contact mode exploits the r^{-6} dependence of tip-surface force interaction from equation (2-1).

Tapping mode is a combination of both contact and non-contact modes. Similar to non-contact mode, the cantilever is driven to oscillate up and down near its resonance frequency. The oscillation is achieved by a small piezoelectric element attached to the AFM tip holder. The amplitude of the oscillation varies between a few to 200nm. The frequency and amplitude of driving signal are kept constant so that the amplitude of oscillation should be the same as long as no interaction between the tip and surface. When the tip approaches the surface, it will 'lightly' tap the surface which causes the decrease in oscillation amplitude. The amplitude is used for the feedback, and the vertical adjustments of the piezo scanner are recorded as the height information.

Benefitting from the oscillating contact, tapping mode can achieve an improved lateral resolution（~5nm）compared to non-contact mode, but without damaging a "soft" organic/biological surface as contact mode would. As is illustrated in **Figure 2-3**, contact mode will damage the surface structure while non-contact mode has a low resolution. Tapping mode eliminates friction forces and avoids the tip to be "trapped" by surface structures.

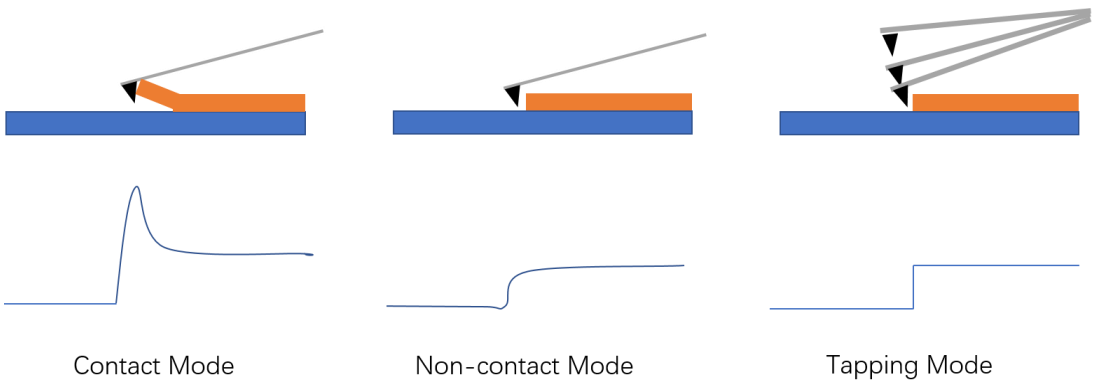

Figure 2-3 Comparison of AFM working modes

Beyond surface topography, other characteristics such as electrical and mechanical properties can be acquired simultaneously at the nanoscale. For example, electrical characteristics such as conductivity can be measured by using a conductive tip. Further discussion will be presented in chapter 2, section 2.3).

Due to the versatility of such methodology, AFM provides possibilities of nano-manipulation by forcing intended contact. By forcing the tip 'hard' contact with the surface, nanolithography can be achieved. More details will be discussed in section

2.2 AFM tip and image correction

In scanning probe microscopy, the tip is playing a key role. It can be used for imaging, measuring mechanical properties at the nanoscale, or as a nanoscale tweezer for manipulation. Since the measurement relies on the interaction between tip and surface, the shape of the tip is important especially for imaging quality. **Figure 2-4** shows the most commonly used tip in this thesis, ScanAsyst-Air (Bruker).

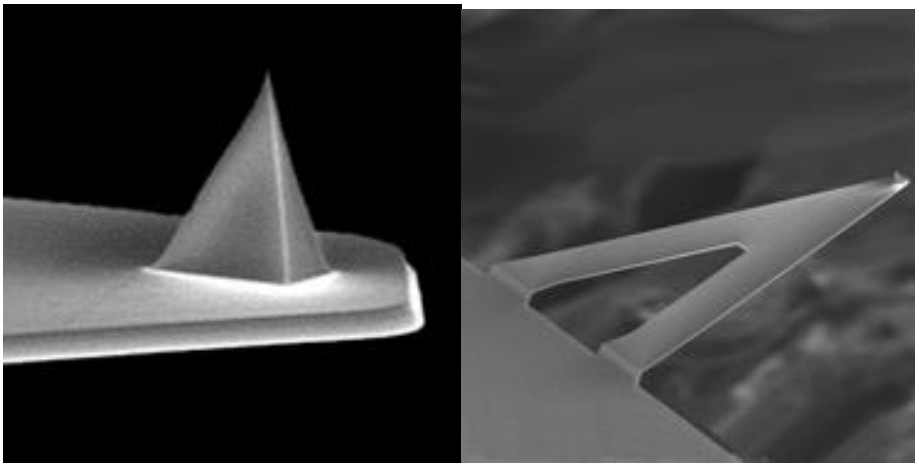

Figure 2-4 Scanning Electron Microscopy images of ScanAsyst-Air tip (Bruker), Left: tip specification; Right: Cantilever specification[6]

It is important to understand the behaviour of the cantilever and the related influencing factor. The schematic of a typical AFM probe is shown in **Figure 2-5**. There are two key equations about the mechanics of the cantilever. The first is Stoney's Formula which describes the relationship between cantilever deflection δ and stress σ. [7]

$$\delta = \frac{3\sigma(1-\nu)}{F}\left(\frac{L}{t}\right)^2 \tag{2-2}$$

Where**:**

ν is the Poisson's ratio, E is Young's modulus, L is the cantilever length, t is the cantilever's thickness.

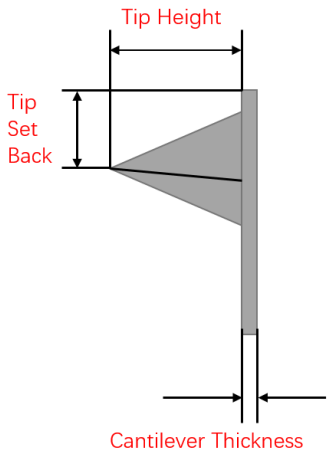

Figure 2-5 Schematic of AFM tip with cantilever

Additionally, another formula (2-3) relates the cantilever spring constant to its dimensions and material constants. [8, 9]

$$\mathrm{k} = \frac{F}{\delta} = \frac{Ewt^3}{4L^3} \tag{2-3}$$

Where**:**

F is the applied force and w is the cantilever width.

By comparing the two above equations, we can easily get force as (2-4) :

$$F = \frac{3\sigma wt(1-\nu)}{4L} \tag{2-4}$$

The defection is largely affected by the cantilever length and thickness. However, the dimensions cannot be controlled well during fabrication. To get a reliable quantitative measurement, a tip calibration before scanning is necessary.

For AFM, the image is captured by moving probe around the surface following the path is shown in **Figure 2-6**.The image resolution can be optimised by scanning more points in a certain area. In this way, the tip is moving in one direction which forms a 2 D cross-section of the interested sample.

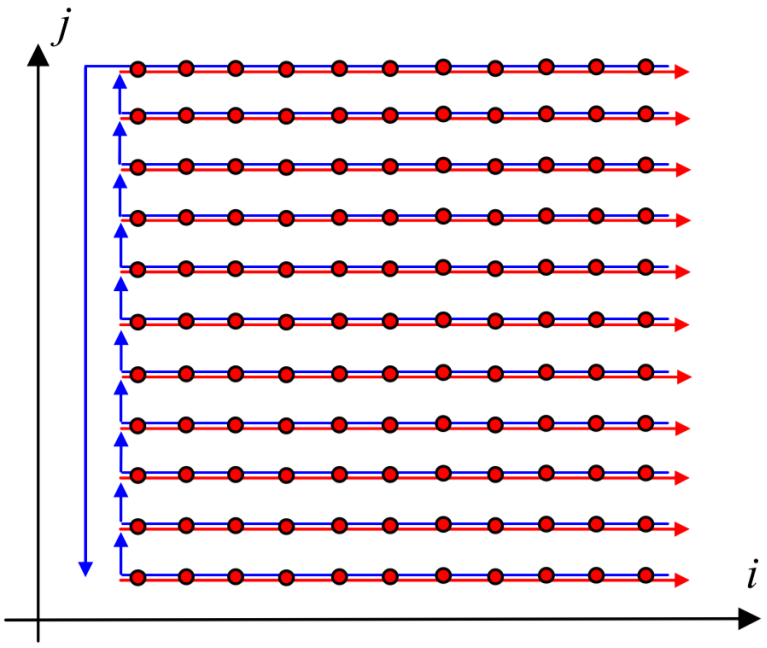

Figure 2-6 AFM tip moving path [5]

By considering tip and the nanostructure as two spheres in the cross section, the actual distance can be calculated. As is shown in **Figure 2-7**, the blue circle corresponds to the AFM tip peak which has a radius of ca.12 nm. The grey circle corresponds to the structure of interest. In this thesis, we are mainly studying nanotubes which have a radius below 5nm (smaller than tip radius).

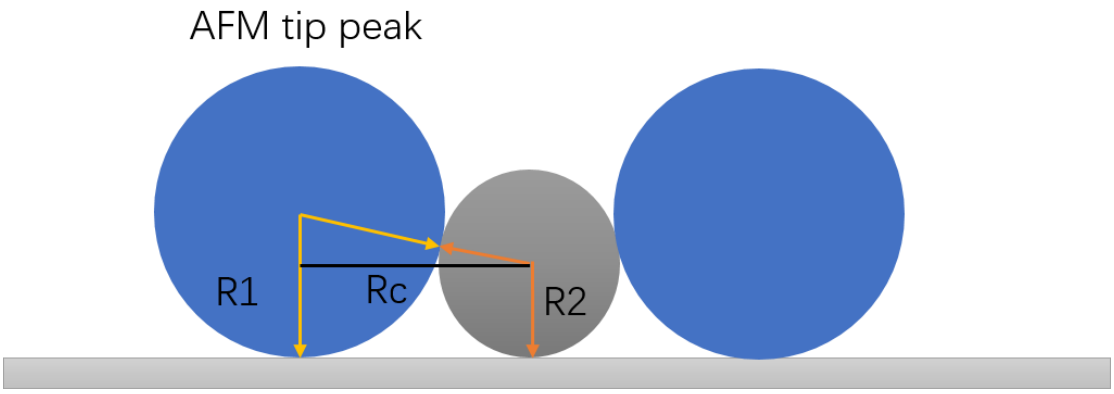

Figure 2-7 Schematic of AFM tip contacting investigated structure

In the setup, the actual contact distance is given in (2-5) :

$$R_c = \sqrt{(R_1 + R_2)^2 - (R_1 - R_2)^2} = 2\sqrt{R_1 R_2} \quad (2\text{-}5)$$

Considering the two-side tip broadening effect, the size of the nanostructure is overestimated by $2R_c$ as $4\sqrt{R_1 R_2}$. All the data measured in the thesis have been corrected based on this theory.

2.3 Conductive Atomic force microscopy

2.3.1 Traditional conductive-AFM

Conductive AFM (C-AFM) is a mode in atomic force microscopy for measuring the electrical properties of samples with nanoscale spatial resolution. The tip of the AFM is used as a mobile electrode, contacting the sample surface. The sample will be in contact itself with a macroscopic electrode. By biasing the tip (or sample) with a DC voltage, the current is measured, and a map of the conductivity (or inversely, resistivity) can be obtained. With the support of a preamplifier, conductive AFM can capture currents from sub-nanoampere to microampere.

The fact that conductive AFM uses two different detection systems (laser-deflection for topography and preamplifier for current) is an enormous advantage compared to scanning tunnelling microscopy. In STM, the topography is formed based on the tunnelling current on the surface which is transformed to distance. However, the topography obtained is a reflection of the current while ignoring areas with different conductivity. On the contrary for conductive AFM, a constant force is maintained during scanning which allows for simultaneous topographic and current images to be generated. This will enable the direct correlation of local topography with electrical properties which makes conductive AFM a powerful technique for the electrical characterisation at the nanometer scale on a wide range of samples. **Figure 2-8** shows a typical conductive AFM configuration.

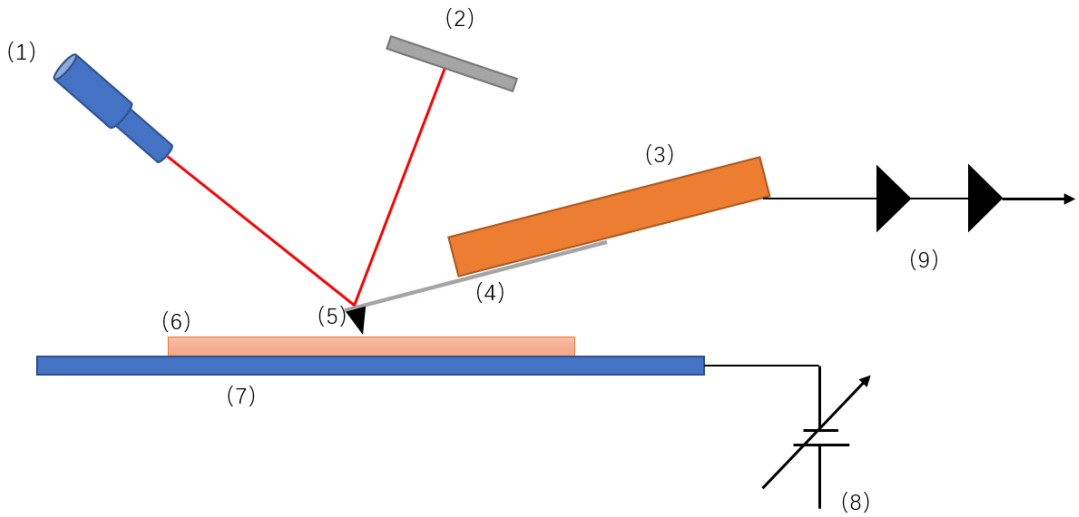

Figure 2-8 (1): Laser beam, (2): Detector of deflection and motion of the cantilever, (3): Piezoelectric element (to oscillate cantilever at its eigen frequency.), (4): Cantilever, (5): Tip (Fixed to open end of a cantilever, acts as the probe), (6): Sample to be measured by AFM, (7): stage, (8): DC bias voltage, (9): current preamplifier.

In conductive AFM, a tip which is coating with a metal to be conductive is brought into contact with the surface at a position of interest at a constant force. Current-Voltage Characteristic Curves can be captured when the sample is biased from the stage(8). The

analogical current signals flowing through the tip/sample nanojunction are sent to the preamplifier(9), which transforms them into digital voltages that can be read by the data acquisition (DAQ) card of the computer.

Since Conductive AFM is based on contact mode AFM, it suffers the problems including tip wearing and surface damage. Both probe and surface experience lateral forces which limit the applications especially for soft materials and loosely attached nanostructures on the surface. Another electrical working mode of AFM named as PeakForce Tunnelling AFM can overcome these limitations, which will be discussed in the next section 2.3.2.

2.3.2 Peakforce tunnelling AFM

As mentioned above, particular attention during C-AFM experiments has to be paid to the contact properties which depend mainly on the tip conditions. There are several common conductive probes employed as conventional AFM probes with one of the following coatings: diamond, PtIr, TiN, W_2C, and Au.[10] The typical curvature radius of the probe with a metal coating is about 35nm.[11] Though much bigger than the conventional probes (normally 12 nm), the tip can still wear quickly during being in contact with the surface.

PeakForce tunnelling AFM is a branded working mode invented by Bruker co. Ltd. In detail, it is a combination of PeakForce mode and tunnelling AFM. PeakForce mode is based on traditional tapping mode while keeping the deflection at pN level through the feedback loop.[12] This direct force control protects the tip and the sample from damage, but more importantly, allows every tip-sample contact to be controlled and recorded for additional mechanical property analysis. In the current implementation, the modulation frequency is 1 to 2 kHz.[13] During which the tip taps the surface

instead of 'hard' contact, the mode reduces the tip surface damage which is crucial for imaging of molecular junctions in this thesis.

Tunnelling AFM (TUNA) works in a similar way as conductive AFM while extending to high resistance samples. TUNA measures sub-picoampere tip/sample currents through highly resistive samples. The mode is originally focusing on evaluating dielectric films subject to breakdown. Tip/sample tunnelling current depends on film thickness leakage paths, possibly caused by defects, charge traps and tip geometry. 'Tunnelling' is named after the application while not limited to tunnelling current.

It is important to note that the PeakForce Tapping, oscillation frequency (1 kHz–2 kHz) falls between the Tapping Mode (>50 kHz),[14] and Contact Mode (DC) interaction cycles. In fact, this mid-band operation is the single most important element for TUNA to work in an intermittent contact mode. In each tapping cycle, the tip is in contact with the sample only for a fraction of the cycle (tens to hundreds of microseconds). The TUNA module must be able to pick up a current signal during this period with acceptable signal-to-noise ratio. A rule of thumb is that the bandwidth of the TUNA module must be 10x greater than the tapping frequency at the chosen gain. At Tapping Mode frequency, this is far beyond the reach of current technology (>500 kHz). At PeakForce Tapping speeds, it is an attainable challenge. The released PeakForce TUNA module（Bruker） is engineered to have a bandwidth around 15 kHz across a range of gains from 10^7 V/A to 10^{10} V/A, with the noise below 100 fA on cycle-averaged current.[13]

Figure 2-9 illustrates what happens when the periodically modulated PeakForce Tapping probe interacts with the surface. The top line represents the Z-position of the cantilever base, as a function of time, as it goes through one period. The middle line

represents the force measured by the probe during the approach (blue) and withdrawal (red) of the tip to the sample. The bottom line (green) represents the detected current passing through the sample.

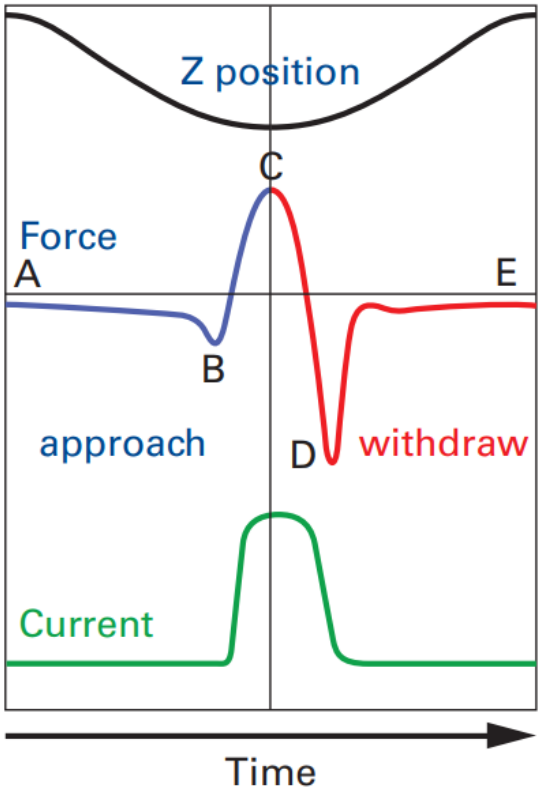

Figure 2-9 Plots of Z position, Force, and Current as a function of time during one PeakForce Tapping cycle, with critical points including (B) jump-to-contact, (C) peak force, (D) adhesion labelled.[13]

Since the modulation frequency is about 1kHz, the time from point A to point E is about 1ms. When the tip is far from the surface (point A), there is little or no force on the tip. As the tip approaches the surface, the cantilever is pulled down toward the surface by attractive forces (usually van der Waals, electrostatic, or capillary forces) as represented by the negative force (below the horizontal axis). At point B, the attractive forces overcome the cantilever stiffness, and the tip is pulled to the surface. The tip then stays on the surface and the force increases until the Z position of the modulation reaches its bottommost position at point C. This is where the peak force occurs. The peak force

(force at point C) during the interaction period is kept constant by the system feedback. The probe then starts to withdraw and the force decreases until it reaches a minimum at point D. Adhesion is measured by the force at this point. The point where the tip comes off the surface is called the pull-off point. This often coincides with the minimum force. Once the tip has come off the surface, only long range forces affect the tip, so once again, the force is very small or zero when the tip-sample separation is at its maximum (point E).

References

1. NT-MDT, *Scanning Force Microscopy-Ultimate resolution in the contact mode*. 2017, Spectrum Instruments.
2. Binnig, G., C.F. Quate, and C. Gerber, *Atomic force microscope.* Physical review letters, 1986. **56**(9): p. 930.
3. Markiewicz, P. and M.C. Goh, *Atomic force microscopy probe tip visualization and improvement of images using a simple deconvolution procedure.* Langmuir, 1994. **10**(1): p. 5-7.
4. Binnig, G. and H. Rohrer, *Scanning tunneling microscopy.* IBM Journal of research and development, 2000. **44**(1/2): p. 279.
5. Mironov, V.L., *Fundamentals of scanning probe microscopy.* Nizhniy Novgorod, 2004. **38**.
6. Bruker. *Bruker AFM Probes* 2017 [cited 2017 July-25]; Available from: http://www.brukerafmprobes.com/p-3726-scanasyst-air.aspx.
7. Stoney, G.G., *The Tension of Metallic Films Deposited by Electrolysis.* Proceedings of the Royal Society of London. Series A, 1909. **82**(553): p. 172.
8. Javier, T., et al., *Quantification of the surface stress in microcantilever biosensors: revisiting Stoney's equation.* Nanotechnology, 2012. **23**(47): p. 475702.
9. Sader, J.E., *Surface stress induced deflections of cantilever plates with applications to the atomic force microscope: Rectangular plates.* Journal of Applied Physics, 2001. **89**(5): p. 2911-2921.
10. Smaali, K., et al., *Band-Gap Determination of the Native Oxide Capping Quantum Dots by Use of Different Kinds of Conductive AFM Probes: Example of InAs/GaAs Quantum Dots.* IEEE Transactions on Electron Devices, 2010. **57**(6): p. 1455-1459.
11. Wiesendanger, R., *Scanning probe microscopy and spectroscopy: methods and applications*. 1994: Cambridge University Press.
12. Bruker, *PeakForce TUNA Nanoelectrical Application Module.* 2010: p. 1-2.
13. Bruker, *Simultaneous Electrical and Mechanical Property Mapping at the Nanoscale with PeakForce TUNA AFM and Conductivity Mapping*. 2013.
14. Bruker, *TappingMode Imaging Applications and Technology.*

Chapter 3 Solution-processable Carbon Nanoelectrodes for Single Molecule Investigations

3.1 Introduction

This chapter describes the assembly and electrical characterisation of solution-processable molecular transport junctions (MTJs) fabricated employing metallic single-walled carbon nanotubes (SWCNTs) as nanoelectrodes. Due to the many potential benefits envisioned for molecular scale electronics, there has been a significant effort in the fundamental understanding of metal-molecule-metal systems and their optoelectronic applications.[1-8] As discussed in chapter 1, section 1.2, different strategies have been developed to form MTJs, including scanning probe techniques, lithographic approaches, and mechanical/electromigration break junctions.[9-13] The use of carbon-based nanoelectrodes, in particular, has emerged as a promising approach[14-20] because of the intrinsic nanoscale size of CNTs and graphene, and the reduced electronic mismatch granted by having molecules and electrodes of the same material (carbon atoms).[21, 22]

Nevertheless, despite the substantial progress in single-molecule electronics from both fundamental and technological standpoints, challenges remain.[21] Principal among these is the time and cost involved in nanogap fabrication, the reliable control of the nanogap size, and the need for a facile (and scalable) technology for the establishment of electrical contact between individual molecules and metal electrodes.

Solution-based self-assembly methods represent a powerful approach to overcome the aforementioned limitations. Work in this context has typically focused on colloidal metallic nanoparticles as building blocks for fabricating nanogaps, which were then bridged to lithographically pre-fabricated electrodes.[23, 24] A combination of top-down and bottom-up approaches have further been exploited by Bjørnholm et al. for the fabrication of gold nanorods as potential nanoelectrodes for single-molecule investigations. [25-27]

Herein I present a facile solution-based assembly method for producing MTJs by covalently linking metallic SWCNTs with electrically functional molecules. As a proof of principle, the single-molecule junction conductance of a series of oligophenyls was successfully measured. This work highlights the potential of an all-carbon based approach for the fabrication of solution-processable single-molecule junctions for molecular electronics.

For our studies, we employed DNA-wrapped SWCNTs[28] separated by chirality and electronic structure via a polymer aqueous two-phase separation method.[29, 30] (DNA-assisted dispersion further leaves only the terminal ends of the SWCNTs available for direct functionalisation[31]). Building on our recent bottom-up assembly strategy for the formation of end-to-end SWCNT junctions,[31] we linked metallic single-chirality (7,4) SWCNTs via amidation reactions with three different diamine

conjugated molecular linkers, containing 1, 2 and 3 phenyl rings. To confirm junction formation, we cast low-coverage films on doped silicon wafer substrates coated with a hydrophobic layer shown to induce partial alignment of DNA-wrapped SWCNTs,[32] and imaged them with Atomic Force Microscopy (AFM).

To investigate the electrical properties of the MTJs assembled in this study, we measured their current−voltage (I−V) characteristics as a function of the distance between a metallic AFM tip used as a mobile electrode and a fixed macroscopic metal electrode. This approach [27, 33, 34] allowed us to record force-controlled I−V responses (in PeakForce TUNA mode, Bruker) at different locations along individual SWCNT molecular junctions.

3.2 Molecular Transport Junction Formation

3.2.1 ss-DNA wrapping of SWCNT

DNA-wrapped Single-walled Carbon Nanotubes (SWCNTs) were dispersed in DI water at a concentration of ca 1 mg/mL, according to published procedures.[28] In a typical dispersion experiment, 1 mg of CoMoCAT SWCNT powders (SG65 grade, lot no. SG65EX-002, Southwest Nanotechnologies) were suspended in 1 mL aqueous DNA (Integrated DNA Technologies) solution (1 mg mL–1 (TCG) 4TC, 0.1 M NaCl). The mixture was sonicated (Sonics, VCX130) in an ice-water bath for 2 hours at a power level of 8W. After sonication, the samples were divided into 0.1 mL aliquots and centrifuged (Heraeus Fresco 17) for 90 min at 17,000 g to remove insoluble material, leaving DNA-dispersed carbon nanotube solutions at a mass concentration around 0.5mg mL-1. DNA-wrapped SWCNTs were separated into single chirality (7,4) to obtain a solution of tubes with metallic properties only via a polymer aqueous two-phase separation method.[30]

3.2.2 EDC-NHS amide bond formation

Acid-cutting and ultrasonication in water on the CNTs produce oxidised defects along the tube.[35, 36]Ss-DNA wrapping protects the sidewalls of the CNTs, therefore leaving only terminal carboxyl groups available for subsequent functionalisation. It was previously demonstrated that CNT segments could be attached to the amine-functionalised molecular linker by via amidation reactions.[31]

The standard amine coupling includes a three-step reaction with EDC(1-ethyl-3-(-3-dimethylaminopropyl) carbodiimide hydrochloride) /NHS (N-hydroxysulfo-succinimide) reactions (shown in **Figure 3-1**).[37] In the first step, EDC reacts with

carboxylic acid groups to form an active o-Acylisourea intermediate that is easily displaced by nucleophilic attack (pH 4.5). The NHS is coupled to carboxyl in the second step to form an NHS ester which is more stable than o-Acylisourea intermediate. In the third step, the primary amine forms an amide bond with the original carboxyl group, and an EDC by-product is released as a soluble urea derivative.

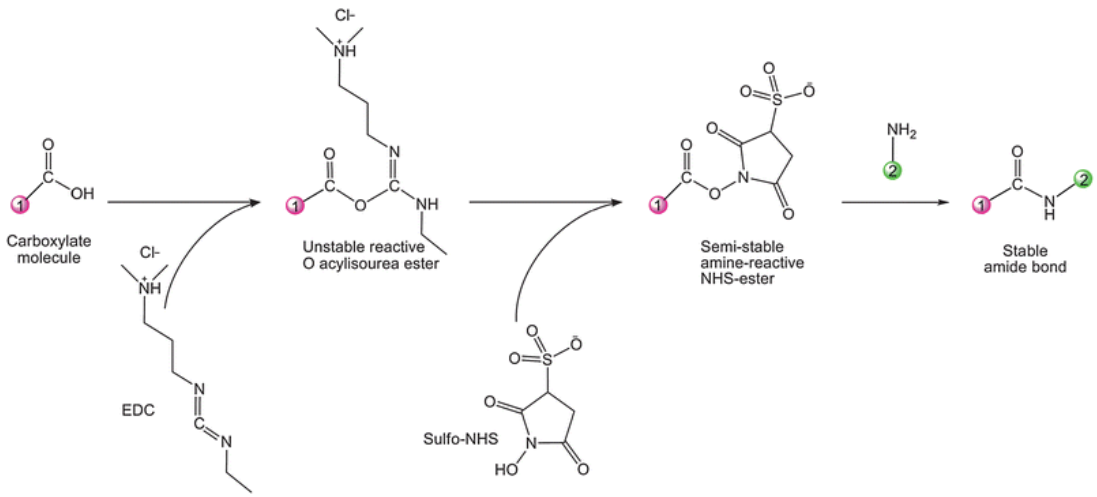

Figure 3-1 EDC–NHS chemistry: EDC reacts with a carboxylic-acid group on molecule 1, forming an amine-reactive O-acylisourea intermediate. This intermediate may react with an amine on molecule 2, yielding a conjugate of the two molecules joined by a stable amide bond. The addition of sulfo-NHS stabilizes the amine-reactive intermediate by converting it to an amine reactive sulfo-NHS ester, thus increasing the efficiency of EDC-mediated coupling reactions.[38]

We have employed this strategy to bridge DNA-wrapped SWCNTs with conjugated molecular linkers. **Figure 3-2** shows the three different diamine conjugated molecular linkers employed in our study, containing 1, 2 and 3 phenyl rings.

p-Phenylenediamine (PPD, Sigma Aldrich)

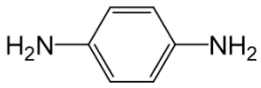

Benzidine (Sigma Aldrich)

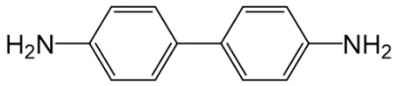

4,4"-diamino-p-terphenyl (Terphenyl, Sigma Aldrich)

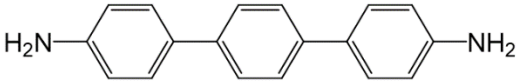

Figure 3-2 The three different molecules employed as linkers

In details, amide bond formation in aqueous conditions was performed with coupling reagents 1-ethyl-3-[3-dimethylaminopropyl] carbodiimide hydrochloride (EDC, 4mM, Sigma Aldrich) and N-hydroxysulfosuccinimide sodium salt (sulfo-NHS, 10mM, Sigma Aldrich) in an MES buffer (pH 4.7, 0.2 M, ThermoScientific). Pristine DNA-wrapped SWCNTs in DI H_2O were added to the activating solution in a 1:1 equivalence and left to incubate for 30 minutes. The solution was then diluted with Dulbecco Phosphate Buffer Saline (pH 7.2, DPBS, ThermoScientific) solution in a 1:1 volume ratio and left incubating for 1 hour.

Each molecular linker was solubilised in an ethyl acetate (VWR) solution (1 μL at 0.1 mM concentration) before being diluted in 1 mL of ultra-pure H_2O (100 nM, 18 MΩ, Millipore). The molecular linker solution (10 nM) was then added to the SWCNT solution and left incubating overnight. A separate solution of activated DNA-wrapped SWCNTs was subsequently added to the reaction mixture in a 1:1 ratio, to increase linker coupling and was left incubating overnight.

3.3 Immobilisation of MTJs on surface

3.3.1 Formation of hydrophobic surfaces

To confirm junction formation, we cast low-coverage films on doped silicon wafer substrates coated with a hydrophobic layer shown to induce partial alignment of DNA-wrapped SWCNTs and MTJs,[32] and imaged them with Atomic Force Microscopy (AFM).

All experiments were performed on 500-550 μm thick silicon wafers (Silicon Quest International) covered on both sides with 295 nm of thermal silicon oxide (SiO_2), cut into 4 cm^2 sections with a diamond tip scriber. Once cut, all SiO_2 substrates were exposed to piranha solution for 5 minutes before being washed with ultra-pure H_2O and ethanol (VWR) and dried under nitrogen flow. Piranha solution is a strong oxidising agent and was made up of sulphuric acid (H_2SO_4, VWR) and hydrogen peroxide (H_2O_2, Sigma Aldrich) in a 3:1 ratio respectively.

Once cleaned, surfaces were treated with Sigmacote® (Sigma Aldrich) self-assembled monolayer (SAM) solution via overnight incubation. Sigmacote® SAM solution consisted of toluene (200 mL, VWR), acetic acid (3mL, Sigma Aldrich) and Sigmacote® (10 mL). Once overnight incubation was complete, surfaces were washed with acetone (VWR), ethanol and ultra-pure H_2O and dried under nitrogen flow.

3.3.2 Fabrication of macroscopic metal electrodes

Micrometre-scale electrodes on SiO_2 substrates were made of Chromium/Gold bi-layer (3 nm Cr/ 20 nm Au) or Chromium/Palladium bilayer (1 nm Cr/ 10 nm Pd) by physical vapour deposition and lift-off procedures(details in chapter 5.1.2.2). Image reversal

photolithography formed a negative pattern of the mask by applying a photoresist (AZ 5214E, Microchem Gmbh) that was first introduced to pattern the substrates to guarantee a sharp edge. AZ 726 MIF was used as a developer to remove the photoresist. After metal deposition, the lift-off procedure was performed in NMP at 70 °C for 2 hours to remove the sacrificial stencil layer (photoresist). Samples were then rinsed with acetone, isopropanol and dried under nitrogen flow. Cr/Au electrodes were additionally flame annealed to flatten electrode surfaces.

3.3.3 Drop casting

Adopting drop casting techniques, solutions were cast onto hydrophobic modified SiO2 surfaces and electrode patterned substrates, and allowed to dry in air. Once fully dried, the samples were washed with ethanol and ultra-pure H_2O followed by blow drying with nitrogen. Surfaces were then placed into an N-methyl-2-pyrrolidone (NMP, Sigma Aldrich) bath overnight. Surfaces were once again washed with ethanol and ultra-pure H_2O and dried under nitrogen flow. For junctions interfaced to macroscopic electrodes, solutions were dropped cast onto patterned samples and once dried and washed as described above; a cleaning procedure was employed via the annealing of the samples in argon for 2 hours at 100 ºC (Lenton Type 3216CC). During all procedures, samples were stored in a desiccator to minimise humidity effects.

3.4 Confirmation of Single-molecule junction formation

3.4.1 Length characterisation by Atomic Force Microscopy

Samples were imaged under ambient conditions with a Bruker Dimension Icon microscope, with a NanoScope IV control unit and PF-TUNA add-on module. Tapping mode AFM imaging was performed with TESPA tips (Bruker, spring constant 40N/m). Images were analysed with NanoScope Analysis (version 1.5, Bruker) software. Segments were counted to estimate the length of CNTs. The starting metallic SWCNTs before reaction had an average length of 473.7 ± 179.5 nm according to the topography as shown in **Figure 3-3**.

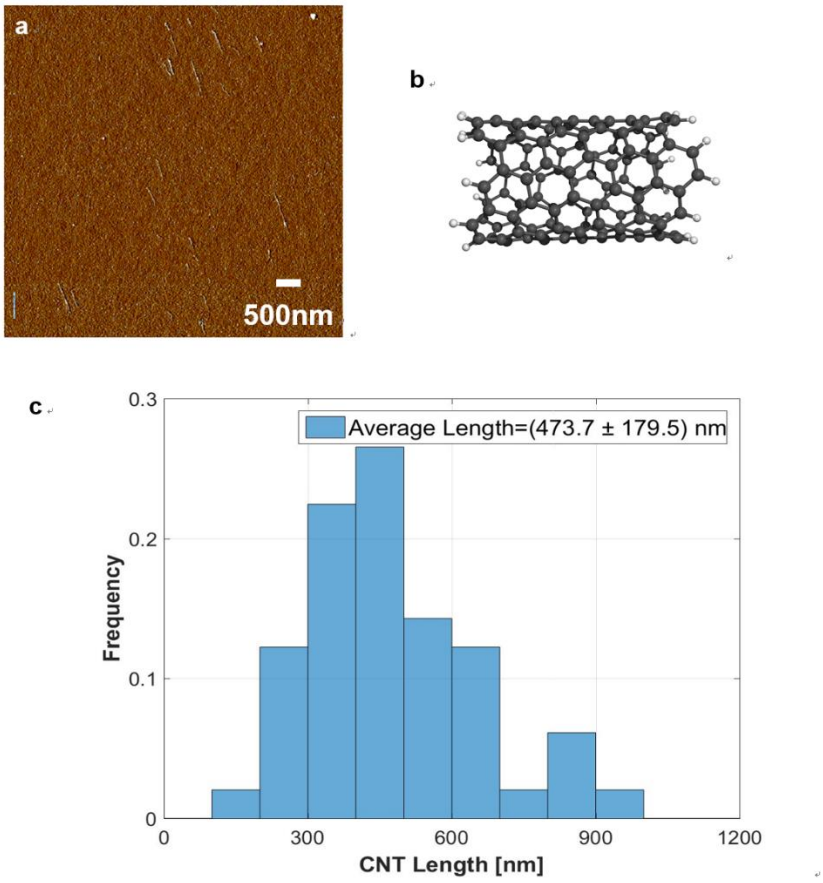

Figure 3-3 a) AFM topographical image displaying metallic pristine DNA-wrapped SWCNTs. b) Schematic of pristine DNA-wrapped SWCNT. c) Histogram of metallic DNA-wrapped SWCNTs measured. Average tube length: 473.7±179.5nm.

Figure 3-4 shows a representative AFM topographical image of linear SWCNT junctions typically obtained employing p-Phenylenediamine (PPD) as the molecular linker. The average length of the segments was found to be 838.3 ± 470.4 nm, strongly indicating the formation of molecular junctions.

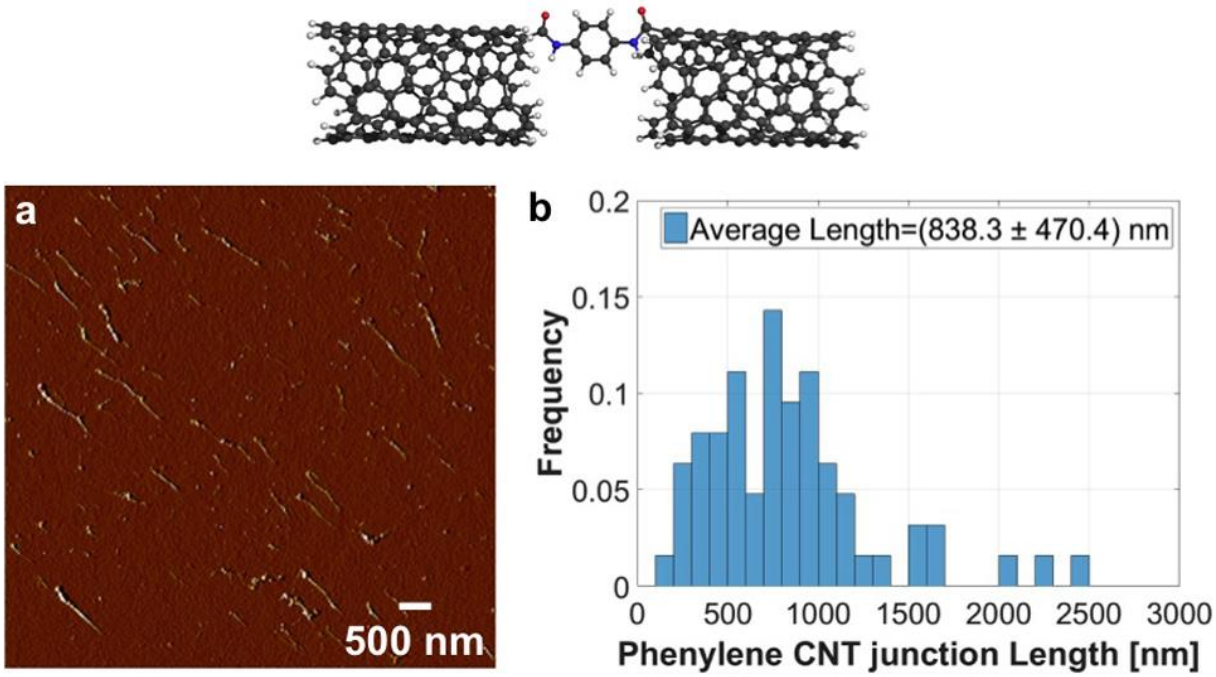

Figure 3-4 (top) Schematic of a PPD-linked molecular junction. (a) AFM topographical image of molecular junctions formed using PPD as the molecular linker. (b) The normalised histogram is showing the length distribution of the observed molecular junctions. The average length of 838.3 ± 470.4nm was determined from ca. 100 nanotubes.

Similar behaviour was found for the other two molecular linkers employed in this study: benzidine and 4,4”-diamino-p-terphenyl, that exhibited an average junction length of 1109.9 ± 546.6 nm and 1105.3 ± 569.1 nm, respectively(shown in **Figure 3-5** and **Figure 3-6**). It should be noted that the length increment with 2 and 3 phenol ring molecular linkers were significant higher compared to the single phenol ring molecule. This could be on account of the extra space provided between SWCNTs due to the longer linkers which could have reduced the steric hinderance during junction formation.

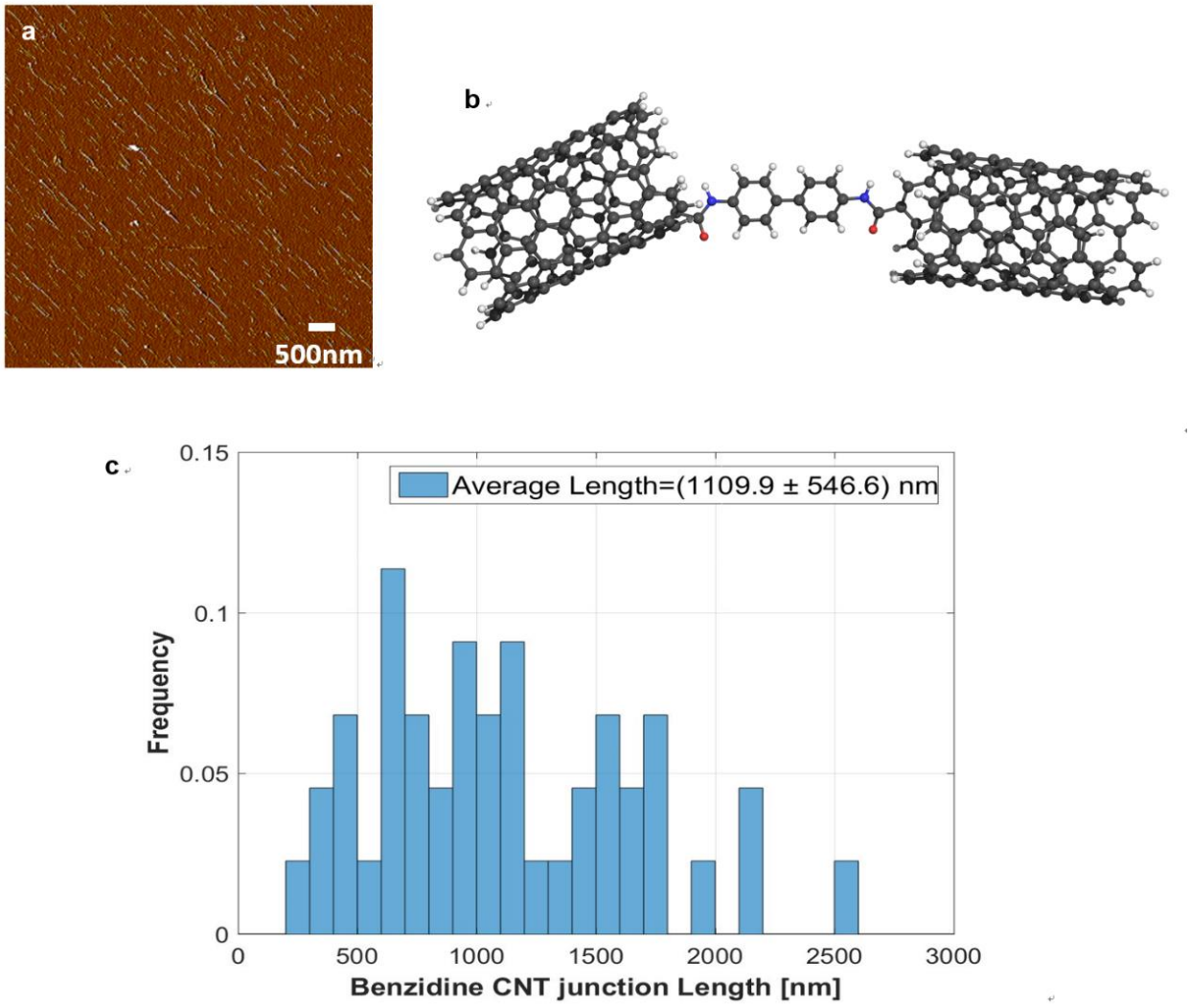

Figure 3-5 a) AFM topographical image displaying benzidine linked metallic DNA-wrapped SWCNTs. b) Schematic of Benzidine linked molecular junction. c) Histogram of metallic DNA-wrapped SWCNTs measured. Average tube length: 1109.9±546.6 nm.

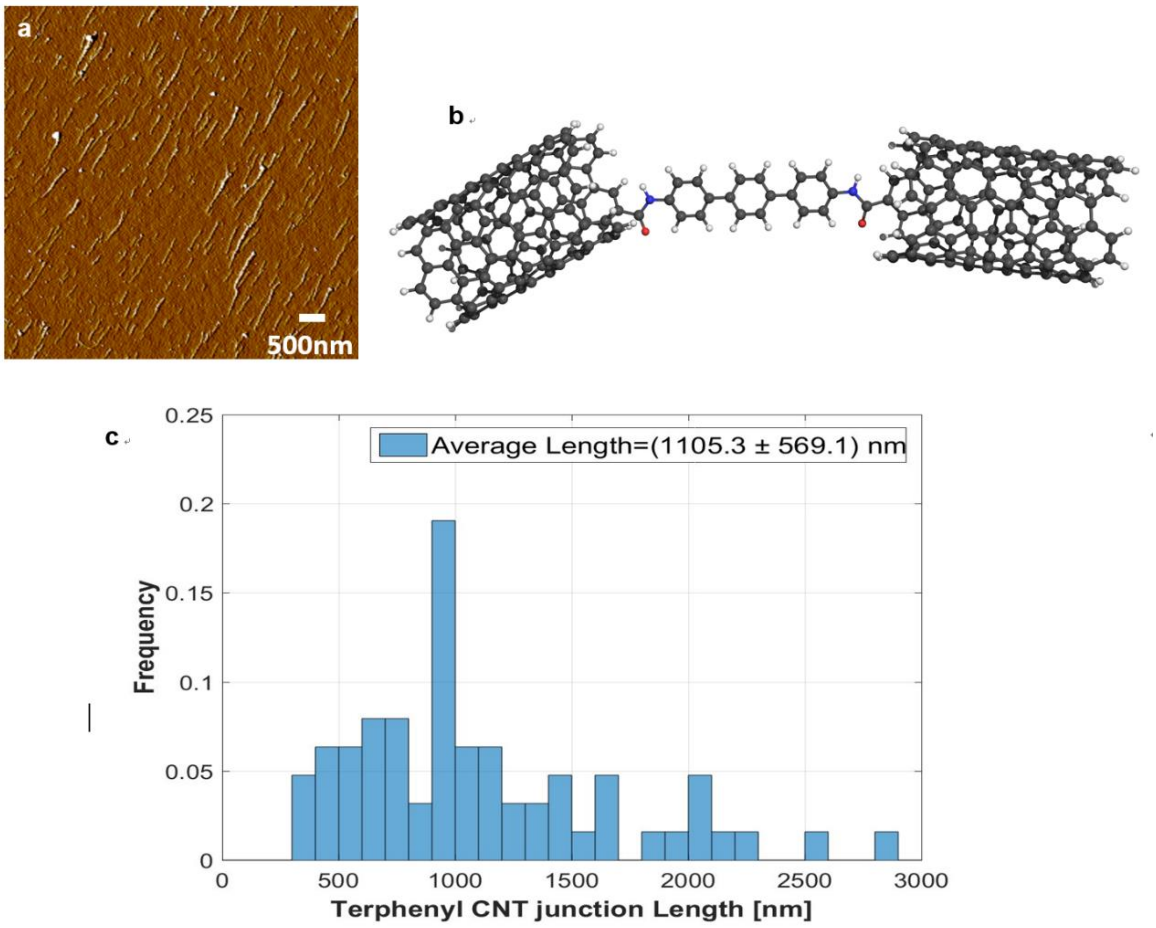

Figure 3-6 AFM topographical image displaying Terphenyl linked metallic DNA-wrapped SWCNTs. b) Schematic of Terphenyl linked molecular junction. c) Histogram of metallic DNA-wrapped SWCNTs measured. Average tube length: 1105.3±569.1 nm.

Because of the small diameter of the SWCNTs employed in this study (ca. 8 Å), and due to steric hindrance effects, it is expected that only one molecule can bridge the nanotubes. Moreover, the presence of predominantly linear junctions, rather than branched, from all the three linkers employed, strongly indicates the presence of a single bridging molecule: two or more molecules would present multiple bindings sites that might induce the formation of branched CNT junctions.

3.4.2 Control experiment for junction formation

As previously demonstrated ([31]), a control experiment was performed to verify that an amidation reaction but not a supramolecular interaction is actually responsible for the formation of SWCNT junctions. We measured the length of the SWCNTs after addition of the diamine molecular linker/s without the amide coupling and activating agents (Sulfo-NHS and EDCI). The average nanotube length in this case (452.7±134.5 nm)was comparable to that of the pristine SWCNTs (467.5±149.8 nm), thus indicating that the amidation reaction is the main driving force for the formation of SWCNT junctions (see **Figure 3-7** and **Figure 3-8**).

Moreover, we characterised the length of our SWCNTs when a 4,4-Toluenesulfonyl molecular linker was employed for junction formation. As clearly shown in the AFM topographical image and the histogram of length distribution in **Figure 3-9**, when employing a phenyl linker without any amine end-groups the average length of the SWCNTs is comparable to the length of pristine SWCNTs. This result further indicates that the amidation reaction is the main driving force towards the formation of the SWCNTs junctions and we can rule out non-covalent binding.

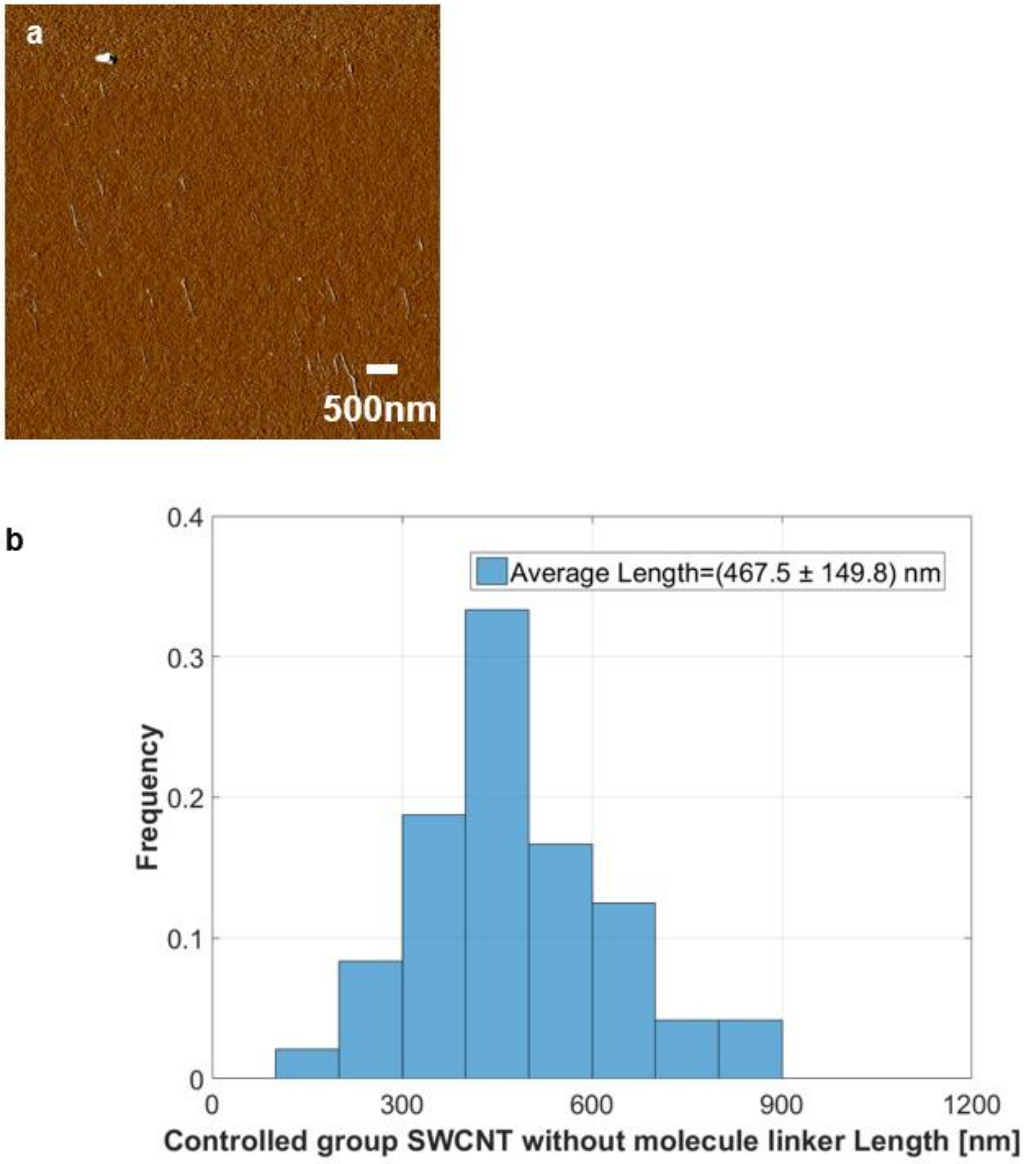

Figure 3-7 a) AFM topographical image displaying DNA-wrapped SWCNTs with activation solution with no linker present. b) Histogram of metallic DNA-wrapped SWCNTs measured. Average tube length: 467.5±149.8 nm. This control experiment shows that no junctions are formed when the molecular linker is not present.

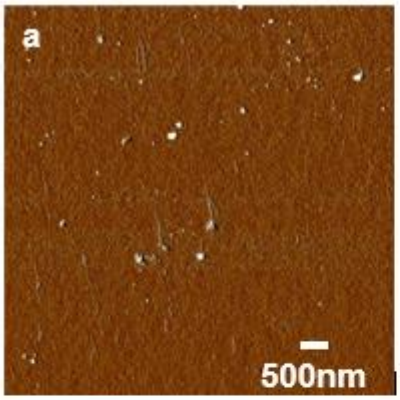

b

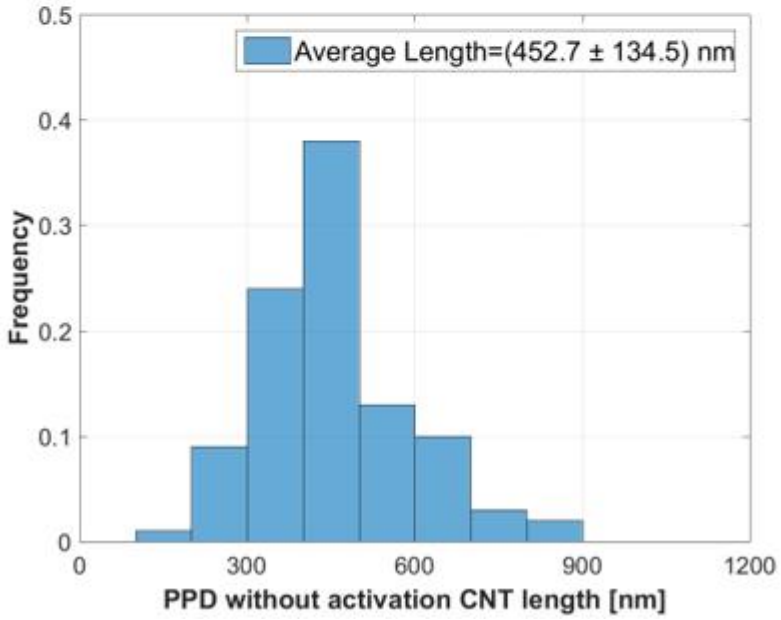

Figure 3-8 a) AFM topographical image displaying DNA-wrapped SWCNTs and PPD linker with no activation solution present. b) Histogram of metallic DNA-wrapped SWCNTs measured. Average tube length: 452.7±134.5 nm. This control experiment shows that no junctions are formed when the activation solution is not present.

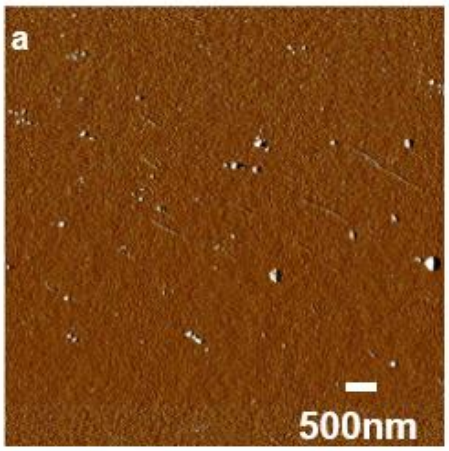

b

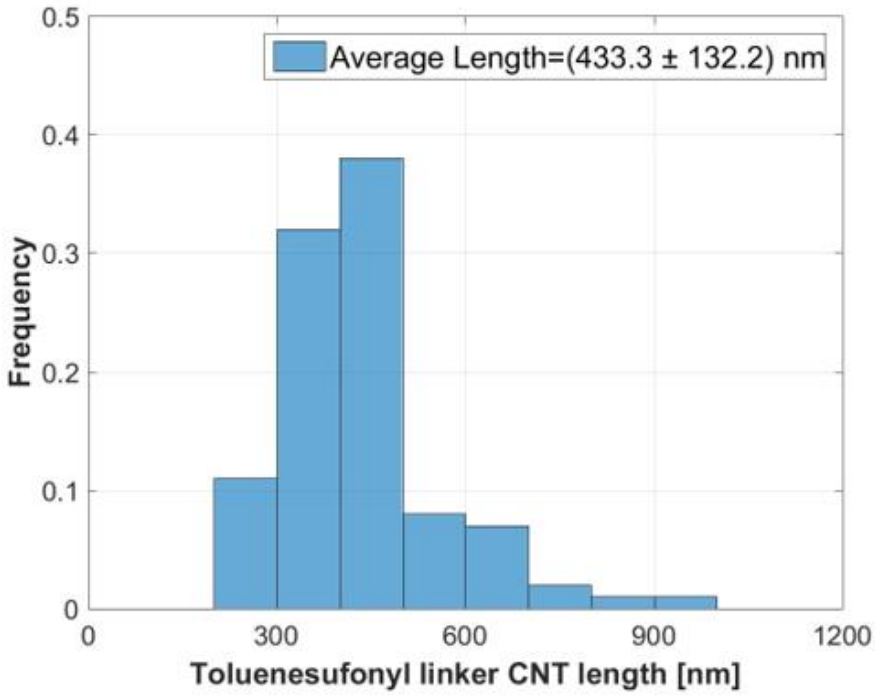

Figure 3-9 a) AFM topographical image displaying DNA-wrapped SWCNTs with 4,4-Toluenesulfonyl (Sigma Aldrich) molecular linker and activation solution. b) Histogram of metallic DNA-wrapped SWCNTs measured. Average tube length: 433.3±132.2 nm. This control experiment shows that no junctions are formed when oligophenyl molecular linkers do not contain amine functional groups.

3.4.3 Determination of single-molecule linker

To further confirm the presence of predominantly one molecule between SWCNTs in the junctions, Density Functional Theory (DFT) calculations at PBE0-D3/SV(P) level of theory considering water as the solvent (COSMO model) were performed by Dr Rachel Crespo-Otero.[39-42]

The energetics of the formation of linear SWCNT junctions with both one- and two-bridging configurations were investigated. The model of the (7, 4) nanotube consists of the unit cell atoms capped with hydrogen atoms (length is ~14.5 Å). To obtain two-molecule junctions, two carboxylic acid groups were added to one of the nanotube endings. The carboxylic acid groups were located as distant as possible to minimise electrostatic repulsion and steric hindrance.

The thermochemistry of the total reaction of formation of the junctions can be studied considering the reaction between the carboxylic defects and the amines. As we only considered the thermochemistry of the total reaction, factors like the size of the reactants in the coupling reaction are not taken into account. These factors could only negatively affect the formation of 2-molecule junctions, which are more influenced by steric hindrance.

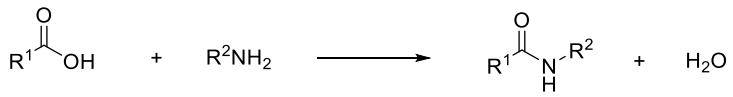

Scheme 1 Amidation reaction scheme.

The calculations show that the formation of linear junctions where two molecules bridge two nanotubes is energetically less favourable than the junctions with one bridging molecule. A second molecule in the junction induces a significant strain,

increasing the energy of formation by about 68 kJ/mol.[43] At the same time, the entropy decreases because of the restrictions to rotations and vibrations induced by the second molecule. Therefore, the formation of SWCNT junctions linked by two molecules is unlikely to occur. These findings allow us to assume that we are assembling predominately single-molecule junctions reasonably.

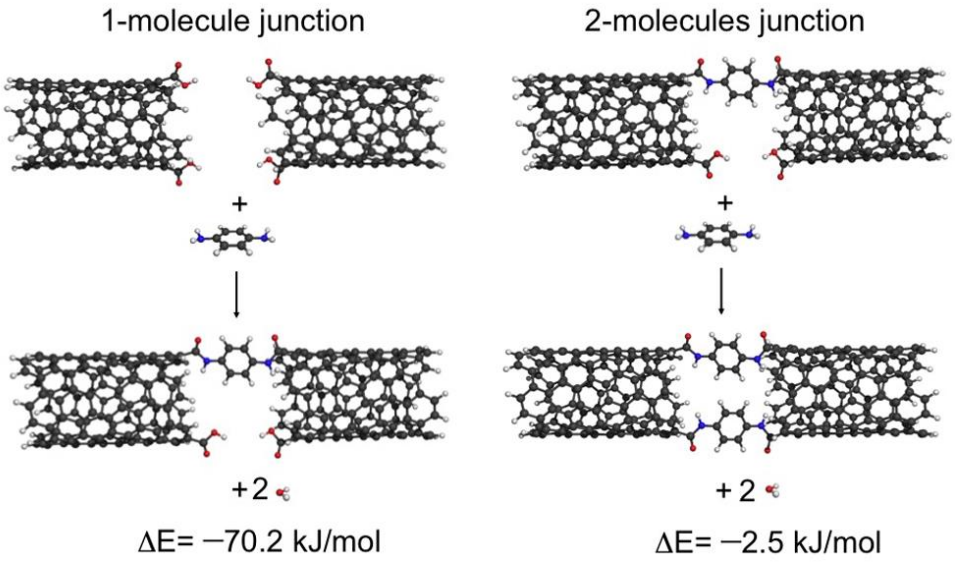

Figure 3-10 Reactions of formation for linear junctions with one and two bringing molecules. The energies were obtained at PBE0-D3/SV(P) level of theory considering water as the solvent (COSMO model).[44]

3.5 Characterisation

3.5.1 Conductive AFM

To investigate the electrical properties of the MTJs assembled in this study we measured their current-voltage (I-V) characteristics as a function of the distance between a metallic AFM tip used as a mobile electrode, and a fixed macroscopic metal electrode (see **Figure 3-11**). This approach [27, 33, 34] allowed us to record force-controlled I-V responses (in PeakForce TUNA mode, Bruker) at different locations along individual SWCNT molecular junctions.

Figure 3-11a shows a representative conductive AFM[45] image of a PPD-SWCNT junction. More data will be displayed and discussed in the next section. The substrates were subject to cleaning procedures to eliminate salt residues from the buffer solution and facilitate the removal of the DNA wrapped around the tubes, as they could affect the electronic properties of the nanotubes. The contact resistance of the SWCNT was determined by acquiring I-V curves in close proximity to the macroscopic electrode (between 30nm and 120nm, see Figure 3-11a and the schematic in Figure 3-11d). We determined in this way a resistance (R) of ~ 25 KΩ, which is the typical contact resistance for single SWCNTs using metal contacts.[34, 46] We did not observe any noticeable increase in resistance along the nanotube within this distance range, as indeed expected for short SWCNTs.[34] On repeating the measurements along the same SWCNT we obtained the same R, within a 4% error, indicating that the AFM tip did not damage the SWCNT surface.

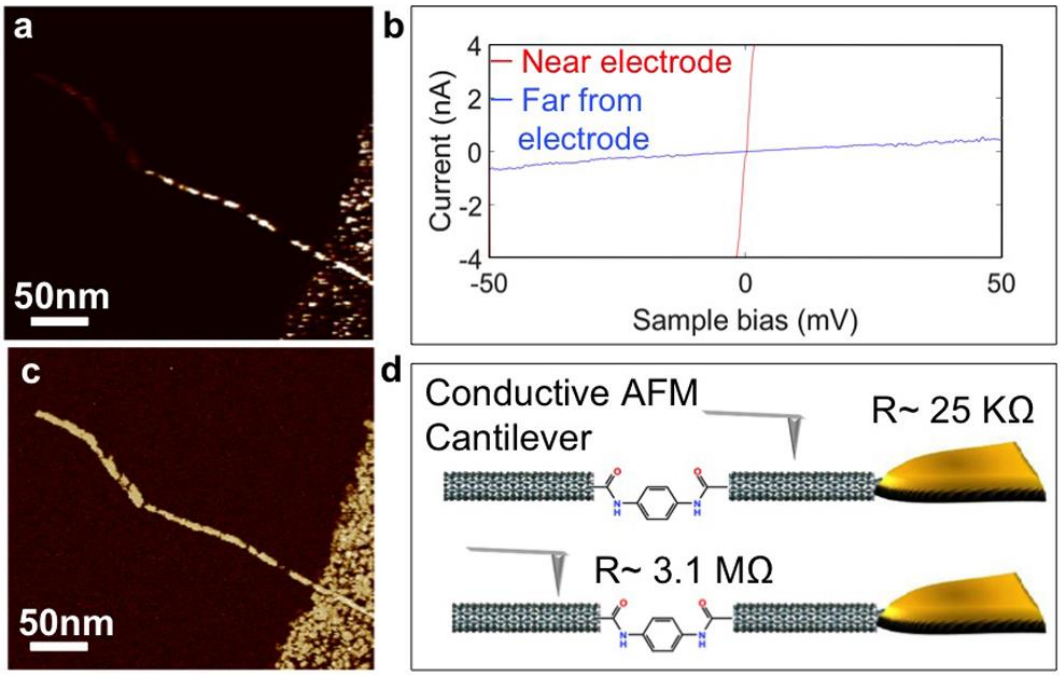

Figure 3-11 a) Representative Conductive AFM image of an MTJ formed using PPD as the molecular linker and interfaced to a macroscopic metal electrode. b) Representative I-V curves recorded at selected points across the MTJ: red line for measurements in close proximity to the macroscopic electrode, and blue line for measurements at the far end of the macroscopic electrode. c) Phase AFM image of the MTJ shown in (a). d) Schematic of the conductive AFM measurements on the MTJs.

An initial C-AFM scan was performed to locate MTJs on the substrate. Junctions were determined from the current map, by observing a sudden decrease of current response along the structure. We performed molecular conductance measurements on ten devices for each molecular linker, therefore a total of ca. 30 devices, and measured up to 800 I-V traces for each SWCNT molecular junction in the devices. Up to 800 I-V traces were recorded at 20-30 sample locations along the molecular junctions (at gaps of 15 nm to 25 nm) for each set of samples.

3.5.2 Results and data analysis

To determine the junction resistance, we measured I-V characteristics of the MTJs at the far end of the macroscopic electrode (see the schematic in Figure 3-11). The

junction resistances were determined from the inverse slope of the I-V curves recorded in the linear region, which was between -50 mV and 50 mV (see Figure 3-11). Employing this approach, we determined a resistance of ~3.1 MΩ for individual PPD-SWCNT junctions. This significant increase in the measured resistance across the MTJ (from KΩs to MΩs) is in line with the expected presence of a PPD molecule bridging SWCNT segments. Similarly, we measured the resistance of SWCNT junctions formed with benzidine and 4, 4"-diamino-p-terphenyl linkers. The resistance values were determined from the inverse-slope of the I-V traces, and compiled into histograms, with each count corresponding to a single I-V curve. **Figure 3-12** shows more representative conductive AFM images for CNT-based molecular junctions. As shown in **Figure 3-13**, **Figure 3-14** and **Figure 3-15**, the histograms plotted on log axes provide normal distributions of resistance.

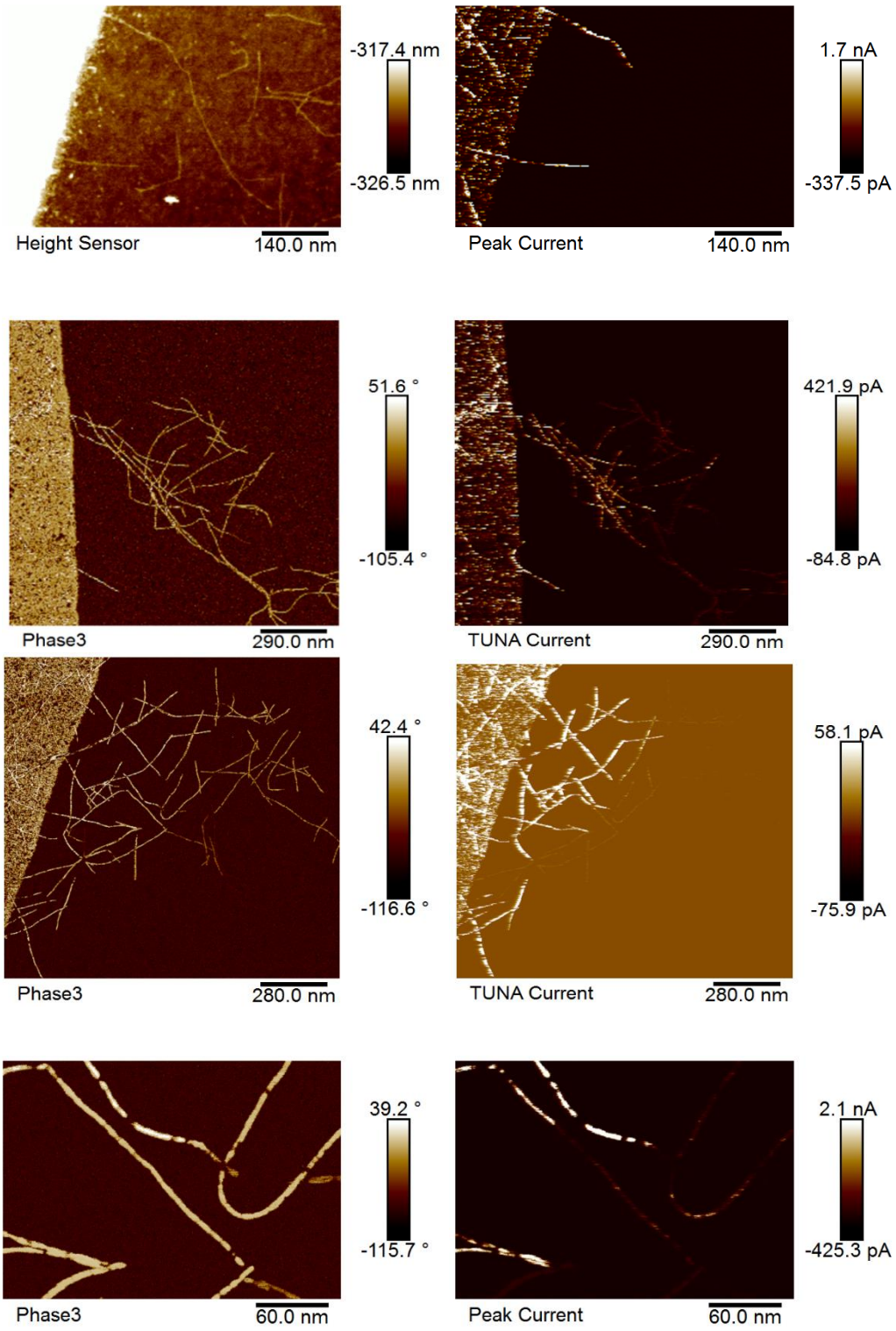

Figure 3-12 Representative AFM and C-AFM images for molecular junctions; Left: Topography/Phase images, Right: Current Maps.

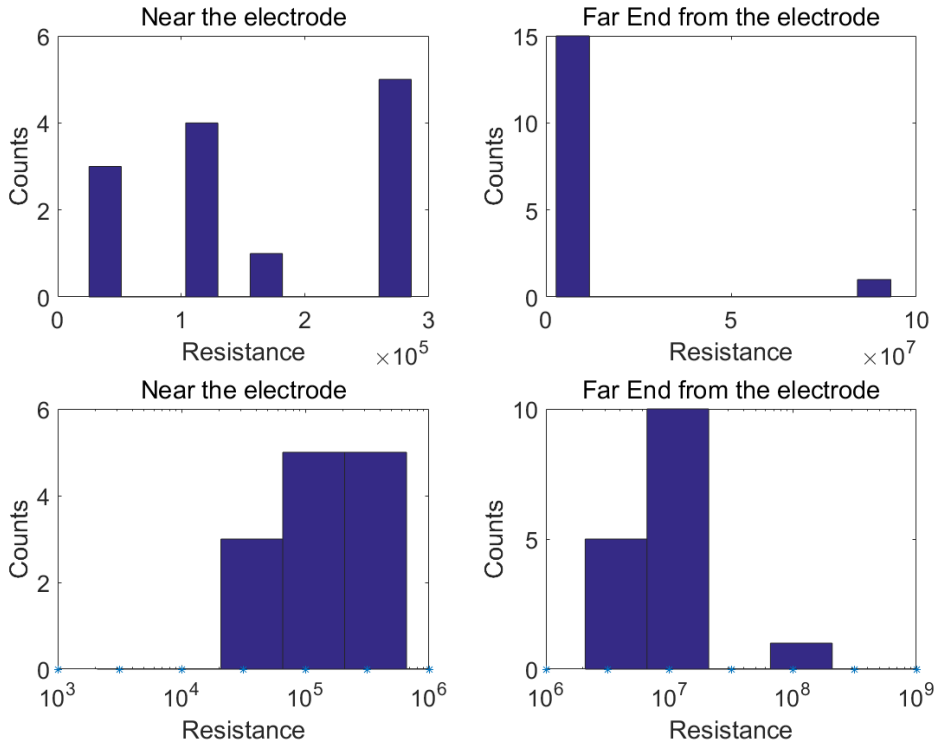

Figure 3-13 a) Example of representative resistance histogram of MTJs of PPD near the macroscopic electrode. b) Resistance histogram of MTJs of PPD at the far end from the electrode. c) Resistance histogram (log axes) of MTJs of PPD near the electrode. d) Resistance histogram (log axes) of MTJs of PPD at the far end from the electrode.

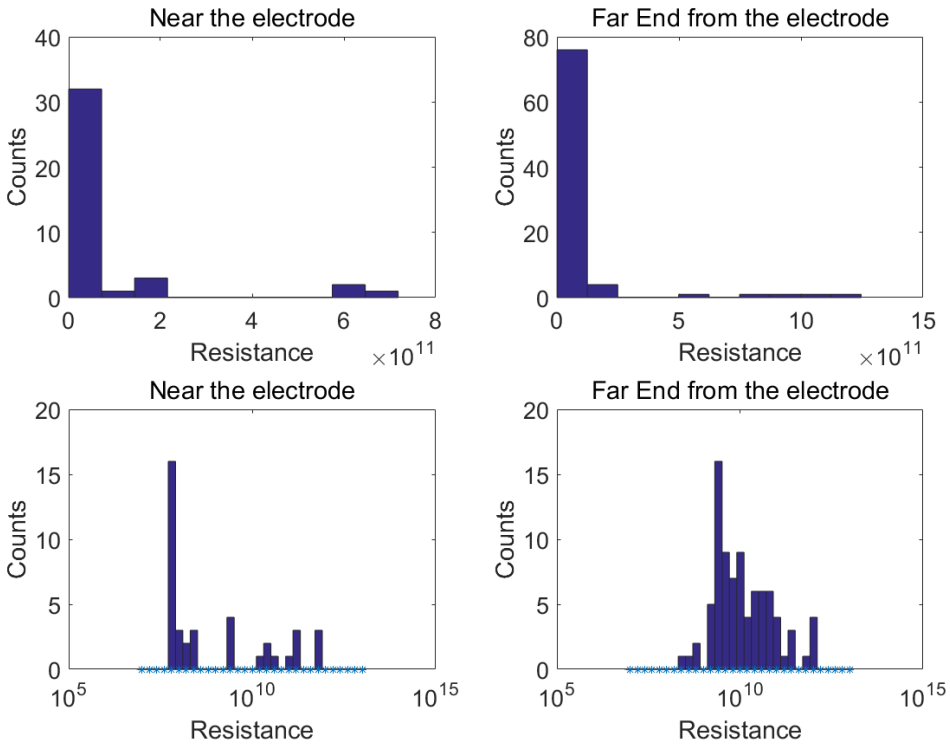

Figure 3-14 a) Resistance histogram of MTJs of benzidine near the macroscopic electrode. b) Resistance histogram of MTJs of Benzidine at the far end of the macroscopic electrode. c) Resistance histogram (log axes) of MTJs of Benzidine near the electrode. d) Resistance histogram (log axes) of MTJs of Benzidine at the far end of the electrode.

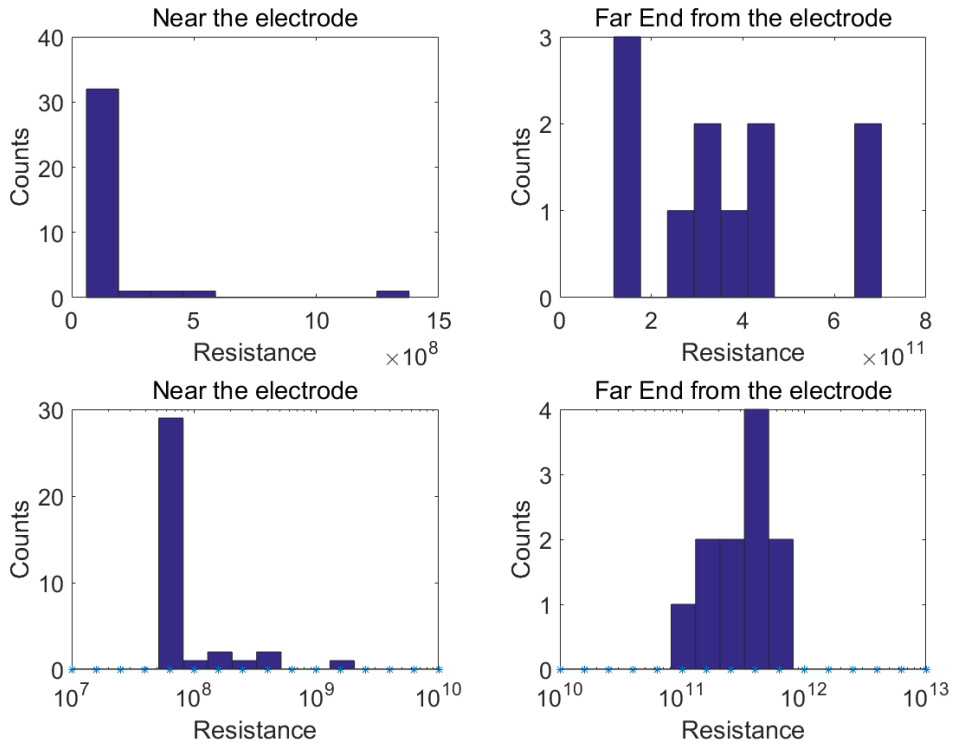

Figure 3-15 a) Resistance histogram of MTJs of Terphenyl near the macroscopic electrode. b) Resistance histogram of MTJs of Terphenyl at the far end from the electrode. c) Resistance histogram (log axes) of MTJs of Terphenyl near the electrode. d) Resistance histogram (log axes) of MTJs of Terphenyl at far end from the electrode.

When plotted on log axes, two peaks for the resistance were obtained, one corresponding to junction positions near the macroscopic electrode and one corresponding to the opposite position at the far end of the junction. The difference in resistance can be ascribed to the presence of the molecule between SWCNTs forming the MTJs. The peaks were fit to Gaussians, and the centre values were then taken as the junction resistances, as shown in **Table 1**. Uncertainty values are derived from the standard deviation of the measurements from the full width at half maximum in the peak area.

Table 1 Measured resistances related to the molecular linker employed and to the position along the MTJ.

PPD		**Benzidine**		**Terphenyl**	
Resistance (Ω)	**Uncertainty (Ω)**	**Resistance (Ω)**	**Uncertainty (Ω)**	**Resistance (Ω)**	**Uncertainty (Ω)**
3.17×10^6	9.51×10^5	4.76×10^{10}	1.79×10^{10}	3.74×10^{11}	8.45×10^{10}

Table 2 summarises our results. The average conductance values for the three oligophenyls are in good agreement with the literature values.[47]

Table 2 Molecular linkers employed and measured molecular junction conductance values

Molecule	**Conductance (G_0)**
PPD	$8.0 \times 10^{-3} \pm 2.4 \times 10^{-3}$
Benzidine	$1.4 \times 10^{-3} \pm 5.5 \times 10^{-4}$
Terphenyl	$1.8 \times 10^{-4} \pm 4.2 \times 10^{-5}$

The measured conductance decays exponentially with molecular length. The tunnelling decay constant β can be estimated making use of the equations typically employed to describe non-resonant tunnelling [48, 49]:

$$\mathrm{G} = G_0 * \exp(-\beta * L) \quad (3\text{-}1)$$

$$\mathrm{R} = R_0 * \exp(\beta * L) \quad (3\text{-}2)$$

Here G_c (R_c) is an effective contact conductance (resistance) of the molecular wire junction, while β is the tunnelling decay constant, and L the tunnelling distance taken to be the length of the molecule. For a conjugated molecule, through-bond tunnelling along the molecular backbone is expected to dominate over through-space tunnelling.

Figure 3-16 shows the plot of junction conductance versus molecular length for the series of oligophenyle employed in our investigations, i.e. with 1, 2 and 3 phenyl rings. The plot fits an exponential form with an estimated decay constant of 0.5 $Å^{-1}$, i.e. 1.9 per phenyl ring. This result is in reasonable agreement with the values of ~1.8[49] and ~1.7[47, 50] per phenyl ring measured in metal-molecule-metal junctions via scanning probe based techniques. Moreover, this is further evidence for tunnelling conductance through the aromatic rings employed in our SWCNT-based MTJs. Mobile counterions associated with the DNA do not dominate charge transport through linked SWCNTs: Mobile counterions would be relevant for measurements in solution, while we work in dry/air.

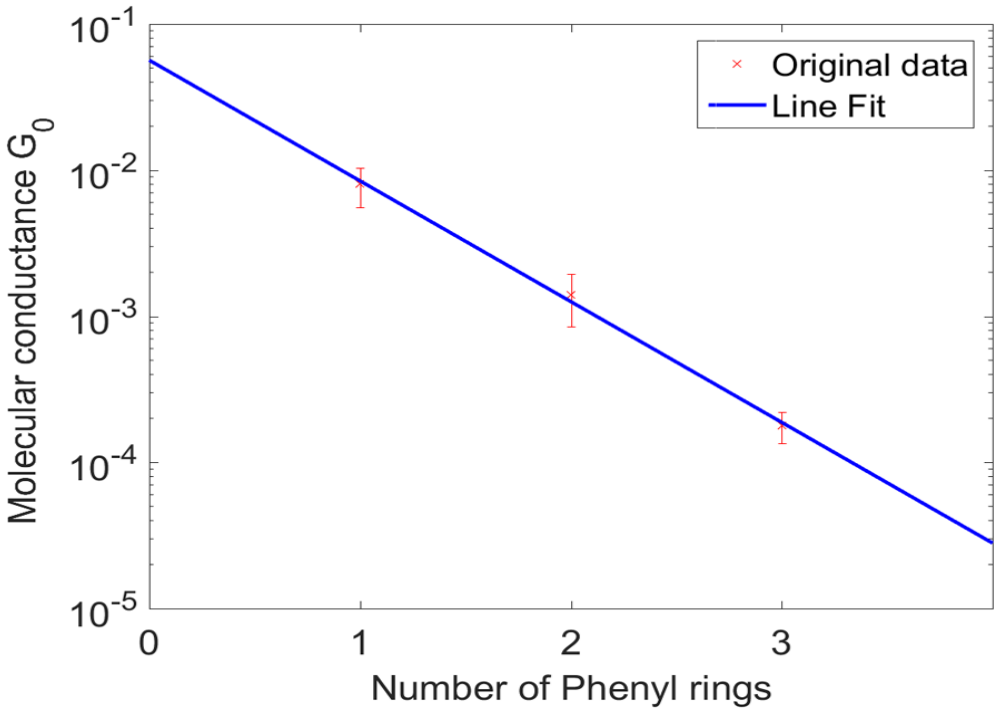

Figure 3-16 Measured conductance of oligophenyle SWCNT-based MTJs plotted against the number of phenyl rings.

Extrapolating the plot fit (for R) to zero length, we can further estimate the contact resistance of the SWCNT/molecule/SWCNT junctions to be ~ 108 KΩ (Figure 3-17), i.e. comparable to the contact resistance found for Au/molecule/Au junctions (~360

KΩ).[50] This value indicates that the molecule/SWCNT coupling is rather strong, as expected for amide bonds linkages, which possess a partial double bond character.

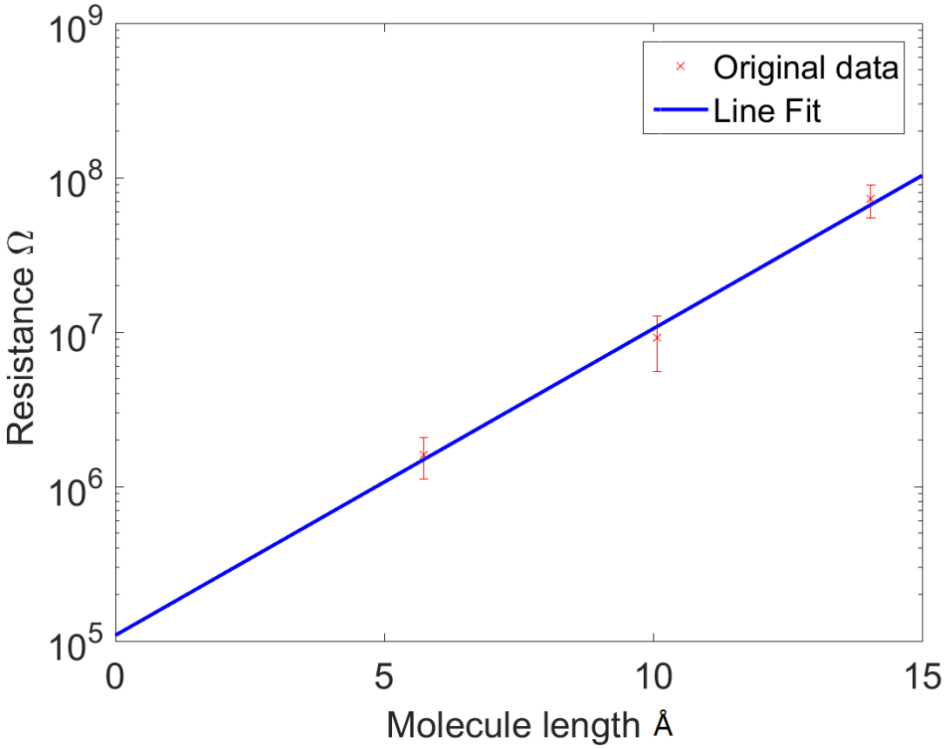

Figure 3-17 extrapolating the plot fit (for R) to zero length we can estimate the contact resistance of the SWCNT/molecule/SWCNT junctions to be ~ 108 KΩ.

3.5.3 Control experiment for conductance measurements

An additional control experiment was performed measuring the resistance of SWCNT junctions formed with Hexamethylenediamine (HMD) as the molecular linker, i.e. employing a non-conjugated molecule. The resistance for HMD-based junctions was found to be $1.12 \times 10^8\ \Omega \pm 6.16 \times 10^7\ \Omega$ (see **Figure 3-18**). This value is in good agreement with the literature value of ~$10^8\ \Omega$ obtained for hexanethiol monolayers in nanoparticle bridges.

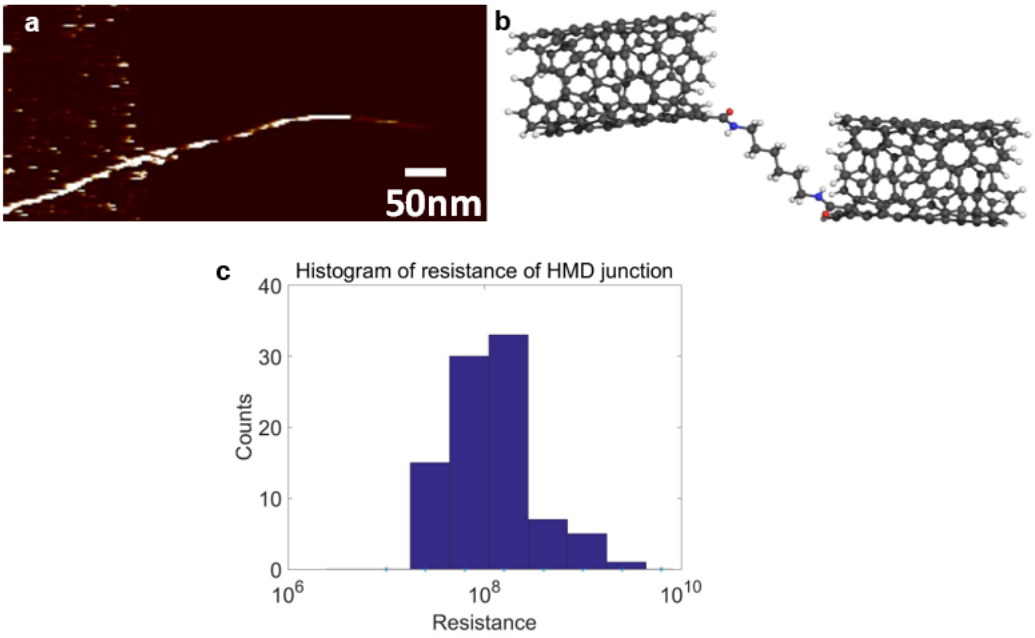

Figure 3-18 a) Representative C-AFM image of an MTJ formed using HMD as the molecular linker and interfaced to a macroscopic metal electrode. b) Schematic of HMD linked MTJ. c) Resistance histogram of MTJs of HMD at the far end from the electrode.

3.6 Conclusions

In conclusion, we have presented a strategy for the fabrication of solution-processable molecular transport junctions that employ molecular building blocks assembled between metallic carbon nanotube electrodes. The molecular conductance of a series of oligophenyls was measured, and the average values were found to be in line with the literature values. The main advantage and novelty of the approach presented here are the low-cost/simplicity of integration via assembly in (aqueous-based) solution: to our knowledge, this is the first example of solution-processable carbon-based MTJs. We anticipate that this new method of fabricating MTJs will be employed to produce a variety of solution-processable nanoelectronic devices. Further work/application would be based on the assembly of MTJs between pair of electrodes. The relevant attempts such as electrode patterning and dielectrophoretic assembly will be present in chapter 5.

References

1. Heath, J.R., *Molecular Electronics.* Annual Review of Materials Research, 2009. **39**(February): p. 1-23.
2. Ratner, M., *A brief history of molecular electronics.* Nature nanotechnology, 2013. **8**(6): p. 378-81.
3. Tao, N.J., *Electron transport in molecular junctions.* Nature nanotechnology, 2006. **1**(3): p. 173-181.
4. Lindsay, S.M. and M.A. Ratner, *Molecular transport junctions: Clearing mists.* Advanced Materials, 2007. **19**(1): p. 23-31.
5. Moth-Poulsen, K. and T. Bjornholm, *Molecular electronics with single molecules in solid-state devices.* Nature Nanotechnology, 2009. **4**(9): p. 551-556.
6. Zheng, M. and B.A. Diner, *Solution redox chemistry of carbon nanotubes.* J Am Chem Soc, 2004. **126**(47): p. 15490-4.
7. Jia, C. and X. Guo, *Molecule-electrode interfaces in molecular electronic devices.* Chemical Society reviews, 2013. **42**(13): p. 5642-60.
8. Algré, E., et al., *Design and construction of the motion mechanism of an XY micro-stage for precision positioning.* Applied Physics Letters, 2014. **11**(1): p. 1-10.
9. Shen, Q., et al., *Integrating reaction chemistry into molecular electronic devices.* Chemistry, an Asian journal, 2010. **5**(5): p. 1040-57.
10. Perrin, M.L., E. Burzuri, and H.S.J. van der Zant, *Single-molecule transistors.* Chemical Society Reviews, 2015. **44**(4): p. 902-919.
11. Aradhya, S.V. and L. Venkataraman, *Single-molecule junctions beyond electronic transport.* Nature Nanotechnology, 2013. **8**(6): p. 399-399.
12. Diez-Perez, I., et al., *Controlling single-molecule conductance through lateral coupling of pi orbitals.* Nature Nanotechnology, 2011. **6**(4): p. 226-231.
13. Xiang, D., et al., *Three-terminal single-molecule junctions formed by mechanically controllable break junctions with side gating.* Nano letters, 2013. **13**(6): p. 2809-13.
14. Guo, X., et al., *Nanotubes with Conducting Molecules Covalently Bridging Gaps in Single-Walled Carbon Covalently Bridging Gaps in Single-Walled Carbon Nanotubes with Conducting Molecules.* 2006. **356**.
15. Feldman, A.K., et al., *Molecular electronic devices based on single-walled carbon nanotube electrodes.* Accounts of chemical research, 2008. **41**(12): p. 1731-41.
16. Cao, Q. and S.J. Han, *Single-walled carbon nanotubes for high-performance electronics.* Nanoscale, 2013. **5**(19): p. 8852-63.
17. Marquardt, C.W., et al., *Electroluminescence from a single nanotube–molecule–nanotube junction.* Nature Nanotechnology, 2010. **5**(12): p. 863-867.
18. Cao, Y., et al., *Building High-Throughput Molecular Junctions Using Indented Graphene Point Contacts.* Angewandte Chemie-International Edition, 2012. **51**(49): p. 12228-12232.
19. Jia, C., et al., *Conductance switching and mechanisms in single-molecule junctions.* Angewandte Chemie - International Edition, 2013. **52**(33): p. 8666-8670.
20. Thiele, C., et al., *Fabrication of carbon nanotube nanogap electrodes by helium ion sputtering for molecular contacts.* Applied Physics Letters, 2014. **104**(10).
21. van der Molen, S.J., et al., *Visions for a molecular future.* Nature Nanotechnology, 2013. **8**(6): p. 385-389.
22. Yan, H.J., A.J. Bergren, and R.L. McCreery, *All-Carbon Molecular Tunnel Junctions.* Journal of the American Chemical Society, 2011. **133**(47): p. 19168-19177.

23. Jain, T., et al., *Wet Chemical Synthesis of Soluble Gold Nanogaps.* Accounts of Chemical Research, 2014. **47**(1): p. 2-11.
24. Sun, L., et al., *Single-molecule electronics: from chemical design to functional devices.* Chem. Soc. Rev. Chem. Soc. Rev, 2014. **43**(21): p. 7378-7411.
25. Tang, Q., et al., *Self-assembled nanogaps for molecular electronics.* Nanotechnology, 2009. **20**(24): p. 245205-245205.
26. Jain, T., et al., *Aligned Growth of Gold Nanorods in PMMA Channels: Parallel Preparation of Nanogaps.* Acs Nano, 2012. **6**(5): p. 3861-3867.
27. Hassenkam, T., et al., *Self-assembly and conductive properties of molecularly linked gold nanowires.* Nano Letters, 2004. **4**(1): p. 19-22.
28. Zheng, M., et al., *DNA-assisted dispersion and separation of carbon nanotubes.* Nature materials, 2003. **2**(5): p. 338-42.
29. Tu, X.M., et al., *DNA sequence motifs for structure-specific recognition and separation of carbon nanotubes.* Nature, 2009. **460**(7252): p. 250-253.
30. Ao, G., C.Y. Khripin, and M. Zheng, *DNA-Controlled Partition of Carbon Nanotubes in Polymer Aqueous Two-Phase Systems.* Journal of the American Chemical Society, 2014. **136**(29): p. 10383-10392.
31. Palma, M., et al., *Controlled formation of carbon nanotube junctions via linker-induced assembly in aqueous solution.* Journal of the American Chemical Society, 2013. **135**(23): p. 8440-3.
32. McLean, R.S., et al., *Controlled two-dimensional pattern of spontaneously aligned carbon nanotubes.* Nano Letters, 2006. **6**(1): p. 55-60.
33. Loiacono, M.J., E.L. Granstrom, and C.D. Frisbie, *Investigation of charge transport in thin, doped sexithiophene crystals by conducting probe atomic force microscopy.* Journal of Physical Chemistry B, 1998. **102**(10): p. 1679-1688.
34. Gomez-Navarro, C., et al., *Tuning the conductance of single-walled carbon nanotubes by ion irradiation in the Anderson localization regime.* Nature Materials, 2005. **4**(7): p. 534-539.
35. Kaempgen, M., et al., *Sonochemical optimization of the conductivity of single-wall carbon nanotube networks.* Advanced Materials, 2008. **20**(3): p. 616-620.
36. Riesz, P. and T. Kondo, *Free radical formation induced by ultrasound and its biological implications.* Free Radical Biology and Medicine, 1992. **13**(3): p. 247-270.
37. Fischer, M.J.E., *Amine Coupling Through EDC/NHS: A Practical Approach*, in *Surface Plasmon Resonance: Methods and Protocols*, N.J. Mol and M.J.E. Fischer, Editors. 2010, Humana Press: Totowa, NJ. p. 55-73.
38. Bart, J., et al., *Room-temperature intermediate layer bonding for microfluidic devices.* Lab on a Chip, 2009. **9**(24): p. 3481-3488.
39. Adamo, C. and V. Barone, *Toward reliable density functional methods without adjustable parameters: The PBE0 model.* The Journal of Chemical Physics, 1999. **110**(13): p. 6158-6170.
40. Grimme, S., et al., *A consistent and accurate ab initio parametrization of density functional dispersion correction (DFT-D) for the 94 elements H-Pu.* The Journal of Chemical Physics, 2010. **132**(15): p. 154104.
41. Klamt, A. and G. Schuurmann, *Cosmo - a New Approach to Dielectric Screening in Solvents with Explicit Expressions for the Screening Energy and Its Gradient.* Journal of the Chemical Society-Perkin Transactions 2, 1993(5): p. 799-805.
42. Schäfer, A., H. Horn, and R. Ahlrichs, *Fully optimized contracted Gaussian basis sets for atoms Li to Kr.* The Journal of Chemical Physics, 1992. **97**(4): p. 2571-2577.
43. Jeong, S.J., et al., *Self-Aligned Multichannel Graphene Nanoribbon Transistor Arrays Fabricated at Wafer Scale.* Nano Lett, 2016. **16**(9): p. 5378-85.

44. Zhu, J., et al., *Solution-Processable Carbon Nanoelectrodes for Single-Molecule Investigations.* Journal of the American Chemical Society, 2016. **138**(9): p. 2905-2908.
45. Mativetsky, J.A., M. Palma, and P. Samori, *Exploring electronic transport in molecular junctions by conducting atomic force microscopy.* Stm and Afm Studies on (Bio)Molecular Systems: Unravelling the Nanoworld, 2008. **285**: p. 157-202.
46. Javey, A., et al., *Ballistic carbon nanotube field-effect transistors.* Nature, 2003. **424**(August): p. 654-657.
47. Venkataraman, L., et al., *Dependence of single-molecule junction conductance on molecular conformation.* Nature, 2006. **442**(7105): p. 904-7.
48. Ratner, M.A., et al., *Molecular Wires: Charge Transport, Mechanisms, and Control.* Annals of the New York Academy of Sciences, 1998. **852**(1): p. 22-37.
49. Wold, D.J., et al., *Distance dependence of electron tunneling through self-assembled monolayers measured by conducting probe atomic force microscopy: Unsaturated versus saturated molecular junctions.* Journal of Physical Chemistry B, 2002. **106**(11): p. 2813-2816.
50. Kim, T., et al., *Charge transport and rectification in molecular junctions formed with carbon-based electrodes.* Proceedings of the National Academy of Sciences, 2014. **111**(30): p. 10928-10932.

Chapter 4 Synthesis of Asymmetric Junctions: towards a Nanoscale Schottky Diode Based on SWCNTs

4.1 Metal semiconductor junction

Metal-semiconductor junctions play a very important role in electronics. For electron transport through metal-semiconductor interfaces, the junction can behave as rectifying, which only allows current to pass in one direction, or ohmic, for which current can pass in either direction.

The key factor deciding the junction characteristic is the barrier height (BH), also called Schottky barrier height (SBH)[1]. The SBH is defined as the potential energy difference between the Fermi Energy of the metal and the band edge where the majority carriers reside (shown in **Figure 4-1**). In the case of a n-type semiconductor, the energy gap between the Fermi level and the conductance band maximum is the energy barrier. For a sufficiently large Schottky barrier height, where SBH is significantly higher than the thermal energy k*T, the semiconductor is depleted near the metal and exhibits rectifying behaviour. [2] For lower Schottky barrier heights, the semiconductor is not depleted and instead forms an ohmic contact to the metal.

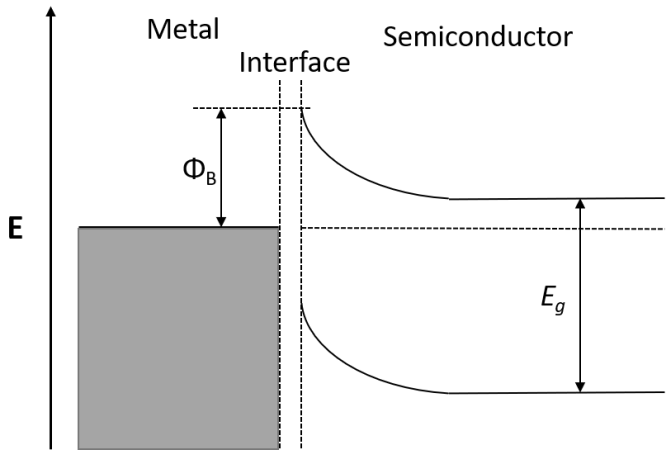

Figure 4-1 Band diagram for n-type Schottky barrier at zero bias.

The formation of a Schottky barrier between metal electrodes and nanotubes increases device resistance and affects device performance. Early attempts were made by Javey [3] by using palladium (Pd) to achieve low resistance barrier-free p-type electrical contacts (shown in **Figure 4-2**). Thermal annealing was as well used to improve the contact between metal and nanotubes. Recently, Qing adopted Mo as an electrode material and forms Mo2C carbide at the end of SWCNT and hence get a reliable electrical contact with remarkably low resistance.[4] However, a barrier between a metal electrode and a semiconductor is desirable in certain applications, such as Schottky diodes used in radio frequency engineering.[5]

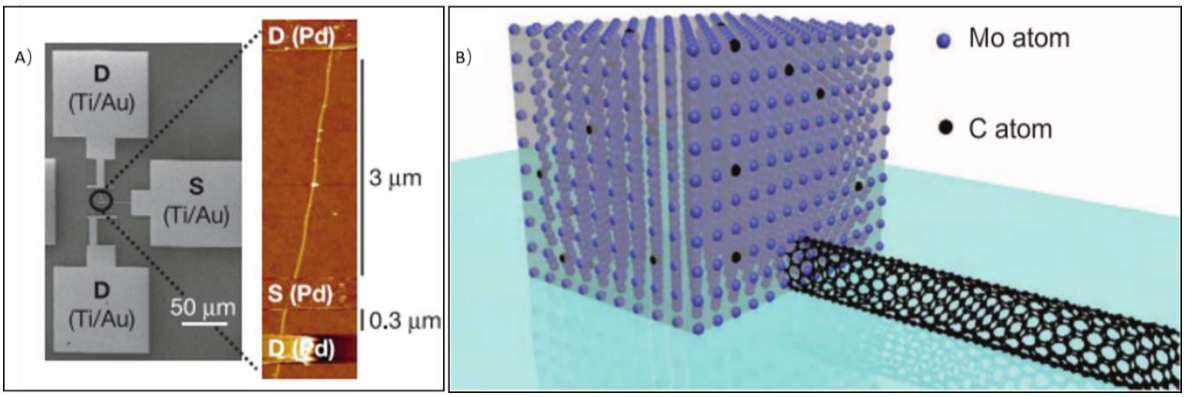

Figure 4-2 A) Pd-contacted long (L ¼ 3 mm) and short (L ¼ 300 nm) back-gated SWNT devices formed on the same nanotubes on SiO2/Si. A scanning electron microscope (SEM) image (left) and atomic force microscope (AFM) image (right) of a representative device[3]; B) Schematics

end-bonded contact , where the SWNT is attached to the bulk Mo electrode through carbide bonds while the C atoms from originally covered portion of the SWNT uniformly diffuse out into the Mo electrode.[4]

The most common type of a diode is a crystalline piece of semiconductor material with a p–n junction connected to two electrical terminals. When the n-type and p-type materials are attached together, a momentary flow of electrons occur from the n to the p side resulting in a third region between the two where no charge carriers are present. This region is called the depletion layer because there are no charge carriers (neither electrons nor holes) in it. At this point, there is a "built-in" potential across the depletion zone. When a sufficiently higher electrical potential is applied to the P side (the anode) than to the N side (the cathode), it allows electrons to flow through the depletion region from the N-type side to the P-type side. The junction does not allow the flow of electrons in the opposite direction when the potential is applied in reverse.

On the other hand, Schottky diode is a semiconductor diode formed by the junction of a semiconductor with a metal, creating a Schottky barrier. The barrier is high enough that there is a depletion region in the semiconductor, near the interface. Under forward bias, there are many thermally excited electrons in the semiconductor that are able to pass over the barrier. The passage of these electrons over the barrier (without any electrons coming back) corresponds to a current in the opposite direction. Under reverse bias, there is a small leakage current as some thermally excited electrons in the metal have enough energy to cross the barrier. The Schottky barrier diode has electrons as majority carriers on both sides of the junction. Because of their majority-carrier conduction mechanism, Schottky diodes can achieve greater switching speeds than p–n junction diodes, making them appropriate to rectify high-frequency signals.

4.1.1 CNT p-n diode

For electronic applications, semiconducting CNTs have drawn great attention as direct band-gap materials. Diode-like rectification across a CNT has been achieved by a form of a p-n junction. In 1999, Farajian first predicted p-n junction formation in an N, P dopant CNT.[6] Later, Kong reported properties of p-n-p junctions chemically defined on individual SWCNTs,[7] while Kato fabricated junction structures of Cs/I and Cs/C60 inside SWNT (Cs/I@SWNT, Cs/C60@SWNT) with an advanced plasma ion irradiation process.[8] Beyond single SWCNT, thin film transistors based on polymer coating percolating SWCNT strips were reported by Zhou.[9] **Figure 4-3** shows the schematics of the CNT p-n diode.

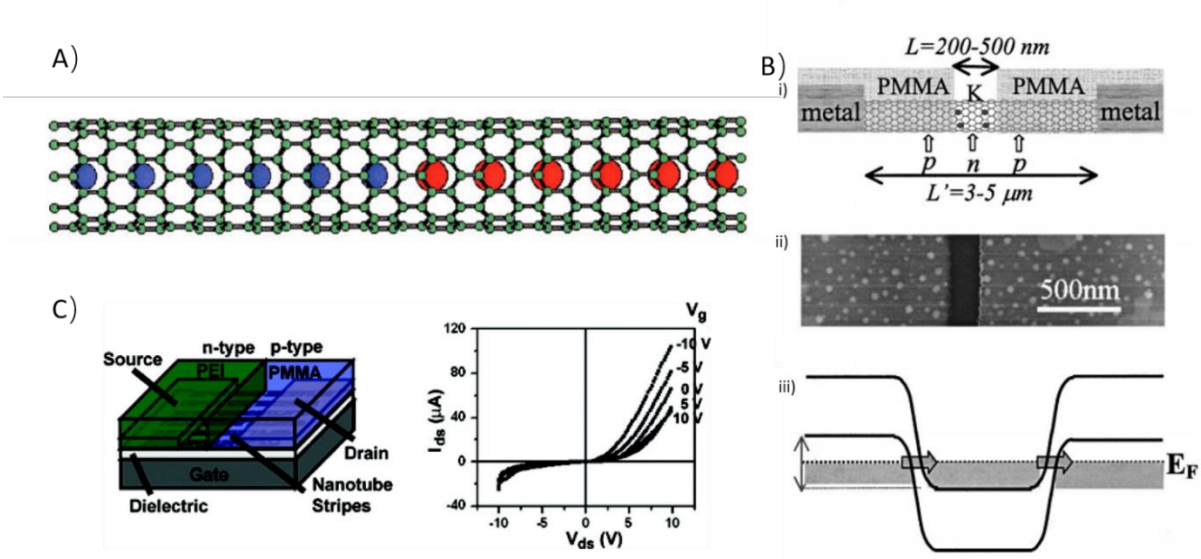

Figure 4-3 A) The geometry of the (10,0) zigzag nanotube and the N-P dopants. The length is 50 Å and the radius 3.8 Å; each ring around the circumference has 10 carbon atoms. The distance between dopant atoms is taken to be 4.2 Å[6]; B) i) : Schematic p – n – p nanotube device. Ii): AFM topographical image showing a 200-nm-wide window (dark trench in the middle) opened in the PMMA layer (300 nm thick) over a nanotube (not visible). iii): Band diagram. Electrons can tunnel through the double p – n junctions when the Fermi level (E_F) is between the arrowed region[7]; C) Left: Schematic illustration of a p-n diode formed by patterning PEI onto one-half of the channel region, by using PMMA resist formed by deep UV lithography. In this case, one-half of the channel is p-type, and the other half is n-type; Right: Output characteristics of the p-n at different gate voltages[9].

Additionally, the p-n junction can be manipulated by electrical gating using the tip of a conductive AFM [10] or using a pair of split gates[11], as shown in **Figure 4-4**. The reported CNT diodes to date have mainly focused on p-n junctions rather than Schottky(metal/semiconductor) junctions.

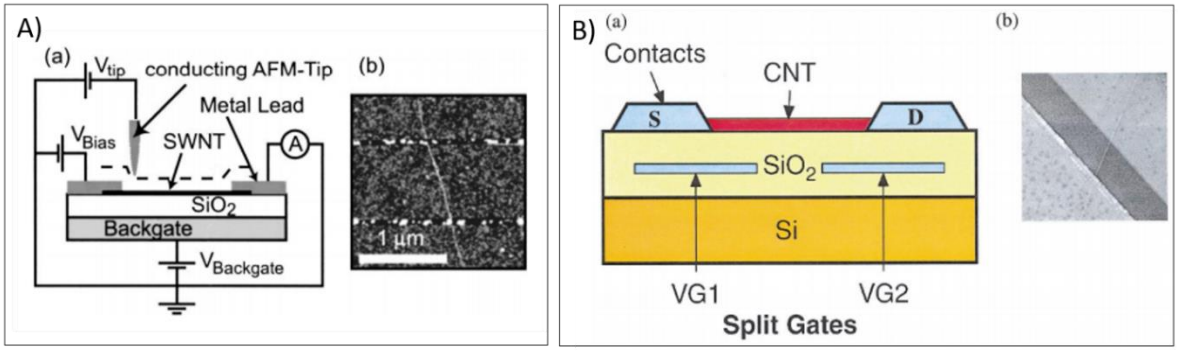

Figure 4-4 A):(a) Schematic of the experiment. A conducting AFM probe is scanned above the TUBEFET. Voltages at the electrodes, the tip gate and the backgate are adjusted separately. The transport current through the device is measured. (b) AFM topographical image of a TUBEFET sample grown by CVD with a nanotube diameter of 1.4 nm. The image has been flattened to increase the contrast of the nanotube[10]; B) (a) Schematic cross section of SWNT p-n junction diode. The split gates VG1 and 2 are used to dope an SWNT electrostatically. For example, a p-n junction with respect to the S contact can be formed by biasing VG1<0 and VG2>0; (b) SEM of an SWNT over a 1 mm split gate[11].

4.1.2 CNT Schottky diodes

CNT Schottky diodes based on asymmetric electrodes were reported by Manohara [12], Yang [13] and Lu [14], as shown in Figure 4-5. The Schottky diode fundamentally operates differently to a p-n diode. For a p-n diode, the reverse current arises from minority carriers diffusing through the depletion layer, and the forward current is due to minority carrier injection from n and p sides. On the other hand, the Schottky diode's reverse current is due to carriers which overcome the barrier, and the forward current is due to majority carrier injection from the semiconductor; this leads to diode devices with a small threshold voltage.

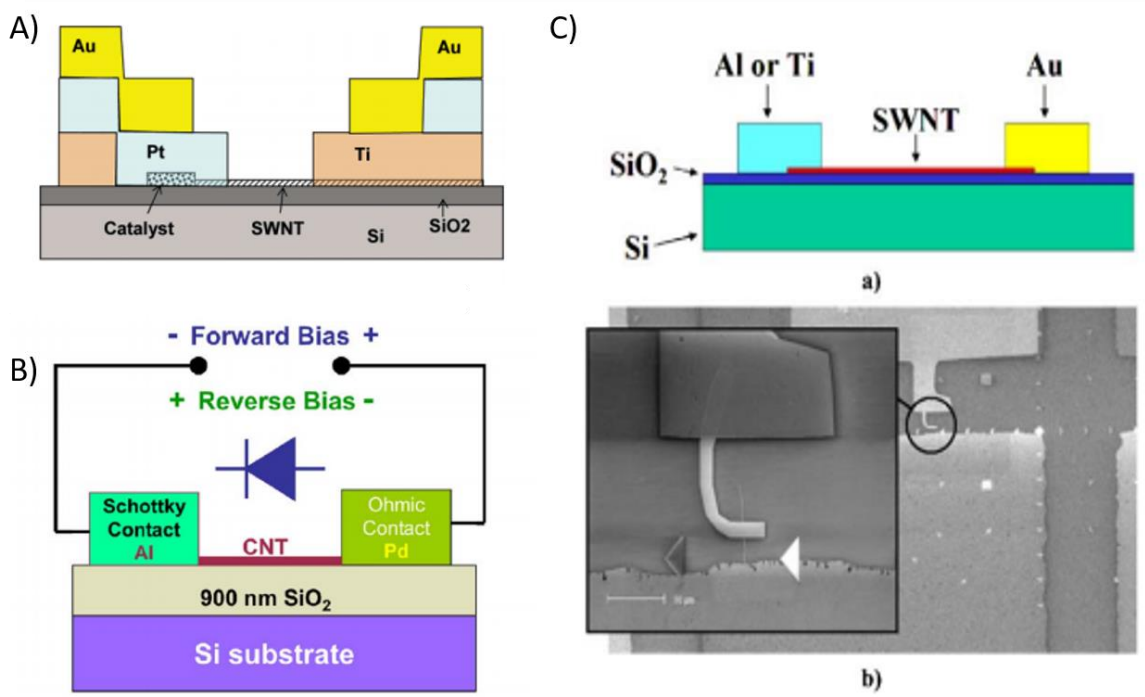

Figure 4-5 A) Schematic representation of the SWNT-Schottky diode showing the Ti-Schottky and the Pt-Ohmic metal layers deposited through angled evaporation[12]; B) Schematic of the CNT Schottky diode and direction dependent FET using Pd and Al contacts[13]; C) upper part: Schematic picture of device structure; Bottom part: SEM image of Al-SWNT-Au device; top electrode is gold and bottom electrode is aluminium[14].

In 1999, Yao [15] found that a metal-semiconductor junction (formed by defects in one SWCNT) behaves like a rectifying diode with nonlinear transport characteristics that are strongly asymmetric with respect to bias polarity. However, only four junctions are selected out of 500 SWCNTs observed in the experiment.[15]: AFM topography imaging and structure of the junction are shown in **Figure 4-6**. The yield was so low that no further application or investigation was pursued due to the lack of a reproducible method for forming the junctions

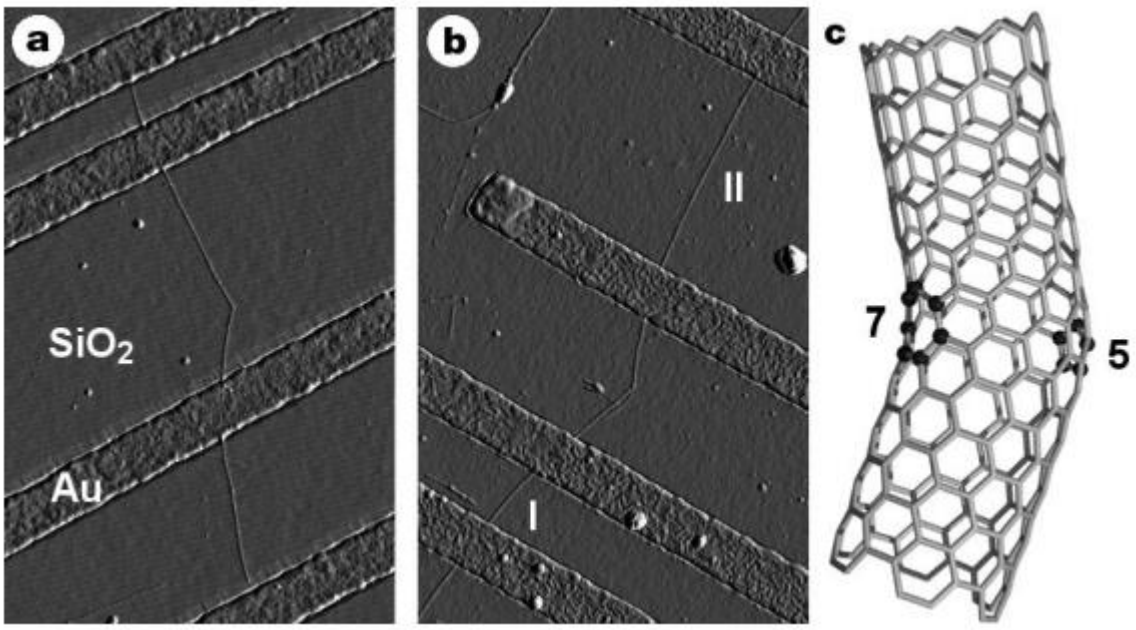

Figure 4-6 a) Tapping-mode atomic force microscope amplitude images of examples of nanotube junction devices. a, b, Nanotubes that contain a single kink of 36° and 41° respectively. These kinks can be associated with pentagon and heptagon defects which join two nanotube pieces with different diameters and chirality. c, Illustration of the carbon-bond network of a kink junction constructed between an `armchair' tube and a `zigzag' tube, where 5 denotes a pentagon, 7 denotes a heptagon, and the atoms in the pentagon and heptagon are highlighted by dark balls.[15]

Therefore, it is still a challenge to develop facile and low-cost approaches for the controlled formation of CNT-based Shottcky barriers. In this regard, an in-solution assembly approach would be highly desirable.

Herein I have fabricated potential Schottky barrier diodes by forming asymmetric junctions with metallic and semiconducting carbon nanotubes, directly in solution. To improve the yield of junction formation, various methods including DNA-hybridization assisted assembly, two-step amidation reactions and click chemistry coupling, were employed.

This type of system can potentially allows us to directly explore metallic-semiconducting CNT contact properties. Additionally, a nanoscale Schottky diode could be widely adopted in molecular electronics for complex circuits.

4.2 Results and discussion: Junction formation

Differently from the junction formation strategy described in chapter 3, the methods presented here coupled two types of carbon nanotubes (metallic and semiconducting) so that a Schottky junction could be achieved. Three strategies have been adopted to fabricate such asymmetric junctions. The first approach is based on the aforementioned two-step amidation reaction (see chapter 3.2.2), but replacing the second additional CNTs with nanotubes of different chirality/electronic character. The other two methods focus on novel asymmetric coupling reaction schemes in which different CNTs are functionalised respectively with two coupling agents. The two mixtures were then added together so that CNTs would only couple to complementary CNTs other than ones of the same type.

4.2.1 Starting material: DNA-wrapped CNT solutions

The starting material consists of single walled carbon nanotubes (SWCNTs) wrapped by DNA, dissolved in deionized water at a concentration of ca 1 mg/mL, according to published procedures.[16] In a typical dispersion experiment, 1 mg of SWCNT powders (HiPco ™, NanoIntegris Technologies) were suspended in 1 mL aqueous DNA (Integrated DNA Technologies) solution (1 mg mL–$(GT)_{20}$, 0.1 M NaCl). The mixture was sonicated (Sonics, VCX130) in an ice-water bath for 2 hours at a power level of 8 W. After sonication, the samples were centrifuged (Heraeus Fresco 17) for 90 min at 17,000 g to remove insoluble material, leaving DNA-dispersed carbon nanotube solutions at a mass concentration around 0.5 $mg*mL^{-1}$. Later, High-performance liquid chromatography was adopted by Dr Geyou Ao and Dr Ming Zheng to collect batches for narrow length distribution sorted carbon nanotubes. DNA-wrapped SWCNTs were separated into single chirality (7,4) to obtain a solution of tubes with metallic properties

only via a polymer aqueous two-phase separation method.[17] Similarly, semiconducting tubes were separated into single chirality (7,6).

The CNTs were analysed in terms of their length distribution by casting solutions on muscovite mica to form a low-density film. In detail, 5-10 μl solution was cast on pre-treated Mg^{2+} mica (freshly cleaved). After sitting for 15 minutes, substrates were rinsed with water (Millipore, 18 MΩ) three times. Samples were then scanned by ScanAsyst Air mode to obtain topography images for the area of 8*8 μm as is shown in **Figure 4-7**.

Moreover, the segments are measured and counted in software (ImageJ). The lengths were than plotted in a histogram to exhibit the distribution of the CNTs length. The average length of segments in metallic CNTs solution is measured to be 246.8 nm with a standard deviation of 99.5 nm.(shown in **Figure 4-7**) For semiconducting CNTs, the average length is 252.8 nm with a standard deviation of 110 nm. Based on the value, the molar concentration of CNT is estimated to be in the 30 nM range according to Appendix B.

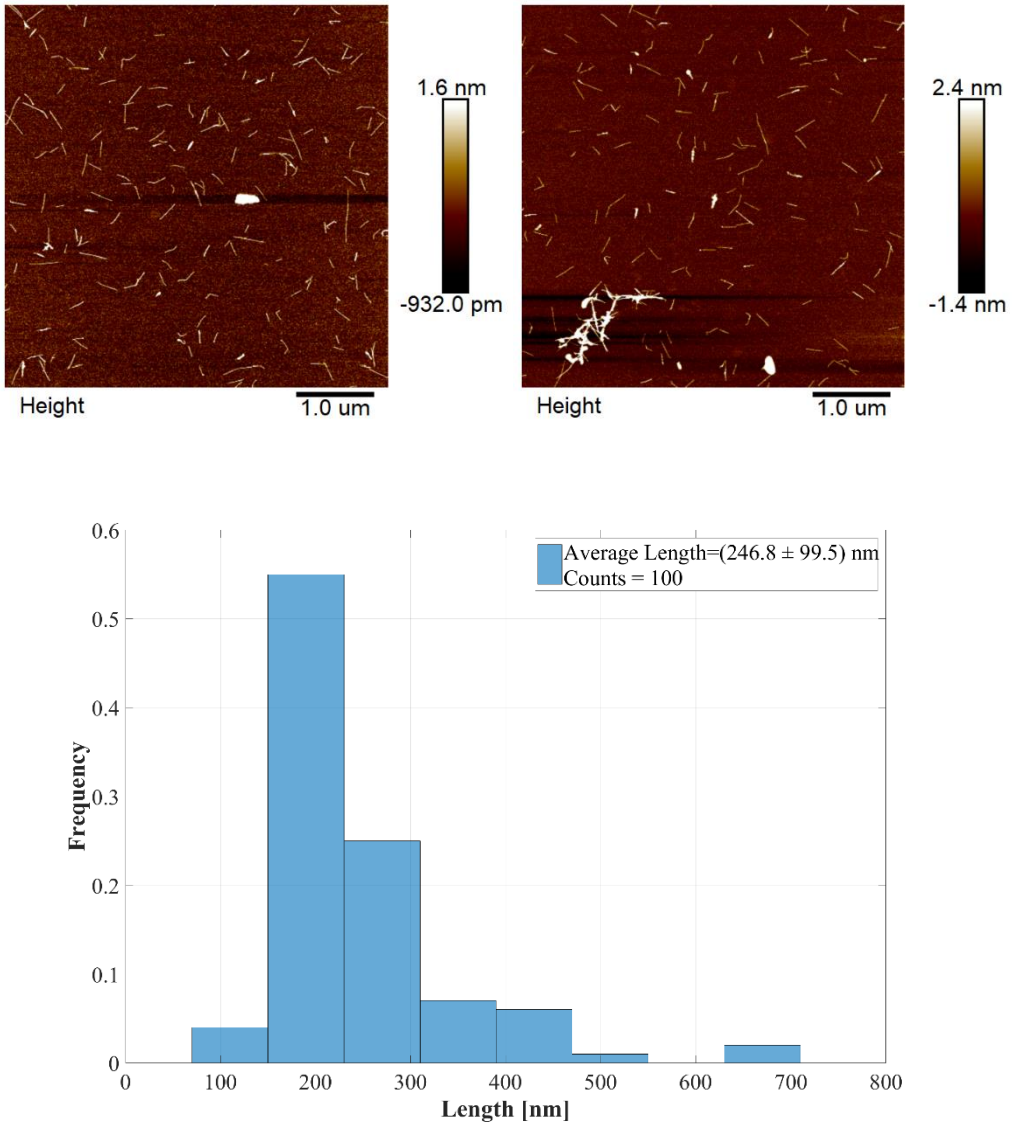

Figure 4-7 Upper: AFM topographical image of pristine DNA-wrapped SWCNTs ; Bottom: histogram of the length of the CNTs.

4.2.2 Two-step amidation reaction coupling

A two-step Amidation reaction was employed based on the EDC-NHS schematic reaction (see chapter 3 section 3.2.2). In detail, 20 ul of the starting SWCNT

solution(metallic) was mixed 1:1 with the activating solution consisting of 4mM EDC, 10mM sulfo-NHS in MES (pH 4.7) buffer. The mixture was left to incubate for 30 minutes. The solution was then diluted with Dulbecco's Phosphate Buffer Saline (pH 7.2, DPBS, ThermoScientific) solution in a 1:1 volume ratio and left incubating for 1 hour. The molecular linker (p-Phenylenediamine) was solubilised in an ethyl acetate (VWR) solution (1μL at 0.1 mM concentration) before being diluted in 1mL of ultra-pure H_2O (100 nM, 18 MΩ, Millipore). The molecular linker solution (1 μM) was then added to the SWCNT solution and left incubating overnight. The resulting concentration of the linker will be 100 nM, making it more than matching compared to the number of CNTs so that both ends will be saturated. The mixture was left to incubate overnight for higher yield.

Subsequently, excess linkers were removed by centrifugated in Millipore Amicon 100K tubes at 6500 rpm for 3 minutes. During centrifugation, the buffer was exchanged to 1X DPBS to keep the pH to 7.0-7.2. A separate solution of activated DNA-wrapped SWCNTs(semiconducting) was subsequently added to the reaction mixture in a 1:1 ratio, to attach the tubes to metallic tubes previously attached to the molecular linker. The reaction was then left incubating overnight.

The solution was cast on mica substrates, and their topography (i.e. length distribution of the CNT junctions) was analysed by AFM. The length distribution of the resulting asymmetric junctions is shown in **Figure 4-8**. While the starting materials, exhibited a length of 246.8 nm and 252.8 nm respectively, the average length of the junctions obtained with this two-step Amidation reaction was found to be 387 ± 213.2 nm. This indicates that the junctions were formed with a yield of junction formation of 72.9%.

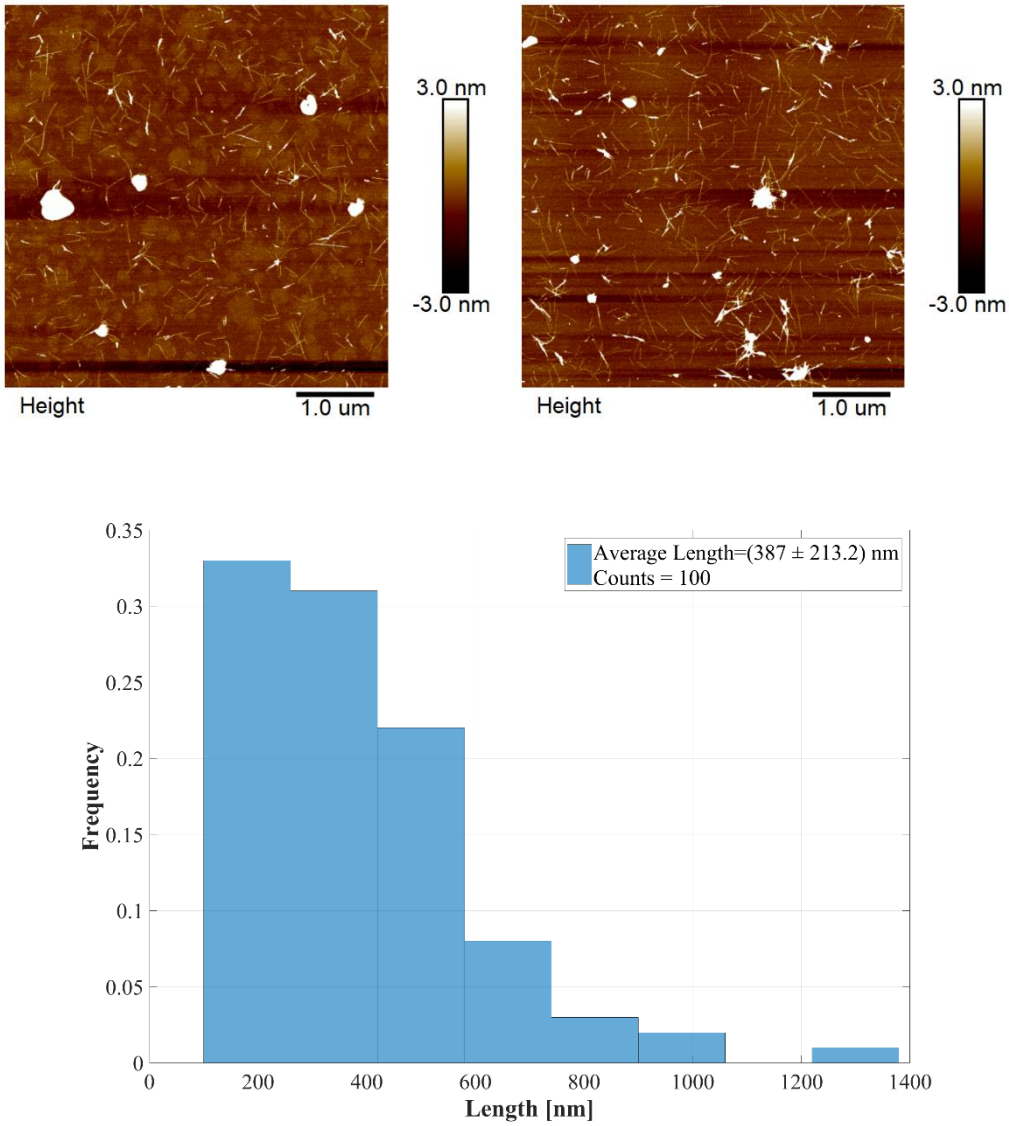

Figure 4-8 Upper: AFM topographical image of asymmetric SWCNT junctions obtained employing the two-step amidation reaction method.; Bottom: histogram of the length of the junctions.

4.2.3 Double stranded DNA assisted junction formation

We have further investigated an additional approach for the controlled formation of SWCNT-based asymmetric junctions in solution, employing a strategy based on Deoxyribonucleic acid (DNA) hybridization. DNA is the molecule that contains the genetic code of organisms. Most DNA molecules consist of two biopolymer strands coiled around each other to form a double helix.[18] The DNA strands are composed of simpler monomer units called nucleotides. Each nucleotide is composed of one of four nitrogen-containing nucleobases — cytosine (C), guanine (G), adenine (A) or thymine (T) — a deoxyribose sugar and a phosphate group.[18] The nucleotides are joined to one another in a chain by covalent bonds between the sugar of one nucleotide and the phosphate of the next, resulting in an alternating sugar-phosphate backbone. The nitrogenous bases of the two separate polynucleotide strands are bound together, according to base pairing rules (A with T and C with G), with hydrogen bonds to make double-stranded DNA.

In our study, two separate solutions of DNA-wrapped SWCNT solutions (metallic and semiconducting) are first terminally functionalised with two complementary single stranded DNAs (ssDNA). By then mixing the two solutions together only asymmetric junctions can be formed (via DNA hybridization), where the complementary DNAs on the terminal end of the SWCNTs would act as molecular linkers.

In detail, four sequences of ssDNA have been designed to form amino-DNA linkers.

α: 5-AGGTG/Amino/-3

β: CACCTTACAG

γ: 5-GGTAT/Amino/-3

θ: ATACCCTGTA

The α and γ ssDNA were designed (and purchased) with amino groups in order to tether them to the terminal ends of SWCNTs via EDC/NHS coupled amidation reactions on the carboxylic groups of the nanotubes. These two pairs of ss DNAs were then hybridized with longer complementary strands in order to rigidify this terminal DNA component of the SWCNTs, leaving a partially (non-hybridized) ssDNA sticky-end on the terminal of the CNTs. This was done as previous studies in our group and in other groups[19] have shown how this increases the yield of hybridization with DNA linked CNTs.

Therefore, for DNA sequences β and θ, 5 bases would be coupled and form double strands while another 5 bases are then left available for further hybridization as shown in Figure 4-9. The double stranded portion serves as a spacer which separates the ssDNA sticky end from the SWCNT.

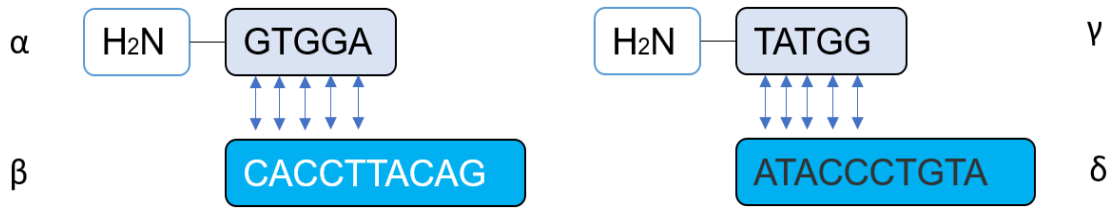

Figure 4-9 Preliminary Hybridization products: a) between DNA sequences α and β; b) between DNA sequences γ and δ.

The two pairs of complementary strands (sequences α-β, and sequences γ-δ) are hybridised by mixing the solutions 1:1 in a 1X DPBS buffer, increasing the temperature to 90 °C and holding this for 1h before slowly cooling down to 4°C.

To prepare the CNTs terminally tethered to DNA, 20ul of the starting SWCNT solution(metallic) were mixed 1:1 with the activating solution consisting of 4mM EDC,

10mM sulfo-NHS in MES (pH 4.7) buffer. The mixture was left to incubate for 30 minutes before being diluted with a Dulbecco's Phosphate Buffer Saline (pH 7.2, DPBS, ThermoScientific) solution in a 1:1 volume ratio; the solution was then left incubating for 1 hour. SWCNTs (semiconducting) solution was prepared in the same way. Following activation, amino DNA duplexes linkers were added to the two CNTs solution separately. A covalent bond was formed between amine groups on DNA and carboxylic groups on CNTs. Excess DNA linkers were removed by centrifugation as described in chapter 5.2.2. The hybridization at two sticky ends of the strand is named ligation. Two purified SWCNT-DNA solutions were mixed in 1:1 volume(10-50 µl). 1 µl of T4 DNA ligase(5 u/µl, Thermo Scientific) in 10 µl of 5X rapid ligation buffer (Thermo Scientific) was added to the SWCNT-DNA solution mixtures. Nuclease free water was added to make the total volume 50 µl. The solution was left incubating at 22 °C overnight. **Figure 4-10** shows the diagram of the separated CNTs with two types of linkers and the junction formation.

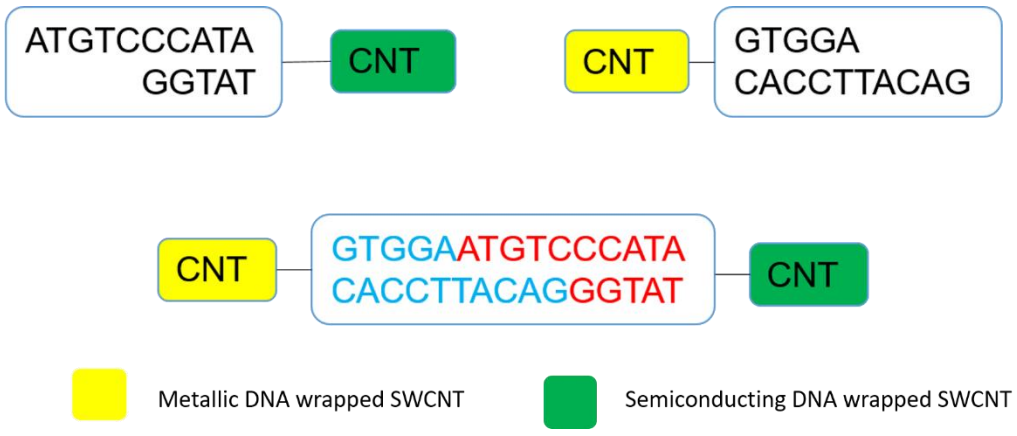

Figure 4-10 Diagram of asymmetric CNT junctions linked by double stranded DNA

The solutions were then cast on mica and analysed via AFM imaging. Characteristic AFM topographical images are shown in **Figure 4-11**, together with the measured size distribution of the DNA-CNT hybrids. The average length of the segments was found

to be 407.4 ± 159.8 nm. The corresponding reaction yield according to equation in appendix A (A-7) is 78.9%.This indicates the successful formation of asymmetric SWCNT junctions via our DNA hybridization strategy described in this section.

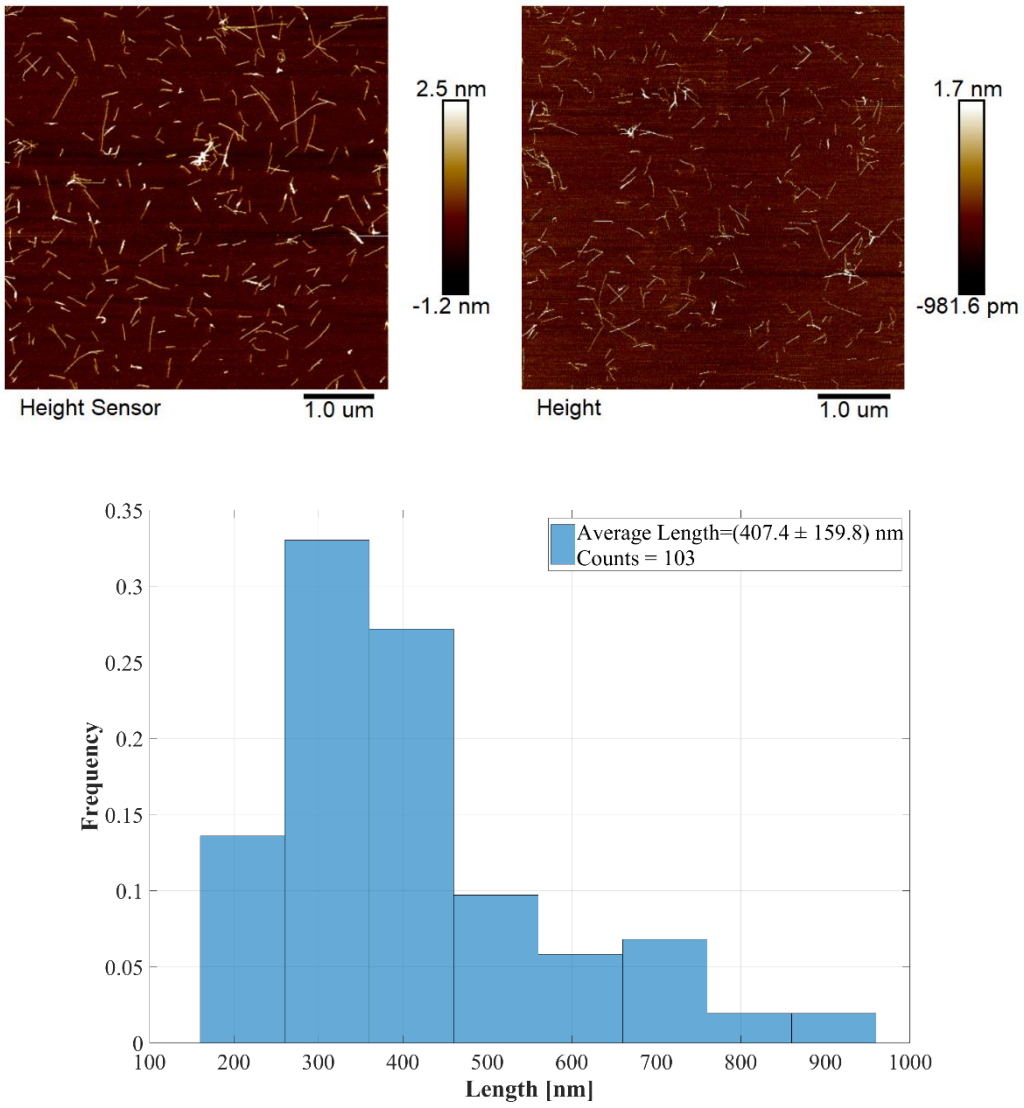

Figure 4-11 Upper: AFM topographical image of asymmetric SWCNT junctions obtained employing DNA hybridisation method; Bottom: histogram of the length of the junctions.

4.2.4 Click chemistry coupling

Click chemistry is a class of reactions which are high yielding, wide in scope, and easy to perform, while also being inert to oxygen or water. First reported by K. Barry Sharpless in 2001[20], click chemistry has been well developed with interest within biological and materials sciences. Click reactions are 'spring-loaded' since thermodynamic driving forces drive quickly and irreversibly to a single reaction product with high reaction specificity. A well-known click reaction is a copper-catalyzed reaction of an azide with an alkyne to form a 5-member ring: a Cu(I)-Catalysed Azide-Alkyne Cycloaddition (CuAAC). As is shown in **Figure 4-12**, copper(I) is the key catalyst for the reaction to be fast and high efficiency.

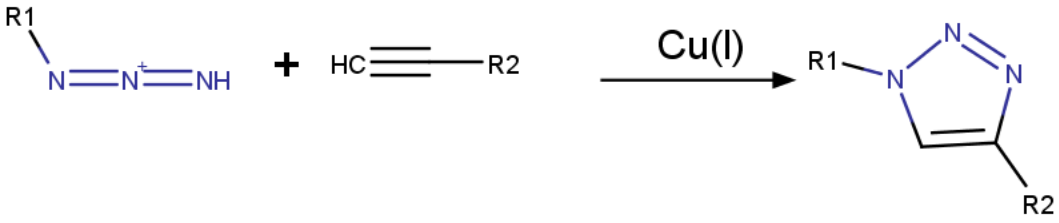

Figure 4-12 Schematic of Copper(I)-Catalysed Azide-Alkyne Cycloaddition reaction

However, copper(I) could be toxic for biological applications and contaminate carbon nanotubes. As an alternative, we have adopted a copper-free click reaction: strain-promoted Azide-Alkyne Cycloaddition (SPAAC). SPAAC reactions rely on the use of strained cyclooctyne that possesses a remarkably decreased activation energy in contrast to terminal Alkynes and thus do not require an exogenous catalyst. The schematic of SPAAC is shown in **Figure 4-13** below.

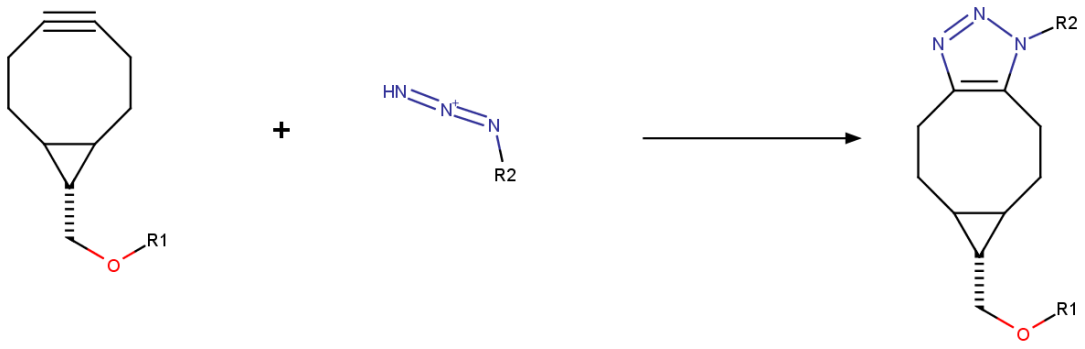

Figure 4-13 Strain-promoted Azide-Alkyne Cycloaddition reaction

In our project, we have adopted one type of SPAAC as BCN(bicyclo[6.1.0]nonyne)-azide reaction to couple the junction. Beyond the advantages of the click reaction itself, the asymmetric reagent offers the possibility to introduce asymmetric molecules without forming self-conjugate products. In detail, we used amino-BCN (N-[(1R,8S,9s)-Bicyclo[6.1.0]non-4-yn-9-ylmethyloxycarbonyl]-1,8-diamino-3,6-dioxaoctane, Sigma-Aldrich) and amino-Azide (4-Aminophenyl azide hydrochloride, Sigma-Aldrich)molecules as junction linkers (shown in **Figure 4-14**).

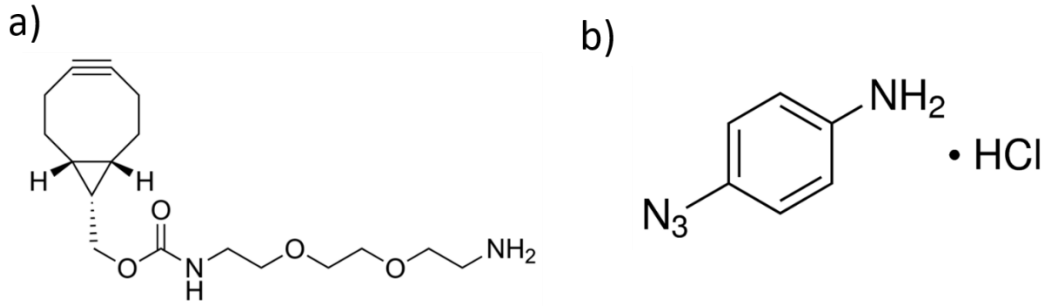

Figure 4-14 Molecular linker: a): (N-[(1R,8S,9s)-Bicyclo[6.1.0]non-4-yn-9-ylmethyloxycarbonyl]-1,8-diamino-3,6-dioxaoctane; b): 4-Aminophenyl azide hydrochloride

To prepare the CNTs attached with BCN/Azide, 20ul of the starting SWCNT solution(metallic) was mixed 1:1 with the activating solution consisting of 4mM EDC, 10mM sulfo-NHS in MES (PH 4.7) buffer. The mixture was left to incubate for 30 minutes before diluted with Dulbecco's Phosphate Buffer Saline (pH 7.2, DPBS,

ThermoScientific) solution in a 1:1 volume ratio and left incubating for 1 hour. Similar SWCNTs (semiconducting) solution was prepared in the same way. Following activation, amino functionalised linkers (BCN/Azide) were added to two CNTs solution separately. A covalent bond was formed between amine groups and carboxyl groups on CNTs. Centrifugation removed excess linkers as chapter 5.2.2. SWCNT(metallic)-BCN and SWCNT(semiconducting)-Azide solutions were then mixed in 1:1 volume (10-50 μl) and left to incubate overnight. To protect the BCN and Azide components from light, all the solutions were covered in the dark during incubation.

In this way, asymmetric CNT-(double stranded DNA)-CNT junctions were formed. Characteristic AFM topographical images of the formed DNA-CNT hybrids and their size distribution is shown in **Figure 4-15**. The average length of the segments was found to be 509.1 nm ± 241.7 nm. The corresponding reaction yield according to equation in appendix A (A-7) is more than 100%. This indicates that SWCNT-based asymmetric junction formation was successfully obtained via the click-reaction methodology we developed. Detailed discussion will be present in conclusion part.

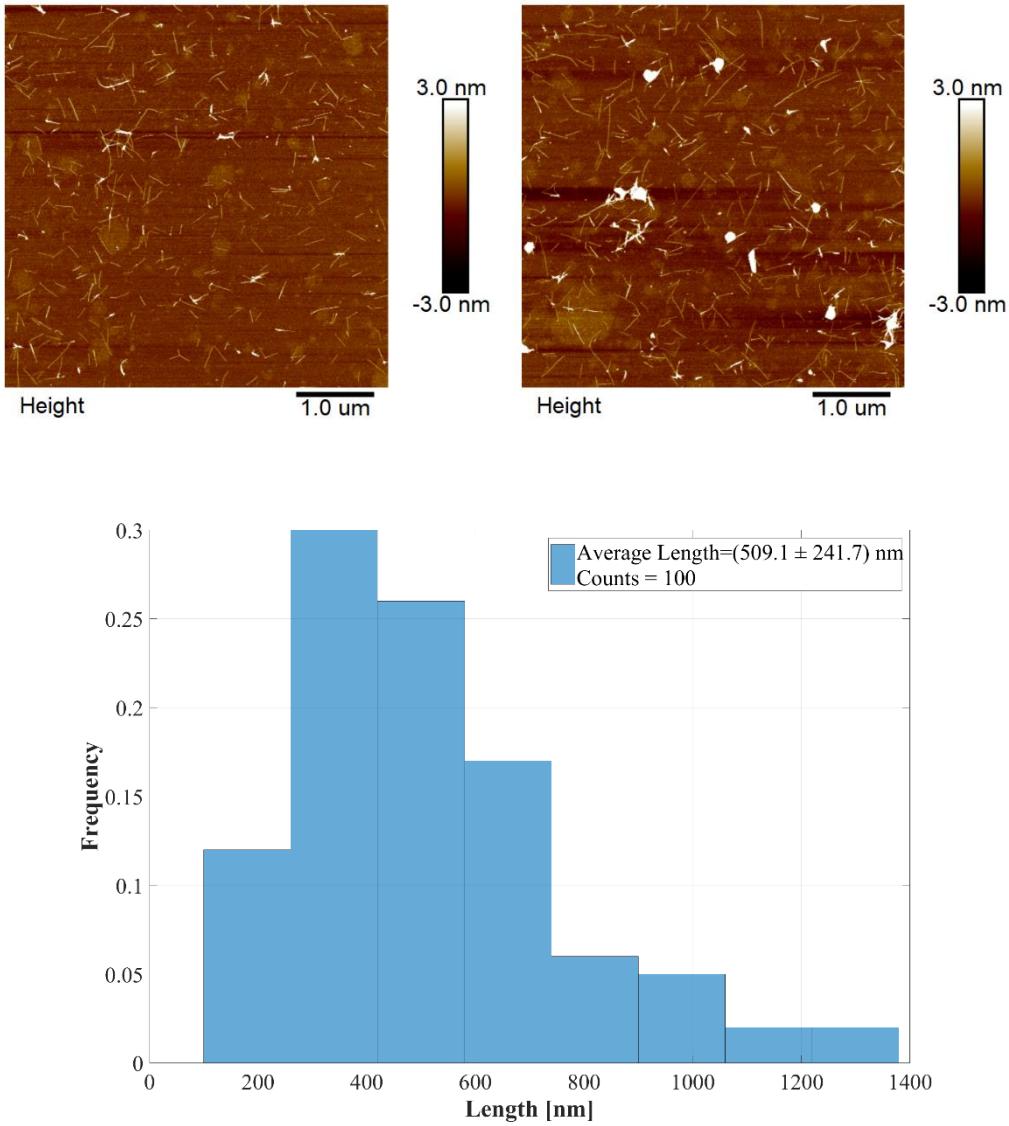

Figure 4-15 Upper: AFM topographical images of asymmetric SWCNT junctions obtained by click chemistry coupling method; Bottom: histogram of the length of the junctions.

4.2.5 Conclusive discussion

The increase in the average length indicates the formation of SWCNT asymmetric junctions for all three synthesis schemes. However, a quantitative comparison is missing to evaluate the yield for different strategies. As is discussed in Appendix A, the relationship between reaction yield and length increment is summarised as below:

$$y = \frac{100x}{200 - x} \; and \; x = \frac{200y}{100 + y} \tag{4-1}$$

Where x is the reaction yield and y is the length increment, both of them are in percentage.

For the two-step amidation synthesis, the length of the CNT segments increased by 57.3% upon junction formation, i.e. from 246.8 nm to 387.0 nm. The corresponding reaction yield according to equation (A-7) in appendix A is 72.9%.

On the other hand, reactions based on the hybridization of complementary ssDNA end-functionalised SWCNT exhibited a length increment of 65.1%, from 246.8 nm to 407.4 nm. The corresponding reaction yield according to equation (A-7) in appendix A is 78.9%.

Finally, for reactions based on click chemistry of BCN and azide end-functionalised SWCNT, the length of segments increased by 107% from 246.8 nm to 509.1 nm. The approximate relationship does not exhaustively describe this situation, but it can be estimated that the yield of junction formation approximates 100% with the formation of additional multiple junctions linked together (i.e. junctions with more than two nanotubes).

The reactions based on the two-step amidation mechanism and the hybridization strategy have a similar yield in terms of average length. However, the hybridization

produces a significantly narrower length distribution (the standard deviation is 213.2 nm for amidation and 159.8 nm for hybridization). We assume this is due to the difference of steric hindrance at the terminal ends of the SWCNTs. The sticky ends of the ssDNA linkers used in the hybridization strategy, are less affected by the nanotubes, being further away from the CNTs; this minimises the steric repulsion between the negatively charged DNA-wrapped CNTs forming the junctions.

Differently, the reaction based on the click chemistry approach results in a more than 100% increase in average length, indicating the formation of junctions with more than two nanotubes. From our results, we can conclude that the click chemistry has the best yield of junction formation.

By far, we have presented the synthesis of asymmetric junctions via three different strategies, namely 'two-step amidation', 'DNA assisted', and 'click chemistry' couplings. Based on the AFM analysis of the obtained junctions' lengths, we estimated and compared the linking yields for the three methods. Notably, this is a preliminary step towards the in-solution assembly of a nanoscale Schottky diode: we have indeed designed our assembly strategies to form metallic-semiconducting CNTs junctions. Despite not having yet performed any conclusive electrical characterisation on these systems, we plan to perform these measurements following the C-AFM method discussed in chapter 3, in order to demonstrate the Schottky diode nature of the systems assembled here: this work has been temporarily set aside due to time constraints. Additionally, other strategies for the junctions organization on patterned electrodes will be considered, in line with the approaches discussed in the next chapter (chapter 5). This will allow the facile fabrication of devices for solution-processable molecular electronics.

References

1. *The physics and chemistry of the Schottky barrier height.* Applied Physics Reviews, 2014. **1**(1): p. 011304-011304.
2. Sharma, B., *Metal-semiconductor Schottky barrier junctions and their applications*. 2013: Springer Science & Business Media.
3. Javey, A., et al., *Ballistic carbon nanotube field-effect transistors.* Nature, 2003. **424**(August): p. 654-657.
4. Cao, Q., et al., *End-bonded contacts for carbon nanotube transistors with low, size-independent resistance.* Science, 2015. **350**(6256): p. 68.
5. Han, R., et al. *280GHz and 860GHz image sensors using Schottky-barrier diodes in 0.13 μm digital CMOS*. in *Solid-State Circuits Conference Digest of Technical Papers (ISSCC), 2012 IEEE International*. 2012. IEEE.
6. Esfarjani, K., et al., *Electronic and transport properties of N-P doped nanotubes.* Applied Physics Letters, 1999. **74**(1): p. 79-81.
7. Kong, J., et al., *Chemical profiling of single nanotubes: Intramolecular p–n–p junctions and on-tube single-electron transistors.* Applied Physics Letters, 2002. **80**(1): p. 73-75.
8. Kato, T., et al., *P-N junction with donor and acceptor encapsulated single-walled carbon nanotubes.* Applied Physics Letters, 2009. **95**(8): p. 083109.
9. Zhou, Y., et al., *p-Channel, n-Channel Thin Film Transistors and p–n Diodes Based on Single Wall Carbon Nanotube Networks.* Nano Letters, 2004. **4**(10): p. 2031-2035.
10. Freitag, M., et al., *Controlled creation of a carbon nanotube diode by a scanned gate.* Applied Physics Letters, 2001. **79**(20): p. 3326-3328.
11. Lee, J.U., P.P. Gipp, and C.M. Heller, *Carbon nanotube p-n junction diodes.* Applied Physics Letters, 2004. **85**(1): p. 145-147.
12. Manohara, H.M., et al., *Carbon nanotube schottky diodes using Ti - Schottky and Pt - Ohmic contacts for high frequency applications.* Nano Letters, 2005. **5**(7): p. 1469-1474.
13. Yang, M.H., et al., *Carbon nanotube Schottky diode and directionally dependent field-effect transistor using asymmetrical contacts Advantages of top-gate, high-k dielectric carbon nanotube field-effect transistors Carbon nanotube Schottky diode and directionally dependent field-effect transistor using asymmetrical contacts.* Citation: Appl. Phys. Lett. Appl. Phys. Lett. Appl. Phys. Lett, 2005. **87**(10).
14. Lu, C., et al., *Schottky diodes from asymmetric metal-nanotube contacts Carbon nanotube Schottky diode and directionally dependent field-effect transistor using asymmetrical contacts Schottky diodes from asymmetric metal-nanotube contacts.* Appl. Phys. Lett. Appl. Phys. Lett, 2006. **88**(87).
15. Yao, Z., et al., *Carbon nanotube intramolecular junctions.* Nature, 1999. **402**(6759): p. 273-276.
16. Zheng, M., et al., *DNA-assisted dispersion and separation of carbon nanotubes.* Nature materials, 2003. **2**(5): p. 338-42.
17. Ao, G., C.Y. Khripin, and M. Zheng, *DNA-Controlled Partition of Carbon Nanotubes in Polymer Aqueous Two-Phase Systems.* Journal of the American Chemical Society, 2014. **136**(29): p. 10383-10392.
18. Dickerson, R.E., *[5] DNA structure from A to Z*, in *Methods in Enzymology*. 1992, Academic Press. p. 67-111.
19. Penzo, E., et al., *Directed Assembly of End-Functionalized Single Wall Carbon Nanotube Segments.* Nano Letters, 2015. **15**(10): p. 6547-6552.

20. Kolb, H.C., M. Finn, and K.B. Sharpless, *Click chemistry: diverse chemical function from a few good reactions.* Angewandte Chemie International Edition, 2001. **40**(11): p. 2004-2021.

Chapter 5 Surface Patterning Techniques for the Assembly of ssDNA-wrapped SWCNTs

5.1 Dielectrophoretic assembly of DNA-wrapped carbon nanotubes on metallic nanotrenches

5.1.1 Introduction

The electrode is a key component in molecular electronics. All the electronic applications including, transistors and rectifiers, are largely dependent on the contact between components and electrodes. As discussed in the previous chapters, so far in this thesis we have adopted carbon nanotubes as nano electrodes for molecular junctions, while a macroscopic electrode was employed as the bridge to the input and output measurement. In this chapter, we present several recent developments in patterning processes to design electrodes, separated by a short distance ranging from 20 nm to a few hundred nm.

5.1.2 Nano-trench fabrication by shadow evaporation

To fabricate metal electrodes in a controlled way, and to fabricate nanoscale electrode gaps, we employed a photolithography based strategy. The method is based on the shadow effect in high vacuum evaporation which offers the possibility of high-

resolution capability.[1-3] Two lithographic steps and metal evaporations are involved in this process. First, a lithographic step introduces the pattern for the initial electrode which will be later used as a shadow mask. Metal deposition is performed by physical vapour deposition followed by a lift-off procedure to remove the metal in the undesired area. A second photolithography is then performed to pattern the second electrode. A special approach, named tilt angle evaporation, is then used to deposit a metal outside the shadow of the first electrode. A similar lift-off process is then applied to remove unwanted metal. The details will be presented in the sections below.

5.1.2.1 Principle of shadow lithography

Photolithography is a process used in the microelectronics industry to pattern a substrate. The pattern predesigned and printed on a transparent mask is transferred by the UV exposure to a light sensitive chemical polymer, named ‘photoresist’, on the substrate. Treated by the UV light, the exposed area turns into soluble or insoluble (based on the chemical components) in the later developing step. Depending on the final pattern, photoresists are divided into positive and negative (relating to original mask pattern) as is shown in **Figure 5-1**.

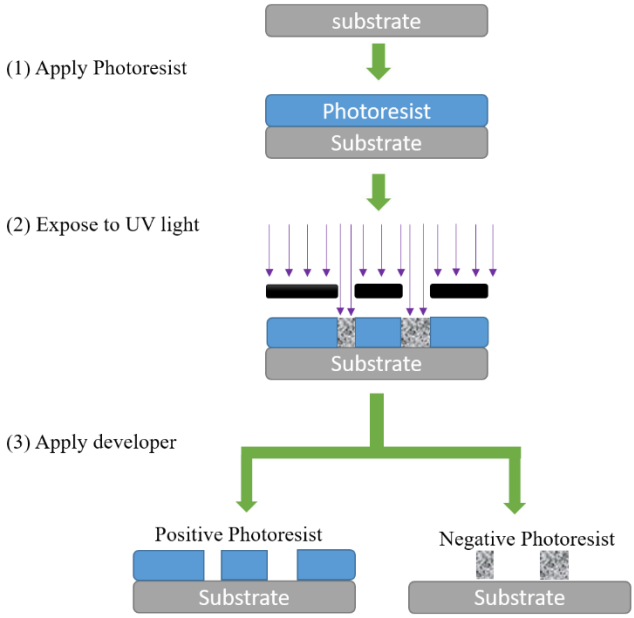

Figure 5-1 Photolithography pattern based on Left: Positive Resist; Right: Negative resist.

In this project, we performed a special type of photolithography named image reversal photolithography which can form a negative pattern of the mask by applying a special photoresist. The method is intended for lift-off techniques which call for a negative wall profile. It is vital in shadow evaporation to have a clear edge. **Figure 5-2** describes the process of image reversal photolithography used. The critical parameters in the method which will impact the undercut profile include exposure dose, reversal bake time and temperature and development time.

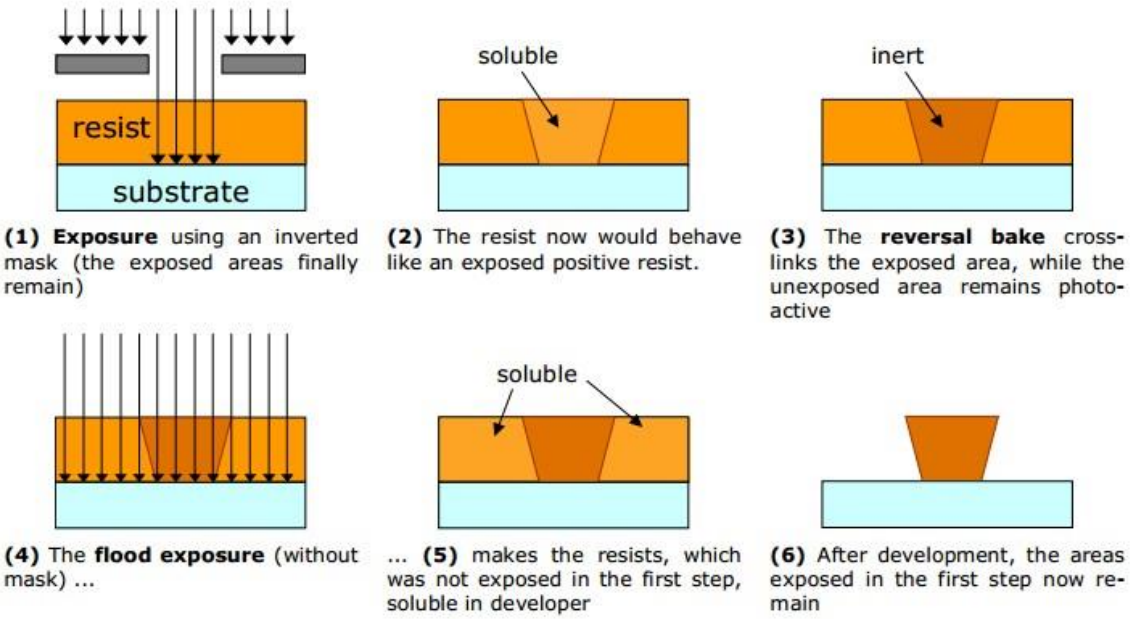

Figure 5-2 Schematic of Image Reversal Photolithography [4]

Thermal physical evaporation in a high vacuum system is applied to coat a gold electrode on the substrate (shown in **Figure 5-3**). The chromium is used as an adhesive layer to attach the gold layer. As a result, the first electrode is made of a Chromium-Gold bilayer. The thickness of the metallic film is measured by a Quartz crystal balance monitor embedded inside the vacuum chamber. The balance monitor's position in the evaporation chamber is relative, so a tooling factor is used to calibrate the meter to its position in the evaporation chamber.

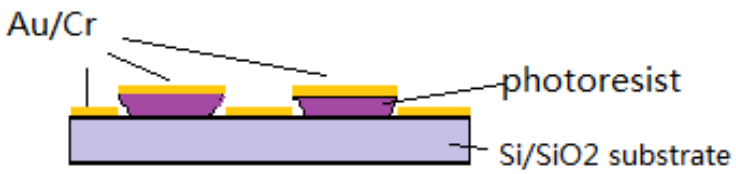

Figure 5-3 First electrode with photoresist beneath metal

After the evaporation, the samples go through a lift-off step in an organic solvent overnight to remove the residual resist together with the unwanted gold. An alternative

way is to put the samples in heated N-Methyl-2-pyrrolidone (NMP) at 55 ℃ to accelerate the process. The samples are then rinsed with acetone, isopropanol and dried under nitrogen flow.

To remove residual collar resist possibly sticking to the metallic electrodes during to the lift-off process, the samples are treated with Oxygen plasma subsequently to lift-off. The first electrode is fabricated on the substrate and can work as a shadow mask. An identical photolithography process is then employed to open a window on the first electrode. Subsequently, a metal evaporation step is required to form the second electrode. This metal deposition step is performed with the sample tilted at a specific angle in order to employ a shadowing effect to tune the width of the gap between the first and the second electrode. The composition and thickness of the second electrode should be the same as the first, (with 5 nm Chromium and 45 nm gold), so not to affect the electrical characterisation. However, the geometry of the shadow effect will affect both the width of the gap and the second electrode thickness, requiring a detailed calculation for proper control. The details of the shadow mask lithography are shown in **Figure 5-4**.

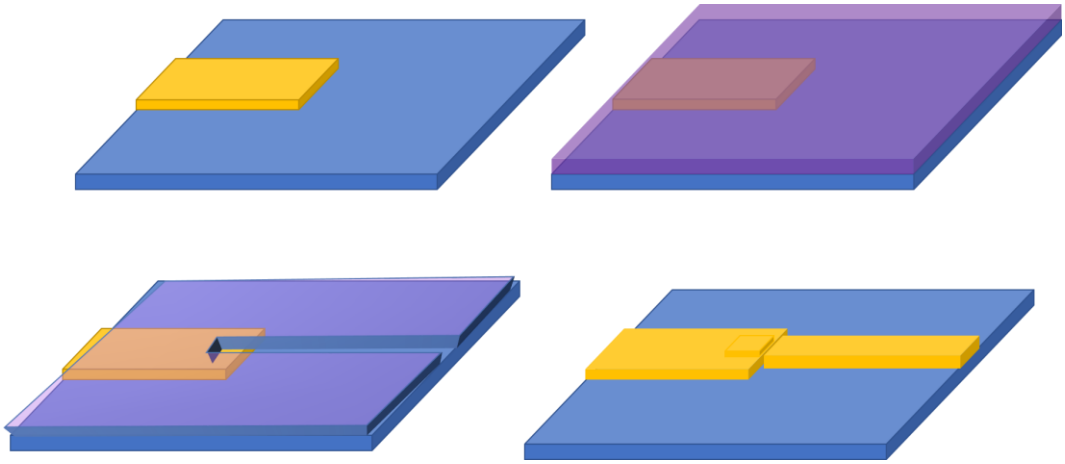

Figure 5-4 Schematic of the edge mediated shadow mask lithography process, (a) A first pattern is made by standard optical lithographic process, (b) and (c) The second layer is patterned by the same method over the first pattern, (d) Metal deposition with the sample tilted at a specific angle is performed to form the second metallic electrode and the nanotrench.

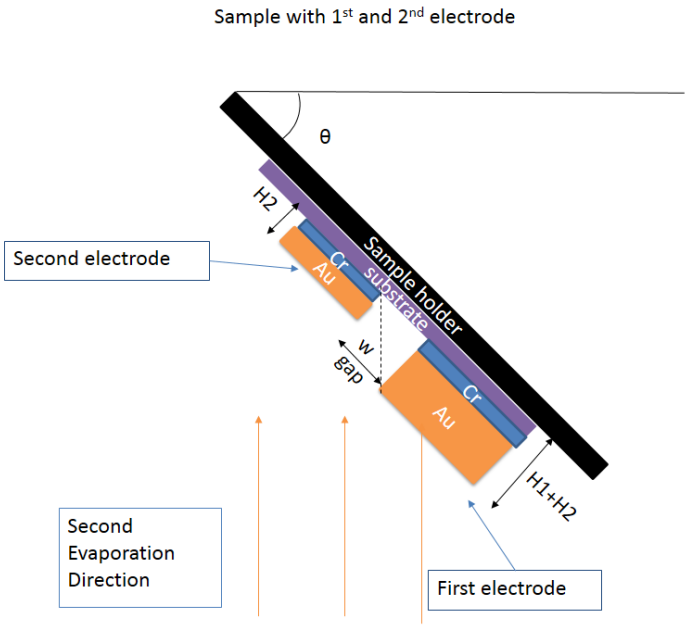

Figure 5-5 Schematic of tilt evaporation

The evaporation source is far enough from the sample holder so that the line from the source to sample position is perpendicular to the sample surface (as shown in **Figure 5-5**). Therefore, the width of the gap formed follows the equation (5-1) and (5-2).

$$w = H_1 * \tan\alpha \qquad (5\text{-}1)$$

$$H_2 = H_0 * \cos\alpha \quad (5\text{-}2)$$

Where w is the width of the gap, H_1 is the thickness of the first electrode before the second evaporation, α is the tilt angle for evaporation, H_2 is the actual thickness of the second electrode on the substrate, while H_0 is the thickness of evaporated metal measured by the quartz micro balance monitor. As a result, the final thickness of the first electrode will be H_1+H_2.

A similar lift-off process will be employed on the samples after the tilt degree evaporation. The nanostructure gap is then formed between the two electrodes.

5.1.2.2 Operations of shadow lithography

The micro fabrication was carried in a class 10000 cleanroom equipped with an MJB4 (SUSS MicroTec) mask aligner, a resistive thermal evaporator (Kurt J. Lesker), for metallic deposition, and several optical microscopes for inspection. We chose the AZ®5214E photoresist (from Microchemicals GmbH) with image reversal properties, following the standard process from the manufacturer. The optical lithography process is summarised below:

1. Check substrate side of silicon dioxide slide.
2. Place silicon substrates in their holders in beakers filled with acetone – run an ultrasonic bath for five minutes – repeat with fresh acetone.
3. Repeat step 2 using isopropanol (2 runs in the sonic bath).
4. After 2nd sonic clean in isopropanol, dry samples using Nitrogen gun.
5. Use clean beaker for photo-resist and sonic clean to place any particles at the bottom of the beaker. Place substrate in spin-coater test up to speed (4000 rpm 30 s, rump 1000 rpm 9 s). Cover in photo-resist (~8-9 drops) – draw photo-resist from the surface of beaker avoiding any air bubbles.
6. Prebake 2 minutes on a hotplate at 120 °C.
7. Expose 3.5 s under 365 nm ultra-violet light.
8. Wait for 1 minute after exposure to outgas the nitrogen.

9. Hard baking for 1.5 minutes at 120 °C.
10. Rehydration of the resist (10 s for 1um, 50 minutes for 7 um, ideal air humidity is 45-50%).
11. Flood exposure for 30 s, for resist image reversal.
12. Develop in AZ726 MIF photoresist developer for 25 s, followed by extensive rinsing with distilled water.
13. Dry with nitrogen, load back into containers.

The exposure time was calculated from the UV illumination intensity (≈ 14.9 mW.cm-2) of the mask aligner, and it varied from 2.3 to 3.6 seconds for the first exposure, in order to reach a dose of ≈ 45 (mJ.cm^{-2}), optimum for our photoresist.

Exposure time is determined by equation(5-3).

$$\text{Exposure time (s)} = \frac{Dose\left(\frac{mJ}{cm^2}\right)}{Intensity\left(\frac{mW}{cm^2}\right)} \quad (5\text{-}3)$$

Optical microscopy inspection reveals the adequacy of edge line profile. The micrometre-scale electrodes are made of a chromium-gold bilayer (45 nm Au /5 nm Cr) deposited using the multiple-pockets thermal evaporation followed by a standard lift-off process. The second layer is evaporated under a tilt angle θ (**Figure 5-5**). The length W of the gap depends straightforwardly on the height h of the first electrode layer, and the angle θ between the substrate normal and the source directions ((5-1)(5-2)). Typically, we adopt the angles to be 45º,65º or 75º to obtain gaps with different width. The details of the results obtained will be discussed in section 5.1.2.3.

5.1.2.3 Results and characterisation

The fabrication produces a substrate with up to 60 pairs of electrodes depending on the lithographic mask employed, as shown in **Figure 5-6**. The first electrode for all pairs is designed to be one common electrode. Five groups of 12 electrodes are designed to be the 2nd electrodes.

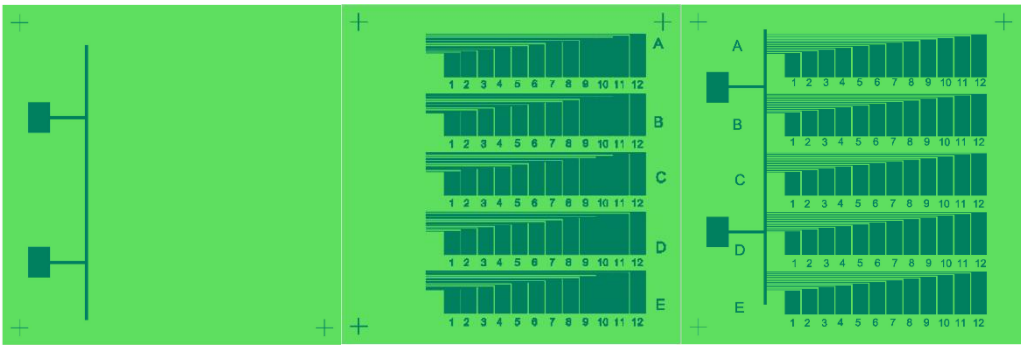

Figure 5-6 Electrodes design for shadow lithography; Left: 1st electrode; Middle: 2nd electrode; Right: Final electrodes configuration.

The geometric effect of the shadow evaporation allows us to reproduce the nanotrench whose width range from 20 nm to 600 nm, along the 10-um length of the pattern. This is achieved by changing the tilt angle and the metal thickness. We used atomic force microscopy (AFM) and scanning electron microscopy (SEM) imaging for calibrating and checking the quality and edges of the nanotrenches (**Figure 5-7**). The width is then determined by taking the cross-section of the trench area. To determine the average width of a nanogap, more than five positions were chosen for each sample as illustrated in **Figure 5-7**.

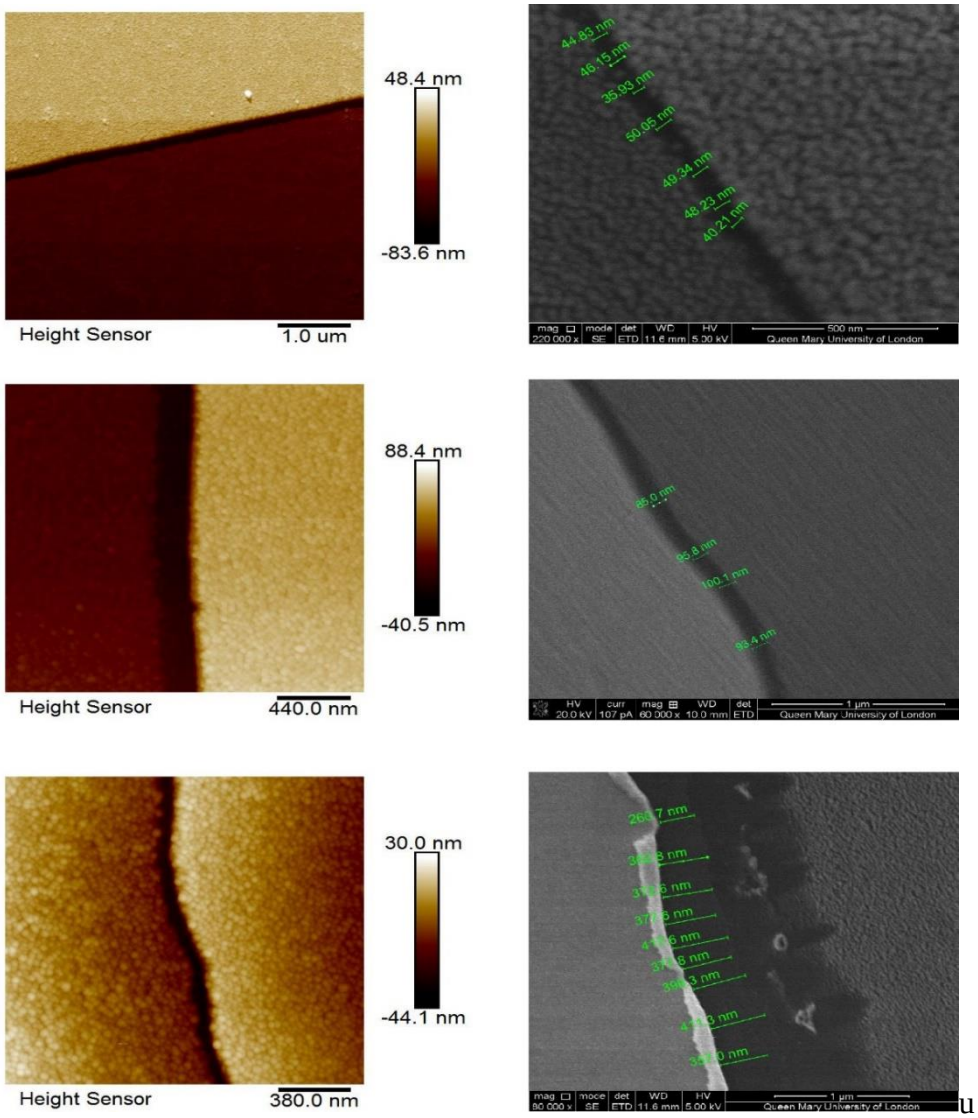

Figure 5-7 AFM and SEM images of various nanotrenches fabricated by shadow lithography: 1&2, AFM and SEM image of nanotrenches of which the average width is 50nm; 3&4, AFM and SEM image of nanotrenches of which the average width is 100nm; AFM and SEM image of nanotrenches of which the average width is 400nm.

Electrical characterisation remained the key characterisation tool for checking the quality of the gaps, expected to exhibit minimal leakage current values. This will be discussed in detail in section 5.1.3.3.

5.1.3 Dielectrophoretic assembly of individual DNA-wrapped carbon nanotubes

5.1.3.1 Principle of Dielectrophoresis

Dielectrophoresis (DEP) has been used to control the deposition of carbon nanotubes between a pair of electrical conductors or to integrate CNTs into a micro- or nanoelectronic system.[5-10] Dielectrophoresis is capable of solving both the separation and assembly problems associated with the fabrication of large-scale nanotube-based electronics, without having to damage or contaminate the carbon nanotubes with chemicals. Moreover, there is an ease for match manipulation of CNTs or other nano structures by DEP.

When a polarizable object is subjected to an electric field, a dipole moment is induced. If the electric field is inhomogeneous, the field strength and thus the force acting on each side of the particle will be different, causing the particle to move with respect to the medium. Depending on the polarizability of the particle compared to that of the medium, the force could push the particle towards regions of high or low electric field, termed positive and negative dielectrophoresis, respectively. This is illustrated in **Figure 5-8** for a carbon nanotube, which is immediately aligned with the field lines and moves perpendicular to the field lines along the gradient. In the case of an alternating electric field (AC), the direction of the force and thus the direction of motion will remain the same even upon field reversal, because the dipole moment will be inverted as well. Furthermore, when the polarizability of the CNTs is greater than that of the liquid, the CNTs move towards the

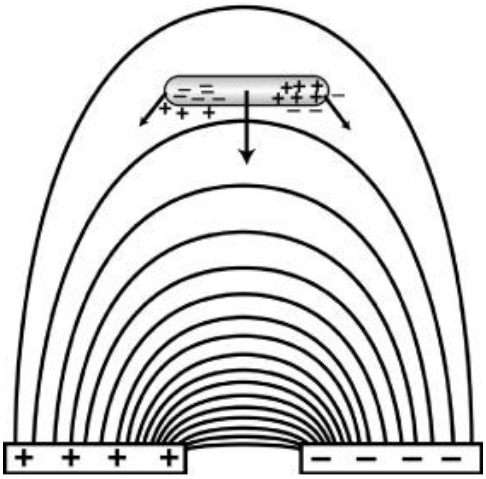

Figure 5-8 Sketch illustrating a carbon nanotube subjected to dielectrophoresis. The nanotube immediately aligns with the field lines and experiences a net force from the ac field.[11]

electrode gap, finally depositing and bridging the gap. During DEP, first one CNT bridges the electrode gap, then a second, third, and so forth will follow. This method can be performed at room temperature with voltages lower than 10V. In addition, a few parameters such as solution concentration, deposition time, AC source amplitude, and frequency can be adjusted to optimise the quality of the aligned SWCNTs. In this section, we present the dielectrophoretic assembly of single-wall carbon nanotubes over the nanotrenches. Different parameters have been tested to achieve a few to one individual nanotube alignment.

To consider only the simplest case, the time-averaged dielectrophoretic force applied on a ballistic nanotube can be expressed as[11, 12]:

$$\vec{F}_{DEP} = \frac{\pi}{6} r^2 * \mathrm{l} * \varepsilon_m * Re\{K_f\} \nabla |E|^2 \qquad (5\text{-}4)$$

Where r is the radius and l is the length of the nanotube, ε_m is the real part of the dielectric constants of the medium, and E is the electric field. For the tube with the long axis aligned with the direction of the electrical field, K_f is then given by:

$$K_f = \frac{\varepsilon_t^* - \varepsilon_m^*}{\epsilon_m^*}, \qquad \varepsilon^* = \varepsilon - i\frac{\sigma}{\omega} \tag{5-5}$$

In the high and low frequency limits, the K_f can be simplified as :

$$\mathrm{Re}\{K_f\} = \begin{cases} \dfrac{\sigma_t - \sigma_m}{\sigma_m}, & \omega \to 0 \\ \dfrac{\varepsilon_t - \varepsilon_m}{\varepsilon_m}, & \omega \to \infty. \end{cases} \tag{5-6}$$

In the low frequency limit the force is independent of the frequency as well as of the permittivity of the nanotube and the medium, while in the high frequency limit the force will be dependent on the permittivity of the nanotube with respect to that of the medium.

The static dielectric constant for semiconducting NTs, ε_s ,and was found to be inversely proportional to the square of the band gap E_G.[13]

$$\varepsilon_s \cong 1 + \left(\frac{\hbar\omega}{5.4 * E_g}\right)^2 \tag{5-7}$$

where $\hbar\omega \approx 5$ eV is the energy of the plasma oscillation along the nanotube axis.[14] Translating band gaps into dielectric constants according to equation (5-7), we obtain finite dielectric constants for semiconducting SWNTs with $\varepsilon_s = 5\ \varepsilon_0$. Metallic and small band gap semiconducting nanotubes have been predicted to have infinite permittivity. Considering the water has a dielectric constant of $\varepsilon_m = 80\ \varepsilon_0$. It is only possible to align the metallic carbon nanotubes at high frequency due to the negative dielectrophoretic force of semiconducting tubes. This is in agreement with the literatures.[15]

However, in the low frequency, the dielectrophoretic force mainly depends on the conductivity of nanotubes and medium. It is reported that conductivity of s-SWNT is dominated by the surface conductivity rather than intrinsic conductivity.[16] Since our SWCNTs are wrapped by DNA molecules, the conductivity of the solvent may be comparable to the intrinsic conductivity of s-SWNT. Therefore, s-SWNTs experience a weak dielectrophoretic force at a lower frequency.

From this discussion, it is clear that both at low frequency and high-frequency limit, the DEP assembly process is not effective. As the frequency is increased, the DEP force will increase, and then at some frequency, it will start to decrease and become negative.[17]

5.1.3.2 Operations of Dielectrophoretic assembly

SWCNTs were prepared in aqueous solution as discussed in section 3.2.1. The solution is then treated with a 24-hour dialysis in ultrapure water to remove the salt. The step is of critical importance as free ions in solution will damage the dielectric of water thus weakening the dielectrophoretic force. Solutions were diluted with ultrapure water to obtain uniformly diluted solutions with concentrations from 0.1 μg/ml. The assembly of SWCNTs by DEP, and the electrical characterisation of assembled SWCNTs was conducted on a probing station (PS-100, Lakeshore) and a semiconductor characterisation system (Keithley, 4200SCS). A tiny volume (3 μl) of the solution was placed in the electrode gap through a micropipette. For metallic CNTs, the magnitude of the applied voltage was 5 V peak-to-peak (Vp–p), and the frequency was fixed at 10 MHz as previously reported.[12] For semiconducting CNTs, the magnitude of the applied voltage was 5 V peak-to-peak (Vp–p), and the frequency was fixed at 100 kHz.[17] A programmable DDS function generator (TG1010A, TTI) was used to generate the required ac electric field for CNT deposition. The I–V characteristics of assembled CNTs were measured using probing station and a semiconducting measurement unit (Keithly 4200-CS).

5.1.3.3 Results and Discussion

As is shown in previous section, nanotrenches, uniform all along the micrometric length of the gap with significantly high reproducibility and efficiency, were obtained with a high success rate. It is vital to ensure the electrodes are insulating from each other to guarantee an effective circuit along the nanostructures instead of leaking.

For an applied bias up to 1 V, sub 10 pA leakage currents were systematically measured, the electrodes sustain high bias voltages (up to 5 V) at room temperature without being destroyed or presenting shorts. **Figure 5-9** presents current versus voltage data in 1 volt sweep range under ambient conditions.

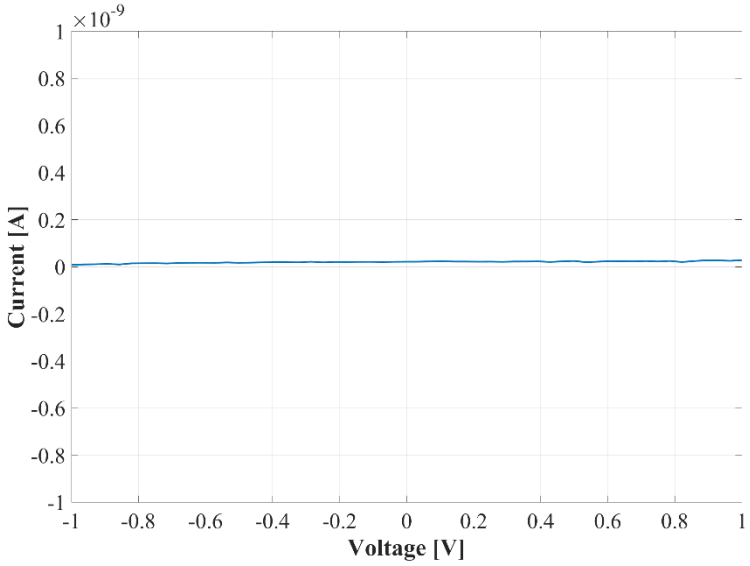

Figure 5-9 Current-Voltage characteristics of empty nanotrench electrodes in ambient conditions

With the technique of dielectrophoresis, metallic SWCNTs were deposited on the electrodes (**Figure 5-10**). Compared to the height hindrance from the electrodes in AFM topography images, SEM offers a better contrast to identify the nanotubes on the nanotrenches.

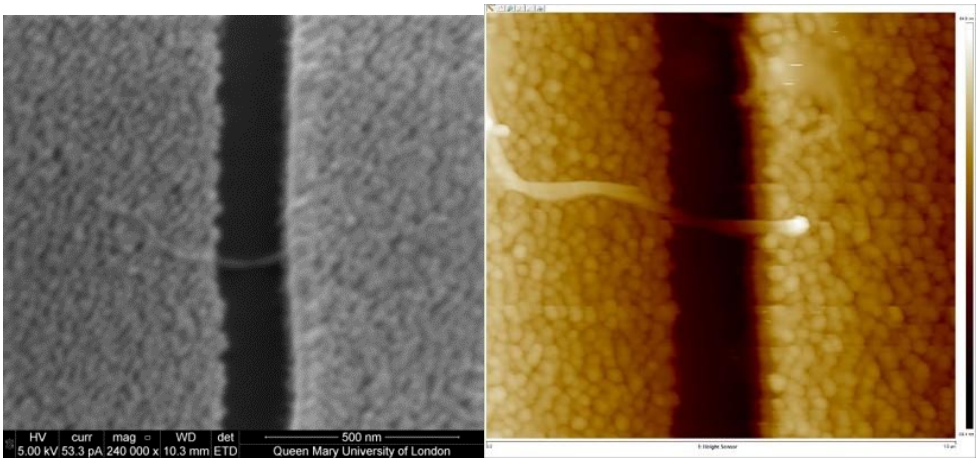

Figure 5-10 Left: SEM image of a metallic SWCNT aligned on the nanotrench; Right: AFM topography of the CNT aligned on the nanogap

Current-voltage data was then recorded on 40 pairs electrodes (100 nm gap) on the same substrate.(**Figure 5-11**) Among them, 35 out of 40 show the on current larger than leakage current indicating a 87.5% yield of tubes alignment.

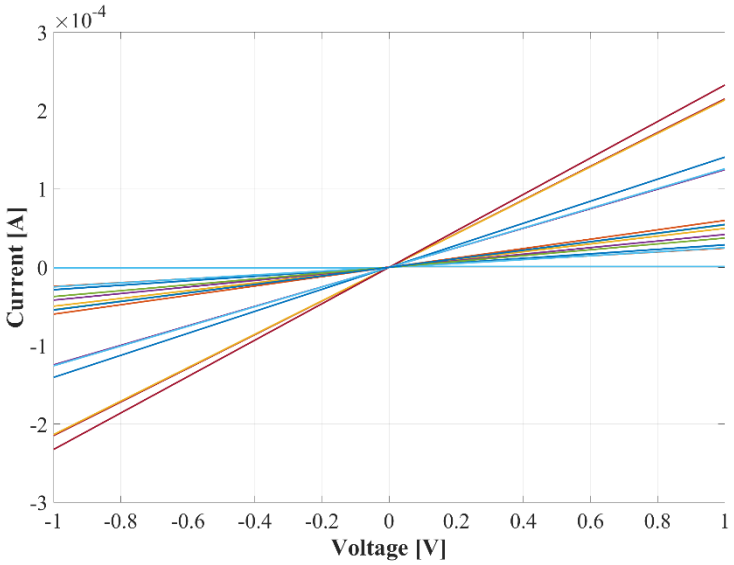

Figure 5-11 Current-Voltage characteristics of metallic CNTs on nanotrenches separated by 100 nm gap in ambient conditions

The average resistance of all the tubes was calculated to be 46.8 kΩ, which is close the theory value of an ideal ballistic 1-D conductor.[18] The fluctuation of resistance may come from the different contact resistance or different defects among the aligned

nanotubes. The minimum resistance measured is 3.8 kΩ which is reasonable since more than one CNTs have been assembled on the same pair of electrodes.

On the other hand, semiconducting nanotubes have been deposited on electrodes (100 nm gap) and characterised in the similar method in addition. The electrical response shows non-linear Schottky contact, indicating the semiconducting property of the assembled SWNTs. [19](**Figure 5-12**)

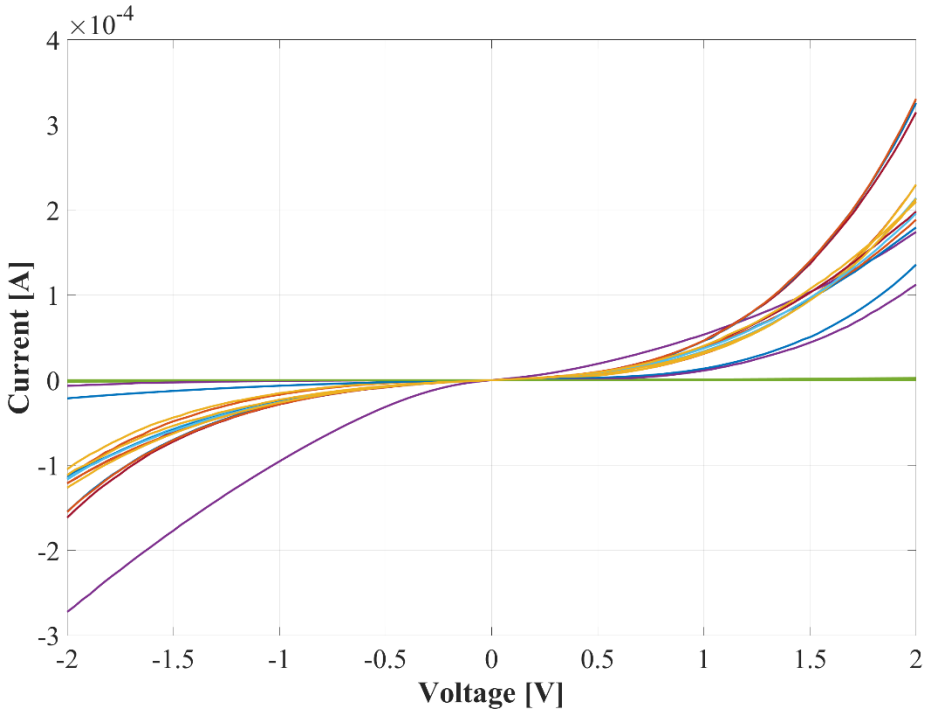

Figure 5-12 Current-Voltage characteristics of semiconducting CNTs on nanotrenches (100 nm gap) in ambient conditions

This measurement further emphasizes the wide range of current from pA to mA that can be observed, illustrating the versatility of nanotrench electrical contacts, being compatible for studying a broad variety of nanostructures for molecular electronics.

5.1.4 Conclusions

In this section, we have discussed the fabrication of a nano gap (10-300nm) between metallic electrodes by means of shadow evaporation techniques. The process is simple and easily scalable for high throughput fabrication, as it uses standard optical lithography techniques and allows parallel processing of many junctions. The nanotrenches are suitable for use in micro and nanoelectronics where the parallel multi-devices assembly is important.

Dielectrophoretic assembly of individual carbon nanotubes over the nanogap was performed based on the electrodes made via the above method. The device functionality was demonstrated by measuring the I–V transport.

One major factor that limits the application of this method for molecular junctions based on SWCNTs, is the gap size. As illustrated in equation (5-1), to pursue a larger gap, the shadow evaporation demands either the first electrode to be high or a large tilt angle. Meanwhile, according to the equation (5-2), the thickness of the second electrode will decrease while increasing the tilt angle during shadow evaporation without a change in the height of first electrode.

In both cases, the height difference between first and second electrodes are broadened (up to 50nm) which hinders the assembly of molecular junctions. The suspended configuration of CNTs/junctions above the electrodes results in a poor contact between electrodes. Further annealing may improve the situation while more work is required.

5.2 Nanolithography based on Atomic Force Microscopy

5.2.1 Principle

In this method, we are going to use the nanoscratching mode of AFM, and dry etching including O_2 plasma to create binding sites for DNA wrapped SWCNTs on Silicon wafer covered with thermal oxide. A pre-patterned Cr/Au electrode is deposited on highly doped silicon substrates with a 300-nm thick thermal oxide layer. A mixture of PEG-silane (2- [methoxy (polyethylene oxy)-propyl]-trimethoxysilane) and PEG-thiol ($HS{-}(CH_2)_{11}{-}(C_2H_6O_2)_3{-}OH$) in anhydrous toluene allow for the simultaneous passivation of the SiO_2 surface and the Au electrodes. The PEG layer was coated with poly (methyl methacrylate) (PMMA) resist, 60 nm thick. The AFM tip will then be used to scratch the resist and create trenches in the PMMA covered silicon chip: see **Figure 5-13**.

By exposing the samples to Oxygen plasma, the residual PMMA in the pattern and the exposed PEG-silane are then removed, leaving only exposed silicon dioxide surface. This will leave the patterned area hydrophilic (exposing SiO_2) while the remaining area will be DNA-repellent which exhibits high selectivity for DNA binding.

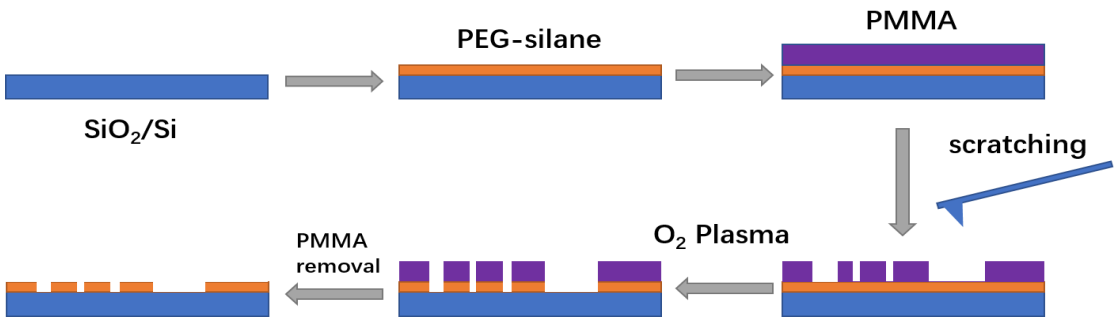

Figure 5-13 Schematic of PEG surface functionalisation with AFM-based scratching

5.2.2 Methods

Procedure for silanization is summarised as below:

1) clean samples in piranha solution (O_2 plasma if prepattern electrode exists), then rinse in water, then in EtOH and blow dry
2) Prepare a solution with: 300 µl of PEG-silane (MW 500 Fluorochem) in ca 25 mL of Anhydrous Toluene; together with 100 µM PEG-thiol ($HS{-}(CH_2)_{11}{-}(C_2H_6O_2)_3{-}OH$) if the substrates had pre-patterned Au electrodes (PEG-silane passivated the SiO_2 surface, whereas PEG-thiol passivated the Au).
3) Add 30 µl of acetic acid as a catalyst
4) Add samples in the solution: seal with parafilm and cover with aluminium foil
5) Incubate overnight (24h)
6) Rinse in Acetone, then EtOH and blow dry

PMMA coating

Samples with PEG are coated with PMMA by spin coating. PMMA (120,000, MW) is dissolved in anisole at a concentration of 2%. According to product manual, the concentration of PMMA in solutions indicates the thickness of the PMMA film (shown in **Figure 5-14**).

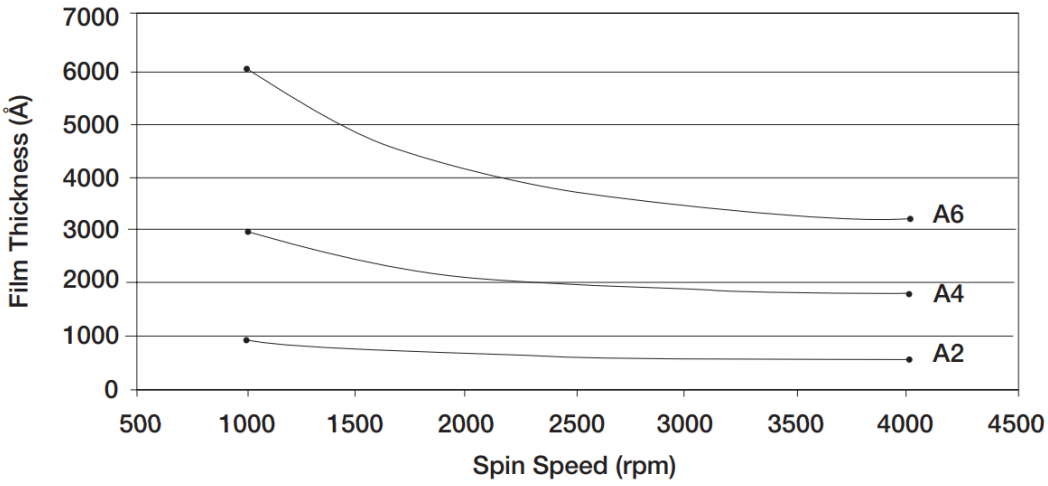

Figure 5-14 Film Thickness versus spin speed for PMMA in anisole: 2% (A2), 4% (A4) and 6% (A6).[20]

Nanoscratching

Atomic Force Microscopy tip can simulate a sharp single asperity scratch over a surface including polymer film.[21, 22] In this work, the nano-scratching was performed by the Atomic Force Microscopy (Dimension Icon, Bruker) with the nanomanipulation software module(NanoMan, Ver 5.0). TESPA (Bruker) probe was selected for the stiff spring constant as 40N/m. A straight nanogroove with the desired length was generated by the tip on the PMMA film at a speed of 1μm/s at a loading force of 25nN. The force and speed is controlled by the feedback loop of AFM.

5.2.3 Results and discussion

As is shown in Figure 5-14, the thickness of PMMA layer can be tuned between 50 to 400nm by changing the concentration of the PMMA solution and spin coating parameters. Topography images of the PMMA film and nano-groove array after nano scratching are shown in **Figure 5-15**. Cross-sections of the gaps are provided **Figure 5-16**. Debris were pile-up in the two sides of the scratched lines which behave as elevated. Limited by the tip radius, the actual width of the gap cannot be acquired accurately by AFM. Furthermore, the observed depth of the scratch is smaller than the actual one as ~ 10 nm. In this way, the control over plasma etching rate is critical when transferring the pattern to the substrate.

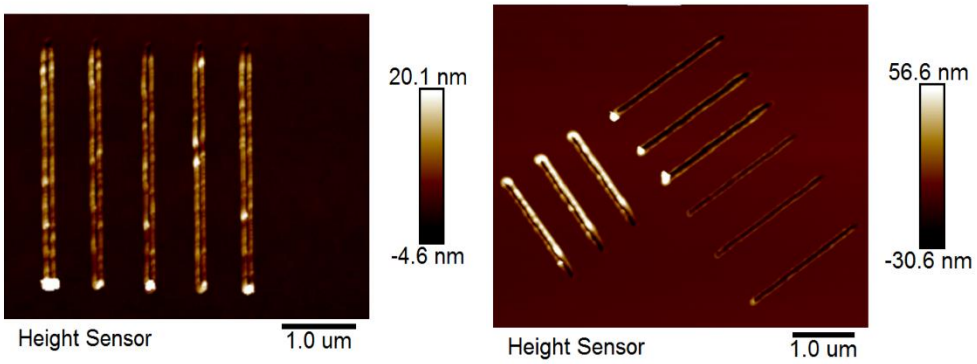

Figure 5-15 AFM of pattenred obtained via nano scratching: Left: an array of lines scratched by AFM tip on 49.2nm thick PMMA layer with same condition; Right, two arrays of lines scratched by AFM tip on 49.2nm thick PMMA layer with different scratching forces;

Figure 5-16 Topographical profiles obtained from AFM topographical images of the trenches : Upper, cross section image of sample from left sample in **Figure 5-15**; bottom, cross section image of right sample in **Figure 5-15**.

By far, we have showed the fabrication of nano-pattern on the PMMA films by nanoscratching based on AFM. However, the O_2 plasma utilized in the project failed to produce a constant plasma especially for the sensitive thickness. Plasma treatment usually resulted in a completely clean substrate or unchanged PMMA films. No preference of deposition of DNA-wrapped CNTs could be observed. Consequently, futher study should be done the effect of plasma on PMMA. Beyond that, the technique of nano-scratching could apply to other fields involving nano-patterning such as electrodes fabrication at 30-1000 nm scale. This could beat e-beam lithography with a much more convenient fabrication procedure and lower cost while resulting in similar resolution.

References

1. Philipp, G., et al., *Shadow evaporation method for fabrication of sub 10 nm gaps between metal electrodes.* Microelectronic Engineering, 1999. **46**(1): p. 157-160.
2. Bai, J.G., W.-H. Yeo, and J.-H. Chung, *Nanostructured biosensing platform-shadow edge lithography for high-throughput nanofabrication.* Lab on a chip, 2009. **9**(3): p. 449-55.
3. Dayen, J.F., et al., *Nanotrench for nano and microparticle electrical interconnects.* Nanotechnology, 2010. **21**(33): p. 335303-335303.
4. MicroChemicals. *Processing Image Reversall Resists (Manual)*. Product instructions 2003-9-25 [cited 2017 09-04]; technical information]. Available from: http://www.microchemicals.com/technical_information/image_reversal_resists.pdf.
5. Zhang, Z.B., S.L. Zhang, and E.E.B. Campbell, *Dielectrophoretic behavior of ionic surfactant-solubilized carbon nanotubes.* Chemical Physics Letters, 2006. **421**(1-3): p. 11-15.
6. Vijayaraghavan, A., et al., *Ultra-large-scale directed assembly of single-walled carbon nanotube devices.* Nano Letters, 2007. **7**(6): p. 1556-1560.
7. Ramón-Azcón, J., et al., *Dielectrophoretically aligned carbon nanotubes to control electrical and mechanical properties of hydrogels to fabricate contractile muscle myofibers.* Advanced materials (Deerfield Beach, Fla.), 2013. **25**(29): p. 4028-34.
8. An, L. and C. Friedrich, *Dielectrophoretic assembly of carbon nanotubes and stability analysis.* Progress in Natural Science: Materials International, 2013. **23**(4): p. 367-373.
9. Blatt, S., et al., *Influence of structural and dielectric anisotropy on the dielectrophoresis of single-walled carbon nanotubes.* Nano Lett, 2007. **7**(7): p. 1960-6.
10. Vijayaraghavan, A., *Bottom-up assembly of nano-carbon devices by dielectrophoresis.* Physica Status Solidi (B) Basic Research, 2013. **250**(12).
11. Maria, D. and B. Peter, *Dielectrophoresis of carbon nanotubes using microelectrodes: a numerical study.* Nanotechnology, 2004. **15**(8): p. 1095.
12. Krupke, R., et al., *Separation of Metallic from Semiconducting Single-Walled Carbon Nanotubes.* Science, 2003. **301**(5631): p. 344-347.
13. Benedict, L.X., S.G. Louie, and M.L. Cohen, *Static polarizabilities of single-wall carbon nanotubes.* Physical Review B, 1995. **52**(11): p. 8541-8549.
14. Pichler, T., et al., *Localized and Delocalized Electronic States in Single-Wall Carbon Nanotubes.* Physical Review Letters, 1998. **80**(21): p. 4729-4732.
15. Duchamp, M., et al., *Controlled positioning of carbon nanotubes by dielectrophoresis: Insights into the solvent and substrate role.* ACS Nano, 2010. **4**(1): p. 279-284.
16. Krupke, R., et al., *Surface Conductance Induced Dielectrophoresis of Semiconducting Single-Walled Carbon Nanotubes.* Nano Letters, 2004. **4**(8): p. 1395-1399.
17. Sarker, B.K., S. Shekhar, and S.I. Khondaker, *Semiconducting Enriched Carbon Nanotube Aligned Arrays of Tunable Density and Their Electrical Transport Properties.* ACS Nano, 2011. **5**(8): p. 6297-6305.
18. Kasumov, A.Y., et al., *Electrical resistance of a single carbon nanotube.* EPL (Europhysics Letters), 1996. **34**(6): p. 429.
19. Joon, S.S., et al., *The precise self-assembly of individual carbon nanotubes using magnetic capturing and fluidic alignment.* Nanotechnology, 2009. **20**(32): p. 325607.
20. MicroChem. *NANO PMMA and Copolymer ™ (product manual)*. 2001; Available from: http://microchem.com/pdf/PMMA_Data_Sheet.pdf.
21. Yan, Y.D., et al., *Effects of scratching directions on AFM-based abrasive abrasion process.* Tribology International, 2009. **42**(1): p. 66-70.
22. Blach, J., et al., *A mechanistic approach to tip-induced nano-lithography of polymer surfaces.* Thin solid films, 2004. **459**(1): p. 95-99.

Chapter 6 Boron Nitride Nanotubes

6.1 Background

With similar structure to carbon nanotubes, boron nitride nanotubes (BNNTs) (see **Figure 6-1**) have drawn attention due to their potential in mechanical, electrical, biological applications. First predicted by Rubio et al. in 1994 [1] and later fabricated by Chopra et al. in 1995 [2], BNNTs have been studied for their characteristics based on their structure. Both CNTs and BNNTs are strong light-weight nanomaterials with Young's modulus greater than 1 TPa [3, 4]; moreover, it has been shown that both tubes have a good thermal conductivity[5, 6]. With the carbon atoms replaced by nitrogen and boron atoms in the cylinder structures, BNNTs are very different compared to CNTs. Unlike carbon nanotubes, which can be metallic conductive or semiconducting depending on their chirality and radius, BNNTs are always considered as insulators with a band gap of around 5.5 eV[7], exhibit higher resistance to oxidation and greater thermal stability. Furthermore, the alternating positions of boron and nitrogen atoms provide intrinsic piezoelectricity[8]. These intriguing properties render BNNTs as ideal candidates for a variety of applications such as mechanical and thermal reinforcements for polymer, ceramic, and metallic composites, self-cleaning materials, sensors as well as for biology/medicine. However, several factors are limiting the application of BNNTs, including their purification, dispersion and controlled functionalisation, in particular from solution.

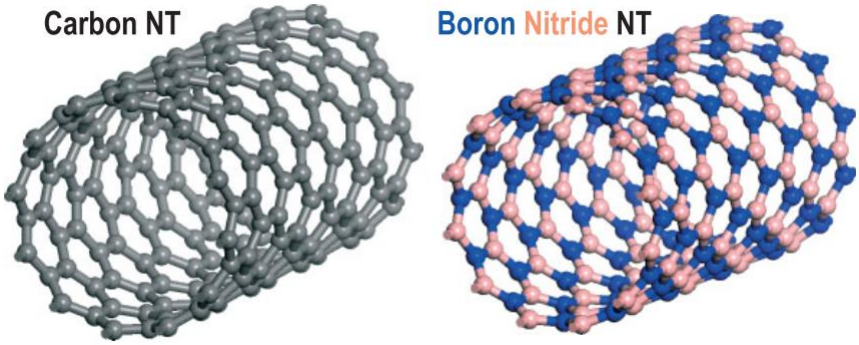

Figure 6-1 Comparative structural models of single-layered carbon and boron nitride nanotubes (CNTs and BNNTs, respectively). The alternating B and N atoms are shown in blue and pink, respectively, on the BNNT model.[9]

6.1.1 Purification and dispersion

Since the discovery of BNNTs, various methods for their synthesis have been investigated including but not limited to: ball-milling annealing methods, [10, 11] catalyst-based chemical vapor deposition (CVD),[12, 13] arc-discharge,[2, 14] laser vaporization,[15, 16] plasma-enhanced pulsed laser deposition (PLD),[17] and catalyst-free pressurized vapor/condenser methods[18]. Although mass production of BNNTs has become feasible, impurities are formed at the same time depending on the employed synthesis techniques; these impurities can come in the form of boron nitride nanoparticles, amorphous and crystalline BN or boron nanoparticles in a BN shell. Bulk BNNTs with high purity are snow-white in appearance [19], while brownish or grey samples provide an indication of impurities within the BNNT fibrils. The presence of these impurities can potentially degrade the advantageous properties of the BNNTs, although additional experiments are needed to compare the properties of raw and purified BNNTs. For example, impurities can act as defect sites at which failure can occur under mechanical testing. Furthermore, impurities could be toxic for biomedical

applications. Hence, purification may be a critical step for fundamental and applied research on BNNTs.

Several approaches have been explored to purify as-grown BNNTs contaminated with metallic catalysts, unreacted precursors and other non-BNNT boron nitride (BNx) by-products, etc. Overall, there are three common categories of purification processes: (i) acid treatment [20], (ii) thermal oxidation/annealing in the air [21], in addition to (iii) surfactant or polymer wrapping separation via functionalisation [22, 23].

For example, acid treatment is aimed at the removal of metallic particles and boron nanoparticles, which will be oxidised to the corresponding salt and boron acid, both of which are soluble in water. As compared to metallic particles, BNx impurities would be more difficult to remove since they are chemically stable and oxidation resistant. Heat treatment (up to 800 ℃ in air) as a purification process is introduced to oxidise BNx into B_2O_3 which can be removed by water. Lastly, surfactant/polymer wrapping is utilised similar to what been done on CNTs to modify the interfacial tension of various species in BNNT sample, enabling the removal of impurity. Even BNNT is thermally stable and inert to oxidisation, long time acid treatment and high-temperature treatment still could damage the nanotube structure introducing more defects. As a result, wrapping method is much preferable for its less destructive products.

Inadequate dispersion of nanomaterials in liquids is a crucial issue that limits many applications and when overcome, will enable further processing and handling. Because of their super hydrophobicity, BNNTs tend to interact by van der Waals forces and aggregate in aqueous liquids. Especially the long BNNTs tend to entangle with each other. It is therefore important to develop techniques to disperse and stabilise BNNTs

in aqueous and non-aqueous media for applications in nanocomposite, and biomedical areas.

The dispersion of pure BNNTs (without chemical functionalisation) with a series of solvents was recently studied based on the comparison of thermodynamic Hansen parameters [24]. The theory is used to predict whether one material will dissolve in another and form a solution. Each molecule is given three Hansen parameters measured in MPa based on energy from dispersion forces between molecules, dipolar intermolecular forces between molecules and hydrogen bonds between molecules. It has been shown that solvents tend to dissolve solutes with parameter values similar to them. It was found that dimethylacetamide (DMAc) can produce the most stable and uniform dispersion of BNNTs, followed by N, N-dimethyl-formamide (DMF), acetone, and N-methyl-2-pyrrolidone (NMP). In addition, co-solvents were investigated to enhance the solubility as compared to a single solvent. Moreover, dispersion of BNNTs in polar solvents including toluene, hexane and ethanol has been improved. As is shown in **Figure 6-2**, this approach enables the use of various organic solvents and polymers for the fabrication of BNNT composites without breaking the high aspect ratio and the sp^2 nature, which accounts for the extraordinary properties.

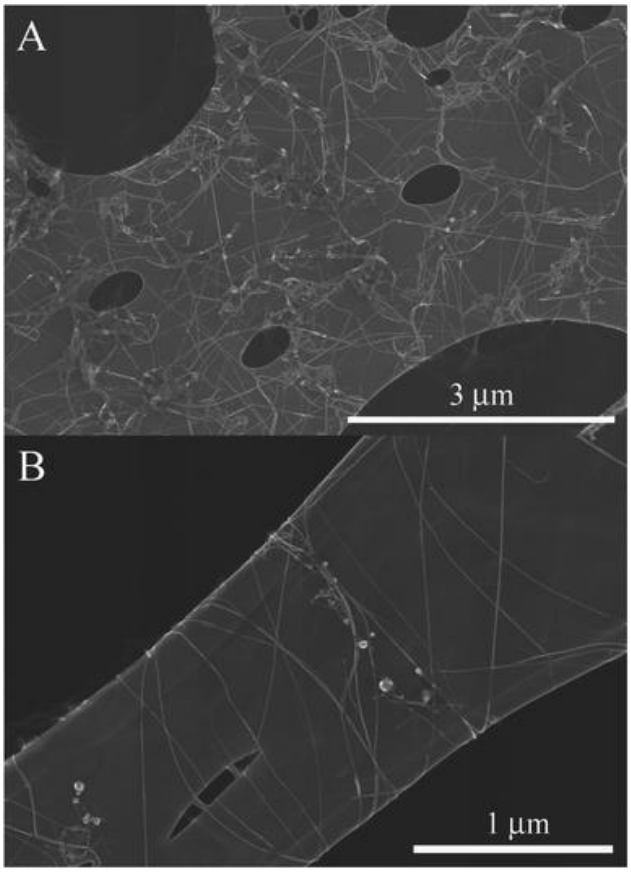

Figure 6-2 Representative SEM images of BNNTs dispersed in DMAc after mild sonication showing a large area covered with nanotubes (A) and a magnified area showing the nanotube structure is intact after sonication (B).[24]

In addition to polar organic solvents, functionalisation has become a customary practice to stabilise BNNTs in aqueous media. Two main approaches, namely covalent and noncovalent functionalisation have been established by many research groups. In the following sections, noncovalent and covalent functionalisation will be discussed as they are relatively promising for large scaled applications.

6.1.2 Functionalisation

6.1.2.1 Covalent functionalisation of BNNTs

The covalent functionalisation of BNNTs has been challenging due to the fact that the tubes are chemically inert. With all the boron and nitrogen atoms bonded to each other,

functional groups can only be introduced at defective points or terminal atoms. Based on the chemistry of the B-N bond, amino groups were widely adopted in the functionalisation. Several methods have been developed for producing amino groups on BNNTs such as heating BNNTs with amine terminated poly(ethylene glycol) which formed ionic bonds with boron sites on BNNTs [25], aggressive non-equilibrium ammonia glow plasma treatment [26], cycling treatment of BNNTs with dimethyl sulfoxide (DMSO) to peel B-N bond [27], and by fluorination during the BNNTs synthesis [28]. Recently, Ciofani et al. have demonstrated the covalent approach to functionalise BNNTs by grafting amino functional group on the surface of BNNTs [29]. In their approach, BNNTs were sonicated in nitride acid to introduce -OH groups at the surface of BNNTs via a strong oxidation process. The oxidised BNNTs were further sonicated in 3-aminopropyltriethoxysilane (APTES) which reacts with the hydroxyl group on the surface of BNNTs [30], thus resulting in free amino groups on the nanotubes side walls allowing further conjugation to form BNNT complexes.

Recently, Shin et al. have shown that the reduction of BNNTs can significantly enhance their chemical reactivity based on density functional theory calculations[31]. A BNNT is reduced first by sodium naphthalide salt in tetrahydrofuran (THF) solution. Using 1-bromohexane, covalent alkylation of BNNTs is achieved and confirmed by the thermogravimetric analysis.

6.1.2.2 Non-covalent functionalisation of BNNTs

Typically, noncovalent functionalisation is achieved based on Van der Waals forces, hydrogen bonding or π-stacking interaction on the nanotube wall as reported on carbon nanotubes. Compared to covalent bonding, non-covalent functionalisation is likely to keep the cylinder surface structure of BNNTs intact. In this context, the π-stacking

interaction between BNNTs and conjugated polymers or aromatic molecules is considered as the effective approach for BNNT dispersion in solvents. This is because of the presence of π-electrons on the hexagonal BN network of BNNTs with the π-electrons localised at N atoms (polarised or ionic B-N bonds). Depending on the wrapping materials, BNNTs have been dispersed in organic solvents or aqueous solution. Zhi et al. have reported that they dissolved BNNTs in several organic solvents by wrapping with poly[m-phenylenevinylene-co-(2,5-dioctyloxy- p-phenylenevinylene)] (PmPV). However, the PmPV-wrapped BNN are insoluble in water, ethanol, etc. [32]

BNNTs in aqueous solutions tend to form bundles and inhomogeneous aggregates. This is limiting the potential biological applications which involve aqueous media. By far, several approaches have been developed to address this problem. Xie et al. firstly reported that BNNT can be solubilised via functionalisation with amine-terminated oligomeric poly(ethyl glycol)(PEG_{1500N}, **Figure 6-3**)[25]. The functionalised BNNTs are soluble in water and organic media as well compatible with $PEG_{1500N.}$ Later, Wang et al. presented BNNT functionalised with an anionic perylene derivative, namely perylene-3,4,9,10-tetracarboxylic acid tetrapotassium salt (PTAS) through π stacking[33]. PTAS functionalisation affords a well-controlled modification of nanotube surfaces with the carboxylate functional groups and thus imparts aqueous solubility to BNNTs. In addition to that, Yu et al dispersed BNNTs in aqueous solution with the help of ionic surfactants-ammonium oleate[23]. The mixture is reported to be stable for several months. Moreover, Fourier Transformed Infrared Spectroscopy (FTIR) and photoluminescence spectroscopy (PL) analysis of the solution indicated unchanged intrinsic properties of BNNTs.

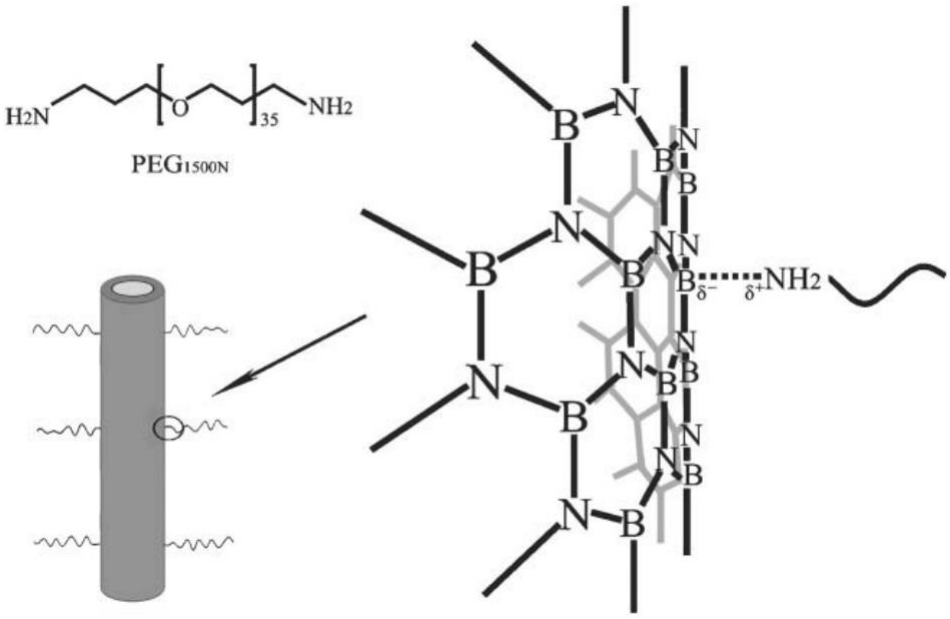

Figure 6-3 Schematic of Amine-terminated oligomeric poly(ethylglcol)(PEG_{1500N}), BNNT wrapped by PEG_{1500N} and noncovalent bond between boron atom and amine group [25]

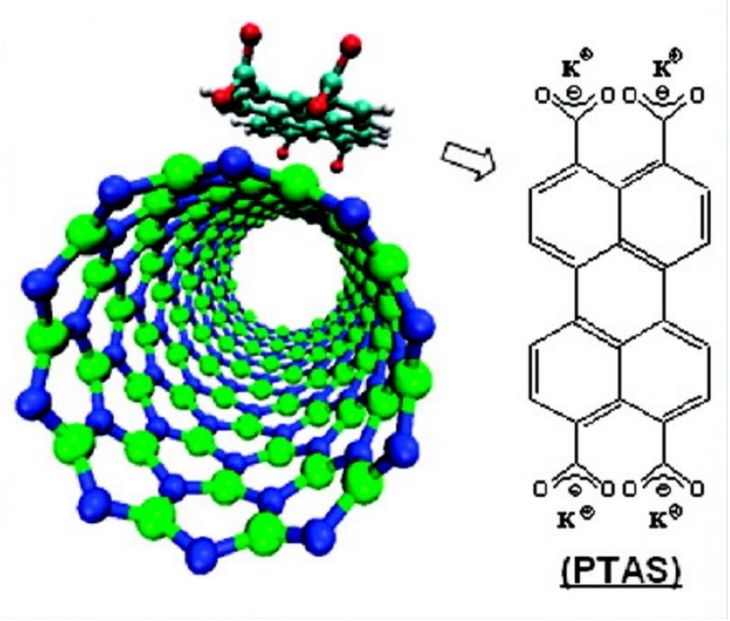

Figure 6-4 Schematic of PTAS functionalisation of BNNTs [23]

Inspired by the natural biological polymers, Zhi et al. assembled boron nitride nanotubes via DNA wrapping[34](shown in **Figure 6-5**). Salmon DNA was heated with deionized water up to 90℃° for 50 minutes; equivalent weight BNNTs were added to the solution and sonicated in water-bath for 3h. According to TEM investigations, a

layer of 5-20 nm thick amorphous DNA was found wrapping the BNNTs. By using thiol-functionalised DNA, the authors of this work could assemble the BNNTs on pre-patterned surfaces taking advantage of thiol-Au chemistry. Recently, Liang has investigated the effect of the type of polynucleotides and the radius of BNNT on wrapping.[35] They found that the interaction between polynucleotides and BNNT(9, 9) is larger than that between polynucleotides and BNNT(5, 5), which leads to the fact that dispersion of BNNT(9, 9) is better than that of BNNT(5, 5) with the assistance of polynucleotides in aqueous solution.

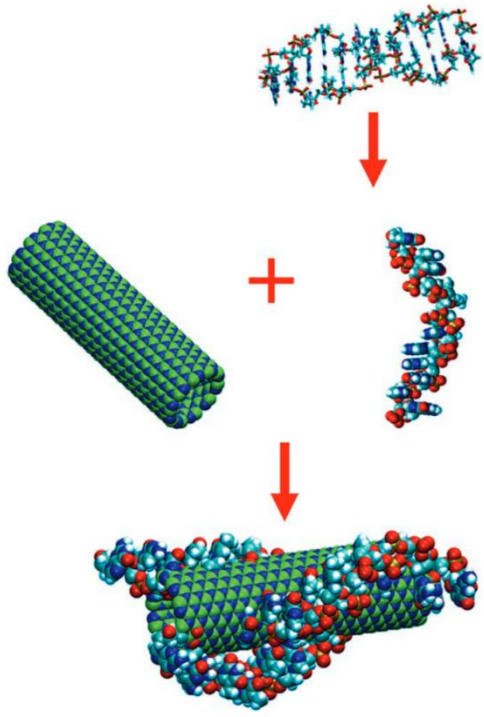

Figure 6-5 The process of fabrication of the DNA–BNNT hybrid[34].

6.1.3 Applications

Various applications of BNNTs have been explored since the first report of their synthesis. Due to their excellent chemical inertness, high thermal stability, strong mechanical properties and electrical insulating properties, BNNTs are good candidates as nanocomposites for mechanical and electronic applications. Zhi et al. initiated the works on polymeric composites of BNNTs.[36] Various reports have been made on the improvement in polymers' physical properties, including their elastic modulus and thermal conductivity [19]. Moreover, it was found that fracture strength, fracture toughness and hardness of ceramics can be increased with small additions (0.5 wt%) of BNNTs[37].

Additionally, applications based on individual BNNTs have been explored at the nanoscale. Yu et al. presented a highly sensitive humidity sensor using Au-decorated BNNTs.[38] The adsorption and desorption tests indicate that the Au-decorated boron nitride nanotube (Au-BNNT) has a fast and sensitive response and recovery to relative humidity at room temperature. Moreover, the use of BNNTs as gas sensors has been studied computationally.[39, 40]

6.2 DNA wrapping of Boron Nitride Nanotubes

6.2.1 Principle of DNA wrapping

Despite Zhi's report of the dispersion of Boron Nitride Nanotubes by DNA wrapping in 2007[41], the mechanism and wrapping parameters have not been studied throughout. Furthermore, the denatured DNA used in the wrapping had significantly affected the topography of the BNNTs potentially limiting the further application. Most importantly, discrete dispersion of individual BNNTs via DNA wrapping has not been reported yet. Therefore, it is still a challenge to control the dispersion of individual BNNTs in aqueous solutions in order to then ideally control their in-solution assembly into heterostructures of interest in materials science, with applications, ranging from biosensors, chemical sensors and fillers as nano composites.

In this chapter, we present a method to wrap individual Boron Nitride Nanotubes with two types of single stranded DNAs (ss-DNA). Bundled BNNTs were effectively separated and dispersed in water by sonication. Strong interactions between DNA and BNNTs were documented and investigated. Optical absorption and fluorescence spectroscopy, as well as AFM investigations, provided evidence for individually dispersed boron nitride nanotubes. **Figure 6-6** shows the schematic of the process employed for the DNA-wrapping of our BNNTs.

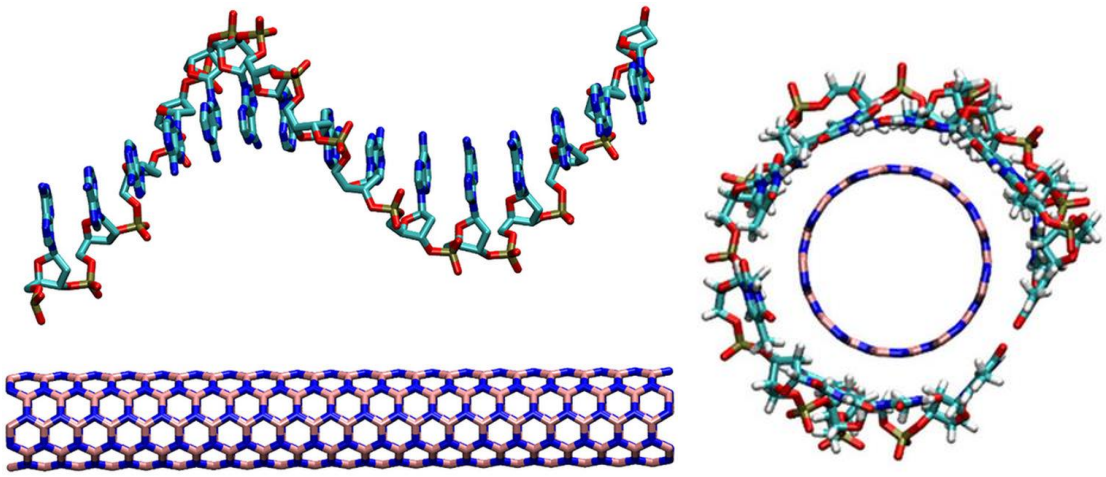

Figure 6-6 Left: The polynucleotides molecule and BNNTs are shown by licorice model; Right: simulated wrapping conformation of polynucleotides T15 on the BNNT(9,9).[35]

6.2.2 Materials and methods

Catalyst-free BNNTs (BNNT P1-Beta) were purchased from BNNT LLC and used as received. DNA and amino-modified DNA were ordered from Integrated DNA Technologies Inc. Inspired by previous work on SWCNTS, two sequences for wrapping were employed, namely $(GT)_{20}$ as GTG TGT GTG TGT GTG TGT GTG TGT GTG TGT GTG TGT GTG T and $(GTT)_3G$ as GTT GTT GTT G. Amino-modified DNA was modified at 5-end based on the two sequences above. Filters (pore size 5 μm) were ordered from Millipore Company. An AFM (Bruker Icon Dimension) was used to characterise the BNNTs. The UV/Vis absorption experiments were carried out on a PerkinElmer Lambda 35 spectrometer.

In a typical dispersion experiment, 1 mg of BNNT powders were suspended in 1 mL aqueous DNA solution (1 mg mL^{-1}, 0.1 M NaCl). The mixture was sonicated (VWR, ultrasonic cleaner) in an ice-water bath for 50 s at a power level of 3W and cool for 1 minute to avoid overheating. For $(GTT)_3G$, the process was repeated for 3 times to obtain a better dispersion. For $(GT)_{20}$, the process was repeated for 6 times to obtain

similar appearance (cloudy solution). After sonication, the samples were divided into 0.1 mL aliquots and centrifuged (Heraeus Biofuge Pico) for 90 min at 17,000 g to remove insoluble material, leaving DNA-dispersed boron nitride nanotube solutions at a mass concentration around 0.5 mg*mL^{-1}. The collected solution was then filtered using the filter column to remove large impurities (boron, BNx, etc.). Moreover, excess DNA strands are removed from the solution by centrifuge filtering or dialysis.

6.2.3 Results and characterisation

To confirm the dispersion of BNNTs as a result of DNA wrapping, a series of control experiments have been performed by separately dissolving BNNTs in water, DMF, and a surfactant solution (SDS). All the mixtures were treated with the same procedure mentioned in section 6.2.2. It can be seen from **Figure 6-7** that all the DNA-wrapped BNNTs solutions exhibit a uniform cloudy appearance (with some unwrapped clusters can be seen in the $(GT)_{20}$ case). For the BNNTs sonicated in water (0.1M NaCl), large aggregates and filiform objects were found. For DMF, which is predicted to be a candidate solvent for BNNTs[24], the poor dispersion was obtained together with some aggregates. The comparison strongly indicates that DNA-wrapping provides an effective method to disperse BNNTs; this leads us to explore more this method and characterise at the nanoscale the dispersed BNNTs, in order to control both their dispersion and assembly in solution.

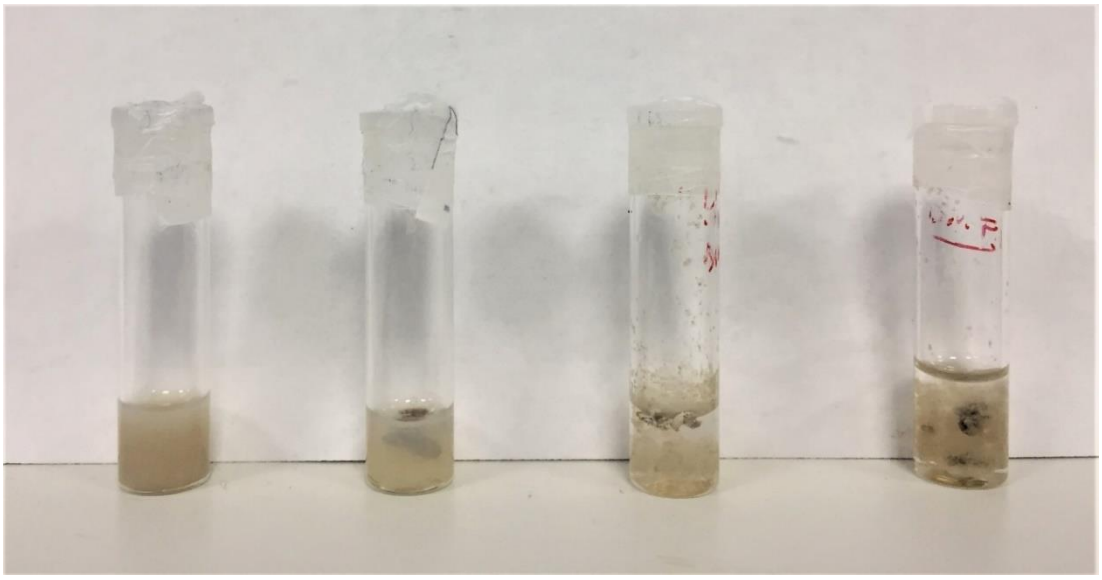

Figure 6-7 Dispersion of BNNTs in (from left to right) $(GTT)_3G$, $(GT)_{20}$, pure water, DMF.

In this regard, after centrifugation of the aforementioned solutions, the supernatant was collected and analysed utilising UV-vis, FT-IR and AFM.

In a separate set of experiments, BNNTs were dispersed in SDS and SDS-DNA mixture solutions following the same method as described above. In detail, 1 mg of BNNT powder was suspended in 1 mL SDS solution (1 mg mL^{-1}) or 1 mL SDS-DNA solution (1 mg*mL^{-1}, 0.1 M NaCl). The mixture was sonicated (VWR, ultrasonic cleaner) in an ice-water bath for 50s at a power level of 3W and cooled for 1 minute to avoid overheat. The process was repeated for 5 times to obtain a better dispersion. After sonication, the samples were divided into 0.1 mL aliquots and centrifuged (Heraeus Biofuge Pico) for 90 min at 17,000 g to remove insoluble material, leaving DNA-dispersed boron nitride nanotube solutions at a mass concentration of around 0.5 mg*mL^{-1}. The collected solution was then filtered using the filter column to remove large impurities (boron, BNx, etc.). Three solutions (SDS, SDS-DNA, DNA) were compared, as shown in **Figure 6-8**.

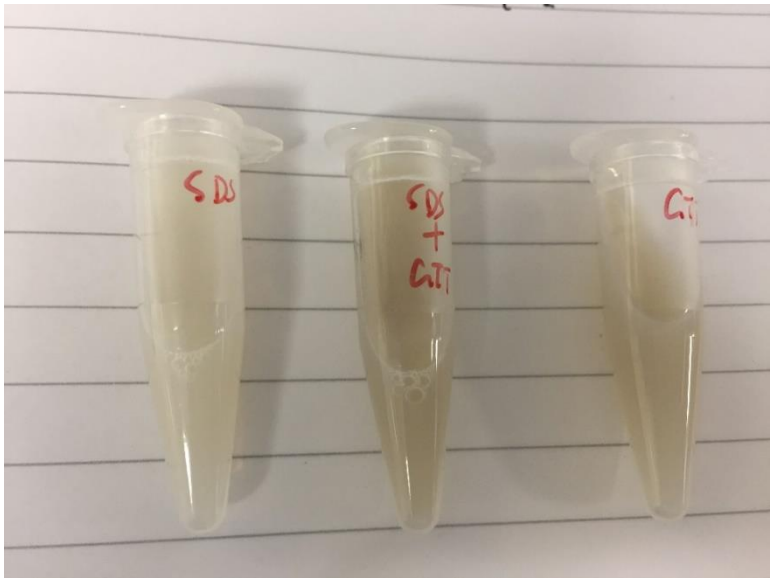

Figure 6-8 Dispersion of BNNTs in (from left to right): SDS surfactant solution, SDS-DNA solution, DNA ($(GTT)_3G$) solution.

It can be seen that the SDS-BNNTs solution is light white which is reasonable since BNNTs themselves are pure white.[19] The brown colours in the other two solutions could be the result of DNA wrapping which needs further confirmation. Moreover, to verify the role of DNA in the wrapping but not as a surfactant in the dispersion, we diluted the above solutions.

Noncovalent functionalisation is realised via either enthalpy-driven interactions, such as π-π between the nanotube surface and the dispersants or entropy-driven interactions; i.e. hydrophobic interactions using surfactants.[42] It is important to understand that the surfactant molecules on the surface of the nanotubes are in a dynamic equilibrium between surfactants in the solution. Therefore, the dispersion based on surfactants will be unstable when the concentration of surfactants decreases.

In this study, we diluted the above three solutions by 10 times with DI water. **Figure 6-9** shows that dispersion in ssDNA ($(GTT)_3G$) didn't change much in appearance while settlement can be observed in the other two. Moreover, the grey colour of the

SDS-DNA solution indicates a different dispersion mechanism compared to the SDS only solution which is clear after dilution.

In conclusion, these qualitative investigations suggest that ssDNA strands didn't work as a surfactant but through π-π stacking in the aqueous dispersion of BNNTs similar to the dispersion of DNA-wrapped CNTs.[43]

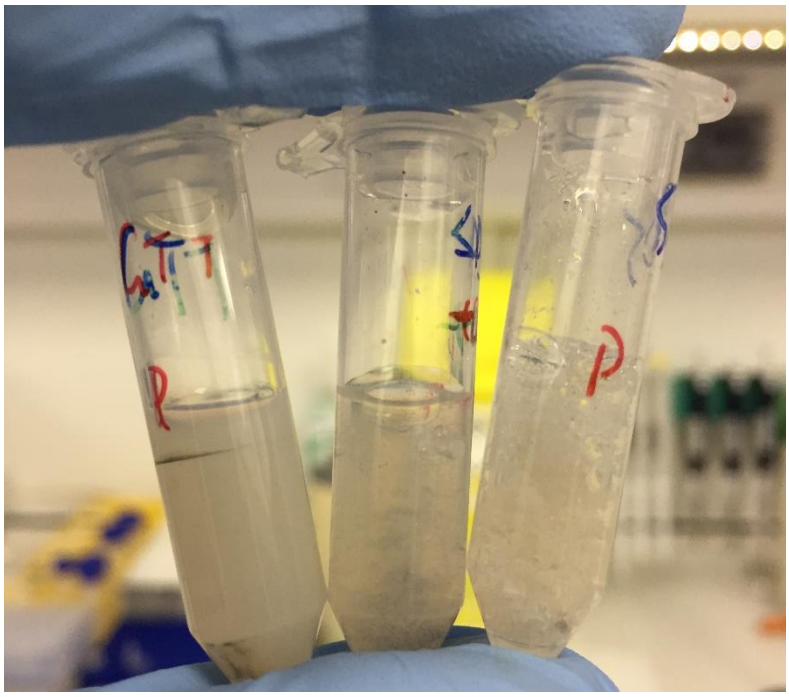

Figure 6-9 Dilution solution of BNNTs dispersed in (from left to right): DNA, SDS-DNA, SDS solutions.

6.2.3.1 UV-vis spectroscopy of BNNTs

UV/Vis absorption spectroscopy was used to investigate the interactions between the DNA and the BNNTs. In details, BNNTs were dispersed in DMF and DNA-wrapped BNNTs were diluted in water. As shown in **Figure 6-10**, pure BNNTs have only one broad absorption peak at ~ 200 nm, which indicates a wide-band gap of 5.2–5.6 eV. [32] The absorption peak shifts to ~ 205 nm (6.1 eV) after the BNNTs have been wrapped with the DNA. The absorption peak around 260nm can be ascribed to the ssDNA molecules.[44] While a small shift is observed after the DNA wrapping, the absorption peak is much sharper compared to pristine BNNTs due to a possible purification effect. As is discussed above, impurities like boron, BNx can be found in the pristine mixture which has slightly different bandgaps.[45] Nevertheless, only the boron nitride nanotubes can be wrapped through π-stacking, via helical wrapping to the surface, resulting in a narrow peak in UV spectrum.

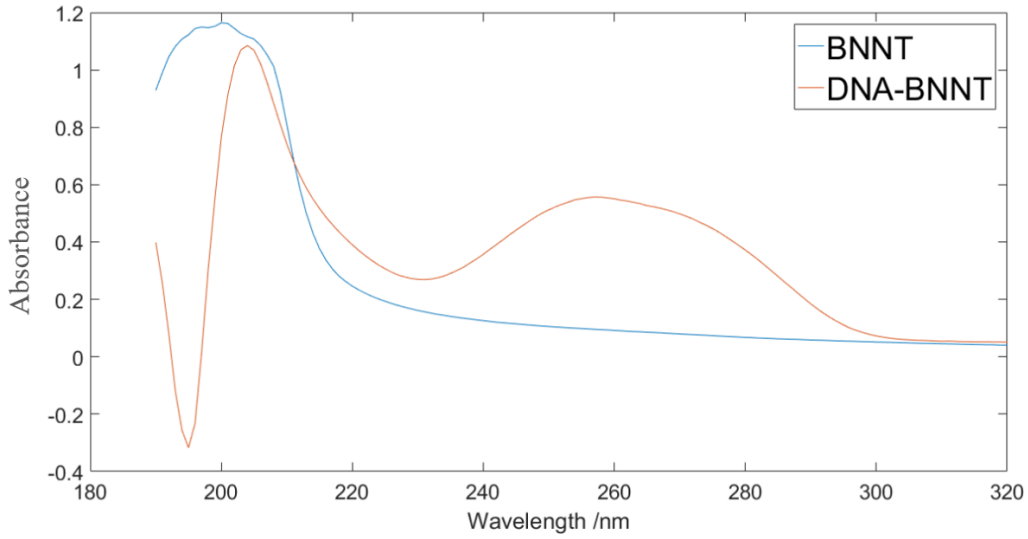

Figure 6-10 UV/Vis spectrum of pristine BNNTs in DMF solvents (blue line) and DNA wrapped BNNTs in water solution (red line).

6.2.3.2 FTIR study of BNNTs

The FTIR spectra of pure BNNTs (dry film) and DNA-BNNT (water solution) are compared in **Figure 6-11** and **Figure 6-12** to corroborate the wrapping process and obtain information about the interactions. The FTIR spectra were taken in a transmission mode on BNNTs powders pressed on the window under a FTIR microscope (Perkin Elmer Spectrum 65 FT-IR).The spectrum of raw BNNTs shows two characteristic peaks at 1347 and 796 cm^{-1} and it is consistent with literature.[46, 47] The dominant BN peak is around 1347 cm^{-1} which is ascribed to the in-plane B–N stretching, while the weak absorption bands at 793 cm-1 correspond to the out-of-plane B–N–B bending vibrations, respectively. A broad hydroxyl peak around 3200 cm^{-1} is found due to hydroxyl defects.

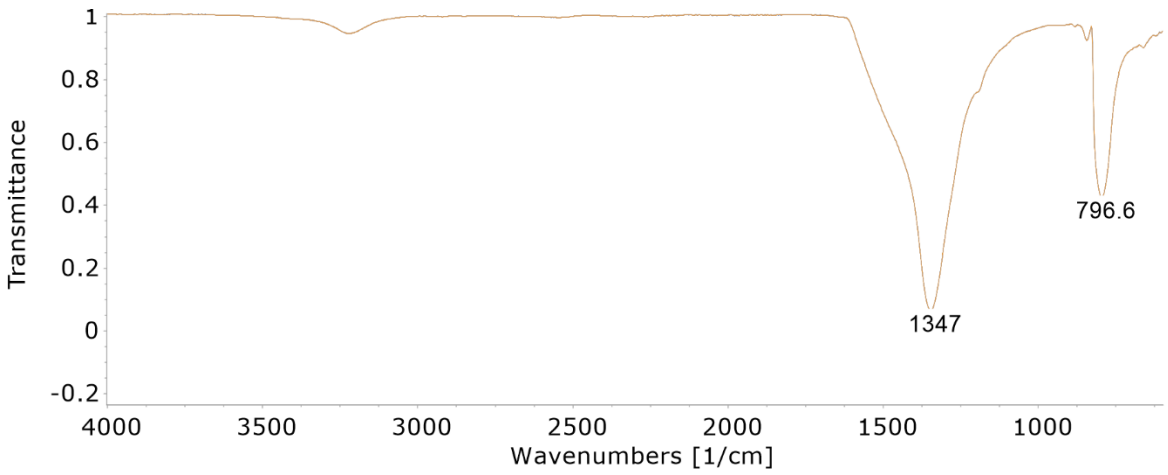

Figure 6-11 FT-IR Spectrum of Boron Nitride Nanotubes (dry film)

Upon DNA-wrapping, the in-plane B–N stretching shifts up to 1370 cm^{-1}, indicating a modification to the lattice vibrations due to the presence of the substituents. This is shown in **Figure 6-12**. Further, small bands appear at 1224 and 1059 cm^{-1}, assigned to the in-plane bending of B–OH and the symmetric B–O stretching, while the shoulder at about 900 cm^{-1} corresponds to the B–OH out-of-plane bending, corroborating the

success of the functionalisation reaction.[48, 49] A broader band appeared around 3401 cm^{-1} , that can be assigned to the O-H stretching. Moreover, the band around 1632 cm^{-1} corresponded to C-O double bond in the aromatic rings of DNA molecule.

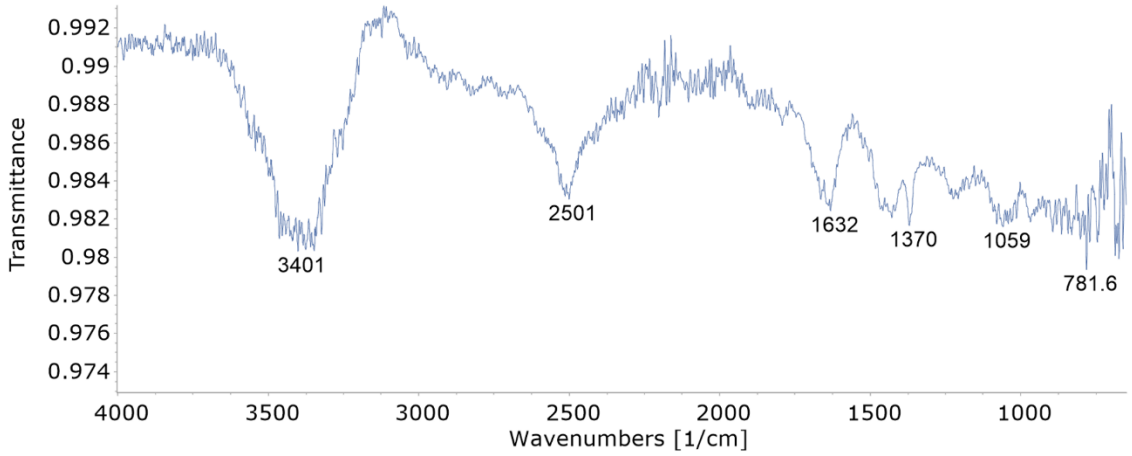

Figure 6-12 Representative FT-IR spectrum of DNA-wrapped BNNTs (in water solution)

6.2.3.3 Topographical Characterisation of DNA-wrapped BNNTs

To evaluate the effectiveness of the DNA wrapping of BNNTs, diluted solutions (1:80 with DI water) were drop cast on a cleaved muscovite mica surfaces. The substrate was treated with 1 M $MgSO_4$ to improve the adhesion between the DNA-wrapped nanotubes and the mica. The length distribution of the BNNT segments was quantified by ScanAsyst mode (Tapping) AFM and software analysis (ImageJ).

When ssDNA was used to wrap the BNNTS, AFM reveals clear individually spread tubes, as shown in **Figure 6-13**. The average length of the BNNT segments was found to be 260.1 nm ± 102.7 nm for $(GT)_{20}$ wrapped BNNTs, and 543.5 nm ± 222 nm for $(GTT)_3G$ wrapped BNNTs. The much shorter average length of $(GT)_{20}$ was due to the longer sonication during dispersion.

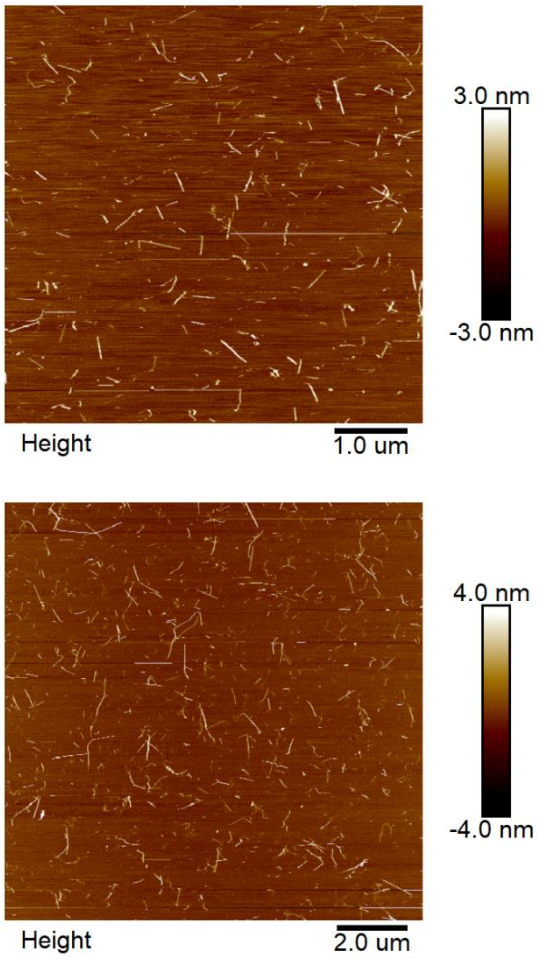

Figure 6-13 AFM topographical image of $(GT)_{20}$-wrapped BNNTs (left) and $(GTT)_3G$ wrapped BNNTs (right).

Furthermore, the diameter of the DNA-BNNTs has been determined based on the height info from the topography images. **Figure 6-14** shows that the average diameter of both $(GT)_{20}$ and $(GTT)_3G$ wrapped BNNTs is 2.7 nm which is reasonable since the wrapping should not significantly affect the diameter of nanotubes. The results indicated that the wrapped BNNTs were mainly 2-3 walls which is consistent with the as-grown material. It should be noted that more than 70% of the NTs have a diameter less than 3nm which indicates a possible purification/separation. Multi-wall BNNTs with more than 4 layers were excluded from DNA wrapping. On the other hand, $(GTT)_3G$ wrapped BNNTs exhibited a narrower diameter distribution between 1-3 nm. The difference may be

derived from the difference in the wrapping of two sequences which needs further computational confirmation.

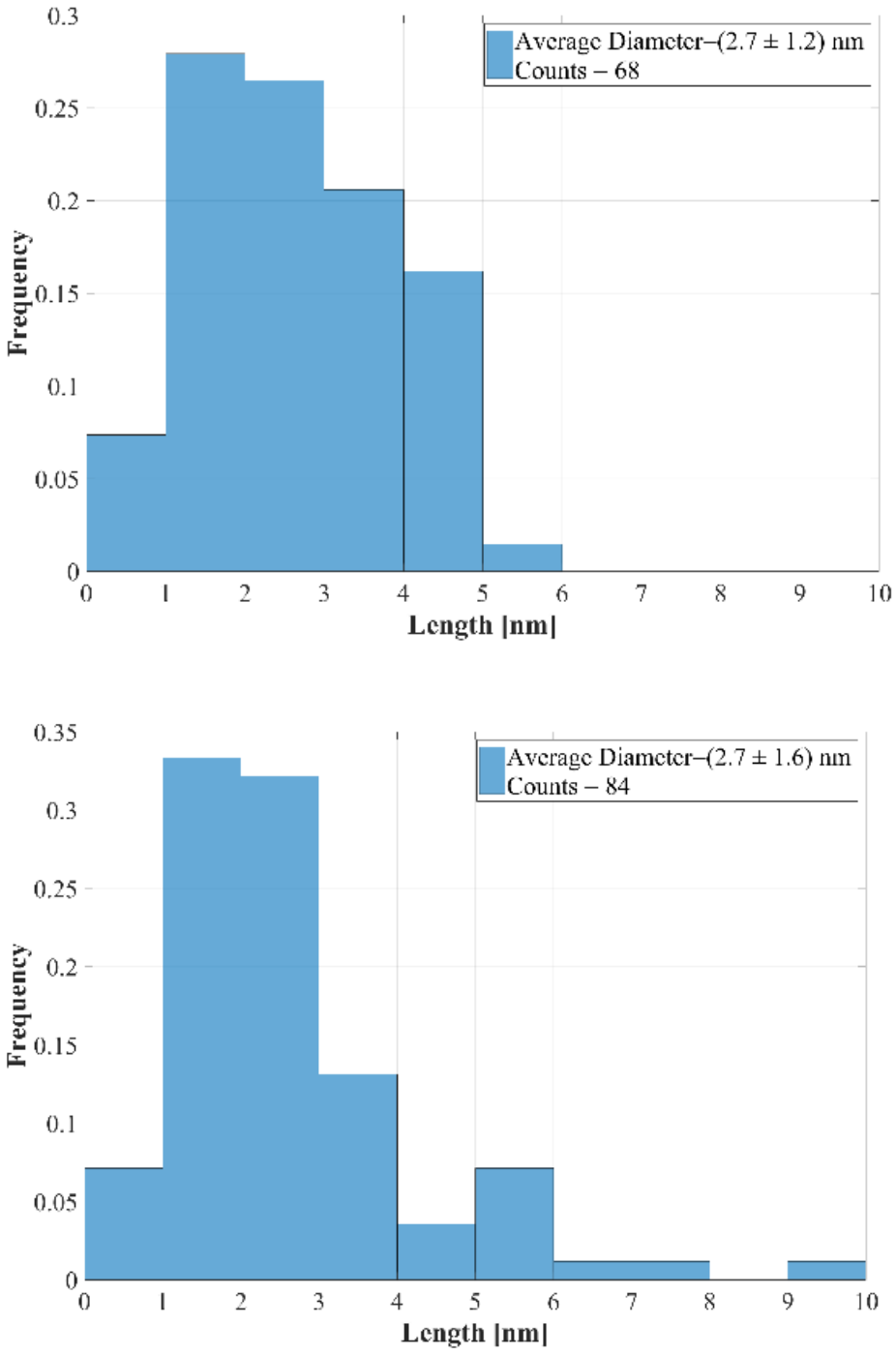

Figure 6-14 Histograms of Diameters of $(GT)_{20}$-wrapped BNNTs (upper) and $(GTT)_3G$ wrapped BNNTs (bottom).

6.3 One-Dimensional heterojunctions based on BNNT-CNT hybrids

To demonstrate applications of DNA-wrapped BNNTs, we present the in-solution assembly of multibranched heterostructures made of DNA-wrapped BNNTs and DNA-wrapped SWCNTs through EDC (carbodiimide) crosslinking reaction. In detail, the BNNTs were wrapped by amino-modified single strand DNA; the amino functionality on the sidewall of the wrapped BNNTs opens interesting perspectives for further modification of BNNTs with other kind of molecules. A schematic in **Figure 6-15** shows the brush-like structure of a heterojunction of BNNTs and CNTs, where the DNA wrapping has been omitted in the schematic. There is an interest in the formation of these kind of heterostructures due to the dielectric nature of BNNTs and the conductive/semiconductive properties of CNTs

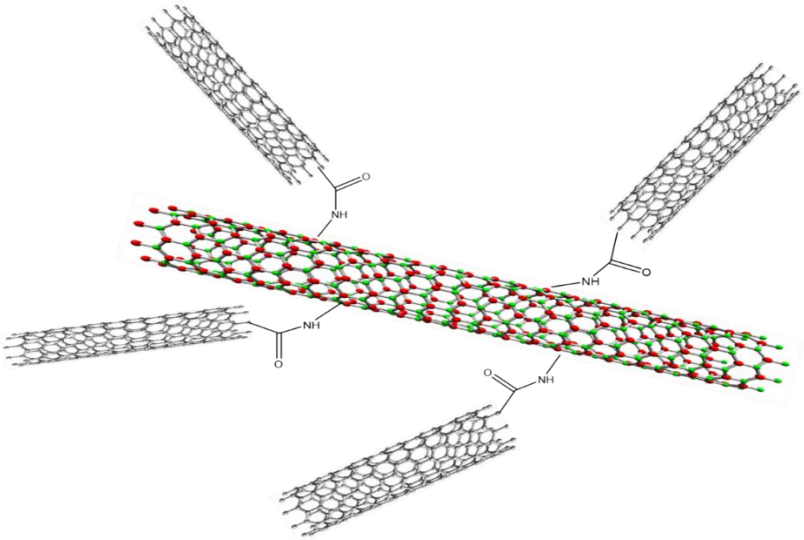

Figure 6-15 Schematic of Heterojunction made of DNA-wrapped CNTs and DNA-wrapped BNNTs

6.3.1 Amino-modified DNA wrapping of BNNT

BNNTs were wrapped with amino-modified DNA by using the procedure mentioned in section 6.2.2. The sequence used for the amino-modified DNA is GTT GTT GTT G. The diluted (1: 100 with DI water) solution of amino-modified ssDNA–BNNTs hybrid was cast on the mica, and the topography was imaged by AFM to confirm the wrapping (shown in Figure 14).

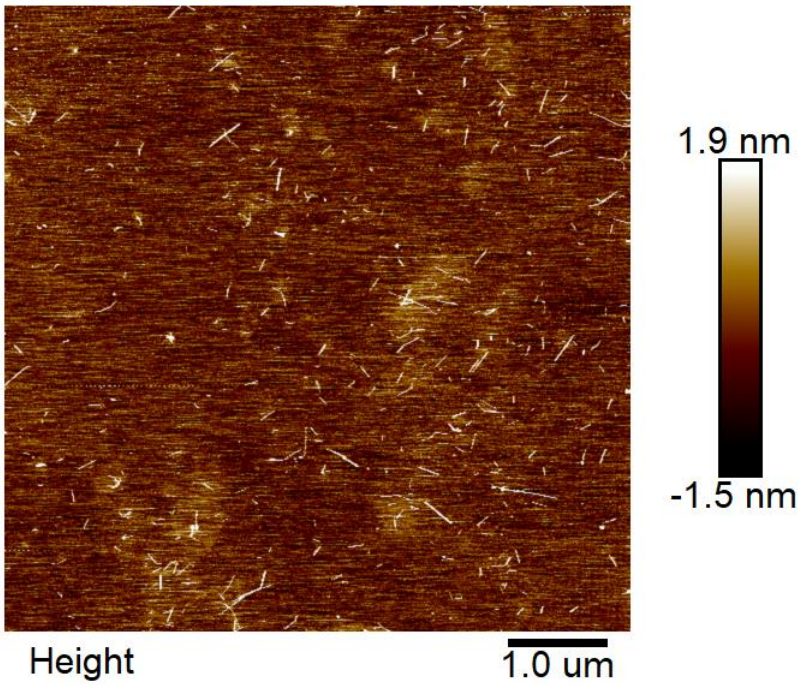

Figure 14 AFM Topographical image of amino-modified DNA wrapped BNNTs

The density of tubes in the scan area is counted to be 4 per μm^2 which is close to the number of pristine DNA wrapped BNNTs. The length distribution and height info of the amino-modified DNA wrapped BNNTs are similar to the original ones.

6.3.2 EDC (carbodiimide) crosslinking reaction

As is discussed in chapter 3, section 3.2.2, acid-cutting and ultrasonication in water of the CNTs produces oxidised defects along the tubes.[50, 51]Ss-DNA wrapping protects the sidewalls of the CNTs, therefore leaving only terminal carboxyl groups available for subsequent functionalisation. It was previously demonstrated that CNT segments could be attached to amine-functionalised molecular linkers via amidation reactions:[52] we have presented the formation of molecular junctions employing this strategy to bridge DNA-wrapped SWCNTs with conjugated molecular linkers in chapter 3. In this section, we present the formation of 1-D heterojunctions by linking SWCNT carboxylic termini with amino groups present on the DNA strands wrapping BNNTs. The formation of end-to-side linked SWCNT and BNNT segments will be discussed.

The standard amine coupling includes a three-step reaction with EDC(1-ethyl-3-(-3-dimethylaminopropyl) carbodiimide hydrochloride)/NHS(N-hydroxysulfosuccinimide) reactions (shown in **Figure 3-1**).[53] In the first step, EDC reacts with carboxylic acid groups to form an active o-Acylisourea intermediate that is easily displaced by nucleophilic attack (pH 4.5). The NHS is coupled to carboxyls in the second step to form an NHS ester which is more stable than o-Acylisourea intermediate. In the third step, the primary amine forms an amide bond with the original carboxyl group, and an EDC by-product is released as a soluble urea derivative.

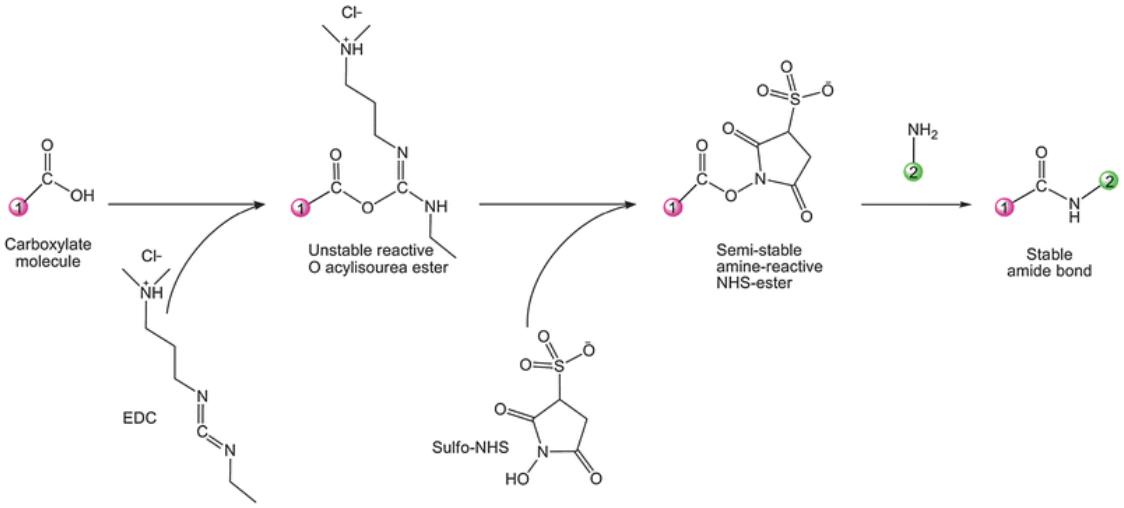

Figure 6-16 EDC–NHS chemistry: EDC reacts with a carboxylic-acid group on molecule 1, forming an amine-reactive O-acylisourea intermediate. This intermediate may react with an amine on molecule 2, yielding a conjugate of the two molecules joined by a stable amide bond. The addition of sulfo-NHS stabilizes the amine-reactive intermediate by converting it to an amine reactive sulfo-NHS ester, thus increasing the efficiency of EDC-mediated coupling reactions.[54]

In detail, amide bond formation in aqueous conditions was performed with coupling reagents 1-ethyl-3-[3-dimethylaminopropyl] carbodiimide hydrochloride (EDC, 4 mM, Sigma Aldrich) and N-hydroxysulfosuccinimide sodium salt (sulfo-NHS, 10 mM, Sigma Aldrich) in an MES buffer (pH 4.7, 0.2 M, ThermoScientific). Pristine DNA-wrapped SWCNTs in DI H_2O were added to the activating solution in a 1:1 equivalence and left to incubate for 30 minutes. The solution was then diluted with Dulbecco Phosphate Buffer Saline (pH 7.2, DPBS, ThermoScientific) solution in a 1:1 volume ratio and left incubating for 1 hour. The amino-DNA-wrapped BNNTs solution (10 nM) was then added to the SWCNT solution and left incubating overnight.

6.3.3 Results and discussion

To obtain the topography of the formed junctions, a given solution was cast on a cleaved mica substrate and imaged with AFM. The substrate was treated with 1M $MgSO_4$ to improve the adhesion between nanotubes and mica. **Figure 6-17** shows various multi-terminal nanotube junctions formed.

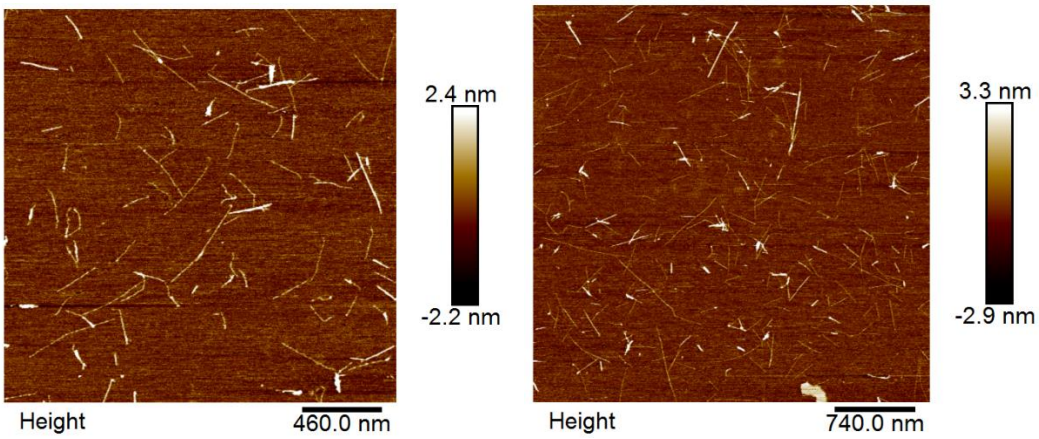

Figure 6-17 AFM topographical images of branched junctions of DNA-wrapped SWCNT and DNA-wrapped BNNT.

To confirm that the end-to-side linkage of SWCNT and BNNT segments is due to amidation rather than physical absorption, a reaction was carried out without the activating agents EDC and sulfo-NHS. In detail, pristine DNA-wrapped SWCNTs in DI H_2O were added to the MES buffer (pH 4.7, 0.2 M, ThermoScientific) in a 1:1 equivalence and left to incubate for 30 minutes. The solution was then diluted with Dulbecco Phosphate Buffer Saline (pH 7.2, DPBS, ThermoScientific) solution in a 1:1 volume ratio and left incubating for 1 hour. The amino-DNA-wrapped BNNTs solution (10 nM) was then added to the SWCNT solution and left incubating overnight. The solution was finally cast on a Mg^{2+} treated cleaved mica substrate. **Figure 6-18** shows the topography image of the film of the mixed solution.

It can be noted that no clear junctions can be found (while in some cases crossing architectures can be seen, but are the result of physical interaction between the tubes with one on top of the other) as confirmed by AFM topographical image analysis below).

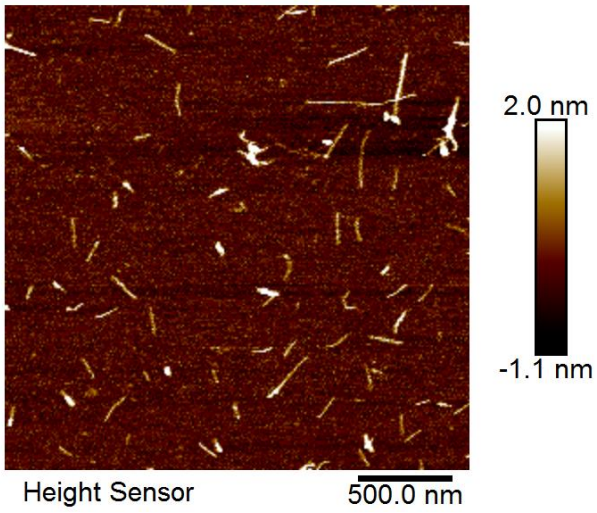

Figure 6-18 AFM topography image of mixture of DNA-wrapped BNNTs and DNA-wrapped SWCNTs solution without EDC/NHS.

The multi-branched junctions predominantly exhibit the same height of the pristine SWCNTs and BNNTs, confirming that the junctions are the result of nanotube interconnections, rather than bundling. As is shown **Figure 6-19**, the height of individual pristine nanotubes is comparable to the height of BNNT-CNT junctions (ca. 1.5 nm in both cases). However, in the case of two overlapping nanotubes, the height of the cross point is close to 2.4 nm (**Figure 6-20**). This indicates the structures formed are not an overlapping phenomenon such as a physical contact, but the result of junction formation.

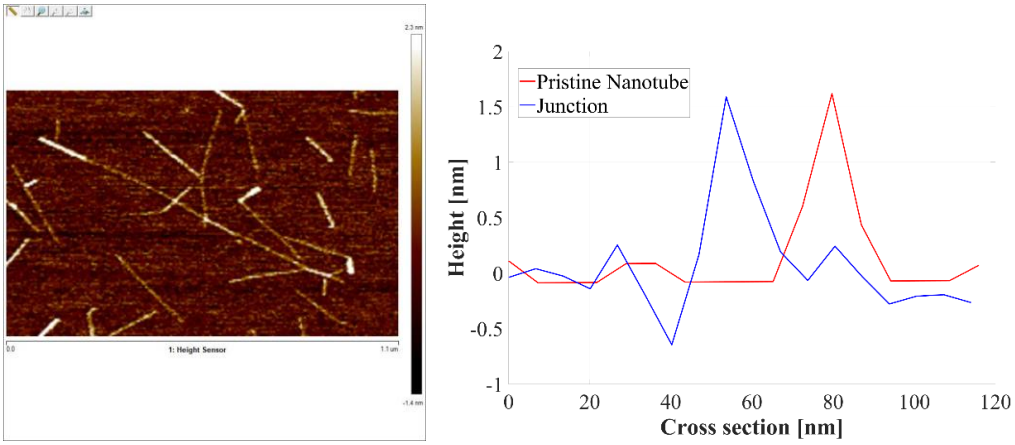

Figure 6-19 Left: AFM topographical image of a BNNT-CNT heterojunction (zoom in) ; Right: the height profile from the cross section of the nanotube (red) and the junction (blue).

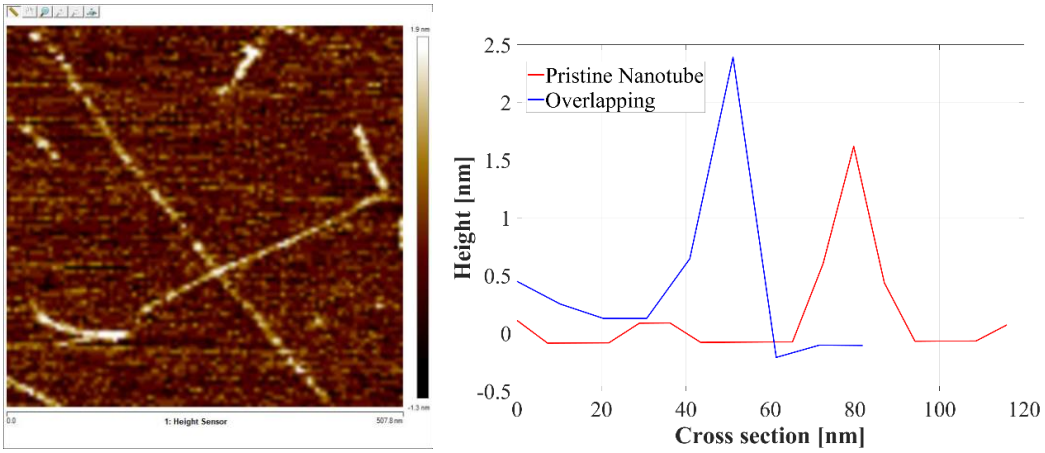

Figure 6-20 Left: AFM topographical image of two overlapping nanotubes (zoom in) ; Right: the height profile from the cross section of the nanotube (red) and the junction (blue).

6.4 Dielectrophoresis of BNNTs

6.4.1 Assembly of BNNTs

Nanoscale dimensions and remarkable properties of boron nitride nanotubes make them promising building blocks for nanodevices. One requirement is the need to manipulate single or multiple boron nitride nanotubes to bridge electronic conductors. Research on BNNTs functionalisation has been widely reported; nevertheless, only a few works on the methods of assembly including thin films, yarns, and buckypapers were published.[55] The most common method for assembling BNNTs on the surface is via random deposition. The BNNTs solution is dispersed on substrates, with nanotubes landing in random locations. However, this method is limited in accuracy at the nanoscale and not scalable for large scale applications.

One special technique reported by Yu et al. is adopting Au-decorated boron-nitride nanotubes as humidity sensors.[38] In such work, they manipulated and placed one single long BNNT into a device and imaged the sample under an optical microscope. It should be noted that the method is highly limited by the quality and length of the NTs and hence is not applicable to common conditions.

In this section, we present a method to assemble DNA-wrapped BNNTs between electrodes via dielectrophoresis inspired by similar work done in section 5.3 on CNTs. To consider only the simplest case, the time-averaged dielectrophoretic force applied on a ballistic nanotube can be expressed as[56, 57]:

$$\vec{F}_{DEP} = \frac{\pi}{6} r^2 * \mathrm{l} * \varepsilon_m * Re\{K_f\} \nabla |E|^2 \tag{6-1}$$

Where r is the radius and l is the length of the nanotube, ε_m is the real part of the dielectric constants of the nanotubes, and E is the electric field. For the tube with the long axis aligned with the direction of the electrical field, K_f is then given by:

$$K_f = \frac{\varepsilon_t^* - \varepsilon_m^*}{\epsilon_m^*}, \qquad \varepsilon^* = \varepsilon - i\frac{\sigma}{\omega} \tag{6-2}$$

In the high and low-frequency limits, the K_f can be simplified as:

$$\mathrm{Re}\{K_f\} = \begin{cases} \dfrac{\sigma_t - \sigma_m}{\sigma_m}, & \omega \to 0 \\ \dfrac{\varepsilon_t - \varepsilon_m}{\varepsilon_m}, & \omega \to \infty. \end{cases} \tag{6-3}$$

In the low-frequency limit, the force is independent of the frequency as well as of the permittivity of the nanotube and the medium, while in the high-frequency limit the force will be dependent on the permittivity of the nanotube with respect to that of the medium.

6.4.2 Materials and methods

Electrodes are fabricated by a combination of photolithography and electron beam lithography followed by metal evaporation and lift off processes. In details, the photolithography was used to pattern the micrometre scale electrodes while the gap of 400nm was achieved by e beam lithography. A metal deposition of Cr/Au (5/45 nm) was performed to fabricate the electrodes.

BNNTs were prepared in aqueous solution as discussed in section 6.2.1. The solution is then treated with two times of 24-hour dialysis in ultrapure water to remove the salt. The step is of critical importance as free ions in solution will damage the dielectric of water thus weakening the Dielectrophoretic force. Solutions were diluted with ultrapure water to obtain uniformly diluted solutions with concentrations as 20 ng/ml. The

assembly of SWCNTs by DEP and the electrical characterisation of assembled SWCNTs were conducted on a probing station (PS-100, Lakeshore) and a semiconductor characterisation system (Keithley, 4200SCS). A tiny volume (3 μl) of the solution was placed onto the electrode gap through a micropipette.

The variables tested in this study included voltage and frequency. Voltage values ranged from 5.0-7.0 V_{pp} (volts, peak-to-peak) and the frequency varied at 50 kHz, 100 kHz, 200 kHz. A programmable DDS function generator (TG1010A, TTI) was used to generate the required ac electric field for CNT deposition. The deposition time is fixed at 40s to obtain the desired density of BNNTs on the electrodes.

6.4.3 Results and discussion

DNA-wrapped BNNT solutions were cast on pre-patterned metal electrodes and the assembly of the nanotubes between the electrodes was obtained via dielectrophoresis employing different voltages. The samples were characterised by AFM to obtain the corresponding topographic images. Figure 6-21 shows the obtained results.

It can be seen that BNNTs were deposited near the electrodes in all conditions while with 5 V the least number of tubes was obtained. Moreover, the electrodes in the case of 6 V and 7 V biases display a network of BNNTs. For these conditions (biases of 6 V and 7 V) while tuning the frequency to obtain a better assembly. **Figure 6-22** presents the depositions at a frequency of 100 kHz. The figures indicate that 7V is too high of a bias which still results in a network of BNNTs on the electrodes.

More experiments were then performed with 6 V under different frequencies as shown in **Figure 6-23**. In this case, some BNNTs could be observed on the electrodes with DEP frequency at 100 kHz. However, aggregation of salt/impurities could be observed

as well. On the other hand, electrodes with DEP frequency at 50 kHz displayed cleaner surfaces, with clear sign of individual BNNTs. It should be noted that electrodes were damaged during the process and a break can be observed at one of the electrodes pair. This was shown to be common for these experimental conditions (6 V and 50 kHz).

In conclusion, the best parameters to assemble the BNNTs over electrodes were found to be 6 V at a frequency of 75 kHz. A clear electrode area with a few individual nanotubes has been shown. Electrical characterisation has been attempted with no valid I-V response compared to the literature where the BNNTs should have a resistance at 10^9 Ω.[58, 59] This could be due to a large contact resistance between BNNTs and electrodes. Furthermore, the investigated nanotubes in this thesis are much thinner (1-3 layers) compared the multi-wall BNNTs in the literature .Future experiments will be performed annealing the samples in inert atmosphere and/or pre-forming a siliane monolayer on the SiO_2 sample surface, a strategy that has shown a successful contact between DNA-wrapped CNTs and metal electrodes deposited by dielectrophoresis, as shown by another member (and PhD candidate) of the Palma laboratory, Xinzhao Xu.

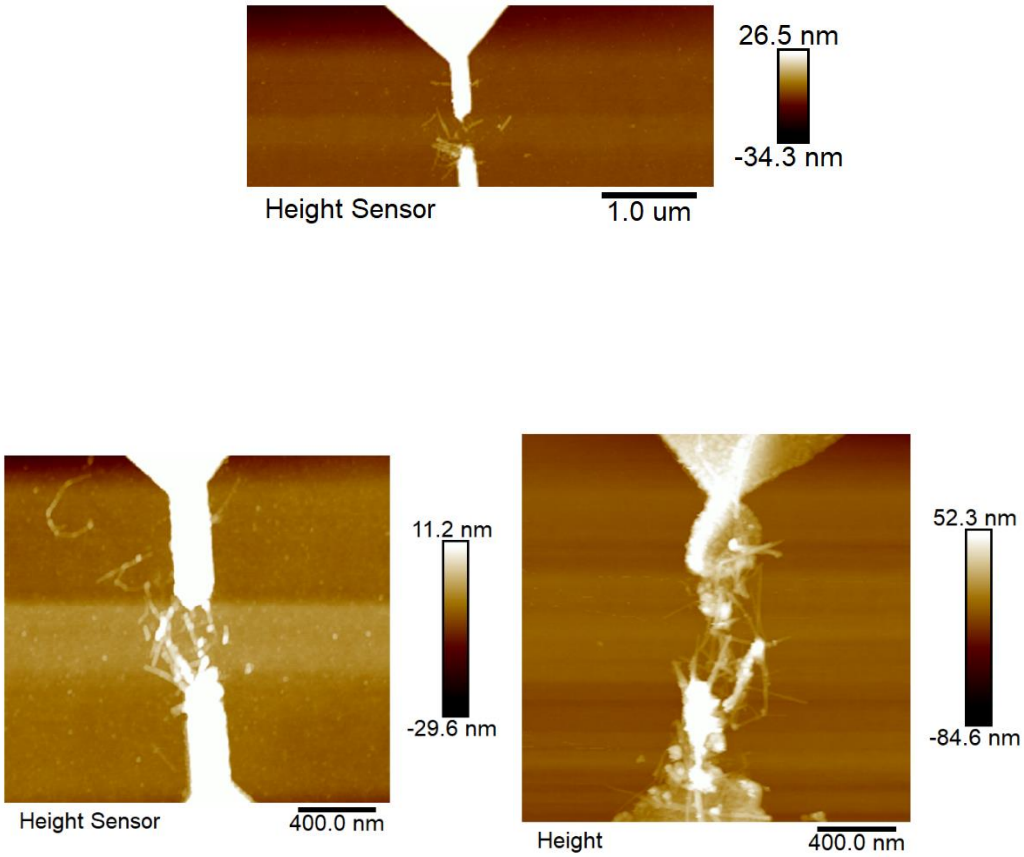

Figure 6-21 AFM topographical images of electrodes after dielectrophoretic assembly of BNNTs; Upper: 5V, 200 kHz; Bottom left: 6V, 200kHz; Bottom right: 7V, 200kHz.

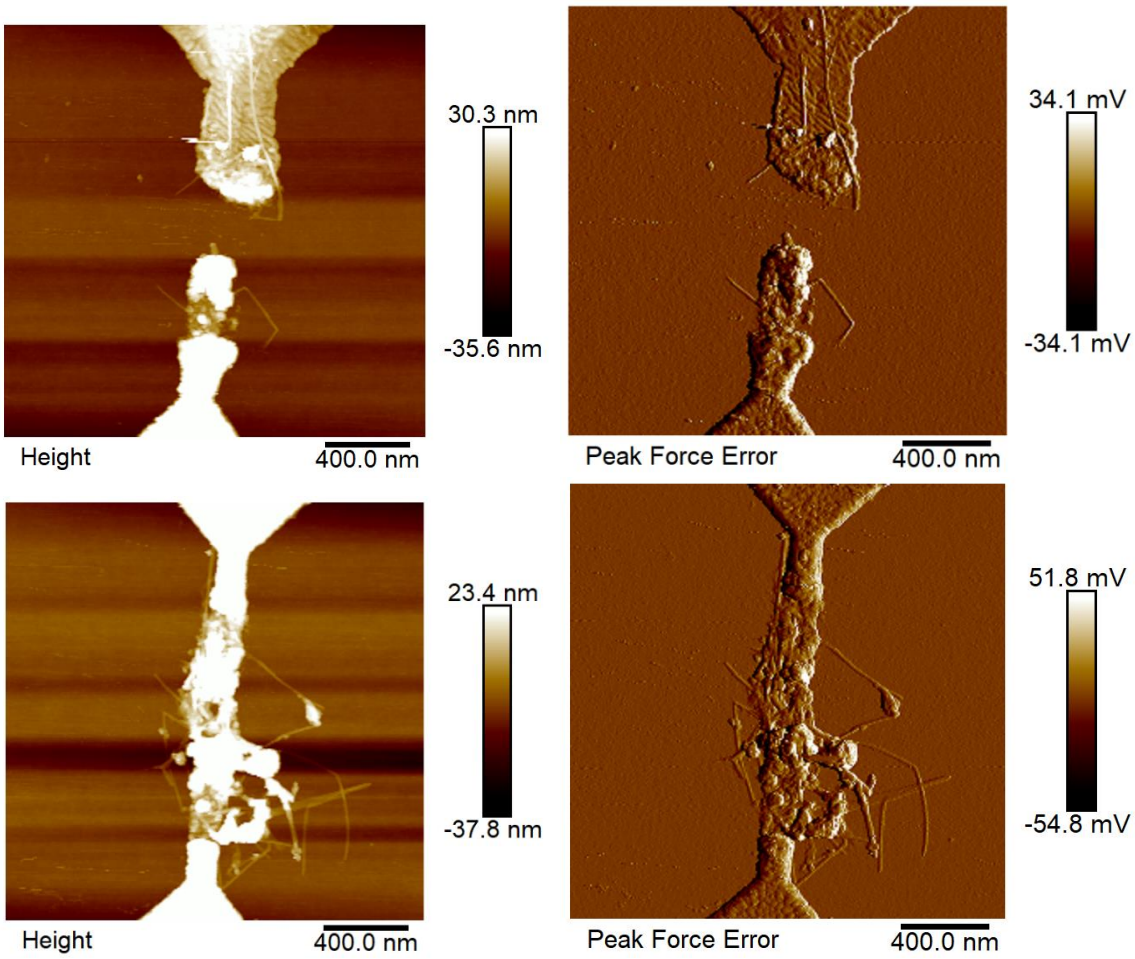

Figure 6-22 AFM topographical images of electrodes after dielectrophoretic assembly of BNNTs; Upper: obtained by 6V and 100kHz; Bottom: obtained by 7V and 100kHz.

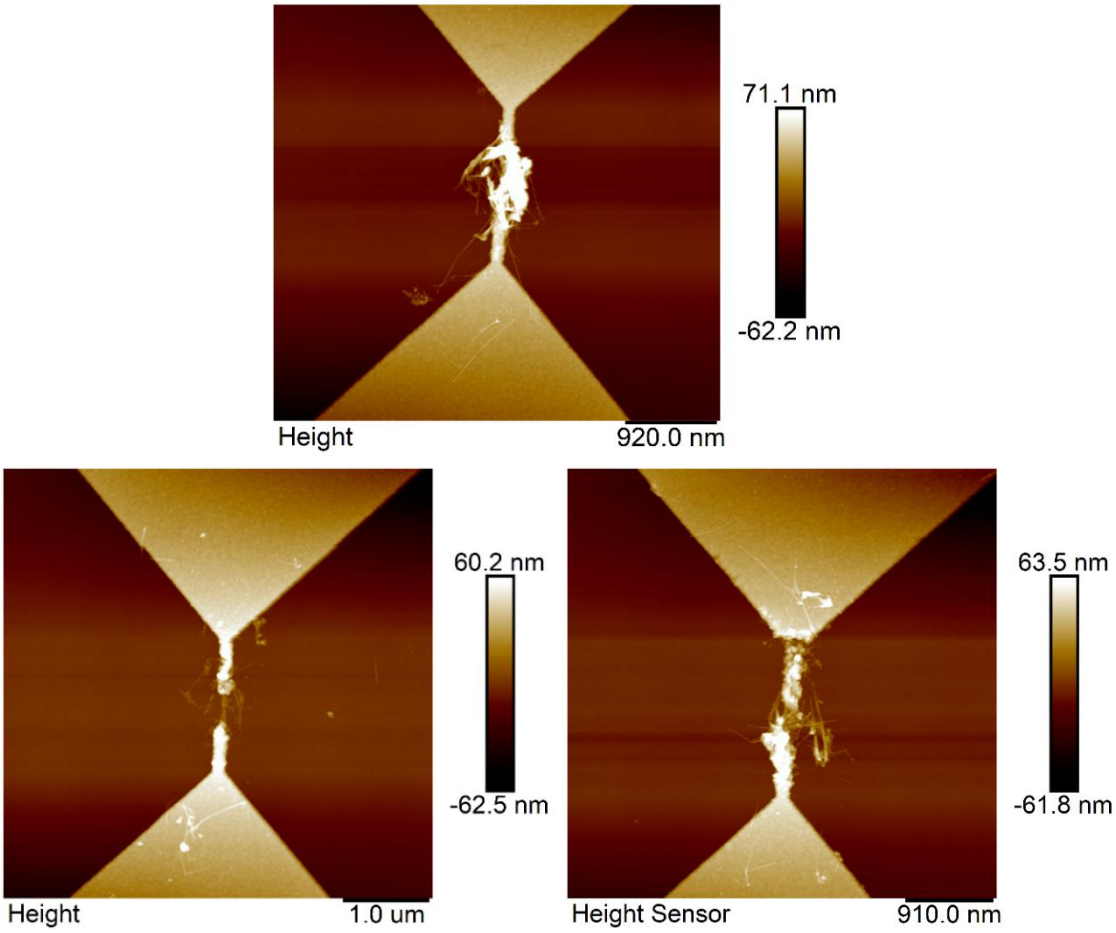

Figure 6-23 AFM topographical images of electrodes after dielectrophoretic assembly of BNNTs; Upper: 6V and 100kHz; Bottom left: 6V and 75kHz; Bottom right: 6V and 50 kHz.

6.5 Conclusions

In this chapter, we have discussed the use of nucleic acid polymers to form a hybrid material with boron nitride nanotubes. The unique attributes of this material provide many ways to manipulate carbon nanotubes in aqueous solutions, including separation and surface modification. This opens the way to a potential differential binding by DNA to boron nitride nanotubes of different diameter and chirality to be explored in future studies.

Furthermore, we presented the synthesis of one-dimensional heterojunctions based on modified-DNA wrapped BNNTs and DNA-wrapped SWCNTs. As BNNTs are quite useful in composites and nano-electronics owing to their dielectric nature, piezoelectricity, and high thermal conductivity, it is envisaged that this study may stimulate applications of such nanohybrids for sensors, actuators and energy harvest.

In addition, the dielectrophoretic assembly of BNNTs between a pair of electrodes was demonstrated. This provides an environment-friendly and facile method to assemble NTs in device configurations directly from solution, which is essential for scaling up the device fabrication. Future work related to this project could focus on better assembly parameters, resulting in the dielectrophoresis immobilisation of a single nanotube. More effective methods to improve the intimacy of a physical contact need to be considered, e.g. nano-welding/annealing and substrate's pre-functionalisation .

Moreover, ultra-sonication in DI water produces BNNTs segments with oxidised ends presenting hydroxyl groups as shown in section 6.2.3.2. DNA wrapping the nanotubes protects the sidewall of nanotubes from further reactions while leaving the terminal end exposed. This would open doors to potential end-to-end junction or end to bonding site applications in the future.

References

1. Rubio, A., J.L. Corkill, and M.L. Cohen, *Theory of graphitic boron nitride nanotubes.* Physical Review B, 1994. **49**(7): p. 5081-5084.
2. Chopra, N.G., et al., *Boron Nitride Nanotubes.* Science, 1995. **269**(5226): p. 966-967.
3. Kim, M.-H.Y., *Performance study of galactic cosmic ray shield materials* NASA technical paper ; 3473, ed. C. Langley Research. 1994, Hampton, Va. : [Springfield, Va: National Aeronautics and Space Administration, Langley Research Center ; National Technical Information Service, distributor.
4. Yu, M.-F., et al., *Strength and Breaking Mechanism of Multiwalled Carbon Nanotubes Under Tensile Load.* Science, 2000. **287**(5453): p. 637-640.
5. Chang, C.W., et al., *Isotope effect on the thermal conductivity of boron nitride nanotubes.* Physical Review Letters, 2006. **97**(8).
6. Che, J.W., T. Cagin, and W.A. Goddard, *Thermal conductivity of carbon nanotubes.* Nanotechnology, 2000. **11**(2): p. 65-69.
7. Lee, C.H., et al., *Patterned Growth of Boron Nitride Nanotubes by Catalytic Chemical Vapor Deposition.* Chemistry of Materials, 2010. **22**(5): p. 1782-1787.
8. Yamakov, V., et al., *Piezoelectric molecular dynamics model for boron nitride nanotubes.* Computational Materials Science, 2014. **95**: p. 362-370.
9. Golberg, D., et al., *Boron Nitride Nanotubes.* Advanced Materials, 2007. **19**(18): p. 2413-2432.
10. Chen, Y., et al., *A solid-state process for formation of boron nitride nanotubes.* Applied Physics Letters, 1999. **74**(20): p. 2960-2962.
11. Li, L.H., Y. Chen, and A.M. Glushenkov, *Boron nitride nanotube films grown from boron ink painting.* Journal of Materials Chemistry, 2010. **20**(43): p. 9679-9683.
12. Lourie, O.R., et al., *CVD growth of boron nitride nanotubes.* Chemistry of Materials, 2000. **12**(7): p. 1808-+.
13. Kim, M.J., et al., *Double-Walled Boron Nitride Nanotubes Grown by Floating Catalyst Chemical Vapor Deposition.* Nano Letters, 2008. **8**(10): p. 3298-3302.
14. Loiseau, A., et al., *Boron nitride nanotubes with reduced numbers of layers synthesized by arc discharge.* Physical Review Letters, 1996. **76**(25): p. 4737-4740.
15. Arenal, R., et al., *Root-growth mechanism for single-walled boron nitride nanotubes in laser vaporization technique.* Journal of the American Chemical Society, 2007. **129**(51): p. 16183-16189.
16. Laude, T., et al., *Long ropes of boron nitride nanotubes grown by a continuous laser heating.* Applied Physics Letters, 2000. **76**(22): p. 3239-3241.
17. Wang, J.S., et al., *Low temperature growth of boron nitride nanotubes on substrates.* Nano Letters, 2005. **5**(12): p. 2528-2532.
18. Smith, M.W., et al., *Very long single- and few-walled boron nitride nanotubes via the pressurized vapor/condenser method.* Nanotechnology, 2009. **20**(50).
19. Zhi, C., et al., *Boron nitride nanotubes.* Materials Science and Engineering: R: Reports, 2010. **70**(3-6): p. 92-111.
20. Chen, H., et al., *Purification of boron nitride nanotubes.* Chemical Physics Letters, 2006. **425**(4-6): p. 315-319.
21. Kim, K.S., et al., *Hydrogen-Catalyzed, Pilot-Scale Production of Small-Diameter Boron Nitride Nanotubes and Their Macroscopic Assemblies.* Acs Nano, 2014. **8**(6): p. 6211-6220.
22. Zhi, C.Y., et al., *Purification of boron nitride nanotubes through polymer wrapping.* Journal of Physical Chemistry B, 2006. **110**(4): p. 1525-1528.

23. Yu, J., Y. Chen, and B.M. Cheng, *Dispersion of boron nitride nanotubes in aqueous solution with the help of ionic surfactants.* Solid State Communications, 2009. **149**(19-20): p. 763-766.
24. Tiano, A.L., et al., *Thermodynamic approach to boron nitride nanotube solubility and dispersion.* Nanoscale, 2016. **8**(7): p. 4348-4359.
25. Xie, S.Y., et al., *Solubilization of boron nitride nanotubes.* Chem Commun (Camb), 2005(29): p. 3670-2.
26. Ikuno, T., et al., *Amine-functionalized boron nitride nanotubes.* Solid State Communications, 2007. **142**(11): p. 643-646.
27. Huang, Y., et al., *Bulk synthesis, growth mechanism and properties of highly pure ultrafine boron nitride nanotubes with diameters of sub-10 nm.* Nanotechnology, 2011. **22**(14).
28. Pal, S., et al., *Functionalization and solubilization of BN nanotubes by interaction with Lewis bases.* Journal of Materials Chemistry, 2007. **17**(5): p. 450-452.
29. Ciofani, G., et al., *Boron Nitride Nanotubes: Biocompatibility and Potential Spill-Over in Nanomedicine.* Small, 2013. **9**(9-10): p. 1672-1685.
30. Ciofani, G., et al., *A simple approach to covalent functionalization of boron nitride nanotubes.* Journal of colloid and interface science, 2012. **374**(1): p. 308-14.
31. Shin, H., et al., *Covalent Functionalization of Boron Nitride Nanotubes via Reduction Chemistry.* Acs Nano, 2015. **9**(12): p. 12573-12582.
32. Zhi, C., et al., *Perfectly dissolved boron nitride nanotubes due to polymer wrapping.* J Am Chem Soc, 2005. **127**(46): p. 15996-7.
33. Wang, W.L., et al., *Aqueous noncovalent functionalization and controlled near-surface carbon doping of multiwalled boron nitride nanotubes.* Journal of the American Chemical Society, 2008. **130**(26): p. 8144-+.
34. Zhi, C., et al., *DNA-mediated assembly of boron nitride nanotubes.* Chemistry - An Asian Journal, 2007. **2**(12): p. 1581-1585.
35. Liang, L., et al., *Theoretic Study on Dispersion Mechanism of Boron Nitride Nanotubes by Polynucleotides.* Scientific Reports, 2016. **6**(1): p. 39747-39747.
36. Zhi, C.Y., et al., *Boron nitride nanotubes/polystyrene composites.* Journal of Materials Research, 2006. **21**(11): p. 2794-2800.
37. Qing, H., et al., *Enhancing superplasticity of engineering ceramics by introducing BN nanotubes.* Nanotechnology, 2007. **18**(48): p. 485706.
38. Yu, Y., et al., *Humidity sensing properties of single Au-decorated boron nitride nanotubes.* Electrochemistry Communications, 2013. **30**: p. 29-33.
39. Yoosefian, M., et al., *The role of boron nitride nanotube as a new chemical sensor and potential reservoir for hydrogen halides environmental pollutants.* Superlattices and Microstructures, 2016. **98**: p. 325-331.
40. Costa Paura, E.N., et al., *CO2 adsorption on single-walled boron nitride nanotubes containing vacancy defects.* RSC Advances, 2015. **5**(35): p. 27412-27420.
41. Zhi, C.Y., et al., *Molecule ordering triggered by boron nitride nanotubes and "Green" chemical functionalization of boron nitride nanotubes.* Journal of Physical Chemistry C, 2007. **111**(50): p. 18545-18549.
42. Tsuyohiko, F. and N. Naotoshi, *Non-covalent polymer wrapping of carbon nanotubes and the role of wrapped polymers as functional dispersants.* Science and Technology of Advanced Materials, 2015. **16**(2): p. 024802.
43. Zheng, M., et al., *DNA-assisted dispersion and separation of carbon nanotubes.* Nature materials, 2003. **2**(5): p. 338-42.
44. Javier, T., et al., *Quantification of the surface stress in microcantilever biosensors: revisiting Stoney's equation.* Nanotechnology, 2012. **23**(47): p. 475702.

45. Stoney, G.G., *The Tension of Metallic Films Deposited by Electrolysis.* Proceedings of the Royal Society of London. Series A, 1909. **82**(553): p. 172.
46. Lee, C.H., et al., *Effective growth of boron nitride nanotubes by thermal chemical vapor deposition.* Nanotechnology, 2008. **19**(45).
47. Zhong, B., et al., *Large-Scale Fabrication of Boron Nitride Nanotubes via a Facile Chemical Vapor Reaction Route and Their Cathodoluminescence Properties.* Nanoscale Res Lett, 2010. **6**(1): p. 36.
48. Sainsbury, T., et al., *Oxygen Radical Functionalization of Boron Nitride Nanosheets.* Journal of the American Chemical Society, 2012. **134**(45): p. 18758-18771.
49. Lehmann, W.J., et al., *Infrared Spectrometry in Boron Chemistry*, in *BORAX TO BORANES*. 1961, American Chemical Society. p. 139-150.
50. Kaempgen, M., et al., *Sonochemical optimization of the conductivity of single-wall carbon nanotube networks.* Advanced Materials, 2008. **20**(3): p. 616-620.
51. Riesz, P. and T. Kondo, *Free radical formation induced by ultrasound and its biological implications.* Free Radical Biology and Medicine, 1992. **13**(3): p. 247-270.
52. Palma, M., et al., *Controlled formation of carbon nanotube junctions via linker-induced assembly in aqueous solution.* Journal of the American Chemical Society, 2013. **135**(23): p. 8440-3.
53. Fischer, M.J.E., *Amine Coupling Through EDC/NHS: A Practical Approach*, in *Surface Plasmon Resonance: Methods and Protocols*, N.J. Mol and M.J.E. Fischer, Editors. 2010, Humana Press: Totowa, NJ. p. 55-73.
54. Bart, J., et al., *Room-temperature intermediate layer bonding for microfluidic devices.* Lab on a Chip, 2009. **9**(24): p. 3481-3488.
55. Li, X., et al., *Fabrication of size-controllable nanofluidic channels using angled physical vapor deposition.* Microelectronic Engineering, 2012. **98**: p. 647-650.
56. Krupke, R., et al., *Separation of Metallic from Semiconducting Single-Walled Carbon Nanotubes.* Science, 2003. **301**(5631): p. 344-347.
57. Maria, D. and B. Peter, *Dielectrophoresis of carbon nanotubes using microelectrodes: a numerical study.* Nanotechnology, 2004. **15**(8): p. 1095.
58. Ghassemi, H.M., et al., *Field emission and strain engineering of electronic properties in boron nitride nanotubes.* Nanotechnology, 2012. **23**(10): p. 105702.
59. Bai, X., et al., *Deformation-driven electrical transport of individual boron nitride nanotubes.* Nano Lett, 2007. **7**(3): p. 632-7.

Chapter 7 Conclusions and outlook

In molecular electronics, single molecules are used as the active/passive elements in hybrid electronics or integrated circuits. Considering the dimension of a single molecule, a nanostructure compromising an individual molecule would represent the bridging element (e.g. a nanoelectrode) between molecules and electronic circuits. This in turn woul allow the understanding and full exploitation of the electrical properties of individual molecules to use them in molecular devices and systems.

In this work, we have focused on the synthesis, fabrication and manipulation of solution-processable nanostructures, in environmentally friendly aqueous solutions. A combination of bottom-up assembly strategies and technologies, and top down lithographic approaches have offered the possibility to organise different nanostructures on the surface in device configurations. Atomic Force Microscopy has been widely used to characterise both the topography and conductance of organic and inorganic nanostructures and nanohybrids. In particular, we studied: the molecular transport junctions based on the use of metallic ssDNA-wrapped SWCNTs as nanoelectrodes; the assembly of asymmetric junctions based on ssDNA-wrapped SWCNTs with different chirality, ssDNA-wrapped BNNTs and 1-D heterostructures of BNNTs and CNTs. In addition to lithography, shadow evaporation and AFM-probe scratching techniques have been explored to assist the deposition of the aforementioned nanostructures on surfaces.

In the context of the current focus on discovering molecules with interesting properties and on finding ways to obtain reliable and reproducible contacts between different molecular components and electrodes, we have present a solution-based assembly method for producing molecular transport junctions employing metallic single-walled carbon nanotubes as nanoelectrodes. With one end of the junctions in contact with a macroscopic electrode and the AFM conductive probe as a mobile electrode, electrical properties along the junctions have been investigated by Conducting Probe Force Microscopy (C-AFM). The molecular junction conductance of a series of oligophenyls was successfully measured and the values were found to be in line with ones obtained with established scanning-probe microscopy methods.

Another accomplishment of this work is the implementation of asymmetric junctions towards the synthesis of potential 1-D Schottky diodes. Metallic and a semiconducting ssDNA-wrapped SWCNTs were linked via three different methods, namely two-step amidation, click chemistry and DNA hybridization. The yield of junction formation was studied and compared for the three different assembly strategies. Overall a high yield up to 100 % was obtained.

Having gained confidence in the formation of molecular junctions, we proposed to assemble the nanostructures between electrodes to obtain devices. For this purpose, we relied on a shadow evaporation technique to make gap devices consisting of two planar electrodes separated by a “nanotrench” 20 to 400 nm wide. Ss-DNA wrapped SWCNTs were assembled on the trench via dielectrophoresis as a proof of principle. Beyond this, we investigated an alternative approach, using the AFM probe scratching, which can draw patterns as small as 10nm, opening the possibility to assemble nanostructures to selective areas.

Additionally, the unique properties (large band gap, piezoelectricity and thermal stability) of Boron Nitride Nanotubes have attracted us to their investigation in molecular electronics. We presented the dispersion of boron nitride nanotubes by DNA wrapping followed by the formation of nano-hybrids of boron nitride nanotubes and carbon nanotubes. Moreover, the successful dielectrophoretic assembly form solution to surface of dispersed BNNTs has been demonstrated.

While in this thesis we have shown the synthesis and assembly of a series of solution-processable nanostructures, some challenges still remain. The formation of asymmetric junctions has been confirmed by length analysis, but the Schottky effect has not been demonstrated yet. The random deposition works well for the molecular transport junctions in chapter 3 but not in the case of asymmetric junctions. The electrical characterisation by conductive AFM is limited by the extra Schottky barrier between the AFM probe and the semiconducting CNTs. Therefore, a more controlled organization of junctions on metal electrodes is required, especially for the asymmetric junctions.

In this regard, the main hurdle has indeed been the accurate assembly of molecular junctions between electrodes. Many attempts were made to contact the junctions to obtain single molecular electronic devices, but the dielectrophoretic assembly of molecular junctions was found to be not controllable enough to obtain a functioning device. Beyond that, the developed AFM probe scratching method patterned the surface successfully, while it failed to transfer that to the passivation surface due to limits in oxygen plasma control. Mainly because of time constraints, the assembly task was, at least temporarily, set aside. Solving the problems will definitely need a thorough study of the factors influencing dielectrophoresis of tube-like segments so that they can be controlled and aimed towards the specific goals of the case.

Despite the aforementioned challenges, the techniques developed in this thesis are directly applicable to fundamental studies of electron transport in molecules and other nanostructures. Plans for future work include the realisation of ss-DNA wrapped CNTs based molecular junctions with different molecules, quantum dots and proteins: this is currently underway in the Palma Laboratory. Moreover, device fabrication should be pursued by optimising the organization of junctions on surfaces, including, but not limited to, dielectrophoresis and selective deposition. Meanwhile, the dispersion of BNNTs may facilitate the advancement of new molecular electronics units for nano-generators and energy harvest applications.

The ultimate goal for electronic device minimization is controlling the building blocks with atomic accuracy. Molecules can provide such precise control over sub-nanometer distances as well as the possibility to reproducibly fabricate identical building blocks. Therefore, molecular electronics is an interesting and valuable option to overcome the bottleneck of semiconductor-based technologies.

Although it is always difficult to predict the future, there are convincing reasons to believe this research will help to bridge hard electronics to the soft molecular world, and the field will continue to grow. For instance, the developed methods for the fabrication of solution processable molecular transport junctions utilising carbon nanotubes as nanoelectrodes is an encouraging outlook for molecular electronics in terms of device yield, device-to-device stability, integration, energy consumption, addressability and low-cost fabrication.

Appendix A

Junction formation yield correction and Simulation

It is important to calculate the reaction yield for a chemical reaction to evaluate how complete the reaction is. The percentage yield is calculated by dividing the amount of obtained product by the theoretical amount of product as below:

$$\text{percentage yield} = \frac{actual\ yield}{theortical\ yield} \times 100\% \quad \text{(A-1)}$$

However, reaction yields for most reactions in nano science are difficult to determine. For instance, in the case of the molecular junction based on SWCNTs, the amount of the final product cannot be measured directly either physically or chemically. As reported previously, researchers found that the length of SWCNT segments measured in AFM topography images increases after junction formation. By plotting the histogram and calculating the average length, the success of reaction/coupling was confirmed without an extensive quantitative analysis (that was beyond the study presented)[1]. In this appendix, we present a simple model to estimate the reaction yield of junction formation based on the length distribution of SWCNT segments, as measured from AFM topographical images.

Appendix A

The starting material is the solution of pristine DNA-wrapped SWCNTs. The length distribution for these SWCNTs is narrow after size exclusion separation by high-performance liquid chromatography. **Figure A-1** shows a typical CNTs length histogram.

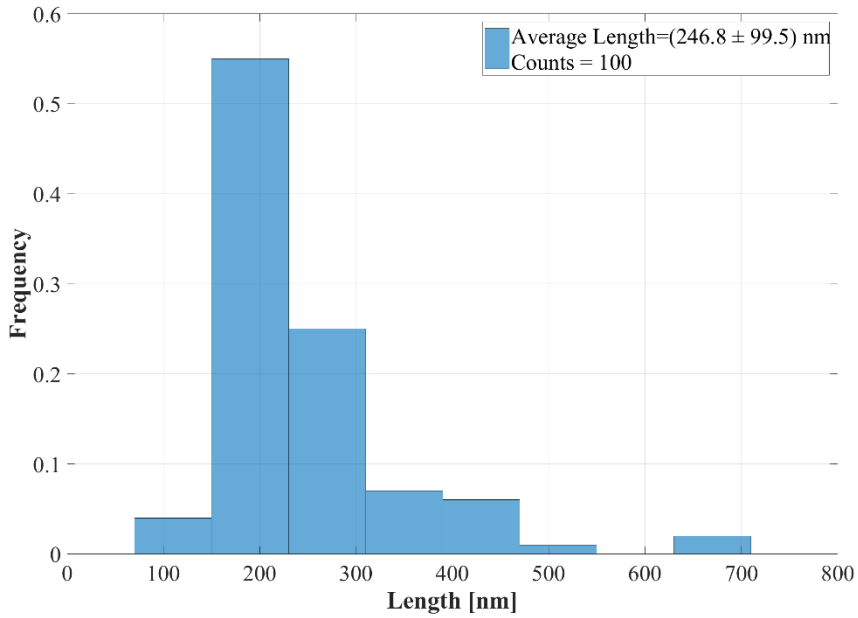

Figure A-1 Example of histogram plots of the length of pristine DNA-wrapped SWCNTs solution.

To find out the relationship between change in length of segments with the reaction yield, we have made a few reasonable assumptions. In the solution, there are N_0 carbon nanotubes to start with. We denote the length of each CNT as L_1, L_2, L_3, … L_{N0}. In this way, the average length of the CNTs (l_0) will be:

$$L_{mean} = \frac{\sum_1^{N_0} L_i}{N_0} = l_0 \qquad \text{(A-2)}$$

During the reaction, a second activated CNTs solution is added to the pre-purified CNT-linker solution as shown in **Figure A-2**.

Appendix A

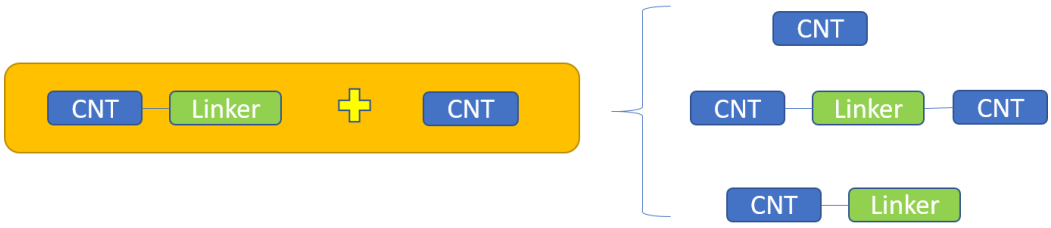

Figure A-2 Schematic of junction formation reaction

The two solutions are identical in terms of length since the length of molecular linker utilised is negligible (a few Å compared to several hundred nm). Statistically, we assume they have the same average length as well as length distribution. In this way, there are 2N nanotubes with an average length as:

$$L_{before,mean} = \frac{\sum_1^{2*N_0} L_i}{2 * N_0} = l_0 \tag{A-3}$$

As displayed in **Figure A-2**, there are three types of components in the final solution: unreacted CNTs, CNTs with a molecular linker, and CNTs junctions. The average lengths of the three components are l_0, l_0, $2l_0$. If we assume the reaction yield of junction formation is *x* percentage, the number of segments in the after-reaction mixture can be written as:

$$N' = N_0 * \left(1 - \frac{x}{100}\right) + N_0 * (1 - \frac{x}{100}) + N_0 * \frac{x}{100} = \left(2 - \frac{x}{100}\right) * N_0 \tag{A-4}$$

The average length of segments can then be written as:

$$L'_{after,mean} = \frac{2 * N_0 * l_0}{\left(2 - \frac{x}{100}\right) * N_0} = \frac{2}{\left(2 - \frac{x}{100}\right)} * l_0 = \frac{200}{200 - x} * l_0 \tag{A-5}$$

The length increase of the segments can be deducted based on the above equations as:

$$\mathrm{y} = \frac{L_{after,mean} - L_{before,mean}}{L_{before,mean}} * 100\% = \frac{\frac{200}{200 - x} * l_0 - l_0}{l_0} * 100\% \tag{A-6}$$

Finally**,** the relationship between length increment *x* and reaction yield *y* is:

$$y = \frac{100x}{200 - x} \; and \; x = \frac{200y}{100 + y} \tag{A-7}$$

Based on this equation, we list the reaction yields and corresponding length increments in intervals of 5, from 0 to 100. **Figure A-3** shows the plot of reaction yields vs length increments.

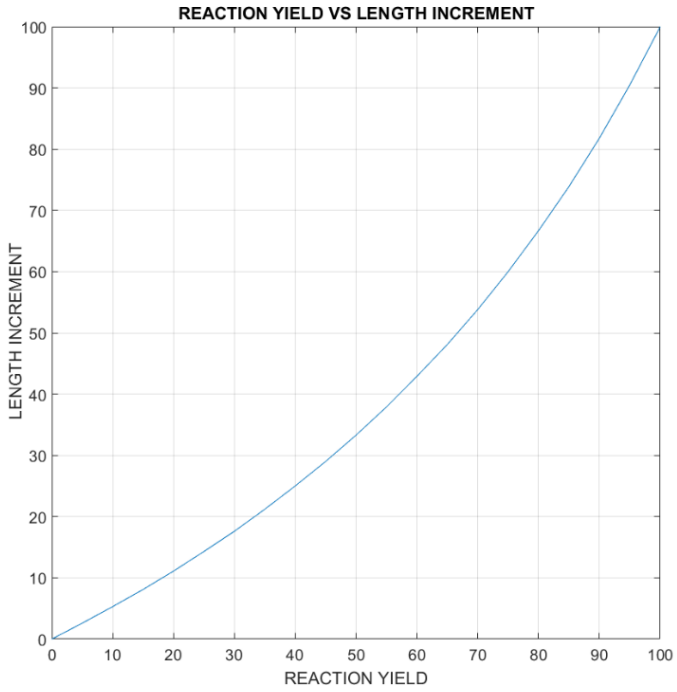

Figure A-3 Plot reaction yields vs length increments

To further confirm the calculations made above, we perform a Matlab simulation using similar conditions. The numerical starting data is utilised as 1000 carbon nanotubes with an average length of 600 nm and a standard deviation of 200 nm. The numbers are selected close to the experimental data in our project. In the simulation, x (reaction yield) percentage of the tubes from two groups are coupled one to one to form the junctions. The length will be the sum of the two component tubes. The length of all the segments is then counted and plotted as the histogram. Four representative histogram plots are shown in **Figure A-4** and Figure A-5. Original length distribution is included in the

figures as well for comparison. The reaction yields are 10%, 40%, 70% and 95%. The length increments are then estimated to be 5%, 25%, 54% and 90% respectively.

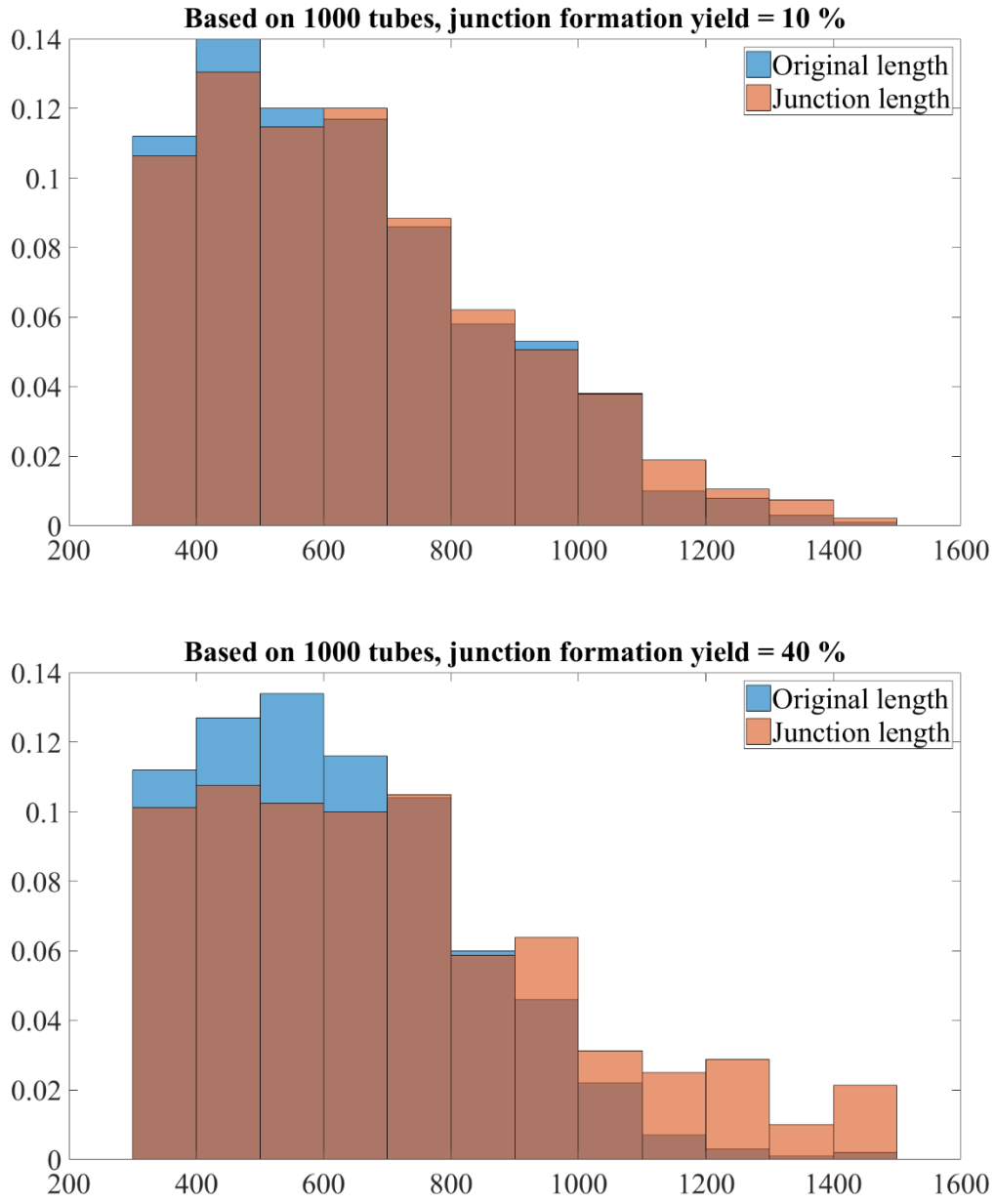

Figure A-4 Comparison Histograms for junction formation with reaction yields as 10% (upper) and 40% (bottom). Blue columns correspond to the histogram of length for original SWCNTs solution while the orange columns correspond to the histogram of length for molecular junctions solution. The brown part in the figure indicate the overlapping data.

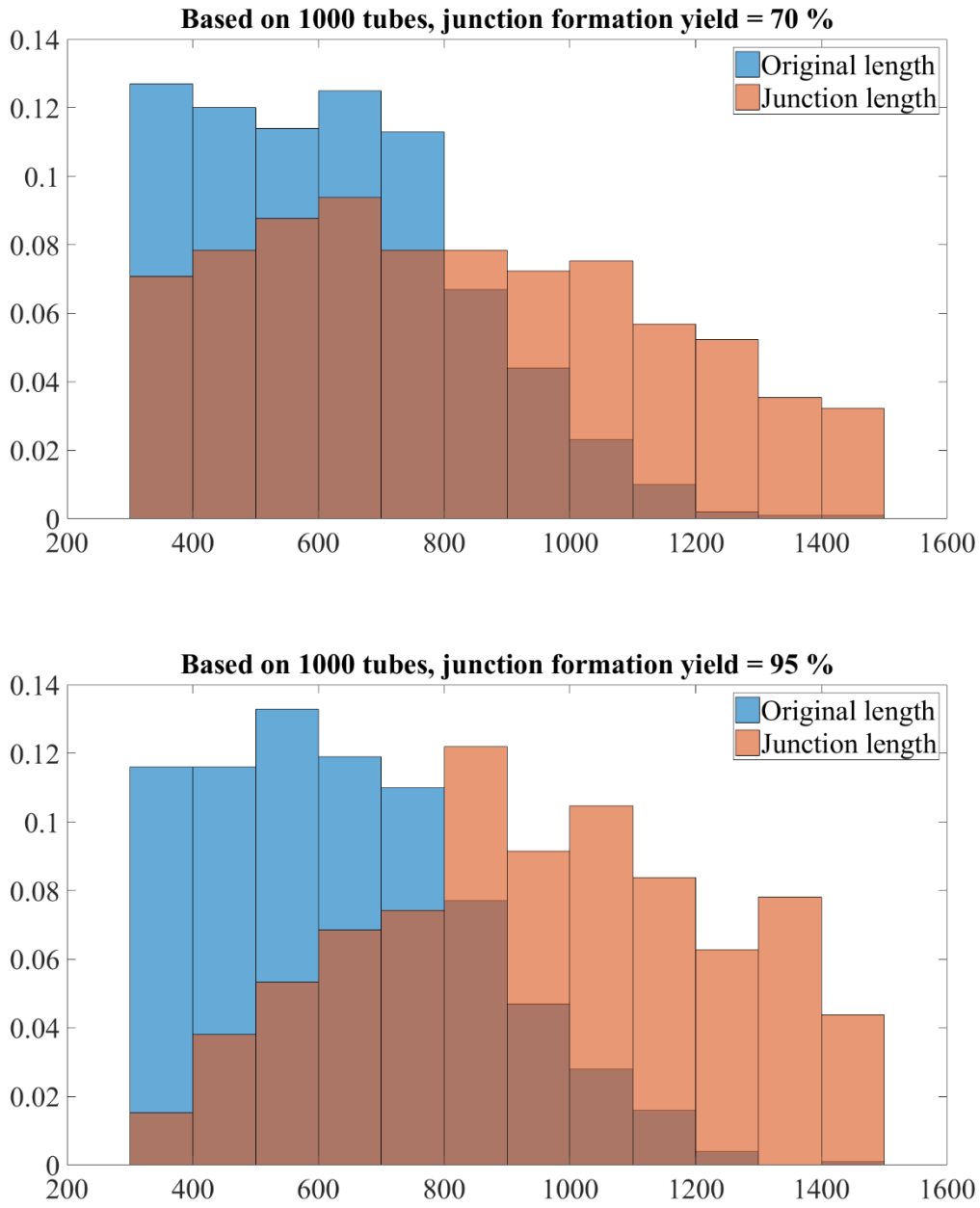

Figure A-5 Comparison Histograms for junction formation with reaction yields as 70% (upper) and 95% (bottom). Blue columns correspond to the histogram of length for original SWCNTs solution while the orange columns correspond to the histogram of length for molecular junctions solution. The brown part in the figure indicate the overlapping data.

Appendix A

The Matlab code for simulation is attached for reference.

```
%%test for histogram of CNT junction
%% Author: Jingyuan Zhu
%  Date: 08/17/2017


clc;
clear;
% for ORGINAL cnt
s_o=input( 'CNT number ? ');
if isempty(s_o)
s_o = 1000;  % number of CNTs
end
l_o =500+300*random('Normal',0,1,s_o,1);
% assume differnet percentage of junction has been formed successfully
r_p=input( 'junction yield ? ');
if isempty(r_p)
r_p = 50;  % 50 percent
end
l_a= randperm(s_o,floor(size(l_o,1)*r_p/200));
l_b= randperm(s_o,floor(size(l_o,1)*r_p/200));
l_j=l_o(l_a)+l_o(l_b);
l_j_summary=[l_j; l_o(randperm(s_o,s_o-floor(size(l_o,1)*r_p/100)))];



figure('units','normalized','outerposition',[0 0 1 1])
edges=[300:100:1500];
histogram(l_o,edges,'Normalization','probability');
hold on;
histogram(l_j_summary,edges,'Normalization','probability');


legend1 = sprintf('Original length');
legend2 = sprintf('Junction length');
legend3 = sprintf('Based on %d tubes, junction formation yield
= %d %%',s_o,r_p);
```

Appendix A

```
h_legend=legend(legend1, legend2,'location','northeast');

set(h_legend,'FontSize',14);

title(legend3'FontSize',14);

legend4 = sprintf('avarage lentgh : %d nm  %d nm;',mean(l_o),std(l_o));

legend5 = sprintf('avarage lentgh : %d nm  %d
nm;',mean(l_j_summary),std(l_o));

text(1100,0.1,legend4,legend5,'FontSize',14);


fname=legend3;

saveas(gcf,fname,'jpg');
```

References

1. Zhu, J., et al., *Solution-Processable Carbon Nanoelectrodes for Single-Molecule Investigations.* Journal of the American Chemical Society, 2016. **138**(9): p. 2905-2908.

Appendix B

Molecular weight of Single Walled Carbon Nanotubes

The calculations are based on the following hypothesis: the length of the C=C bonds in the curved graphene sheets is the same than in the planar sheet, i.e. $d_{C=C}$ = 0.1421 nm.

As reported earlier [1], the specific surface area of an SWCNT, whatever its diameter/chirality, is that of one side of a graphene sheet, i.e. 1315 m^2 /g. Thus, the molecular weight of any SWCNT (WSW) of diameter d and length L can be calculated from the surface area of the graphene sheet:

$$M_w = \frac{1}{1315} * \pi * L * d * N_A \quad \text{(B-1)}$$

By substituting the numerical value into the above equation, we can have the molecular weight as:

$$M_w = 1.44 * 10^{21} * L * d \quad \text{(B-2)}$$

References

1. Peigney, A., et al., *Specific surface area of carbon nanotubes and bundles of carbon nanotubes.* Carbon, 2001. **39**(4): p. 507-514.

Appendix B